DOCTORAL THESIS

2019

COALESCENCE OF EXOTIC COMPACT OBJECTS IN THE NEW ERA OF GRAVITATIONAL WAVE ASTRONOMY

Miguel Bezares Figueroa

DOCTORAL THESIS

2019

Doctoral Programme of Physics

COALESCENCE OF EXOTIC COMPACT OBJECTS IN THE NEW ERA OF GRAVITATIONAL WAVE ASTRONOMY

Miguel Bezares Figueroa

Thesis Supervisor: Carlos Palenzuela Luque
Thesis tutor: Carles Bona García

Doctor by the Universitat de les Illes Balears

Universitat
de les Illes Balears

WE, THE UNDERSIGNED, DECLARE:

That the Thesis titled

Coalescence of Exotic Compact Objects in the new era of gravitational wave astronomy ,

presented by Sr. Miguel Bezares Figueroa to obtain a doctoral degree, has been completed under the supervision of Dr. Carlos Palenzuela.

For all intents and purposes, we hereby sign this document.

Palma de Mallorca,

_____
Sr. Miguel Bezares

_____
Dr. Carlos Palenzuela Luque

UNIVERSITAT DE LES ILLES BALEARS

Summary

The direct detection of gravitational waves by **LIGO** and **Virgo** interferometric observatories has opened a new multi-messenger era to study some of the most energetic phenomena occurring in the Universe. Although the detections are so far consistent with the coalescence of binary black holes and the inspiral of binary neutron stars systems, in the future we could detect gravitational waves from new binary systems composed of different compact objects. These putative *Exotic Compact Objects* (**ECOs**) could exist in theory but have not yet been found in Nature, since they are supposed to be too dim to be detected by current electromagnetic telescopes.

In this Thesis we study, through full three dimensional numerical relativity simulations, the dynamics of these **ECOs** and the gravitational radiation emitted during their coalescence, focusing in binaries formed by boson stars (i.e., self-gravitating objects modeled with a complex scalar field), dark matter stars (i.e., astrophysical compact objects that only interact with other stars through gravity) and neutron stars with a small fraction of dark matter on their interiors (i.e., modeled by mixed fermion-boson stars).

Gravitational waves from the coalescence of compact objects play an important role probing gravity in the strong-field regime. Hence, our studies are crucial to discriminate whether future non-standard gravitational wave detections come from unknown sources such as **ECOs**. Consequently, exploring the signature of these gravitational waves could reveal their existence.

UNIVERSITAT DE LES ILLES BALEARS

Resum en català

La detecció directa d'ones gravitacionals a través dels observatoris interferomètrics **LIGO** i **Virgo** obre una nova era de multimissatgers per estudiar alguns dels fenòmens més energètics que ocorren en l'univers. Tot i que, fins ara, les deteccions són coherents amb la fusió de sistemes binaris de forats negres i amb la col·lisió entre dues estrelles de neutrons, en el futur es podran detectar ones gravitacionals provinents de nous sistemes binaris composts de diferents objectes compactes. Aquests aparents *objetes compactes exòtics* (**ECOs**) podrien existir en teoria, però encara no han estat trobats en la natura, ja que se suposa que són massa tènues com per poder ser detectats pels telescopis electromagnètics actuals..

En aqueta tesi estudiam, a través de simulacions numèriques tridimensionals de relativitat, la dinàmica d'aquests **ECOs** i la radiació gravitacional emesa durant la seva coalescència, enfocant-nos en sistemes binaris formats per estrelles de bosons (és a dir, objectes auto-gravitants modelats amb un camp escalar complexe), estrelles de matèria obscura (és a dir, objectes compactes astrofísics que només interactuen amb d'altres estrelles a través de la gravetat) i estrelles de neutrons amb una petita fracció de matèria obscura en el seu interior (és a dur, modelades per estrelles mixtes de fermió-bosó).

Les ones gravitacionals de coalescència d'objectes compactes juguen un important rol en l'estudi de la gravetat forta. És per això que el nostre estudi és crucial per discriminar si futures deteccions d'ones gravitacionals atípiques serien provinents de fonts desconegudes, tals com els **ECOs**. Per consegüent, explorar la impromta d'aquestes ones gravitacionals podria revelar la seva existència.

UNIVERSITAT DE LES ILLES BALEARS

Resumen en castellano

La detección directa de ondas gravitacionales a través de los observatorios interferométricos **LIGO** y **Virgo** abre una nueva era de multimensajeros para estudiar algunos de los fenómenos más energéticos que ocurren en el Universo. Aunque hasta ahora las detecciones son coherentes con la fusión de sistemas binarios de agujeros negros y con la colisión entre dos estrellas de neutrones, en el futuro podremos llegar a detectar ondas gravitacionales provenientes de nuevos sistemas binarios compuestos de objetos compactos diferentes. Estos aparentes *objetos compactos exóticos* (**ECOs**) podrían existir en teoría, pero aún no se han encontrado en la naturaleza, ya que se supone son demasiado tenues para ser detectados por los telescopios electromagnéticos actuales.

En esta tesis estudiamos, a través de simulaciones numéricas tridimensionales de relatividad, la dinámica de estos **ECOs** y la radiación gravitacional emitida durante su coalescencia, enfocándonos en sistemas binarios formados por estrellas de bosones (es decir, objetos auto-gravitantes modelados con un campo escalar complejo), estrellas de materia oscura (es decir, objetos compactos astrofísicos que solo interactúan con otras estrellas a través de la gravedad) y estrellas de neutrones con una pequeña fracción de materia oscura en su interior (es decir, modeladas por estrellas mixtas de fermión-bosón).

Las ondas gravitacionales de la coalescencia de objetos compactos juegan un importante rol en el estudio de la gravedad fuerte. Es por ello que nuestro estudio es crucial para discriminar si futuras detecciones de ondas gravitacionales atípicas serían provenientes de fuentes desconocidas, tales como los **ECOs**. Por consiguiente, explorar la huella de estas ondas gravitacionales podría revelar su existencia.

List of publications derived from this thesis

1. ***Final fate of compact boson star mergers***.
   Authors: **M. Bezares**, C. Palenzuela and C. Bona.
   Journal: Physical Review D, 95, Issue 12 (2017), p. 124005.
   DOI: 10.1103/PhysRevD.95.124005. arXiv: 1705.01071 [gr-qc].
   URL: https://link.aps.org/doi/10.1103/PhysRevD.95.124005

2. ***Gravitational Wave Signatures of Highly Compact Boson Star Binaries***
   Authors: C. Palenzuela, P. Pani, **M. Bezares**, V. Cardoso, L. Lehner, S. Liebling.
   Journal: Physical Review D, 96, Issue 10 (2017), p. 104058.
   DOI: 10.1103/PhysRevD.96.104058. arXiv: 1710.09432 [gr-qc].
   URL: https://link.aps.org/doi/10.1103/PhysRevD.96.104058

3. ***A Simflowny-based finite-difference code for high-performance computing in Relativity***.
   Authors: C. Palenzuela, B. Miñano, D. Vigano, A. Arbona, C. Bona-Casas, A. Rigo, **M. Bezares**, C. Bona and J. Mass.
   Journal: Classical and Quantum Gravity, Vol. 32, Number 18 (2018).
   DOI: 10.1088/1361-6382/aad7f6. arXiv: 1806.04182 [physics.comp-ph].
   URL: http://iopscience.iop.org/article/10.1088/1361-6382/aad7f6/meta

4. ***Gravitational Waves from Dark Boson Star binary mergers***
   Authors: **M. Bezares** and C. Palenzuela.
   Journal: Classical and Quantum Gravity (2018), Volume 35, Number 23. Focus Issue on Numerical Relativity Beyond General Relativity.
   DOI: 10.1088/1361-6382/aae87c. arXiv:1808.10732 [gr-qc]
   URL: https://iopscience.iop.org/article/10.1088/1361-6382/aae87c/meta

5. ***Signatures of dark matter cores in binary neutron star mergers.***
   Authors: **M. Bezares**, D. Vigano and C. Palenzuela.
   Journal: Submitted to Physical Review D (2019). arXiv ID: 1905.08551 [gr-qc]

List of publications NOT included in this thesis

1. ***Anisotropic stars as ultracompact objects in General Relativity.***
   Authors: G. Raposo, P. Pani, **M. Bezares**, C. Palenzuela and V. Cardoso.
   Journal: Physical Review D (2019). arXiv ID: 1811.07917 [gr-qc]

2. $3+2$ ***Cosmology: unifying FRW metrics in the bulk.***
   Authors: C. Bona, **M. Bezares**, B. Pons and D. Vigano.
   Journal: Physical Review D 99, 043530 (2019).
   DOI: 10.1103/PhysRevD.99.043530. arXiv ID:1810.04429. [gr-qc]
   URL: https://journals.aps.org/prd/abstract/10.1103/PhysRevD.99.043530

3. ***Kaluza-Klein Cosmology: the bulk metric.***
   Authors: C. Bona and **M. Bezares**.
   Journal: Submitted to Physical Review D (2019). arXiv ID: 1904.11239 [gr-qc]

Agradecimientos

Sin lugar a dudas, una de las cosas más importante que la vida me ha ensañado es a agradecer. A lo largo de estas líneas quiero agradecer a todas las personas que estuvieron en este camino, los cuales me han brindado su amistad, apoyo y hasta sus fuerzas para poder finalizar esta cautivante etapa.

En primer lugar a mi amada esposa Any, la cual desde un comienzo no dudo en emprender este camino junto a mí. Muchas gracias por tu altruismo, tu me acompañaste a cumplir mis sueños. Durante estos cuatro años hemos vivido momentos bondadosos y otros un tanto difíciles, sin embargo siempre has estado ahí para animarme y motivarme, te agradezco por todo ello. Indudablemente, tu apoyo y coraje me ayudaron a finalizar este ciclo.

Me gustaría agradecer a mi director de tesis Dr. Carlos Palenzuela. Esta tesis sin duda alguna es gracias a ti. Te agradezco por creer en mi y darme la oportunidad de desarrollarme como investigador. Muchas gracias por ser un líder, por motivarme, inspirarme y guiarme con mucha paciencia cada día. Gracias por cada detalle que tuviste hacia mi persona, en lo académico y en lo personal, los cuales fueron innumerables. Gracias por cada consejo. Siempre estaré en deuda contigo.

También me gustaría agradecer al Profesor Dr. Carles Bona por permitirme investigar con él, ha sido un honor colaborar con usted y por supuesto agradecerle toda la ayuda otorgada en términos administrativos, fundamentales para mi estancia en Mallorca.

Mi vida en Mallorca durante estos cuatro años ha sido especialmente amena, gracias a grandes personas que he conocido. Quizás emprender un desafío en otro país lejos de tus seres queridos puede ser difícil, pero por estas personas que han sido como una familia aquí, todo se ha hecho mas fácil. Me gustaría agradecer a ellos, Joan Barceló i Aguiló y Xisco Jiménez por todo el apoyo brindado, por la comprensión y las palabras justas en los momentos difíciles. Gracias Joan por tu traducción al Catalán del resumen de mi tesis. Gracias Xisco por darte el tiempo de leer mi tesis y ayudarme con el manuscrito. Gracias Tania, Daniele, Reachel, Fede, Lu, Borja, Magda, Gemma, Monir, Antonio, Ricard, por su sincera amistad y hacer de mi estadía en Mallorca la mejor.

Finalmente, quiero agradecer a CONICYT Chile (concurso de becas de doctorado en el extranjero) por su apoyo financiero, el cual me permitió realizar mi doctorado.

Contents

List of Figures

List of Tables

Abbreviations

ADM	**A**rnowitt **D**eser **M**isner
aLIGO	**a**dvanced **LIGO**
AMR	**A**daptive **M**esh **R**efinement
BH	**B**lack **H**ole
BSs	**B**oson **S**tars
BSSN	**B**aumgarte **S**hapiro **S**hibata **N**akamura
CCZ4	**C**ovariant **C**onformal Z4 formalism
CFL	**C**ourant **F**riedrichs **L**ewy
DBSs	**D**ark **B**oson **S**tars
DM	**D**ark **M**atter
DSs	**D**ark **S**tars
EM	**E**lectro**M**agnetic
ECOs	**E**xotic **C**ompact **O**bjects
EKG	**E**instein **K**lein **G**ordon
EOB	**E**ffective **O**ne **B**ody
EoS	**E**quation **o**f **S**tate
FBs	**F**ermion-**B**oson stars
FDA	**F**inite **D**ifference **A**pproximation
GR	**G**eneral **R**elativity
GRHD	**G**eneral **R**elativistic **H**ydro-**D**ynamics
HD	**H**ydro-**D**ynamics
HLL	**H**arten-**L**ax-van **L**eer-Einfeldt flux formula
HRSC	**H**igh **R**esolution **S**hock **C**apturing
IBVP	**I**nitial **B**oundary **V**alue **P**roblem
ISF	**I**nteracting **S**calar **F**ield

KG	**K**lein **G**ordon
KO	**K**reiss-**O**liger
LIGO	**L**aser **I**nterferometer **G**ravitational Wave **O**bservatory
LLF	**L**ocal-**L**ax-**F**riedrichs
LISA	**L**arge **I**nterferometer **S**pace
MoL	**M**ethod **o**f **L**ines
MPI	**M**essage **P**assing **I**nterface
NISF	**N**o-**I**nteracting **S**calar **F**ield
NS	**N**eutron **S**tar
NR	**N**umerical **R**elativity
ODE	**O**rdinary **D**ifferential **E**quation
PDE	**P**artial **D**ifferential **E**quation
PN	**P**ost-**N**ewtonian Approximation
PPM	**P**iecewise **P**arabolic **M**ethod
QNM	**Q**uasi **N**ormal **M**odes
RK	**R**unge-**K**utta
SSS	**S**pherically **s**ymmetric **s**pacetime
TT	**T**ransverse **T**raceless

Preface

The recent detections of gravitational waves by the **LIGO** and **Virgo** interferometric observatories, consistent with the merger of binary black hole systems – ten up to April 2019, see in Figure 1 and in Refs. [9–14]–, has opened a new era of gravitational wave astronomy leading to unprecedented discoveries. The existence of gravitational radiation was indirectly inferred since 1974 with the first indirect measurements by Hulse and Taylor, who showed that the changes in the orbital motion of two pulsar in a binary system **PSR B1913+16** were consistent with the energy loss due to the emission of gravitational waves [15]. Conversely, these new recent discoveries are the first direct proof of the existence of gravitational waves, confirming that black holes exist and are able to form binary systems. In particular, during the first advanced detector **LIGO** run from 12 September 2015 until 16 January 2016, usually called O1, gravitational waves from three binary black holes were detected (**GW150914, GW151012, GW151226**). During the second observing run from November 2016 to August 2017, O2, seven more binary black hole merger were reported (**GW170104, GW170608, GW170814, GW170729, GW170809, GW170818** and **GW170823**). The total mass of these binaries ranged from $18.6^{+3.1}_{-0.7} M_\odot$ to $85.1^{+15.6}_{-10.9} M_\odot$, leading to a single rotating black hole after the merger between $17.8^{+3.2}_{-0.7} M_\odot$ and $80.3^{+14.6}_{-10.2} M_\odot$. The estimate distances range from 320^{+120}_{-110} Mpc to 2750^{+1350}_{-1320} Mpc, see Table III in Reference [14].

More recently, during the observing run O2, the gravitational wave corresponding to the inspiral of a binary composed by neutron stars has also been observed [16, 17]. This signal was followed by a plethora of electromagnetic counterparts, including a gamma-ray burst [18] and a thermal infrared/optical spectra consistent with a kilonova [19], which was detected by both the Fermi and Integral satellites, starting a fruitful era of multi-messenger astronomy, see Figure II in [17] that shows the time-line of that event.

The reason behind more than forty years between the measurements of Hulse and Taylor and the direct detection by **LIGO/Virgo** interferometers is the intrinsically small amplitude of gravitational waves, which makes their detection extremely challenging. For

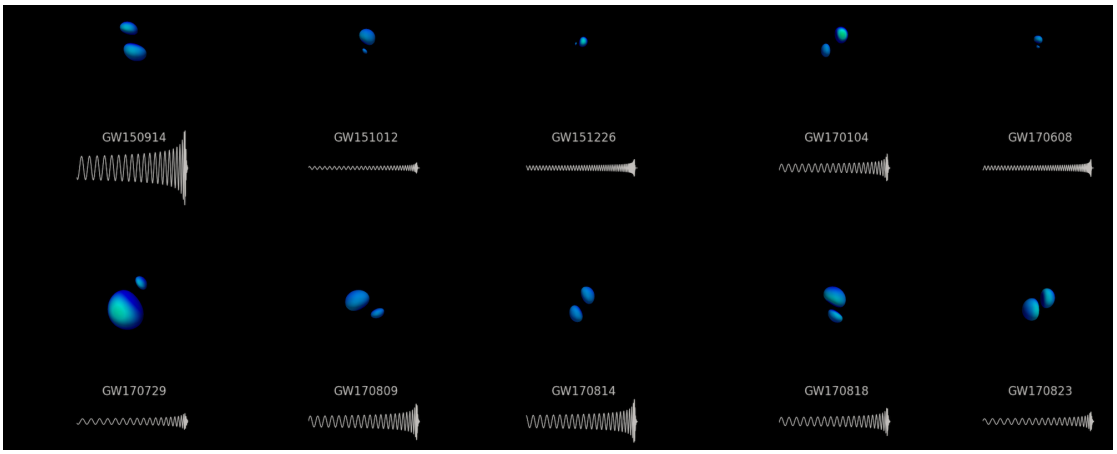

FIGURE 1: An illustration of the ten mergers of binary black holes detected so far. Figure from: SXS Collaboration/LIGO-Virgo Collaboration.

instance, the relative change in the local distances (strain[1]) produced in the detectors due to the gravitational waves emitted by two black holes of masses $M = 10M_{\odot}$ orbiting around each other with a separation of $600km$ at a distance of $100\,Mpc$ from Earth, is only $\sim 10^{-21}$. This means that such an energetic event in our neighborhood only will change the Earth detector geometry in one part of 10^{21} [20].

There are many different sources of gravitational waves. The strongest and most plausible ones include: (i) binary coalescence of massive compact objects like black holes and/or neutron stars [9, 16], (ii) continuous gravitational waves, which are produced by non-axisymmetric spinning compact stars that rotates with a quite constant frequency, typically pulsars [21, 22], (iii) gravitational waves bursts, which are coming mostly from unknown or unexpected sources with a short-duration, as for example supernova core-collapse supernova [23–25], and finally (iv) stochastic gravitational waves, produced from a wide random number of independent events (i.e., such as those described above). They form a stochastic background of gravitational waves made by the superposition of numerous incoherent sources [26–28]. One of the expected stochastic gravitational waves is the Big Bang, which could help us describe the Universe at its earliest instants [26, 29].

Undoubtedly, as the ground-detectors **LIGO** and **Virgo** improve their sensibilities and new ground-based detectors like **KAGRA** in Japan [30] and **IndIGO** (LIGO-India) [31] are included to the network, many more gravitational wave detections will be soon available. In addition, the space-based detector **LISA** will be launched in the years to come. This detector will give us the opportunity to observe the heaviest and most diverse object in our Universe by detecting low-frequency waves that will probably never be accessible from the Earth detector [32] (see Figure 2). These detections are inevitably leading to breakthroughs in our understanding of some of the most exciting objects and

[1] See Chapter 1 equation (1.32).

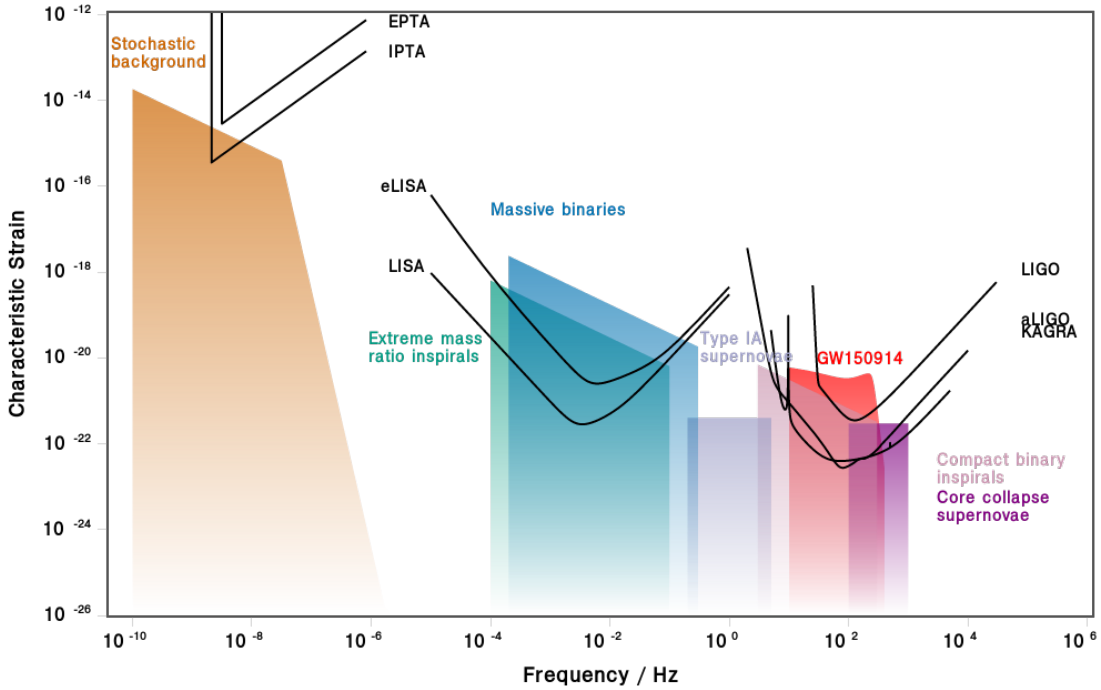

FIGURE 2: *Gravitational waves detectors and sources.* The plot shows the gravitational wave sensitivity-curve plot using characteristic strain of different gravitational waves sources. A source will be detectable if the characteristic strain is above of the detector curve. Figure adapted from [1, 2]

phenomena in the Universe, as well as providing clues to fundamental physics, such as the properties of matter at nuclear densities [33–36] and stringent tests of general relativity [37–42].

One of the most prominent opportunities in this rising era of gravitational wave astronomy is to study the strong-gravity regime through the signals produced during the coalescence of compact objects. The anatomy of gravitational wave signals from this coalescence can be divided in three stages, illustrated in Figure 3, namely:

(i) **inspiral:** the two compact objects are still far from each other such that the dynamics of the system (i.e., the amplitude and the phase of gravitational waves increases as the orbit separation decreases) can be described by Post-Newtonian [43] or Effective-One-Body approximation [44];

(ii) **merger:** once the compact objects pass the last stable circular orbit their separation quickly decreases until that they merge. Here, the relativistic effects are important, non-linear effects are dominant the gravitational wave emission reaches its peak in amplitude. The full solution of the Einstein equations are needed in order to reproduce this stage, which can only be solved by numerical simulations;

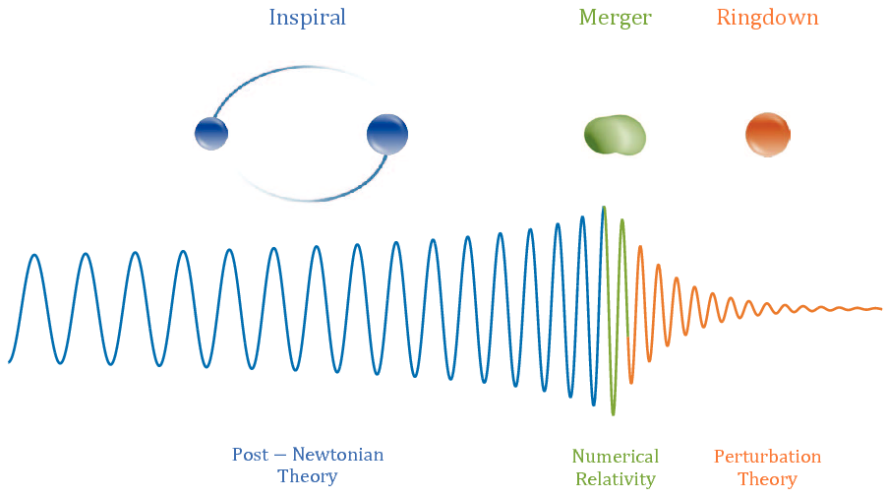

FIGURE 3: *Anatomy of gravitational wave signals.* The three stages during the temporal evolution of a binary system. During the inspiral stage, the two object are orbiting and approaching each other. During the merger phase, the two objects get close enough colliding, here relativistic effects become important. During the post-merger phase the resulting object dissipates energy away and tends to settle down to a new equilibrium state. Figure from [3].

(iii) **post-merger:** the remnant of the merger, after a transient, settles down into a quasi-equilibrium state. At that stage, the gravitational wave signal shows characteristic frequencies called quasi-normal modes. Such modes can be studied by using the perturbation theory [45–47]. For binary black holes this stage is known as ring-down, since the amplitude of the signal decays exponentially as the remnant (i.e., a perturbed black hole) settles down into a Kerr black hole.

More detections will surely increase our knowledge and understanding of compact objects in the Universe. Besides studying binaries made of black holes and neutron stars, which now represent the standard compact objects, exploring the extent to which alternatives differ in their gravitational waves signatures remains as an important test to carry on. In addition to these standard sources, gravitational waves can allow us to find unknown (and unexpected!) astrophysical compact objects which have not been observed yet due to their low brightness. These alternative objects are known generically as Exotic Compact Objects (i.e., see Reference [48] for a review) and include, for example, fuzzballs [49], gravastars [50], wormholes [51], anisotropic stars [52], boson stars [53], Proca stars [54], etc.

Here, we will present our numerical studies on the mergers of binary Exotic Compact Objects performed by solving Einstein equations with different types of exotic matter. Our aim is to analyze the gravitational waves emitted during their mergers and identify signatures which could help us to distinguish them from standard compact objects. We will consider three different types of binaries:

(i) **Boson Stars:** solutions made of a complex scalar field with a time harmonic dependence [53, 55], representing the macroscopic wave-function of a Bose-Einstein condensate. The stability properties of a boson star resemble those of neutron stars, and, in particular, they are stable below a critical mass. The discovery of the Higgs boson in 2012 [56, 57] shows that at least one scalar field exists in Nature; if other (stable) bosonic particles exist in the universe they might clump together to form self-gravitating objects (i.e., Bose-Einstein condensates). Boson stars provide a simple and useful model to study compact bodies in very different scenarios, ranging from dark matter candidates to black hole mimickers, see [58, 59] for a review.

(ii) **Dark Stars:** defined as self-gravitating astrophysical compact objects which only interact through gravity with other stars. These regular objects may be thought as a generalization of a black hole but without horizon and with a wider range of compactness. Here we construct these objects by using bosonic matter, but fermionic matter can be used as well [60].

(iii) **Fermion-Boson Stars:** Dark matter particles might cluster inside neutron stars. This system can be modeled by using two types of matter, the neutron star matter with a fermionic perfect fluid and dark matter as bosonic matter by using a complex scalar field. The stationary compact solutions of this system are called fermion-boson stars [61, 62].

Last but not least, Numerical Relativity is the key tool to explore the non-linear strong regime of gravity, as we mentioned above, and in particular, the collision of binary compact objects. With accurate numerical simulations we can decode the information carried out by gravitational radiation. The success of a binary simulation relies on a well-posed formulation at the continuum level combined with suitable numerical schemes to achieve a stable and convergent solution at the discrete level [63].

Although each Chapter is well-motivated and summarized in the preamble, for reader convenience we give a sum up of the structure of the Thesis. Chapter 1 is a brief overview of some notions of differential geometry which are used throughout this Thesis, setting the notation and conventions for the basic mathematical objects. In Chapter 2, the so called 3+1 decomposition is studied. We present our modification of the covariant conformal Z4 formalism and study its characteristic structure, showing that the evolution system remains well-posed. Chapter 3 is based on the Einstein field equations coupled to matter, focusing on models with either scalar fields or perfect fluids. Here we present the relativistic Klein-Gordon equations and Relativistic Hydrodynamical equations, which are the evolution systems governing these two model. Finally, we explain

how to construct isolated boson and neutron stars. In Chapter 4, we study the numerical method used for solving the discretized Einstein field equations with matter sources. Chapter 5 is focused in the coalescence of boson stars, investigating the properties of the remnant resulting from the merger and the gravitational waves radiated during the collisions. Chapter 6, we analyze the dynamics and gravitational waves produced during the binary coalescence of equal mass dark stars composed by bosonic fields. We compare our results both with Post-Newtonian approximations and with previous simulations of binary boson stars. In Chapter 7, we present a recent study that consists in simulations of binary fermion-boson star mergers. Finally, we present the concluding remarks and future works. The Appendix presents some estimative of the total gravitational radiation in the post-merger employed in Chapter 5 and Chapter 6 of this Thesis.

Conventions and Notation

Throughout this thesis, we are using the system of geometric units, where the speed of light c and Newton's gravitational constant G are set equal to one, unless otherwise stated. Roman letters from the beginning of the alphabet $a, b, c, \ldots$, denote space-time indices ranging from 0 to 3, while letters near the middle $i, j, k, \ldots$ range from 1 to 3, denoting spatial indices. The covariant derivative of a quantity T is noted as $\nabla_a T$ and the partial derivative as $\partial_a T = \frac{\partial}{\partial x^a} T$. The Einstein summation rule applies, namely repeated indices are summed over all their possible values.

Chapter 1

Some elements of General Relativity

General Relativity is the modern theory of gravitation, formulated by A. Einstein in 1915 [64]. Einstein's theory established that gravity was no longer to be considered a force, but a manifestation of the curvature of spacetime itself. Therefore, the curvature of spacetime (as a continuum space) can not be formulated in term of an Euclidean space. Instead, it is required a sophisticated mathematical structure, based on differential geometry, called differential manifold.

This Chapter summarizes some basics concepts of differential geometry which are used throughout this Thesis, presenting the mathematical language of General Relativity. Therefore, in Section 1.1 basic mathematical concepts are described, emphasizing in: (i) differential manifolds, which give us the structure where the objects of General Relativity are defined, (ii) vectors and tensor fields, objects which encode the physical information of this theory and (iii) derivatives onto differential manifold. In Section 1.2, the field equations are presented. Finally, in Section 1.3, we study the weak field regime of Einstein's equations to obtain the quadrupole formula for gravitational radiation. This Chapter is based on the books [63, 65–68].

1.1 Basics concepts of Differential Geometry

The foundations of General Relativity rely on some basic concepts and tools of differential geometry. We shall start defining a *n-dimensional differential manifold* $\mathcal{M}$, that is a topological space which can be covered by a collection of *charts* $\{U_\alpha, \phi_\alpha\}_{\alpha\in A}$, where U_α is an open subset of $\mathcal{M}$, for each $\alpha \in A$ and $\phi_\alpha : U \to \mathbb{R}^n$ is a smooth injective mapping.

Given a point $p \in U$, $\phi_\alpha(p) = (x^1, \ldots, x^n) =: (x^a)$ are called the *local coordinate* on U_α, for each $\alpha \in A$.

A *curve* on $\mathcal{M}$ is a map $\gamma : I \to \mathcal{M}$, being $I \subseteq \mathbb{R}$ an interval, such that for each chart (U_α, ϕ_α) the composition $\phi_\alpha \circ \gamma : I \subseteq \mathbb{R} \to \mathcal{M}$ is a smooth map. In term of local coordinates (x^a) defined over a chart $\{U_\alpha, \phi_\alpha\} \subset \mathcal{M}$, the curve is written as $x^a(\lambda) = (x^1(\lambda), \ldots, x^n(\lambda))$, where $\lambda \in I \subseteq \mathbb{R}$ is the parameter of the curve. Here, the *tangent vector* to the curve $x^a(\lambda)$ is given by $v^a = dx^a/d\lambda$. At every point $p \in \mathcal{M}$, we can associate a vector space T_pM, called the *tangent space* at p, whose element are known as *vectors*. The tangent space can be defined as a equivalence classes of curves through p under a suitable equivalence relation. The collection of all tangent spaces on $\mathcal{M}$ is called the *tangent bundle* $T\mathcal{M} = \cup_{p\in\mathcal{M}} T_p\mathcal{M}$. The curve γ on $\mathcal{M}$ is the *integral curve* of a vector v if the tangent vector of the curve coincides with v, and therefore, a congruences curves is the set of integral curves of a vector field v on M.

A *one-form* (or covector) is real valued function of a vector. The set of *covectors* at a point $p \in \mathcal{M}$ for a vector space named *cotangent space* $T_p^*\mathcal{M}$, and we shall denote ω_a. The set of all cotangent spaces on $\mathcal{M}$ is the *cotangent bundle* $T^*\mathcal{M} = \cup_{p\in\mathcal{M}} T_p^*\mathcal{M}$, for further mathematical details see [65]. Using elements of $T_p\mathcal{M}$ and $T_p^*\mathcal{M}$, we can construct higher rank objects called tensors. A *tensor* of type (m, n) is a real valued function of m covectors and n vectors linear in all their arguments. From now on, we use the abstract index notation [66], i.e., for example a (k, l)-tensor T will be denoted by $T^{abc\ldots}{}_{efg\ldots}$, where the superindex are a list of k letters and are called *contravariant*, while subindex are a list of l letters and are called *covariant*.

The *metric tensor* on $\mathcal{M}$ is defined as a $(0, 2)$ non-degenerate symmetric tensor field, usually called $\mathbf{g}$. Therefore, a pseudo-Riemannian manifold is defined as a couple $(\mathcal{M}, \mathbf{g})$ where $\mathcal{M}$ is a differential manifold and $\mathbf{g}$ is a metric tensor on $\mathcal{M}$. The metric gives us two important geometric notions of: (i) measuring distances on $\mathcal{M}$, (ii) define orthogonality and norm concepts of vectors. The *norm* of a vector is given by $||v||^2 = g_{ab}v^a v^b$. In term of a local coordinate (x^a), the components of the tensor metric g_{ab} are a $n \times n$[1] matrix and, at the same time defines an inverse matrix which are the component of the inverse tensor metric g^{ab}, that is a $(2, 0)$ tensor. Therefore, by definition the component of the metric tensor and its inverse satisfies $g_{ac}g^{cb} = \delta_a^b$, where δ_a^b is the Kronecker delta. One of the most important properties of the metric tensor is that allows a one-to-one mapping between vectors and covectors, namely $v_a = g_{ab}v^b$ or $v^a = g^{ab}v_b$, known as *lowering* and *raising* of indices. The *signature* of g_{ab} is defined as the difference between the number of positive and negative eigenvalues. If the signature is $\pm n$, we shall said the metric is *Riemannian*, otherwise if the signature is $\pm(n-2)$ the metric is said *Lorentzian*. Given

[1] Recall that n is the dimension of $\mathcal{M}$.

a Lorentzian metric it is possible to classify vectors through its norm: v^a is *timelike* if $g_{ab}v^a v^b < 0$, *spacelike* if $g_{ab}v^a v^b > 0$, and *null* if $g_{ab}v^a v^b = 0$.

Another important structure that can be defined is the *covariant derivative*, which allows to relate tensors at different points on $\mathcal{M}$. On a pseudo-Riemannian manifold $\mathcal{M}$, the metric g_{ab} allows to define a covariant derivative ∇_a over $\mathcal{M}$, called *Levi-Civita connection*. This connection satisfies two conditions: it is torsion-free[2] and the covariant derivative of the metric tensor vanishes identically, $\nabla_a g_{bc} = 0$. In this Thesis, we shall consider only this kind of connection.

Given a coordinate system (x^a) on $\mathcal{M}$ and a natural coordinates basis $\{e_c\}$ on T_pM, i.e., $e_c = \partial_c$, the covariant derivative can be expressed as $\nabla_b e_c = \nabla_{e_a} e_b = \Gamma^c_{ab} e_c$. The connection coefficients Γ^a_{bc} of the Levi-Civita connection with respect to the natural basis are called the *Christoffel symbols*. Using the above relations, these Christoffel symbols can be written in function of metric g_{ab} as:

$$\Gamma^a_{bc} = \frac{1}{2}\, g^{ad} \left(\partial_c g_{db} + \partial_b g_{dc} - \partial_d g_{bc}\right) \ , \tag{1.1}$$

which is symmetric in the subindex. In the same frame, the covariant derivative of a scalar field, vector, covector and $(1,1)$-tensor can be expressed as follows:

$$\nabla_a f := \partial_a f \ , \tag{1.2}$$

$$\nabla_a v^b := \partial_a v^b + \Gamma^b_{ac} v^c \ , \tag{1.3}$$

$$\nabla_a v_b := \partial_a v_b - \Gamma^c_{ba} v_c \ , \tag{1.4}$$

$$\nabla_a T^b{}_c = \partial_a T^b{}_c + \Gamma^b_{ad} T^d{}_c - \Gamma^d_{ac} T^b{}_d \ . \tag{1.5}$$

Note that, every additional index needs its own Christoffel symbol. The covariant derivative is the generalization of partial derivative to a differential manifold.

It is possible to define other type of derivative on $\mathcal{M}$ which is independent of the tensor metric $\mathbf{g}$. For instance, the *Lie derivative* $\mathcal{L}_v$ measures the change of a tensor as it is transported along the direction of a given vector field v^a. For example, a $(1,1)$-tensor can be expressed as follows:

$$\mathcal{L}_v T^a{}_b = v^c \nabla_c T^a{}_b - T^c{}_b \nabla_c v^a + T^a{}_c \nabla_b v^c . \tag{1.6}$$

Once again, note that, every additional index needs its own Christoffel symbol. The Lie derivative is the generalization of the directional derivative to a differential manifold. One of the most important properties of the Lie derivative is that allows to define the

[2] For any scalar field f, $\nabla_a \nabla_b f$ is symmetric bilinear form, which satisfies (in coordinates) $\nabla_a \nabla_b f - \nabla_b \nabla_a f = 0$.

concept of symmetry. We say that $\mathcal{M}$ has a specific symmetry if the Lie derivative of the metric $\mathbf{g}$ with respect to a vector field ξ is vanish:

$$\mathcal{L}_\xi g_{ab} = 0 \Leftrightarrow \nabla_a \xi_b + \nabla_b \xi_a = 0 \ . \tag{1.7}$$

If a vector field satisfies the equation (1.7) is called a *Killing vector* of the manifold $\mathcal{M}$.

One of the fundamental objects in our pseudo-Riemannian manifold $\mathcal{M}$ is the *Riemann curvature tensor*, which can be defined through its action on arbitrary vector v^a

$$\nabla_a \nabla_b v^c - \nabla_b \nabla_a v^c = R^c_{dab} v^d \ . \tag{1.8}$$

Note that above equation (called *Ricci identity*) gives us the notion of curvature by considering the non-commutativity of covariant derivatives. The Riemann curvature tensor can be interpreted as the one measuring the deviation from Euclidean manifold (or flat manifold, see definition below). The Riemann tensor R^c_{dab} defined by (1.8) can be computed in local coordinates (x^a), in terms of the Christoffel symbols, as follows:

$$R^c_{dab} = \partial_a \Gamma^c_{db} - \partial_b \Gamma^c_{da} + \Gamma^c_{ae} \Gamma^e_{db} - \Gamma^c_{be} \Gamma^e_{da} \ , \tag{1.9}$$

We say that the manifold $\mathcal{M}$ is flat if the curvature tensor is identically zero, $R^c_{dab} = 0$. As a consequence of the Christoffel symbols definition, the Riemann tensor satisfies the following symmetries

$$R_{abcd} = R_{bacd} = R_{abdc} = R_{badc} \ . \tag{1.10}$$

and the well-known *first Bianchi identity*

$$R_{abcd} + R_{acdb} + R_{adbc} = 0 \ . \tag{1.11}$$

Note that, these symmetries identities imply that although the Riemann tensor in four dimensions has 256 components, there are only 20 algebraic degrees of freedom[3]. Furthermore, the Riemann tensor satisfies the following differential identity

$$\nabla_a R_{bcde} + \nabla_b R_{cade} + \nabla_c R_{abde} = 0 \ . \tag{1.12}$$

known as *second Bianchi identity*. Contracting twice the second Bianchi identity (1.12), we have the following important geometrical relation:

$$\nabla_a \left(R^{ab} - \frac{1}{2} g^{ab} R \right) = 0 \ . \tag{1.13}$$

[3]In a n dimensional manifold the degrees of freedom are given by the following formula: $n^2(n^2-1)/12$.

where we have introduced other important two tensors being R_{ab} is the *Ricci tensor* defined as $R_{ab} = R^d_{adb}$ and R is the *Ricci scalar* give by $R = g^{ab}R_{ab}$. Note that, the Ricci tensor is obtained from the Riemann tensor by contracting over two of the indices and it is symmetric. Taking into account all the symmetries of these tensors, one can show that the Ricci tensor has only 10 independent components.

1.2 General Relativity

Albert Einstein considered that gravity is not a force, but as a manifestation of the curvature of spacetime, which is produced by the presence of matter. Therefore, to describe gravitational interactions, it is necessary to postulate that spacetime is a four dimensional manifold $\mathcal{M}$ endowed with a Lorentzian metric g_{ab} with signature +2, i.e., $(-+++)$.

In addition, consistent with the theory of special relativity, the energy, momentum and matter stresses of the spacetime can be described by a symmetric tensor T_{ab}, called energy-momentum (or stress-energy) tensor, satisfying

$$\nabla_a T^{ab} = 0 \ . \tag{1.14}$$

Note that, equation (1.14) is the covariant generalization of the conservation law $\partial_a T^{ab} = 0$ in special relativity [63, p.7]. The components of the energy-momentum tensor are defined as: T^{00} *energy density*, T^{0i} *momentum density* and T^{ij} *stress* tensor.

By defining the *Einstein tensor* as $G_{ab} = R_{ab} - \frac{1}{2}g_{ab}R$, the contracted second Bianchi identity leads to the following conservation equation

$$\nabla_a G^{ab} = 0 \ . \tag{1.15}$$

Therefore, the simplest solution from the previous relations is the widely-known Einstein's field equations, namely

$$G_{ab} = \kappa\, T_{ab} \ , \tag{1.16}$$

where κ is a proportionality constant. The system (1.16) describes the fundamental equations governing General Relativity (**GR**), which relate the spacetime metric to the distribution of matter. The constant κ is the Einstein gravitational constant, which is related to Newtonian constant G and c light speed trough $\kappa = 8\pi G/c^4$, where these factors are required in order to recover the weak-field limit of Newtonian gravity.

Therefore, with the Einstein flied equations defined, spacetime is understood as a pair $(\mathcal{M}, g)$ such that the metric g_{ab} satisfies (1.16). These equations determine how much

space time is curved in the presence of a distribution of matter. There is a famous quote made by John Archibald Wheeler which summarize entirely Einstein's equations: *Spacetime tells matter how to move, matter tells spacetime how to curve.* Finally, in the absence of matter, i.e., $T_{ab} = 0$, the Einstein equations (1.16) are reduced to the vacuum field equations

$$R_{ab} = 0. \tag{1.17}$$

From a mathematical point of view, the Einstein tensor has a dependence on the metric and its derivatives, namely $G_{ab} = G_{ab}(g_{ab}, \partial_c g_{ab}, \partial_c \partial_d g_{ab})$. Besides, due to the symmetry relations, G_{ab} only has ten independent components. It means that (1.16) form a system of ten coupled nonlinear second order partial differential equations (**PDEs**) that must be solved for the metric g_{ab}. In the next Chapter 2, we shall explain with more detail the mathematical structure and meaning of the Einstein equations.

1.3 Linearized Einstein Equations

One of the most outstanding predictions of the theory **GR** is the existence of gravitational waves (**GWs**) [69]. **GWs** are defined as perturbations of the spacetime, produced by accelerated massive objects, which propagates at the speed of light. The existence of **GWs** can be demonstrated by linearizing Einstein's equations around a flat spacetime. Let us consider a metric of the form

$$g_{ab} = \eta_{ab} + h_{ab} \ , \tag{1.18}$$

where η_{ab} is the flat Minkowski metric and h_{ab} a small metric perturbation satisfying $|h_{ab}| << 1$, meaning that the spacetime is quite close to the spacetime of special relativity. In addition, the index will be raised and lowered with the Minkowski metric η_{ab} and η^{ab}. The inverse metric is given by $g^{ab} = \eta^{ab} - h^{ab}$, where the second order term of the metric contribution h_{ab} have been neglected. Using the metric (1.18) it is possible to calculated the Christoffel symbols, Riemann tensor, Ricci tensor and Ricci scalar, and therefore the Einstein tensor [67]. Then, at linear order, gravity is described by the following equation

$$\Box \bar{h}_{ab} - \partial_a \partial^c \bar{h}_{cb} - \partial_b \partial^c \bar{h}_{ca} + \eta_{ab} \partial^c \partial^d \bar{h}_{cd} = 2\kappa T_{ab} \ , \tag{1.19}$$

where $\Box := \eta^{ab} \partial_a \partial_b$ is the d'Alembert operator. For convenience, it has been introduced the *trace-reversed* metric perturbation $\bar{h}_{ab} := h_{ab} - \frac{h}{2}\eta_{ab}$, being $h := \eta^{ab} h_{ab} = h^a_a$. Note that, in the linearized Einstein equations (1.19) one assumed that the scale of T_{ab} has the same order of magnitude than the perturbation h_{ab}. Equation (1.19) can be further

simplified by a coordinate transformation, taking advantage of the gauge freedom in **GR**. We can exploit this gauge freedom by choosing the well-known Lorentz (or Hilbert) gauge

$$\partial_a \bar{h}^{ba} = 0 \ , \tag{1.20}$$

such that equation (1.19) is simply reduced to a wave equation with sources term

$$\Box \bar{h}_{ab} = 2\kappa \, T_{ab} \ . \tag{1.21}$$

Far from the matter sources, in the vacuum region, it can be further reduced to

$$\Box \bar{h}_{ab} = 0 \ . \tag{1.22}$$

Equation (1.22) shows that the metric perturbation propagates as waves distorting the flat spacetime. These metric deformations are known as gravitational waves.

We can get a deeper insight onto the structure of these waves by analyzing one of the simplest solutions of the equation (1.22), which is the plane harmonic wave, given by

$$\bar{h}_{ab} = \mathrm{Re}(A_{ab} \exp(i k_c \, x^c)), \tag{1.23}$$

with a real wave covector[4] k_c and a symmetric amplitude tensor A_{ab}. The plane harmonic waves satisfies the linearized vacuum field equation if and only if $k^a k_a = 0$, which means that k_c is a lightlike covector. In this solution, the plane wave travels along the spatial direction $\vec{k} = (k_x, k_y, k_y)/k^0$. Moreover, the plane harmonic wave has to satisfy the Lorentz gauge condition, i.e., $k^a A_{ab} = 0$, implying that the amplitude of the oscillations is transverse to the direction of propagation. Although A_{ab} has ten independent components, the Lorentz gauge conditions (1.20) impose four additional scalar constraints, leading to six independent components. Furthermore, the Lorentz gauge condition is preserved under coordinate transformation $x^a \to x^a + f^a(x)$ with $\Box f^a = 0$. Therefore, the following claim is satisfied: assuming a plane harmonic wave solution as (1.23) of the linearized vacuum field equation in the Lorentz gauge, and let u^a be a constant four-velocity. Then, a coordinate transformation can be made such that the Lorentz gauge condition is preserved and such that

$$\left.\begin{array}{l} u^a A_{ab} \ = 0 \\ \eta^{ab} A_{ab} = 0 \end{array}\right\} \textbf{transverse-traceless gauge} \ ,$$

[4]Recall that, the wave vector in coordinates is given by $k^c = (\omega, \vec{k})$ where ω is the angular frequency of the waves and $\vec{k} = (k^x, k^y, k^z)$ is the wave number vector with the propagation direction of the waves, being the component of the covector $k_c = (\omega, -k_x, -k_y, -k_z)$.

in the new coordinates. The proof of this assertion can bee seen in [70, p.43]. This is called *transverse-traceless gauge* or **TT**-gauge. In this gauge, the amplitude tensor A_{ab} has only two non-zero independent components, which means that the **GW** has only two physical degrees of freedom that correspond to the polarization state, namely, plus mode $+$ and cross mode $\times$. Their names come from the effect of these **GWs**: the plus mode polarization deforms a circle ring of test particles, elongated and compressed along the axis x and y direction, while the cross mode polarization deforms in the same way along the diagonal directions. Consequently, in the rest frame of the observer u^a, for a **GW** propagating along the z-axis, the tensor A_{ab} can be written as:

$$A_{ab} = \begin{pmatrix} 0 & 0 & 0 & 0 \\ 0 & A^+ & A^\times & 0 \\ 0 & A^\times & -A^+ & 0 \\ 0 & 0 & 0 & 0 \end{pmatrix} , \tag{1.24}$$

where A_+ and $A_\times$ are the two independent polarization of **GWs**.

1.3.1 Generation of gravitational waves: Quadrupole formula

Let us consider now the linearized field equations with a non-vanishing source, i.e., $T_{ab} \neq 0$. Recall that, choosing the Lorentz gauge, the weak field equations reduce to

$$\Box \bar{h}_{ab} = 2\kappa T_{ab} \tag{1.25}$$

$$\partial_a \bar{h}^{ba} = 0, \tag{1.26}$$

which can be easily solved by using the retarded potential from linear wave equation theory. Therefore, for each component $\bar{h}_{ab}$ one gets

$$\bar{h}^{ab}(t, \vec{r}) = \frac{1}{4\pi} \int_{\mathbb{R}^3} \frac{2\kappa\, T^{ab}(t_{ret}, \vec{r}\,')dV'}{|\vec{r}\,' - \vec{r}|} , \tag{1.27}$$

where $t_{ret} = t - \frac{|\vec{r}\,' - \vec{r}|}{c}$ is the retarded time. In addition, $\vec{r} = (x, y, z)$ with $|\vec{r}| = r$ and dV' is the volume element with respect to primed coordinates. Since we are only concerned to some particular solutions, far way solution from the sources, we assume that T^{ab} is different from zero only in a compact region of space S_R, namely, a sphere of radius R (i.e., $T^{ab}(t, \vec{r}) = 0$ if $r \geq R$) see Figure 1.1. We are interested in the field $\bar{h}^{ab}$ at point $\vec{r}$, being $r >> R$. In this limit, terms of order $\mathcal{O}(r'/r)$ can be neglected and we get

$$\bar{h}^{ab}(t, \vec{r}) = \frac{\kappa}{2\pi} \frac{1}{r} \int_{S_R} T^{ab}\left(t - \frac{r}{c}, \vec{r}\,'\right) dV' , \tag{1.28}$$

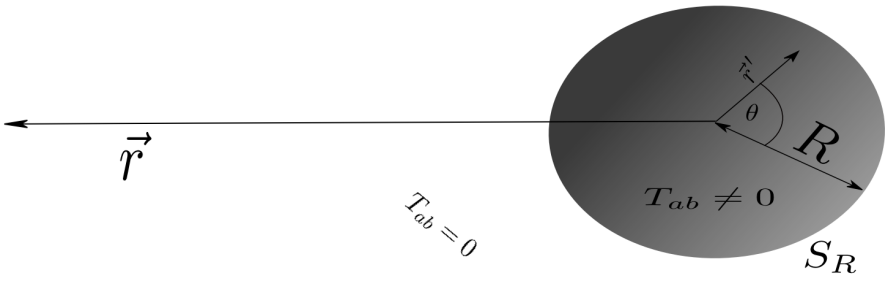

FIGURE 1.1: *Far zone regime.* Compact region S_R of the spacetime where T_{ab} is non-vanishing.

Equation (1.28) is known as the far-field approximation.

On the other hand, using the conservation law for T_{ab}, which in the weak-field regime is only $\partial_a T^{ab} = 0$, it is easy to prove that

$$\int_{S_R} T^{a0} dS_R = 0 \,, \tag{1.29}$$

$$\int_{S_R} T^{ij} dS_R = \frac{1}{2c^2}\frac{d^2}{dt^2}\int_{S_R} T^{00} dS_R \,, \tag{1.30}$$

where dS_R is the volume element of the sphere S_R. Finally, using the previous results, we find that in the far-field approximation the solution of (1.28) is

$$\bar{h}^{ij}(t,\vec{r}) = \frac{2\,G}{c^4\,r}\frac{d^2}{dt^2}Q^{ij}\left(t - \frac{r}{c}\right) \,, \tag{1.31}$$

where $Q^{ij} = \int_{S_R} T^{00} x^i x^l dS_R$ is the quadrupole moment (or second mass moment). Finally, **GWs** have to be extracted in the TT-gauge, in order to make explicit the physical degree of freedom. Defining the TT-projector as $P_{ijkl} = P_{ik}P_{jl} - \frac{1}{2}P_{ij}P_{kl}$, where $P_{ij} = \delta_{ij} - n_i n_j$ is the projector operator[5] and $\vec{n}_i = \vec{r}/r$ is the direction of the unit vector orthogonal to the wavefront, one can obtain the famous quadrupole emission formula of gravitational waves

$$\bar{h}^{TT}_{ij}(t,\vec{r}) = \frac{2\,G}{c^4\,r}P_{ij}{}^{kl}\frac{d^2}{dt^2}\mathcal{Q}_{kl}\left(t - \frac{r}{c}\right) \,, \tag{1.32}$$

where $\mathcal{Q}_{kl} = Q_{kl} - \frac{1}{3}\delta_{kl}Q^j_j$. Some important observations can be made: (i) $\bar{h}^{TT}_{ij}$ decay as $1/r$ [6], (ii) the first non-vanishing contribution correspond to quadrupole radiation, which means there are no contribution of monopole and dipole radiation [68, p.302] and (iii) these equations have been derived in the weak-field regime and using the fact $\partial_a T^{ab} = 0$, that does not contain information of the curved spacetime. For that general frame derivation see [67, p.250].

[5] We will discuss about this projector in the Chapter 2.
[6] We will see this property when we study **GW** extraction in the Chapter 2.

Chapter 2

Continuum Problem

In this Chapter we describe briefly the mathematical theoretical background, used in this Thesis, related to the continuum problem in Numerical Relativity. In particular, we review the well posed formulations of Einstein's equations and the important concept of hyperbolicity. We do not go further doing a extensive review of these topics, since there are plenty of bibliography dealing these topics.

The solution of Einstein's equations (1.16) provides a solution for the four dimensional metric g_{ab} in the entire spacetime or a certain domain defined $\mathcal{D} \subset \mathcal{M}$, given an appropriate initial data and boundary conditions. As it was mentioned before, Einstein's equations are a system of ten nonlinear second order **PDEs**. Unfortunately, there are not general methods to obtain exact solutions for most of the non-linear partial differential equations. Due to the complexity of the Einstein equations, analytical solutions are known only for problems with many symmetries, such as the solutions for spherically [71] or axially [72] symmetric black holes. Another important example would be the cosmological solutions for studying the expansion of the Universe through the Friedmann-Lemaitre-Robertson-Walker metric [73], that assumes that the three dimensional space has constant curvature.

Otherwise, Einstein's equations can be formulated as an initial value problem, which allows us to study existence and uniqueness of more general solutions [74], i.e., not assuming any symmetry.

Let us assume that the Einstein equations (1.16) can be written as the following second order evolution system

$$\partial_t^2 g_{ab} = S_{ab}\left(\partial_t g_{ab}, \Gamma^c_{ab}, \partial_c \Gamma^c_{ab}\right) \ , \tag{2.1}$$

for all $t > 0$. The Cauchy problem for (2.1) consist on, given and initial data $\{g_{ab}, \partial_t g_{ab}\}$ at initial time $t = t_0$, finding the solution g_{ab} for $t \geq t_0$. At first glance, we know that

there are ten independent metric coefficients g_{ab}, hence ten field equations are needed in order to study their dynamical evolution. Nevertheless, the Bianchi identities (1.13)

$$\nabla_t \left(G^{0a} - \kappa T^{0a}\right) + \nabla_k \left(G^{ka} - \kappa T^{ka}\right) = 0 \ , \tag{2.2}$$

implies that the four equations $G^{0a} = \kappa T^{0a}$ are first integral of the system, thus they must be preserved for all time. Subsequently, these four equations do not contain any additional information about the dynamical evolution of the fields. Rather, they are constraints on the initial data $\{g_{ab}, \partial_t g_{ab}\}$. This means that only six of the ten Einstein's equations are independent. Indeed, it is not a surprise, since the four remaining metric coefficients are directly related to a choice of coordinate system on $\mathcal{M}$, called *gauge conditions*. Thanks to the general covariance in **GR**, it is always possible to choose the coordinates, since the Einstein equations (1.16) are invariant under general coordinate transformation.

The covariant nature of Einstein's equations implies that there is not an a priori distinction between time and space. Therefore, an evolution system, namely of first-order in time, can not be written in a simple way. There are different ways to recast Einstein equations (1.16) as an evolution system. Here we will study the $3+1$ formulation [75], that will allow us to split space and time explicitly, leading to a evolution system with partial derivatives of first order in time and second order in space.

This chapter is essentially divided in four parts. In Section 2.1, we review the $3+1$ decomposition used in Numerical Relativity, by rewriting the field equations in General Relativity as set of evolution equations plus four constraints. In Section 2.2, we give an overview of some important concepts regarding **PDEs**, namely, well-posedness and hyperbolicity. Then, in Section 2.3, we present the formalism used in this Thesis, namely the conformal and covariant **Z4** system (**CCZ4**). We also present the choice of gauge (or slicing) conditions used to evolve our formalism. and we analyze the characteristic structure of the **CCZ4** formalism. Finally, the section 2.4 culminates with a description of the most important analysis quantities computed in our simulations: the Arnowitt-Deser-Misner (**ADM**) mass, the angular momentum, and the gravitational radiation.

2.1 Splitting Spacetime into time and space

In order to decompose the spacetime into time and space it is necessary to introduce some mathematical concepts. The first one is a certain class of spacetime, called *globally hyperbolic spacetimes*. This class of spacetime allows: (i) the existence of no closed causal path, (ii) $\mathcal{M}$ has a Cauchy surface Σ, which is defined as a spacelike hypersurface $\Sigma \subset \mathcal{M}$

such that each causal(timelike or null) curve without point intersects Σ once and only once[66, 76] , (iii) the Cauchy surface Σ is described by a universal time function, i.e., its gradient is timelike and (iv) $\mathcal{M}$ has a topology given by $\mathbb{R} \times \Sigma$, [76]. Additionally, a subset $\mathcal{V} \subset \mathcal{M}$ is a spacelike hypersurface if $\mathcal{V}$ is the image of a three dimensional manifold $\mathcal{W}$ by an embedding $\varphi : \mathcal{W} \to \mathcal{M}$ such that $\varphi(\mathcal{W}) = \mathcal{V}$ and the metric g induce a metric γ on $\mathcal{V}$ with signature $(+,+,+)$.

2.1.1 $3+1$ decomposition

Let us consider a globally hyperbolic spacetime $\mathcal{M}$ foliated by a one-parameter family of three dimensional spacelike hypersufaces Σ_t. By a foliation of the spacetime $\mathcal{M}$, it is understood that there exist a family of disjoint of spacelike hypersurface $\{\Sigma_t\}_{t\in\mathbb{R}}$ covering $\mathcal{M}$, i.e., $\mathcal{M} = \cup_{t\in\mathbb{R}}\Sigma_t$ and $\Sigma_{t_i} \cap \Sigma_{t_j} = \emptyset$ for $i \neq j$. Each Σ_{t_i} is called a leave or slice. The foliation can be defined as a function of a scalar field Φ on $\mathcal{M}$ such that the slices of the foliation correspond to a surface level of Φ, i.e.,

$$\Sigma_t = \{x^a \in \mathcal{M} : \Phi(x^a) = t\} \ , \ \text{for all } t \in \mathbb{R} \ , \tag{2.3}$$

satisfying that the gradient of Φ never vanishes and is normal to the spacelike hypersurfaces. Defining a timelike 1-form

$$\Omega_a = \nabla_a \Phi \ , \tag{2.4}$$

such that its normalization is given by

$$||\Omega||^2 \equiv g^{ab}\nabla_a\Phi\nabla_b\Phi = -\frac{1}{\alpha^2} \ . \tag{2.5}$$

The function $\alpha(x^a)$ is defined as the *lapse function*, which measures the proper time of the observers moving along the normal direction and it is strictly positive for spacelike hypersufaces. In fact, the lapse function allows to define the unit normal vector field n^a to Σ_t as

$$n^a := -\alpha\Omega^a = -\alpha g^{ab}\nabla_b\Phi \ , \tag{2.6}$$

the minus sign is chosen in order to vector n^a be future-directed, i.e., the direction of n corresponds to the direction to which t increases.

The metric g_{ab} induces a three dimensional Riemannian metric γ_{ab} (or first fundamental form) onto Σ_t as:

$$\gamma_{ab} := g_{ab} + n_a n_b \ , \tag{2.7}$$

$$\gamma^{ab} := g^{ab} + n^a n^b \ . \tag{2.8}$$

The geometrical elements n^a and γ_{ab} play a role as projectors, allowing to decompose an arbitrary four dimensional spacetime tensor into its purely time and spatial parts, respectively. The spatial projector is defined:

$$\gamma_a^b \;:=\; \delta_a^b - n^b n_a \;, \tag{2.9}$$

where $n^a\gamma_{ab} = 0$ by construction.

Recalling that $\Omega_a = \nabla_a\Phi$ and $n^a\Omega_a \neq 1$, the following time vector can be considered

$$t^a = \alpha n^a + \beta^a \;, \tag{2.10}$$

The time vector connects points with the same spatial coordinates between neighboring slices Σ_t to another $\Sigma_{t+\Delta t}$ and satisfies $t^a\Omega_a = 1$. The vector β^a measures the deviations of the time lines with respect to the normal lines and it is called *shift vector* (see Figure 2.1 for a intuitive interpretation of lapse function α and shift vector β^i). In fact, observers at rest in Σ_t following the congruence given by n^a are called *Eulerian observers*. Introducing coordinates adapted to the foliation, i.e., on each hypersurface Σ_t a coordinate system $x^i = (x^1, x^2, x^3)$ can be introduced and a well-defined coordinated system on $\mathcal{M}$ given by $x^a = (t, x^i)$, where the natural basis of tangent space on $\mathcal{M}$ is given by $\partial/\partial x^a = (\partial/\partial t, \partial/\partial x^i)$. In this adapted coordinates we have that

$$\beta^a \;=\; (0, \beta^i), \quad n^a = \frac{1}{\alpha}(1, -\beta^i), \tag{2.11}$$

$$\beta_a \;=\; \gamma_{ab}\beta^b, \quad n_a = (-\alpha, 0, 0, 0). \tag{2.12}$$

Using equations (2.11)-(2.12), the four dimensional components of the metric (and its inverse, respectively) in a $3+1$ decomposition has the following form:

$$g_{ab} = \begin{pmatrix} -\alpha^2 + \beta_i\beta^i & \beta_i \\ \beta_i & \gamma_{ij} \end{pmatrix}, \quad g^{ab} = \begin{pmatrix} -1/\alpha^2 + \beta_i\beta^i & \beta^i/\alpha^2 \\ \beta^i/\alpha^2 & \gamma_{ij} - \beta_i\beta^j/\alpha^2 \end{pmatrix} \;, \tag{2.13}$$

such that, the $3+1$ line element is given by:

$$ds^2 = g_{ab}dx^a dx^b = -\alpha^2\, dt^2 + \gamma_{ij}\big(dx^i + \beta^i dt\big)\big(dx^j + \beta^j dt\big) \;. \tag{2.14}$$

Finally, the determinant of four dimensional metric is related with the determinant of the tree metric through $\sqrt{-g} = \alpha\sqrt{\gamma}$.

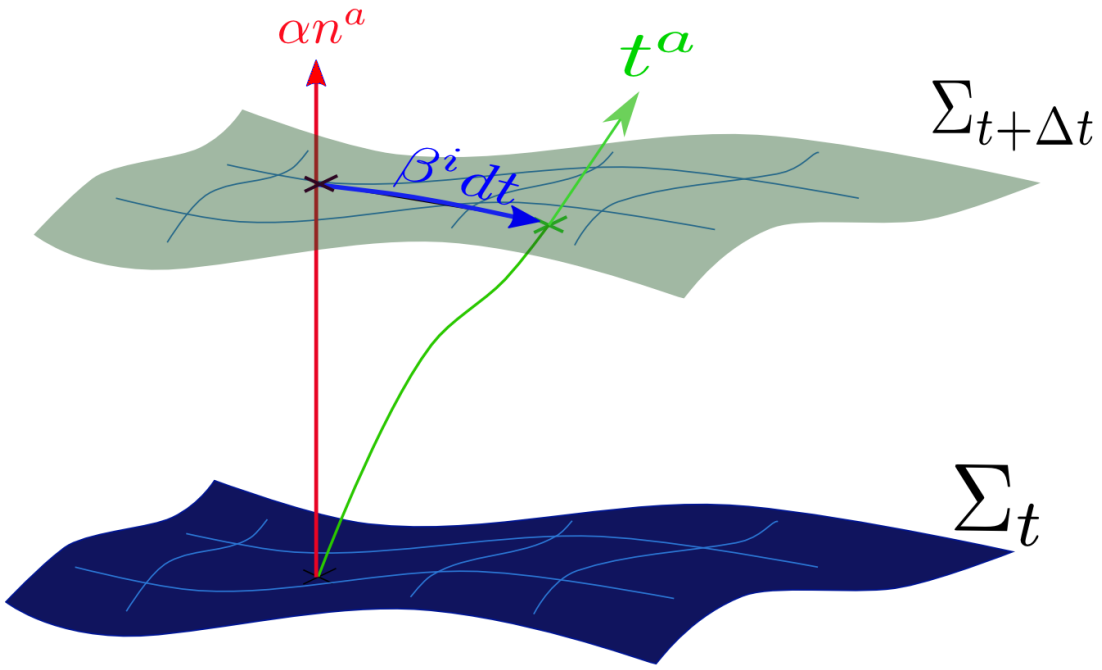

FIGURE 2.1: *Foliation of the spacetime* $\mathcal{M}$ *by the hypersurfaces* Σ_t. Intuitively, α measures the proper time of the coming observers and β^i measures the displacement of the observes between consecutive hypersurfaces.

2.1.2 Projecting tensors and equations

The covariant derivative onto Σ_t, denoted as D, acting on a tensor T on Σ is defined by

$$D_c T^{a_1 \ldots a_r}{}_{b_1 \ldots b_l} := \gamma_c^d \gamma_{p_1}^{a_1} \ldots \gamma_{p_r}^{a_r} \gamma_{b_1}^{q_1} \ldots \gamma_{b_l}^{q_l} \nabla_d T^{p_1 \ldots p_r}{}_{q_1 \ldots q_l} \tag{2.15}$$

and satisfies the following conditions: (i) it is a linear operator, (ii) it has torsion free, (iii) it is compatible with the metric and (iv) Leibnitz's rule holds. Any four dimensional tensor can be projected onto Σ_t, as for example Riemann tensor. The three dimensional Riemann tensor associated to metric γ in Σ is defined as:

$$(D_a D_b - D_b D_a) v_c = v_d \, {}^{(3)}R^d_{abc} \tag{2.16}$$

for any spatial vector v^a. Additionally, the second fundamental form on Σ_t can be defined as follows:

$$K_{ab} := -\gamma_a^c \nabla_c n_b = -D_c n_b = -\frac{1}{2} \mathcal{L}_n \gamma_{ab} \ , \tag{2.17}$$

being n^a unit normal vector to Σ_t, which can be interpreted either as the change of the normal vector under parallel transport, or as the rate of change of the three-metric as measured by Eulerian observers. Since it provides a measure of how the hypersurface is curved, it is called extrinsic curvature of Σ_t. From its definition (2.17) one can extract

the following direct properties: it is purely spatial $K_{ab}n^b = 0$, and it is a symmetric tensor $K_{ab} = K_{ba}$.

Moreover, there exist some important geometrical relations between the Riemann tensor in $\mathcal{M}$ and the hypersurface Σ_t. The first, called *Gauss relation*, relates to three dimensional Riemann tensor ${}^{(3)}R^d_{abc}$ with the four dimensional one, namely

$$\gamma^p_a\gamma^q_b\gamma^r_c\gamma^s_d\,{}^{(4)}R^c_{spq} = {}^{(3)}R^r_{dab} + K^r_a K_{bd} - K^r_b K_{ad} \ . \tag{2.18}$$

Furthermore, the covariant derivatives of the extrinsic curvature are related as well to the four dimensional Riemann tensor through the *Codazzi equation*

$$\gamma^p_a\gamma^q_b\gamma^r_c n^s\,{}^{(4)}R_{pqrs} = D_b K_{ac} - D_a K_{bc} \ . \tag{2.19}$$

Note that the Gauss and Codazzi relations (2.18)−(2.19) represent integrability conditions for which γ_{ab} and K_{ab} must be satisfied for any Σ_t embedded in the spacetime $\mathcal{M}$.

There are other useful relations, called *Ricci equations*, which are obtained projecting twice onto Σ_t and twice on n^a

$$\gamma^p_a\gamma^q_b n^r n^s\,{}^{(4)}R_{prqs} = \mathcal{L}_n K_{ab} - \frac{1}{\alpha}D_b D_b\alpha + K^c_b K_{ca} \ . \tag{2.20}$$

Proof of these relations can be found in detail in [77, p.29]

2.1.3 Evolution and Constraint equations

Here, 3 + 1 decomposition is applied to Einstein's equations, leading to a system of **PDEs** of first order in time. First of all, let us start with the energy momentum tensor, which can be decomposed as

$$T_{ab} = n_a n_b \tau + S_a n_b + S_b n_a + S_{ab} \ , \tag{2.21}$$

where $\tau := n_a n_b T^{ab}$ is the energy density, $S_a := -\gamma^c_a n_b T_{ab}$ is the momentum density and $S_{ab} := \gamma^c_a\gamma^d_b T_{cd}$ is the stress tensor. Now, the Einstein equations can be projected as follows:

(i) **Full time-projection:**

$$\begin{aligned} 2n^a n^b G_{ab} &= 16\pi n^a n^b T_{ab} \ , \\ n^a n^b \left(R_{ab} - g_{ab}R\right) &= 16\pi\tau \ , \\ \gamma^{ab}\gamma^{pq}\,{}^{(4)}R_{apbq} &= 16\pi\tau \ , \end{aligned} \tag{2.22}$$

where $K = \gamma^{ab}K_{ab}$ is the trace of extrinsic curvature. The left-hand side of (2.22) is the double trace of Gauss relation (2.18), leading to the so-called the equation *Hamiltonian constraint*

$${}^{(3)}R + K^2 - K_{ab}K^{ab} = 16\pi\tau. \tag{2.23}$$

(ii) **Mixed time-space projection:**

$$\begin{aligned} \gamma^b_a n^c G_{bc} &= 16\pi n^a n^b T_{ab} \ , \\ \gamma^b_a \gamma^{cd} n^e\,{}^{(4)}R_{cbde} &= 8\pi S_a \ , \end{aligned} \tag{2.24}$$

the left-hand side of (2.24) is the trace of Codazzi relation (2.19), therefore we obtain the *Momentum constraint*

$$D_b(K^b_a - \delta^b_a K) = 8\pi S_a \ . \tag{2.25}$$

Note that equations (2.23)-(2.25) do not have explicit time derivatives. Consequently, they are not evolution equations but rather constraints on $\{\gamma_{ij}, K_{ij}\}$ which should be satisfied at all times. The Hamiltonian and Momentum constraint equations (2.23)-(2.25) form a set of four elliptic equations that are crucial in the construction of the initial data: not all the components of the spatial metric and the extrinsic curvature can be chosen freely as initial conditions. The solution should satisfy the constraints both initially and during the evolution. Finally,

(iii) **Full space-projection:** Multiplying the Gauss equation (2.18) by γ^{ac} and using then the Ricci equation, we obtain

$$\mathcal{L}_n K_{ab} = -\frac{1}{\alpha}D_a D_b\alpha + R_{ab} - 2K_{ac}K^c_b + K\,K_{ab} - 8\pi\left(S_{ab} - \frac{1}{2}(S-\tau)\gamma_{ab}\right) \ , \tag{2.26}$$

where $S := \gamma^{ij}S_{ij}$.

Recalling the equations as a function of the time vector (2.10) and using the properties of the Lie derivative (1.6), we obtain that the $3+1$ decomposition of Einstein equations

is given by:

$$(\partial_t - \mathcal{L}_\beta)\gamma_{ij} = -2\alpha K_{ij} \ , \tag{2.27}$$

$$(\partial_t - \mathcal{L}_\beta)K_{ij} = D_i D_i \alpha + \alpha \left(R_{ii} - 2K_{ik}K^k_j + K\, K_{ij} \right) - 8\pi\alpha \left(S_{ij} - \frac{1}{2}(S-\tau)\gamma_{ij} \right) \ , \tag{2.28}$$

$${}^{(3)}R + K^2 - K_{ij}K^{ij} = 16\pi\tau \ , \tag{2.29}$$

$$D_j(K^j_i - \delta^i_i K) = 8\pi S_i \ , \tag{2.30}$$

where we have used that in adapted coordinates $(\mathcal{L}_t F)^{a\cdots}{}_{b\ldots} = \partial_t F^{a\cdots}{}_{b\ldots}$. The **PDE** system (2.27) − (2.30) is also called the **ADM** equations in reference of the work by Arnowitt, Deser, and Misner [78], whose wrote a Hamiltonian formulation for **GR**. Nevertheless, the evolution system above was developed by York [75].

The evolution **ADM** equations is a system of first order derivatives in time and second order in space. They are six evolution equations that describes how the spatial geometry changes from Σ_t to $\Sigma_{t+\Delta t}$, given by the relations (2.28), which are supplemented by the relation (2.27) between the evolution of three-dimensional metric with the extrinsic curvature. As we said before, the initial data $\{\gamma_{ij}, K_{ij}\}$ of these evolution equations must satisfy the four elliptic constraint equations (2.29)-(2.30) at all times. Indeed, by virtue of Bianchi identities, they will remain satisfied during the evolution if they are satisfied at the initial time [79].

Eventually, in order to obtain the four dimensional metric g_{ab} on the whole spacetime $\mathcal{M}$, the equations (2.27)-(2.28) have to be solved satisfying (2.29)-(2.30). There are two different approaches to solve numerically this evolution system. The first one consists on starting with a solution of the constraint equations (2.29)-(2.30) and just evolve numerically by solving the equations (2.27)-(2.28). This method is called *free evolution* [63, p.49]. As the constraint equations are not solved during the numerical evolution, we must carefully monitor the constraints violations at each time step because of the generation and propagation of numerical errors. The presence of large constraint violations indicates that the physical state obtained numerically is not a physical solution of Einstein's equations. Another approach is known as *constrained evolution* and involves to solve all the elliptic constraints at each time step for some of the components of (γ_{ij}, K_{ij}), while evolving the remaining components using the Ricci equations [80].

2.2 Well-Posedness Problem and the hyperbolicity concept

Let us consider a dynamical mathematical model that represents some interesting physical phenomena. Assuming that it is possible to formulate an initial value formulation of this model, we will say that, according to *Hadamard criteria* [81], the problem is well-posed if there exist a unique solution that depends continuously on its initial data. Since any physical solution must satisfy these basic properties, one can conclude that ill-posed mathematical models can not describe physical systems.

Since proving that an initial value formulation is well-posed could be quite difficult in general, is more convenient to study the hyperbolicity of the system [63, 70, 82]. Hyperbolicity is a key property for the stability. In fact, whether we have strongly hyperbolic system the initial boundary value problem (**IBVP**) is well-posed, and therefore, the solution at a finite time is bounded. As a corollary, with suitable numerical methods [83], stable numerical solutions can be obtained. Otherwise, for weakly hyperbolic systems the **IBVP** is not well-posed, and the solution can grow faster than an exponential, implying unstable numerical evolutions. This section is based on books [63, 70, 83] and paper [84].

Let us be more precise on these concepts by considering the following system of partial differential equations on a $n-$dimensional space:

$$\partial_t u = P\left(t, x, \frac{\partial}{\partial x}\right) u, \quad x \in \mathbb{R}^n, \ t \geq t_0 \ , \tag{2.31}$$

with initial data

$$u(t_0, x) = f(x) \ . \tag{2.32}$$

Here, $u(t,x) \in \mathbb{C}^m$ is a vector with m-components, and $P(t, x, \partial/\partial x)$ is a general differential operator given by

$$P\left(t, x, \frac{\partial}{\partial x}\right) = \sum_{|\eta| \leq p} A_\eta(t,x) \left(\frac{\partial}{\partial x^1}\right)^{\eta_1} \cdots \left(\frac{\partial}{\partial x^d}\right)^{\eta_d} \ , \tag{2.33}$$

of order p. In this case η is a multi-index with nonnegative integer elements, i.e., $\eta = (\eta_1, \ldots, \eta_d)$ and $|\eta| = \sum_i \eta_i$. The coefficients $A_\eta = A_{\eta_1,\ldots,\eta_d}$ are $m \times m$ matrix functions. For simplicity, we assume that $P\left(t, x, \frac{\partial}{\partial x}\right) = P\left(\frac{\partial}{\partial x}\right)$ and A_η are matrix with constant coefficients. Mathematically speaking, we say that the problem (2.31) with initial data (2.32) is well-posed if, for every t_0 and every $f \in C^\infty(x)$:

(a) There exists a unique solution $u(t,x) \in C^\infty(t,x)$, and

(b) There are constants α and $K \geq 1$, independent of f and t_0, such that

$$||u(t,x)|| \leq K \exp(\alpha(t-t_0)) \, ||u(t_0,x)|| \, , \tag{2.34}$$

for a suitable norm $||\cdot||$.

This would mean that, the problem (2.31)-(2.32) is well-posed: *There exists a unique solution $u(t,x)$ and this solution depends continuously on the initial and boundary data of the problem.* As we said before prove the above definition for a **IBVP** could be tough. Therefore, let us consider a first order system of evolution equations of the form:

$$\partial_t u + A^k \partial_k u = S(u) \, , \tag{2.35}$$

where A^k are $n \times n$ matrices, with the index k running over the spatial dimensions, and $S(u)$ is a source vector that may depend on the function u but not on their derivatives. Let us also define the *principal symbol* of (2.35) as $P(s_k) = A^k s_k$, where s_k is an arbitrary spatial unit vector. We say that:

- The system (2.35) is *strongly hyperbolic* if the principal symbol has real eigenvalues and a complete set of eigenvectors for all s_i.
- The system (2.35) is *weakly hyperbolic* if the principal symbol has real eigenvalues but an incomplete set of eigenvectors for all s_i.

Therefore, with this definition, hyperbolicity of the system translates into a set of algebraic conditions [85]. Indeed, it is possible to prove that whether the system is strongly hyperbolic guarantees well-posedness of the initial value problem posed [82, 84, 86], providing by a suitable initial and boundary conditions.

Therefore, looking for strongly hyperbolic formulations to evolve the Einstein equations in numerical relativity (**NR**) is a crucial issue. We would like to emphasize that, since Einstein's equations are highly non-linear, the arguments presented above could not be adopted directly, but are only valid on the linearized solutions on a given background.

2.3 Evolution formalism

There are several well-know formulations in **NR** which have been shown to be strongly hyperbolic, and therefore well-posed, like for example: Baumgarte-Shapiro Shibata-Nakamura (**BSSN**) [87, 88] which is one of the most popular formulations used by **NR** community. This formulation is a modification of the **ADM** formulation which

introduces a conformal decomposition, a new evolved field for the contracted Christoffel symbols and adds energy-momentum constraints to the evolution of the equations in order to obtain a strongly-hyperbolic system. We would like to stress that there are other formulations which does not use explicitly the $3+1$ formalism, as for example, the generalized harmonic formulation [89, 90] or the fully-constrained formulations [80, 91]. Here, we focus on describe in detail the **CCZ4** [92] formulation that will be used in the numerical simulations throughout this Thesis.

2.3.1 Z4 formulation

The **Z4** formalism was first proposed as a covariant extension of Einstein equations to achieve an hyperbolic evolution system free of elliptic constraints [93, 94]. The equations of motion can be derived from a Palatini-type variation [93] using the Lagrangian

$$L = R + 2\nabla_a Z^a + \mathscr{L}_M \ , \tag{2.36}$$

where Z^a is a extra vector added to the standard Einstein-Hilbert action and $\mathscr{L}_M$ is the Lagrangian representing the matter fields. Performing the variation with respect to the metric, the **Z4** equations are obtained [95]

$$R_{ab} + \nabla_a Z_b + \nabla_a Z_b = 8\pi \left(T_{ab} - \frac{1}{2} g_{ab} \ \mathrm{tr}\, T \right) \ , \tag{2.37}$$

where R_{ab} is the Ricci tensor associated to the spacetime metric g_{ab} and T_{ab} is the stress-energy tensor, with trace $\mathrm{tr}\, T \equiv g^{ab} T_{ab}$. The Z_a four-vector can be interpreted as a four-vector which measures deviations from Einstein's solutions. One convenient way of enforcing a dynamical decay of the constraint violations associated to Z_a is by including the additional damping terms proportional to κ_z as follows

$$R_{ab} + \nabla_a Z_b + \nabla_a Z_b = 8\pi \left(T_{ab} - \frac{1}{2} g_{ab} \ \mathrm{tr}\, T \right) + \kappa_z \ (n_a Z_b + n_b Z_a - g_{ab} n^c Z_c) \ . \tag{2.38}$$

As it was shown in [96], the energy and momentum constraint modes are exponentially damped if $\kappa_z > 0$. However, since the damping terms are proportional to the unit normal of the time slicing n_a, the full covariance of the system is broken due to the presence of a privileged time vector. Notice that, the full set dynamical fields consists now of the pair $\{g_{ab}, Z_a\}$. It is also worth stressing that the solutions of the original field equations can be recovered by imposing the vanishing of the additional terms, namely [63, p.68]

$$\nabla_a Z_b + \nabla_b Z_a = 0 \ , \tag{2.39}$$

which is the Killing equation for the four vector Z_a. In a generic case, the only solution of this equation is the trivial one

$$Z_a = 0 \ . \tag{2.40}$$

Taking the divergence of (2.38) and using the conservation laws for the Einstein and stress-energy tensor respectively, we obtain

$$\Box Z_a + R_{ab} Z^b - \kappa_z \nabla^b \left(n_a Z_b + n_b Z_a - g_{ab} n^c Z_c \right) = 0 \ . \tag{2.41}$$

Equation (2.41) has some important features. First, this equation plays the role of the subsidiary system, that is, it describes the evolution equations of the constraints (2.23)-(2.25). Furthermore, this subsidiary system (2.41) contains second order time derivatives in Z_a [63]. Therefore, in order to preserve the algebraic constraint (2.40) during the time evolution, both conditions $Z_a|_{t=0} = 0$ and $\partial_t Z_a|_{t=0} = 0$ need to be imposed in the initial slice. It means that, the initial data for the Z4 equations must satisfy the energy and momentum constraint and have a vanishing value of the four-vector Z_a. Finally, equation (2.41) has the form of telegraph equation [1] [97], which solution behaves as $Z_a \approx e^{-\kappa_z t}(F(x-t) + G(x-t))$. It is clear then that κ_z plays a role of the attenuation term.

The **Z4** equations (2.38), as the Einstein equations, can be written as an evolution system using the $3+1$ decomposition, namely:

$$(\partial_t - \mathcal{L}_\beta)\gamma_{ij} = -2\alpha\, K_{ij} \ , \tag{2.42}$$

$$\begin{aligned}(\partial_t - \mathcal{L}_\beta)K_{ij} = &-D_i(D_j\alpha) + \alpha \Big(K_{ij}(\operatorname{tr} K - 2\Theta) - 2K_{ki}K^k_j + {}^{(3)}R_{ij} \\ &+ D_i Z_j + D_j Z_i \Big) - 8\pi \left(S_{ij} - \frac{1}{2}\gamma_{ij}(S^i_j - \tau) \right) \ ,\end{aligned} \tag{2.43}$$

$$\begin{aligned}(\partial_t - \mathcal{L}_\beta)\Theta = &\frac{\alpha}{2} \Big(\alpha \operatorname{tr} K(\operatorname{tr} K - 2\Theta) + {}^{(3)}R + 2D^i Z_i - K^i_k K^K_i \\ &- 2\frac{\partial^k \alpha}{\alpha} Z_k - 16\pi\tau \Big) \ ,\end{aligned} \tag{2.44}$$

$$(\partial_t - \mathcal{L}_\beta)Z_i = \alpha \left(D_j K^j_i - D_i \operatorname{tr} K + \partial_i \Theta - \frac{\partial_i \alpha}{\alpha}\Theta - 2K^k_j Z_k - 8\pi S_i \right) \ , \tag{2.45}$$

where we have introduced the scalar Θ as the projection of Z_a along the normal direction to the spatial hypersurfaces:

$$\Theta := n_a Z^a = -\alpha\, Z^0 = -\frac{1}{\alpha} Z_0 \ . \tag{2.46}$$

[1] The telegraph equation is given by [97]

$$\underbrace{\partial_{tt}u - a^2\partial_{xx}u}_{\text{Wave equation}} + \underbrace{b\,\partial_t u}_{\text{Dissipation term}} + \underbrace{c\,u}_{\text{Disppertion term}} = 0 \ ,$$

where c play a role as an attenuation term or exponential decay depending of its sign.

Therefore, the **Z4** formalism lead to evolution equations for the evolved fields $\{\gamma_{ij}, K_{ij}, Z_i, \Theta\}$ where the constraint equations has been naturally included in the evolution system.

2.3.2 Conformal and Covariant Z4 formulation

A conformal and covariant version of the **Z4** formalism, called **CCZ4**, can be obtained from the 3+1 decomposition of the evolution equations by using conformal variables [92] (i.e., see also [98] for other conformal but non-covariant **Z4** formulation called Z4c). We shall briefly summarize the derivation of the equations, starting with the conformal decomposition (in Cartesian coordinates) of the evolved fields. A conformal metric $\tilde{\gamma}_{ij}$ with unit determinant and a conformal trace-less extrinsic curvature $\tilde{A}_{ij}$ can be defined as

$$\tilde{\gamma}_{ij} = \chi\,\gamma_{ij}\ , \tag{2.47}$$

$$\tilde{A}_{ij} = \chi\left(K_{ij} - \frac{1}{3}\gamma_{ij}\ \mathrm{tr}\,K\right)\ , \tag{2.48}$$

where $\mathrm{tr}\,K \equiv \gamma^{ij}K_{ij}$. These definitions lead to the following new constraints

$$\tilde{\gamma} = 1\ ,\quad \mathrm{tr}\,\tilde{A} \equiv \tilde{\gamma}^{ij}\tilde{A}_{ij} = 0\ , \tag{2.49}$$

which will be denoted as *conformal constraints* from now on in order to distinguish them from the *physical constraints* associated to Z_a. As a consequence, we have the following relations $\tilde{\gamma}^{ij} = \chi^{-1}\,\gamma^{ij}$ and $\gamma = \chi^{-3}$ for the inverse and determinant of the induced metric respectively. Notice that now the list of evolved fields is $\{\chi, \tilde{\gamma}_{ij}, \mathrm{tr}\,K, \tilde{A}_{ij}, Z_i, \Theta\}$. Instead of using $\mathrm{tr}\,K$ and Z_i, it is more convenient to use the following quantities

$$tr\hat{K} \equiv trK - 2\,\Theta\ , \tag{2.50}$$

$$\hat{\Gamma}^i \equiv \tilde{\Gamma}^i + \frac{2}{\chi}Z^i\ , \tag{2.51}$$

so that the evolution equations are closer to those of the **BSSN** formulation [87, 88], where the quantity $\tilde{\Gamma}^i = \tilde{\gamma}^{jk}\,\tilde{\Gamma}^i{}_{jk} = -\partial_j\tilde{\gamma}^{ij}$ is directly evolved. After some algebra, the

evolution equations for the final list of evolved fields $\{\chi, \tilde{\gamma}_{ij}, tr\hat{K}, \tilde{A}_{ij}, \hat{\Gamma}^i, \Theta\}$ are:

$$\begin{aligned}
\partial_t\tilde{\gamma}_{ij} &= \beta^k\partial_k\tilde{\gamma}_{ij} + \tilde{\gamma}_{ik}\,\partial_j\beta^k + \tilde{\gamma}_{kj}\partial_i\beta^k - \frac{2}{3}\,\tilde{\gamma}_{ij}\partial_k\beta^k - 2\alpha\Big(\tilde{A}_{ij} - \frac{\lambda_0}{3}\tilde{\gamma}_{ij}\ \mathrm{tr}\,\tilde{A}\Big) \\
&\quad - \frac{\kappa_c}{3}\,\alpha\tilde{\gamma}_{ij}\ln\tilde{\gamma}\ , \qquad (2.52)\\
\partial_t\tilde{A}_{ij} &= \beta^k\partial_k\tilde{A}_{ij} + \tilde{A}_{ik}\partial_j\beta^k + \tilde{A}_{kj}\partial_i\beta^k - \frac{2}{3}\,\tilde{A}_{ij}\partial_k\beta^k - \frac{\kappa_c}{3}\,\alpha\,\tilde{\gamma}_{ij}\ \mathrm{tr}\,\tilde{A} \\
&\quad + \chi\Big[\,\alpha\,\big({}^{(3)}R_{ij} + D_iZ_j + D_jZ_i - 8\pi\,S_{ij}\big) - D_iD_j\alpha\,\Big]^{\mathrm{TF}} \\
&\quad + \alpha\,\Big(\mathrm{tr}\,\hat{K}\,\tilde{A}_{ij} - 2\tilde{A}_{ik}\tilde{A}^k{}_j\Big)\ , \qquad (2.53)\\
\partial_t\chi &= \beta^k\partial_k\chi + \frac{2}{3}\,\chi\left[\alpha(tr\hat{K} + 2\,\Theta) - \partial_k\beta^k\right]\ , \\
\partial_t\,\mathrm{tr}\,\hat{K} &= \beta^k\partial_k tr\hat{K} - D_iD^i\alpha + \alpha\,\Big[\frac{1}{3}\big(tr\hat{K} + 2\Theta\big)^2 + \tilde{A}_{ij}\tilde{A}^{ij} + 4\pi\big(\tau + trS\big) \\
&\quad + \kappa_z\Theta\,\Big] + 2\,Z^iD_i\alpha\ , \qquad (2.54)\\
\partial_t\Theta &= \beta^k\partial_k\Theta + \frac{\alpha}{2}\left[{}^{(3)}R + 2D_iZ^i + \frac{2}{3}\,tr^2\hat{K} + \frac{2}{3}\,\Theta\Big(tr\hat{K} - 2\Theta\Big) - \tilde{A}_{ij}\tilde{A}^{ij}\right] \\
&\quad - Z^iD_i\alpha - \alpha\left[8\pi\,\tau + 2\kappa_z\,\Theta\right]\ , \qquad (2.55)\\
\partial_t\hat{\Gamma}^i &= \beta^j\partial_j\hat{\Gamma}^i - \hat{\Gamma}^j\partial_j\beta^i + \frac{2}{3}\hat{\Gamma}^i\partial_j\beta^j + \tilde{\gamma}^{jk}\partial_j\partial_k\beta^i + \frac{1}{3}\,\tilde{\gamma}^{ij}\partial_j\partial_k\beta^k \\
&\quad - 2\tilde{A}^{ij}\partial_j\alpha + 2\alpha\left[\tilde{\Gamma}^i{}_{jk}\tilde{A}^{jk} - \frac{3}{2\chi}\,\tilde{A}^{ij}\partial_j\chi - \frac{2}{3}\,\tilde{\gamma}^{ij}\partial_j tr\hat{K} - 8\pi\,\tilde{\gamma}^{ij}\,S_i\right] \\
&\quad + 2\alpha\left[-\tilde{\gamma}^{ij}\left(\frac{1}{3}\partial_j\Theta + \frac{\Theta}{\alpha}\,\partial_j\alpha\right) - \frac{1}{\chi}Z^i\left(\kappa_z + \frac{2}{3}\,(tr\hat{K} + 2\Theta)\right)\right], \qquad (2.56)
\end{aligned}$$

where the expression $[\ldots]^{\mathrm{TF}}$ indicates the trace-free part with respect to the metric $\tilde{\gamma}_{ij}$ and the Lie-derivatives of β has been written explicitly. The non-trivial terms inside this expression can be written as

$${}^{(3)}R_{ij} + 2D_{(i}Z_{j)} = {}^{(3)}\hat{R}_{ij} + \hat{R}^{\chi}_{ij}\ , \qquad (2.57)$$

where

$$\begin{aligned}
\hat{R}^{\chi}_{ij} &= \frac{1}{2\chi}\,\partial_i\partial_j\chi - \frac{1}{2\chi}\,\tilde{\Gamma}^k_{ij}\partial_k\chi - \frac{1}{4\chi^2}\,\partial_i\chi\partial_j\chi + \frac{2}{\chi^2}Z^k\tilde{\gamma}_{k(i}\partial_{j)}\chi \\
&\quad + \frac{1}{2\chi}\tilde{\gamma}_{ij}\left[\tilde{\gamma}^{km}\Big(\partial_k\partial_m\chi - \frac{3}{2\chi}\,\partial_k\chi\partial_m\chi\Big) - \hat{\Gamma}^k\partial_k\chi\right]\ , \qquad (2.58)\\
{}^{(3)}\hat{R}_{ij} &= -\frac{1}{2}\,\tilde{\gamma}^{mn}\partial_m\partial_n\tilde{\gamma}_{ij} + \tilde{\gamma}_{k(i}\partial_{j)}\hat{\Gamma}^k + \hat{\Gamma}^k\tilde{\Gamma}_{(ij)k} + \tilde{\gamma}^{mn}\Big(\tilde{\Gamma}^k_{mi}\tilde{\Gamma}_{jkn} \\
&\quad + \tilde{\Gamma}^k_{mj}\tilde{\Gamma}_{ikn} + \tilde{\Gamma}^k{}_{mi}\tilde{\Gamma}_{knj}\Big)\ , \qquad (2.59)\\
D_iD_j\alpha &= \partial_i\partial_j\alpha - \tilde{\Gamma}^k_{ij}\partial_k\alpha + \frac{1}{2\chi}\Big(\partial_i\alpha\,\partial_j\chi + \partial_j\alpha\,\partial_i\chi - \tilde{\gamma}_{ij}\,\tilde{\gamma}^{km}\,\partial_k\alpha\,\partial_m\chi\Big)\ , \qquad (2.60)
\end{aligned}$$

The matter terms of this conformal approach are computed by contracting the stress-energy tensor (2.21), namely

$$\tau = n_a\, n_b\, T^{ab} = \alpha^2\, T^{00} \ , \tag{2.61}$$

$$S_i = -n^a T_{ai} \equiv \frac{\tilde{S}_i}{\chi} \ , \ S_{ij} = T_{ij} \equiv \frac{\tilde{S}_{ij}}{\chi^2} \ , \tag{2.62}$$

$$\tilde{S}_i = \alpha\, \tilde{\gamma}_{ik} \Big(T^{0k} + \beta^k\, T^{00} \Big) \ , \tag{2.63}$$

$$\tilde{S}_{ij} = \tilde{\gamma}_{ik}\, \tilde{\gamma}_{jm}\, \beta^k \beta^m\, T^{00} + \Big(\tilde{\gamma}_{ik}\, \beta_j + \tilde{\gamma}_{jk}\, \beta_i \Big) T^{0k} + \tilde{\gamma}_{ik}\, \tilde{\gamma}_{jm}\, T^{km} \ , \tag{2.64}$$

The evolution equations (2.52)-(2.56) are equivalent to those obtained in the original work [92], by defining the conformal factor as $\chi = \gamma^{-1/3}$ instead of $\phi = \gamma^{-1/6}$, except by two significant differences. First, there is a new term proportional to $\mathrm{tr}\, \tilde{A}$. This term, which was already suggested in [92], is crucial to obtain a well-posed evolution system if the algebraic conformal constraints $\ln \tilde{\gamma} = \mathrm{tr}\, \tilde{A} = 0$ are not enforced during the evolution, as we shall illustrate in Section 2.3.4. Second, damping terms proportional to κ_c have been included in order to control dynamically the conformal constraints, exactly in the same way as it is done with the physical ones, as we shall show with some tests in Section 4.5. A common feature of the current conformal formulations, like the different flavors of **BSSN**[87, 88] and **CCZ4** [92, 98], is that a subset of the constraints of the system must be enforced after each time step of the simulation in order to obtain a stable evolution. Although this feature does not present a problem when using explicit time integrators, it might be not so straightforward for more sophisticated numerical methods or for automatically generated codes [99–102]. Note that, with the new terms introduced in the equations, it is ensured that the full system is strongly hyperbolic (and well-posed), as we will show in the section 2.3.4, and that the constraints are dynamically enforced during the evolution. Hence, our modified **CCZ4** formalism does not require the algebraic enforcing of any constraint.

2.3.3 Slicing conditions

Einstein's equations do not impose any condition on neither the lapse function α nor the shift-vector β^i, which are directly related to the specific choice of time and spatial coordinates. The choice related to lapse time coordinates function is called *slicing condition*, and for the spatial coordinates on the hypersurface Σ_t, shift vector, is called *spatial gauge condition*. As a consequence of the general covariance in **GR**, there is infinite possibilities to set the coordinate freedom.

The simplest choice would be to set some algebraic form for the lapse and shift-vector. For instance, the geodesic slicing condition is recovered with $\alpha = 1$ and $\beta^i = 0$, so that

the time coordinate coincide with the proper timer of the Eulerian observers. However, this condition is not a good choice [103], since it leads to coordinate singularities, i.e., Eulerian observers will focus into a single point, or equivalently, the spatial volume $\sqrt{\gamma}$ will tend to zero.

Other ways of fixing the lapse and shift-vector would involve some geometrical property, as for example, the *maximal slicing condition* $\operatorname{tr} K = 0$, which implies

$$D^i D_i \alpha = \alpha \left(K_{ij} K^{ij} + 4\pi(\tau + S) \right) \ . \tag{2.65}$$

This election of the lapse function is a *singularity-avoiding* condition [103], i.e., the lapse function α goes to zero when the spatial volume $\sqrt{\gamma}$ goes to zero [104, 105]. The maximal slicing condition (2.65) is an elliptic equation. In the context of free evolution scheme, this kind of equation is theoretically more involved and computationally expensive. In order to circumvent these problems, one could transform this elliptic equation into a parabolic one [106].

Another interesting choice is the so called *harmonic slicing*, which considers that the harmonic condition[2] holds for the $x^0 = t$ coordinate, leading to the following evolution equation for the lapse function

$$\partial_t \alpha = \beta^i \partial_i \alpha - \alpha^2 \operatorname{tr} K \ . \tag{2.66}$$

The harmonic slicing contrast with both slicing conditions explained before, since it involves a time evolution for the lapse. This time coordinate choice can be generalized by defining a family of slicing conditions, called *Bona-Massó gauge* [105],

$$\partial_t \alpha \ = \ \beta^i \partial_i \alpha - \alpha^2 \, f(\alpha) \, \operatorname{tr} K \ , \tag{2.67}$$

which has the desired properties for any $f(\alpha) \geq 0$: the lapse sector is strongly hyperbolic and it can mimic the behavior of the maximal slicing condition. Note that the case $f(\alpha) = 1$ correspond to the harmonic slice condition, while that $f(\alpha) \to \infty$ allows to recover the maximal slicing condition. For our numerical simulations, we shall use the so-called $1 + \log$ *slicing condition*, corresponding to[3] $f(\alpha) = 2/\alpha$. This choice has very good singularity avoidance conditions, since near the singularity $\alpha \to 0$ and $f(\alpha) \to \infty$, behaving as the maximal slicing condition.

[2] The harmonic condition for the spacetime coordinates (x^a) is given by $\Box_g x^a := g^{bc} \nabla_b \nabla_c x^a = 0$.
[3] Changing trK by $\operatorname{tr} \hat{K}$.

We can also define the shift-vector β^i through a time evolution equation. In particular, we use the hyperbolic Gamma-driver condition [107, 108], namely

$$\partial_t \beta^i = \beta^j \partial_j \beta^i + g(\alpha)\, B^i \ , \tag{2.68}$$

$$\partial_t B^i = \beta^j \partial_j B^i - \eta B^i + \partial_t \hat{\Gamma}^i - \beta^j \partial_j \hat{\Gamma}^i \ , \tag{2.69}$$

being $g(\alpha)$ an arbitrary function depending on the lapse function and η is a constant parameter that was introduced as a *damping term* in order to avoid strong oscillations during the shift evolution. In fact, these hyperbolic conditions can be deduced from a geometrical elliptic condition called *minimal distortion* condition [77, 103], which tries to minimize the stretching of the spatial coordinates. For our numerical simulations, we shall use the values of $g(\alpha) = 3/4$ and $\eta = 2$. In the following Section 2.3.4, we discuss these values by analyzing the characteristic structure of **CCZ4**. As we will see, the **CCZ4** formalism used in this Thesis, when supplied with the $1 + \log$ and Gamma-freezing condition,will lead to a hyperbolic system, as we will see in the following section.

In that follows, we shall discuss the characteristic structure of **CCZ4** formalism, showing that there exist a completed set of eigenvectors and real eigenvalues.

2.3.4 Characteristic structure of CCZ4

The hyperbolicity of the evolution system (2.52)-(2.56) (in the absence of boundaries or with periodic boundaries) can be studied for systems of first order in time and space. Here, instead, we use the concept of pseudo-hyperbolicity [63, 109, 110], that generalizes the hyperbolicity analysis to systems with second order derivatives in space. In particular, we reproduce in detail the analysis made in Ref. [111], which relies on a plane-wave analysis applied to the linearized Einstein equations around a background metric. Notice also the work in Ref. [112] that extend these ideas using pseudo-differential operators.

Hence, we consider the line element [63, p.42]

$$ds^2 = -\alpha_0^2 dt^2 + \tilde{\gamma}^0_{ij}(dx^i + \beta^i_0 dt)(dx^j + \beta^j_0 dt) \ , \tag{2.70}$$

and study the dynamics of perturbations over this background spacetime which propagates along a given normalized direction s_i (i.e., such that $\gamma^0_{ij} s^i s^j = 1$). The perturbation for the metric fields $\{\alpha, \beta^k, \tilde{\gamma}_{ij}, \chi\}$ has a generic plane-wave form,

$$\alpha - \alpha_0 = e^{i\omega\cdot\vec{x}}\, \bar{\alpha}(\omega, t) \ \ , \ \ \beta^k - \bar{\beta}^k_0 = e^{i\omega\cdot\vec{x}}\, \bar{\beta}(\omega, t) \ , \tag{2.71}$$

$$\tilde{\gamma}_{ij} - \tilde{\gamma}^0_{ij} = e^{i\omega\cdot\vec{x}}\, \bar{\gamma}_{ij}(\omega, t) \ \ , \ \ \chi - \chi_0 = e^{i\omega\cdot\vec{x}}\, \bar{\chi}(\omega, t) \ , \tag{2.72}$$

where ω^k is the wavenumber and $\omega \equiv \omega_k\, s^k$. An additional factor $i\omega$ appears in the perturbations of the fields $\{\tilde{A}_{ij}, \hat{K}, \Theta, \hat{\Gamma}^i, B^i\}$, which are first derivatives of the metric, namely

$$\tilde{A}_{ij} = i\omega e^{i\omega\cdot\vec{x}}\,\bar{A}_{ij}(\omega,t) \;\;,\;\; \hat{K} = i\omega e^{i\omega\cdot\vec{x}}\,\bar{K}(\omega,t) \;\;,\;\; \Theta = i\omega e^{i\omega\cdot\vec{x}}\,\bar{\Theta}(\omega,t)\;, \tag{2.73}$$

$$\hat{\Gamma}^i = i\omega e^{i\omega\cdot\vec{x}}\,\bar{\Gamma}^i(\omega,t) \;\;,\;\; B^i = i\omega e^{i\omega\cdot\vec{x}}\,\bar{B}^i(\omega,t)\;. \tag{2.74}$$

Replacing the above mentioned definitions in (2.52) - (2.56) one can obtain the following system:

$$\partial_t\bar{\gamma}_{ij} = -i\,\omega\left(-\tilde{\gamma}^0_{ik}\,s_j\,\bar{\beta}^k - \tilde{\gamma}^0_{kj}\,s_i\,\bar{\beta}k + \frac{2}{3}\,\tilde{\gamma}^0_{ij}s_k\bar{\beta}^k + 2\alpha_0\Big(\bar{A}_{ij} - \frac{\lambda_0}{3}\tilde{\gamma}^0_{ij}\,\bar{A}\Big) - \bar{\beta}^s_0\,\bar{\gamma}_{ij}\right)\;, \tag{2.75}$$

$$\partial_t\bar{A}_{ij} = -i\,\omega\left\{\left[\alpha_0\,\chi_0\left(\frac{1}{2\chi_0}\bar{\gamma}_{ij} - \frac{1}{2}\,\tilde{\gamma}^0_{ki}\,s_j\,\bar{\Gamma}^k - \frac{1}{2}\,\tilde{\gamma}^0_{kj}\,s_i\,\bar{\Gamma}^k - \frac{1}{2\chi_0}s_is_j\,\bar{\chi} - \frac{1}{2\chi_0^2}\,\tilde{\gamma}^0_{ij}\,\bar{\chi}\right) + s_is_j\,\frac{\bar{\alpha}}{\alpha_0}\right]^{TF} - \bar{\beta}^s_0\,\bar{A}_{ij}\right\}\;, \tag{2.76}$$

$$\partial_t\bar{\chi} = -i\,\omega\left(-\frac{2}{3}\alpha_0\,\chi_0\,\bar{K} - \frac{4}{3}\alpha_0\,\chi_0\,\bar{\Theta} + \frac{2}{3}\,\chi_0\bar{\beta}^s - \bar{\beta}^s_0\,\bar{\chi}\right)\;, \tag{2.77}$$

$$\partial_t\bar{K} = -i\omega(\bar{\alpha} - \bar{\beta}^s_0\,\bar{K})\;, \tag{2.78}$$

$$\partial_t\bar{\Theta} = -i\,\omega\left(\frac{\alpha_0}{2}\left[\frac{1}{2}tr\bar{\gamma} - \chi_0\,\bar{\Gamma}^s - \frac{2}{\chi_0}\bar{\chi}\right] - \bar{\beta}^s_0\,\bar{\Theta}\right)\;, \tag{2.79}$$

$$\partial_t\bar{\Gamma}^i = -i\,\omega\left(-\tilde{\gamma}^{0\,jk}s_js_k\,\bar{\beta}^i - \frac{1}{3}\tilde{\gamma}^{0\,ij}s_js_k\,\bar{\beta}^k + \frac{4}{3}\alpha_0\tilde{\gamma}^{0\,ij}s_is_j\,\bar{K} + \frac{2\,\alpha_0}{3}\tilde{\gamma}^{0\,ij}s_j\bar{\Theta} - \bar{\beta}^s_0\,\bar{\Gamma}^i\right)\;, \tag{2.80}$$

$$\partial_t\bar{\alpha} = -i\,\omega\left(\alpha_0^2\,f(\alpha_0)\,\bar{K} - \bar{\beta}^s_0\,\bar{\alpha}\right)\;, \tag{2.81}$$

$$\partial_t\bar{\beta}^i = -i\,\omega\left(-g(\alpha_0)\,\bar{B}^i - \bar{\beta}^s_0\,\bar{\beta}^i\right)\;, \tag{2.82}$$

$$\partial_t\bar{B}^i = -i\,\omega\left(-\tilde{\gamma}^{0\,jk}s_js_k\,\bar{\beta}^i - \frac{1}{3}\tilde{\gamma}^{0}{}_{ij}s_js_k\,\bar{\beta}^k + \frac{4}{3}\alpha_0\tilde{\gamma}^{0\,ij}\,s_is_j\,\bar{K} + \frac{2\,\alpha_0}{3}\tilde{\gamma}^{0\,ij}s_j\bar{\Theta} + (\lambda_4 - 1)\bar{\beta}^s_0\,\bar{\Gamma}^i - \bar{\beta}^s_0\,\bar{B}^i\right)\;, \tag{2.83}$$

which can be easily written as follows

$$\partial_t\bar{u} = -i\,\omega(\mathcal{A} - \bar{\beta}^s_0\mathrm{I})\bar{u}\;, \tag{2.84}$$

where $\bar{u}$ is a vector containing the perturbation of the fields, $\mathcal{A}$ is the characteristic matrix and I the identity one. The index s means a contraction with the propagation direction s_i (i.e., $\bar{\beta}^s_0 = s_i\bar{\beta}^i_0$). The projection orthogonal to s_i will be denoted by the index $\perp$. Following what was described in the previous section, we shall say that the system (2.84) is pseudo-hyperbolic if and only if the characteristic matrix $\mathcal{A}$ has real eigenvalues and a

complete set of eigenvectors. Therefore, with this definition, hyperbolicity of the system translates into a set of algebraic conditions [85]. The analysis of the characteristic structure can be simplified by splitting the perturbations in different sectors which do not interact (i.e., or at least, not strongly) with the others.

It is instructive to analyze first the effect of the term proportional to λ_0. There is a sector, involving only the perturbations of $\tilde{\gamma}$ and $tr\tilde{A}$, given by:

$$\partial_t \begin{pmatrix} \tilde{\gamma} \\ tr\tilde{A} \end{pmatrix} \approx \alpha \begin{pmatrix} 0 & 2(\lambda_0 - 1) \\ 0 & 0 \end{pmatrix} \begin{pmatrix} \tilde{\gamma} \\ \mathrm{tr}\,\tilde{A} \end{pmatrix} + \dots \,, \tag{2.85}$$

where $\approx$ means that only the principal part is considered. Obviously, for the original choice $\lambda_0 = 0$, there is not a complete set of eigenvectors[4]. Then, the system is only weakly pseudo-hyperbolic system and, consequently, the problem is ill-posed. The same problem appears for any other value except for $\lambda_0 = 1$. Only for this choice both $\{\tilde{\gamma}, \tilde{A}\}$ are standing modes, implying that this sector has a complete set of eigenvectors. As it is shown next, the other sectors are also complete, meaning that the full system is strongly pseudo-hyperbolic. Notice that this lack of strong hyperbolicity (together with the unbound growth of the conformal constraints) prevents to evolve directly the unconstrained **CCZ4**, unless the conformal constraints are algebraically enforced during the evolution [82].

We can now study the characteristic structure of the other modes. The lapse sector, constituted by $\{\bar{\alpha}, tr\bar{K}\}$, has a complete set of eigenvectors with eigenvalues $-\bar{\beta}_0^s \pm \alpha_0\sqrt{f}$. The longitudinal shift and energy modes form another closed sector with a complete set of eigenvectors including $\{\bar{\chi}, \bar{\Theta}, \bar{\Gamma}^s, \bar{\beta}^s, \bar{B}^s\}$ with characteristic speeds given by $\{-\bar{\beta}_0^s, -\bar{\beta}_0^s \pm \sqrt{4\,g/3\chi_0}, -\bar{\beta}_0^s \pm \alpha_0\}$. The transverse shift sector, including $\{\bar{\beta}^\perp, \bar{\Gamma}^\perp, \bar{B}^\perp\}$, is also complete with characteristic speeds $\{-\bar{\beta}_0^s, -\bar{\beta}_0^s \pm \sqrt{g/\chi_0}\}$. The light sector also has a complete set of eigenvectors including the projections $\{\overline{\gamma}_{\perp\perp}, \bar{A}_{\perp\perp}, \overline{\gamma}_{s\perp}, \bar{A}_{s\perp}\}$, with characteristic speeds $\{-\bar{\beta}_0^s \pm \alpha_0\}$. Finally, notice that the choice $g(\alpha) = 3/4$ is especially delicate because the characteristic velocities of the longitudinal shift modes collapse to light speed: no complete set of eigenvectors can be found, and the strong pseudo-hyperbolicity of the system is spoiled. This might be a problem, at least around Minkowski spacetimes, as it has been reported previously by several authors [110, 113, 114].

[4] Notice that the solutions of (2.85) are given by

$$\begin{aligned} \tilde{\gamma} &\approx 2\alpha(\lambda_0 - 1)\,\mathrm{tr}\,\tilde{A}_0\, t + \tilde{\gamma}_0 \\ tr\tilde{A} &= \mathrm{tr}\,\tilde{A}_0 \,. \end{aligned}$$

Clearly, this sector presents a linear mode.

Finally, it is worth stressing that the main reason of the numerical instabilities found when trying to solve the **ADM** equation with **NR** codes is due to the weakly hyperbolicity of the system, at least for the generic family of lapse-shift usually considered [63].

2.4 Analysis quantities

In order to monitor the evolution and analyze the results of our simulations it is interesting to compute some analysis quantities like for example the Hamiltonian and momentum constraint, **ADM** mass, angular momentum and gravitational waves. Here, these quantities are written as a function of our evolution (conformal) variables.

Assuming that $\theta = Z_i = 0$, we have that the Hamiltonian and momentum constraint are given by

$$\mathcal{H} = R + \frac{2}{3}(trK)^2 - \tilde{A}_{ij}\tilde{A}^{ij} - 16\pi G\rho \ , \tag{2.86}$$

$$\mathcal{M}_i = \tilde{\gamma}^{jk}\partial_j \tilde{A}_{ki} - \tilde{\Gamma}^j_{ki}\tilde{A}^k_j - \tilde{\Gamma}^j \tilde{A}_{ij} - \frac{3}{2\chi}\tilde{A}^j_i \partial_j \chi - \frac{2}{3}\partial_i trK - 8\pi G \frac{\tilde{S}_i}{\chi} \ . \tag{2.87}$$

Other interesting quantities are **ADM** mass and angular momentum [70, 77, 115]. As it is well-known that the mass-energy of a system can not be defined locally in **GR**, but only assuming an asymptotically flat spacetimes. The **ADM** mass measures the total mass-energy of an isolated gravitating system at any instant of time [116]. It can be computed by performing a surface integral at spatial infinity

$$M_{ADM} \equiv \frac{1}{16\pi}\lim_{r\to\infty}\int_S \gamma^{ij}\left(\partial_j \gamma_{ik} - \partial_k \gamma_{ij}\right) dS^k = \frac{1}{8\pi}\lim_{r\to\infty}\int_S \left(\tilde{\gamma}^{ik}\partial_k \chi + \frac{\chi}{2}\tilde{\Gamma}^i\right) dS_i \ , \tag{2.88}$$

where dS_i the surface element of S, for simplicity, it is convenient to consider S a two dimensional sphere, therefore, the surface element is given by

$$dS_i = \frac{x_i}{r}\chi^{-3/2} r^2 \sin\theta d\theta d\phi \ . \tag{2.89}$$

Likewise, the angular momentum, in Cartesian coordinates, is

$$J^i_{ADM} \equiv \frac{1}{8\pi}\lim_{r\to\infty}\int_S \epsilon^{ijk} x_j K_{kl} dS^l = \frac{1}{8\pi}\lim_{r\to\infty}\int_S \hat{\phi}_j \chi \left(\tilde{A}^{ji} + \frac{\tilde{\gamma}^{ji}}{3} trK\right) dS_i \ , \tag{2.90}$$

where $\hat{\phi}_j = (-y, x, 0)$ is the Cartesian coordinate basis axial vector.

2.4.1 Gravitational wave signal extraction

The most common techniques used to extract the gravitational radiation from numerical simulations are either the Newman-Penrose scalar Ψ_4 or the Regge-Wheller-Zerilli theory, see [117] for a vast review of gravitational waves extraction. Here, in order to analyze the gravitational radiation emitted during the coalescence of our binary systems, we use the Newman-Penrose Ψ_4 scalar as described in Ref. [117, 118].

The Newman-Penrose scalars are scalar quantities defined trough contraction of Weyl tensor, defined over our four dimensional manifold $\mathcal{M}$ as

$$\begin{aligned} C_{acbd} \;:=\; & R_{acbd} - \frac{1}{2}\left(g_{ab}R_{cd} - g_{ad}R_{bc} - g_{bc}R_{ad} + g_{cd}R_{ab}\right) \\ & -\frac{1}{6}R\left(g_{ab}g_{cd} - g_{ad}g_{bc}\right) \;, \end{aligned} \tag{2.91}$$

and an orthonormal null tetrad $\{l^a, \bar{m}^a, k^a, \bar{m}^a\}$ [66]. Therefore, the Newman-Penrose scalar [119] are defined as

$$\Psi_0 \;\equiv\; -C_{abcd}l^a m^b l^c m^d \;, \tag{2.92}$$

$$\Psi_1 \;\equiv\; -C_{abcd}l^a k^b l^c m^d \;, \tag{2.93}$$

$$\Psi_2 \;\equiv\; -C_{abcd}l^a m^b \bar{m}^c k^d \;, \tag{2.94}$$

$$\Psi_3 \;\equiv\; -C_{abcd}l^a k^b \bar{m}^c k^d \;, \tag{2.95}$$

$$\Psi_4 \;\equiv\; -C_{abcd}k^a \bar{m}^b k^c \bar{m}^d \;. \tag{2.96}$$

As a consequence of the peeling theorem [120–122], some of components of the Weyl tensor can be decomposed as follows:

$$C_{abcd} \approx \frac{\Psi_4}{r} + \frac{\Psi_3}{r^2} + \frac{\Psi_2}{r^3} + \frac{\Psi_1}{r^4} + \frac{\Psi_0}{r^5} + \mathcal{O}(r^{-6}) \;, \tag{2.97}$$

and, the information carrying out outgoing gravitational waves far from the source can be calculated from the Newman-Penrose scalar Ψ_4 [123, p.422] Actually, equation (2.97) shows that the gravitational radiation falloff as $1/r$. In our framework, we have constructed the null tetrad in Cartesian coordinates as follows [124]:

(a) Let us first define a orthogonal spatial triad

$$\phi^i = (-y, x, 0) \;,\; s^i = (x, y, z) \;,\; \theta^i = (xz, yz, -(x^2 + y^2)) \;. \tag{2.98}$$

(b) Using Gram-Schmidt orthogonalization procedure a orthonormal basis can be obtained

$$\hat{\phi}^i = \frac{\phi^i}{\sqrt{\omega_{\phi\phi}}} \ , \ \hat{s}^i = \frac{s^i - \hat{\phi}^i\omega_{\phi s}}{\sqrt{\omega_{ss}}} \ , \ \hat{\theta}^i = \frac{\theta^i - \hat{\phi}^i\omega_{\phi\theta} - \hat{s}^i\omega_{s\theta}}{\sqrt{\omega_{\theta\theta}}} \ , \tag{2.99}$$

where $\omega_{ab} = v^i_a v^j_b \gamma_{ij}$, being $v^i_a = \{\phi^i, s^i, \theta^i\}$.

(c) With this triad and the normal n^avector to the hypersurfaces a null tetrad can be constructed

$$l^a = \frac{1}{\sqrt{2}}\left(\hat{n}^a + \hat{s}^a\right) \ , \ k^a = \frac{1}{\sqrt{2}}\left(\hat{n}^a - \hat{s}^a\right) \ , \tag{2.100}$$

$$m^a = \frac{1}{\sqrt{2}}\left(\hat{\theta}^a + i\hat{\phi}^a\right) \ , \ \bar{m}^a = \frac{1}{\sqrt{2}}\left(\hat{\theta}^a - i\hat{\phi}^a\right) \ . \tag{2.101}$$

One of the important properties of the Weyl tensor (2.91) is that it can be calculated in terms of $3+1$ quantities [70], namely

$$\Psi_4 = (E_{ij} + iB_{ij})\bar{m}^i\bar{m}^j \ , \tag{2.102}$$

where the *electric*, E_{ij}, and *magnetic*, B_{ij}, parts of the Weyl tensor are

$$\begin{aligned} E_{ij} &= -R_{ij} - trK K_{ij} + K_{ik}K^k_j \ , \\ &= -R_{ij} + \frac{1}{\chi}\tilde{A}_{ik}\tilde{A}^k_j - \frac{1}{3\chi}trK\tilde{A}_{ij} - \frac{2}{9\chi}\tilde{\gamma}_{ij}\,\mathrm{tr}^2\,K \ , \end{aligned} \tag{2.103}$$

$$B_{ij} = \epsilon_i{}^{kl}\nabla_k K_{lj} = \frac{\tilde{\gamma}_{mi}}{\chi^{5/2}}\eta^{mkl}\nabla_k K_{lj} \ . \tag{2.104}$$

In our numerical simulations Ψ_4 is calculated on a spherical surface far from the sources using (2.102). Then, it is expanded in terms of spin-weighted spherical harmonics (with spin weight $s = -2$) [117, 124], namely

$$r\Psi_4(t, r, \theta, \phi) = \sum_{l,m} \Psi_4^{l,m}(t, r)\ {}^{-2}Y_{l,m}(\theta, \phi) \ , \tag{2.105}$$

where $\Psi_4^{l,m}(t, r) = \int_{S^2} \Psi_4\, {}^{-2}Y_{l,m} d\Omega$. Furthermore, the instantaneous angular frequency of the gravitational wave can now be calculated easily from the Ψ_4 as

$$f_{GW} = \frac{\omega_{GW}}{2\pi} \ , \quad \omega_{GW} = -\frac{1}{2}\Im\left(\frac{\dot{\Psi}_4^{l,m}}{\Psi_4^{l,m}}\right) . \tag{2.106}$$

A more direct quantity, related directly to the response of the detector is the strain defined as $h(t) = h_+(t) - i\,h_\times(t)$, where $(h_+, h_\times)$ are the plus and cross modes of gravitational waves, as described in Section 1.3 . The Newman-Penrose scalar Ψ_4 (2.102) is

related to the strain via [117]:

$$\Psi_4 = \ddot{h}_+ - i\,\ddot{h}_\times. \tag{2.107}$$

We can calculate the strain through a direct double integration in the time domain, leading to

$$h_+ - i\,h_\times = \int_t \left(\int_{t'} \Psi_4(t'')dt'' \right) dt' + At + B \ , \tag{2.108}$$

where the constant of integration A and B have to be fixed by the imposition of some physical condition [125, 126]. However, this procedure has to be performed carefully to prevent a contamination of the purely harmonic behavior of the strain. One way to avoid the appearance of these constants is calculating the strain in the frequency domain [127]. The components of the strain in the time domain can be calculated by performing the inverse Fourier transform of the strain in the frequency domain, $h^{l,m}(t) \equiv \mathcal{F}^{-1}[\tilde{h}^{l,m}(f)]$, which can be calculated as

$$\tilde{h}^{l,m}(f) = \begin{cases} -\dfrac{\mathcal{F}[{\Psi_4}^{l,m}(t)]}{f_0^2} \ , & f < f_0 \\ \\ -\dfrac{\mathcal{F}[{\Psi_4}^{l,m}(t)]}{f^2} \ , & f \geq f_0 \end{cases} , \tag{2.109}$$

where f_0 is the initial orbital frequency.

Finally, the **GWs**, the **ADM** mass, and the angular momentum are computed as spherical surface integrals at different extraction radii in order to check the consistency of the results.

Chapter 3

Matter Spacetimes

So far, we have not provided any prescription about the matter content that will produce the spacetime curvature. As it was explained in Chapter 1, the energy, momentum and stresses of matter can be defined through a symmetric tensor T_{ab}, satisfying the conservation law

$$\nabla_a T^{ab} = 0 \ . \tag{3.1}$$

In this Chapter, we shall focus on the right-hand-side of the Einstein's equations (1.16). In particular, we present the two main matter models which will be studied in this Thesis: complex scalar fields to describe macroscopic Bose-Einstein condensates and perfect fluids to describe neutron stars.

A scalar field is probably the simplest model of matter. A complex scalar field, coupled with the Einstein equations, allow us to study self-gravitating compact solutions, representing Bose-Einstein condensates, known commonly as Boson Stars. The evolution of these complex scalar fields are governed by the Klein-Gordon equation, which is just only a wave equation with sources. Therefore, from a mathematical point of view, this equation is well-posed and does not develop shocks or discontinuities during the evolution, given a smooth initial data.

Several astrophysical scenarios can be described by using fluids approximation, whose evolution is governed by the relativistic hydrodynamics equations. Although these equations are also well-posed, they could generate shocks or discontinuities during the evolution. There are different fluid models to describe, for instance, dust, radiation fluid or perfect fluids. Here, we shall focus in perfect fluids, which allows us to model self-gravitating astrophysical objects such as neutron stars.

This chapter is organized as follows. First, in Section 3.1, a generic matter field is presented by using the variation principle in the Hilbert-Einstein action coupled to

matter. Then, we focus in the $3+1$ decomposition of the conservation law for the energy-momentum tensor in Section 3.2. A short summary on the spherical symmetric spacetimes is provided in Section 3.3. Complex scalar field model are discussed in detail in section 3.4, describing also the Einstein-Klein-Gordon (**EKG**) evolution system and how to construct boson stars. Finally, perfect fluids are discussed in Section 3.5, deriving the general relativistic hydrodynamics equations and analyzing its conservative form, which will be crucial to numerical simulations. We also show how to construct neutron stars and discuss its properties. We have based this Chapter mainly on [58, 63, 77, 116, 123, 128–130].

3.1 Matter Field

As we have seen in Section 1.2, Einstein's equations can be inferred from the conservation law of the stress-energy tensor on one hand, and from the Einstein tensor on the other hand. A more fundamental derivation of Einstein's equations can be made trough a variation principle from an appropriate action [66, p.450]. To obtain the Einstein's equation in presence of matter, we assume that there are matter field present besides the gravitational field, and they are described by an appropriate Lagrangian density $\mathscr{L}_M$.

The action is defined as the integral of the Lagrangian over a open set $\mathcal{V} \subset \mathcal{M}$

$$S = \int_{\mathcal{V}} d^4x\sqrt{-g}\,(\mathscr{L}_g + \mathscr{L}_M) \ , \tag{3.2}$$

where $\mathscr{L}_g = \frac{1}{16\pi}R$ is the Einstein Lagrangian density associated to gravitational field. The variation of the action with respect to the metric[1] g^{ab} together with the properties [131]

$$\delta(\sqrt{-g}) = -\frac{\sqrt{-g}}{2}\,g_{ab}\,\delta g^{ab} \ , \tag{3.3}$$

$$\delta(\sqrt{-g}R) = \sqrt{-g}\,G_{ab}\,\delta g^{ab} \ , \tag{3.4}$$

leads to Einstein's equations in presence of matter fields,

$$G_{ab} = R_{ab} - \frac{1}{2}g_{ab}R = 8\pi\,T_{ab} = \frac{-2}{\sqrt{-g}}\frac{\delta}{\delta\, g^{ab}}\left(\sqrt{-g}\mathscr{L}_M\right) \ . \tag{3.5}$$

[1] Recall that, $\delta S = \int_{\mathcal{V}} \frac{\delta S}{\delta g^{ab}} h^{ab} dx^4 = \lim_{\epsilon\to 0} \frac{S(g^{ab}+\epsilon h^{ab}) - S(g^{ab})}{\epsilon}$, where h^{ab} is an arbitrary metric in $\mathcal{V}$.

3.2 3+1 decomposition of matter equations

The conservation of the energy-momentum tensor T_{ab}, equation (3.1), provides the equation of motion of the matter fields, corresponding to the conservation of energy and linear momentum in **GR**. Furthermore, in section 2.1, we have seen that the energy-momentum tensor can be decomposed as

$$T_{ab} = n_a n_b \tau + S_a n_b + S_b n_a + S_{ab} \ , \tag{3.6}$$

where $\tau := n_a n_b T^{ab}$ is the energy density, $S_a := -\gamma^c_a n_b T_{ab}$ is the momentum density and $S_{ab} := \gamma^c_a \gamma^d_b T_{cd}$ is the stress tensor. Therefore

$$\begin{aligned} \nabla_a T^{ab} &= \nabla_a T^a{}_b \\ &= \nabla_a \left(n_a n_b \tau + S_a n_b + S_b n_a + S_{ab} \right) \\ &= \nabla_a S^a_b - \operatorname{tr} K \, S_b + n^a \nabla_a S_b + n_b \nabla_a S^a - S^a K_{ba} - \operatorname{tr} K \tau n_b \\ &\quad + D_b \ln \alpha \, \tau + n_b n^a \nabla_a \tau \ , \end{aligned} \tag{3.7}$$

where we have used the useful relation $\nabla_a n_b = -K_{ba} - n_a D_b \ln \alpha$ and some orthogonality conditions. Projecting the equation (3.7) along the normal to the hypersurfaces Σ_t and onto Σ_t, we have that:

$$n^b \nabla_a T^a_b = 0 \quad \Leftrightarrow \quad n^b \nabla_a S^a_b + n^a n^b \nabla_a S_b - \nabla_a S^a + K\tau - n^a \nabla_a \tau = 0 \ , \tag{3.8}$$

$$\gamma^b_c \nabla_a T^a_b = 0 \quad \Leftrightarrow \quad \gamma^b_c \nabla_a S^a_b - \operatorname{tr} K S_c + \gamma^b_c n^a \nabla_a S_b - S^a K_{ca} + D_c \ln \alpha \, \tau = 0 \ , \tag{3.9}$$

or equivalently using [77, p.103]

$$n^a \nabla_a S^a_b = K_{ab} S^{ab} \ , \tag{3.10}$$

$$\nabla_a v^a = D_i v^i + v^i D_i \ln \alpha \ , \ \text{for all } v \in T_p \Sigma_t \ , \tag{3.11}$$

$$\nabla_b (\alpha n^a) = -\alpha K^a_b - D^a \, \alpha n_b + n^a \nabla_b \alpha \ , \tag{3.12}$$

the projections are:

$$-\frac{1}{\alpha}(\partial_t - \mathcal{L}_\beta)\tau - D_i S^i - 2 S^i D_i \ln \alpha + S_{ij} K^{ij} + K \tau = 0 \ , \tag{3.13}$$

$$\frac{1}{\alpha}(\partial_t - \mathcal{L}_\beta) S_j + D_i S^i_j + S^i_j D_i \ln \alpha - S_j K + \tau \, D_j \ln \alpha = 0 \ . \tag{3.14}$$

Equations (3.13) and (3.14) are the evolution equation of the *energy* and *momentum density* respectively

3.3 Stationary Spherically Symmetric solutions

Spherically symmetric spacetimes (**SSSs**) are very useful in **GR** [132], since these symmetries allow to simplify the equations of motion and reduced the original four dimensional problem to a two dimensional one. Furthermore, assuming also stationarity, **SSS** allows us to construct equilibrium configuration for non-rotating self-gravitating objects, as for example, boson stars (**BSs**) or neutron stars (**NSs**).

From a practical point of view, our strategy is going to be the following. First, calculate the initial data using a 1D numerical code. Then, extend this spherically symmetric solution into a 3D initial data, in Cartesian coordinate [128, 129], to study the evolution of those configurations.

Let us start by considering the most general metric for a time-dependent spherical symmetry in the $3+1$ form, with coordinates (t, r, θ, φ), being θ and φ the polar and azimuthal angular coordinates on the hypersurface,

$$ds^2 = (-\alpha^2 + a^2\beta^2)dt^2 + 2a^2\beta dt dr + a^2 dr^2 + r^2 b^2 d\Omega^2 \ , \tag{3.15}$$

where $\alpha(t, r)$ is the lapse function, $\beta^i = (\beta(t, r), 0, 0)$ is the shift vector in a spherical basis, $a(t, r)$ and $b(t, r)$ represents the components of the spatial metric and $d\Omega^2 = d\theta^2 + \sin^2\theta d\varphi^2$ is the metric of a unit two-sphere. By using Equation (2.17), it is straightforward to show that the extrinsic curvature has only two independent components in this geometry, given by

$$K^i_j = \begin{pmatrix} K^r_r(t, r) & 0 & 0 \\ 0 & K^\theta_\theta(t, r) & 0 \\ 0 & 0 & K^\theta_\theta(t, r) \end{pmatrix} \ . \tag{3.16}$$

Due to the symmetry, the other vectors behave as the shift one, namely $Z^i = (Z^r(r, t), 0, 0)$.

Putting the above ingredients in Equations (2.42)-(2.45), one can write the **Z4** in spherical symmetry as

$$\partial_t a = \partial_r a \beta^r - a K^r_r \alpha + a \partial_r \beta^r \ , \tag{3.17}$$

$$\partial_t b = \partial_r b \beta^r - b K^\theta_\theta \alpha + \frac{b \beta^r}{r} \ , \tag{3.18}$$

$$\begin{aligned}\partial_t K^r_r = {} & \partial_r a \left(\frac{2 \partial_r b \, \alpha}{a^3 b} + \frac{\partial_r \alpha}{a^3} + \frac{2 \alpha}{r a^3} \right) - \frac{4 \partial_r b \, \alpha}{r a^2 \, b} - \frac{2 \partial_{rr} b \, \alpha}{a^2 \, b} - \frac{\partial_{rr} \alpha}{a^2} + \frac{2 \alpha \partial_r \, Z^r}{a^2} \\ & + \partial_r K^r_r \beta^r + 2 K^\theta_\theta K^r_r \alpha - 2 K^r_r \alpha \Theta + {K^r_r}^2 \alpha + 8 \pi S^\theta_\theta \alpha - 4 \pi S^r_r \alpha - 4 \pi \tau \alpha \ ,\end{aligned} \tag{3.19}$$

$$\begin{aligned}\partial_t K^\theta_\theta = {} & \partial_r a \left(\frac{\partial_r b \, \alpha}{a^3 b} + \frac{\alpha}{r \, a^3} \right) + \partial_r b \left(- \frac{\partial_r \alpha}{a^2 \, b} - \frac{4 \, \alpha}{r \, a^2 \, b} \right) - \frac{\partial_r b^2 \alpha}{a^2 \, b^2} - \frac{\partial_{rr} b \alpha}{a^2 b} - \frac{\alpha}{r^2 \, a^2} \\ & - \frac{\partial_r \alpha}{r \, a^2} + \frac{\alpha}{r^2 \, b^2} + \partial_r K^\theta_\theta \beta^r - 2 K^\theta_\theta \alpha \Theta + 2 {K^\theta_\theta}^2 \alpha + K^\theta_\theta K^r_r \alpha \\ & + 4 \pi S^r_r \alpha - 4 \pi \tau \alpha \ ,\end{aligned} \tag{3.20}$$

$$\begin{aligned}\partial_t \Theta = {} & \partial_r a \left(\frac{2 \partial_r b \, \alpha}{a^3 \, b} + \frac{2 \, \alpha}{r \, a^3} \right) - \frac{\partial_r b^2 \alpha}{a^2 \, b^2} - \frac{6 \partial_r b \alpha}{r a^2 \, b} - \frac{2 \partial_{rr} b \, \alpha}{a^2 b} - \frac{\alpha}{r^2 \, a^2} + \frac{\alpha \, \partial_r Z^r}{a^2} \\ & - \frac{\partial_r \alpha \, Z^r}{a^2} + \frac{\alpha}{r^2 \, b^2} - 2 K^\theta_\theta \, \alpha \Theta + {K^\theta_\theta}^2 \alpha + 2 K^\theta_\theta K^r_r \alpha - K^r_r \alpha \Theta - 8 \pi \tau \alpha \\ & - \alpha \left(\frac{\partial_r a}{a^3} - 2 \left(\frac{b + r \partial_r b}{r a^2 b} \right) \right) Z_r + \beta^r \partial_r \Theta \ ,\end{aligned} \tag{3.21}$$

$$\begin{aligned}\partial_t Z^r = {} & \partial_r b \left(\frac{2 K^r_r \alpha}{b} - \frac{2 \, K^\theta_\theta \alpha}{b} \right) - 2 \partial_r K^\theta_\theta \alpha - \frac{2 K^\theta_\theta \alpha}{r} + \frac{2 K^r_r \alpha}{r} - 2 K^r_r \alpha \, Z^r \\ & - 8 \pi S_r \alpha - \partial_r \alpha \Theta + \alpha \partial_r \Theta + \beta^r \partial_r Z^r + \partial_r \beta^r Z^r \ ,\end{aligned} \tag{3.22}$$

where $\{\tau, S_r, S^r_r, S^\theta_\theta\}$ are the non-vanishing components of the stress-momentum tensor. In order to obtain equilibrium configuration for non-rotating self-gravitating object in spherically symmetric, one needs to impose the condition of stationary solutions, namely $\partial_t U = 0$, where $U = \{a, b, K^r_r, K^\theta_\theta, \Theta, Z_r\}$. The resulting equations can be further simplified if the maximal polar slicing condition is imposed, i.e., $\mathrm{tr}\, K = K^r_r$, which transforms the line element (3.15) for stationary solutions in the so called *polar-areal* line element [133]

$$ds^2 = -\alpha^2(\tilde{r}) dt^2 + a^2(\tilde{r}) d\tilde{r}^2 + \tilde{r}^2 d\Omega^2 \ . \tag{3.23}$$

The name *polar-areal* is due to the fact that, in a given hypersurface, a fixed coordinate $\tilde{r}$ defines a two dimensional sphere with surface area $4\pi\tilde{r}^2$. In these coordinates, the **Z4** in spherical symmetry (3.17)-(3.49) reduces to a set of ordinary differential equations (**ODEs**)

$$\partial_{\tilde{r}} a = -\frac{a}{2\tilde{r}} \left(a^2 - 1 \right) + 4 \pi \, \tilde{r} \, a^3 \tau \ , \tag{3.24}$$

$$\partial_{\tilde{r}} \alpha = -\frac{\alpha}{2\tilde{r}} (1 - a^2) + 4 \pi \, \tilde{r} \, \alpha \, a^2 \, S^{\tilde{r}}_{\tilde{r}} \ . \tag{3.25}$$

Note that the **ODE** system (3.24)-(3.25) must be supplemented with the equilibrium

equations for the matter. Therefore, the matter model considered, either boson star or neutron star, will uniquely define the τ and $S^{\tilde{r}}_{\tilde{r}}$ quantities.

In order to obtain suitable physical solutions, appropriate boundary conditions have to be imposed in order to ensure regularity at the origin and asymptotic flatness at large distances, namely

$$a(\tilde{r}=0) = 1\ ,\ \alpha(\tilde{r}=0)=1\ , \qquad \textbf{(regularity at the origin)}\ , \tag{3.26}$$

$$\lim_{\tilde{r}\to\infty} a(\tilde{r}) = 1\ ,\ \lim_{\tilde{r}\to\infty}\alpha(\tilde{r}) = \frac{1}{a(\tilde{r})}\ ,\textbf{(asymptotic flatness)}\ . \tag{3.27}$$

Taking these into consideration, the problem can be solved integrating for $\tilde{r}=0$ toward the exterior boundary $\tilde{r}=\tilde{r}_{out}$ using a Runge-Kutta integrator, see Section 4.1.3. After integration of the equilibrium equation, we can rescale $\alpha \to c\alpha$ at the same time satisfying the boundary condition (3.27) for α with the aim of obtaining $\lim_{\tilde{r}\to\infty}\alpha(\tilde{r})=1$, where scalar factor is $c = 1/a(\tilde{r}_{out})\alpha(\tilde{r}_{out})$. Furthermore, note that the metric (3.15) is related to Schwarzschild metric through the relation $a^2 = (1-2\,M/\tilde{r})^{-1}$, where M is the **ADM** mass. Therefore, the total mass enclosed in a sphere of radius $\tilde{r}$ can be expressed as:

$$M(\tilde{r},t) = \lim_{\tilde{r}\to\infty}\frac{\tilde{r}}{2}\left(1-\frac{1}{a(\tilde{r})^2}\right)\ . \tag{3.28}$$

Once the solution is found, a coordinate transformation can be performed, from areal polar-coordinate to maximal isotropic coordinates, which is given by the following element line

$$ds^2 = -\alpha^2(r) + \psi^4(r)(dr^2 + r^2 d\Omega^2)\ , \tag{3.29}$$

where ψ is the conformal factor. As shown in detail in [128, p.140], this transformation consist of solving backward numerically the following **ODE**

$$\frac{dr}{d\tilde{r}} = a\left(\frac{r}{\tilde{r}}\right)\ , \tag{3.30}$$

with the boundary condition given by Birkhoff of theorem, i.e., the spacetime far away from the self-gravitating object is Schwarzschild solution, therefore:

$$r(\tilde{r}_{out}) = \left[\left(\frac{1+\sqrt{a}}{2}\right)^2\frac{\tilde{r}}{a}\right]\Bigg|_{r=\tilde{r}_{out}}\ . \tag{3.31}$$

Once the solution is computed, the conformal factor is $\psi = \sqrt{\tilde{r}/r}$. These kind of coordinate can be transformed to Cartesian ones [129, p.96], since the spatial part of

metric (3.29) is conformally flat, namely

$$(dr^2 + r^2 d\Omega^2) = \delta_{ij} dx^i dx^j \ , \tag{3.32}$$

which will be used in our numerical evolution from now on.

3.4 Complex Scalar Field

One of the simplest non-vacuum spacetimes is the one where the matter content is described by a scalar field. We consider physical systems described by a complex scalar field satisfying the Klein-Gordon (**KG**) equation under the effect of some potential $V\left(|\Phi|^2\right)$. The dynamics of the spacetime curvature and the complex scalar field Φ are described by the following Lagrangian density:

$$\mathscr{L}_{KG} = \frac{R}{16\pi} + \mathscr{L}_{M^\Phi} \ , \tag{3.33}$$

where $\mathscr{L}_{M^\Phi}$ is the matter Lagrangian for the scalar field given by

$$\mathscr{L}_{M^\phi} = -g^{ab} \nabla_a \Phi^* \, \nabla_b \Phi - V\left(|\Phi|^2\right) \ , \tag{3.34}$$

where Φ^* is the complex conjugate of Φ. Note that the dependency of $|\Phi|^2$ of the potential is required to be consistent with the invariance of the Lagrangian (3.34) under unitary group $U(1)$. The variation of the action associated with the Lagrangian (3.33) with respect to the metric g_{ab} leads to field equations given by (3.5), where T_{ab} is the stress-energy tensor of a complex scalar field

$$T_{ab} = \nabla_a \Phi^* \, \nabla_b \Phi + \nabla_b \Phi \, \nabla_a \Phi^* - g_{ab} \left(g^{cd} \nabla_c \Phi^* \, \nabla_d \Phi + V\left(|\Phi|^2\right) \right) \ . \tag{3.35}$$

As we said before, the Lagrangian (3.34) is invariant under unitary group of degree one, $U(1)$, that is, :

$$\Phi \to e^{i\theta} \Phi \quad , \quad \Phi^* \to e^{-i\theta} \Phi^* \ . \tag{3.36}$$

According to Noether's theorem [58, 129], these symmetries imply that there exist a conserved current density, namely *Noether current*, given by:

$$J^a = i g^{ab} (\Phi^* \, \nabla_b \Phi - \Phi \, \nabla_b \Phi^*) \tag{3.37}$$

and satisfying the conservation law $\nabla_a J^a = 0$. As a consequence, its time component represent a conserved charge associated to the system. This *Noether charge* is given by

$$N \equiv \int_{\Sigma_t} (-n_a J^a)\sqrt{\gamma}\, d^3x \ , \tag{3.38}$$

where Σ_t is a three dimensional hypersurface associated to the foliation of the spacetime $\mathcal{M}$.

3.4.1 Klein-Gordon equations

The evolution of the complex scalar field Φ is described by the Klein-Gordon equation, which is obtained by performing the variation of the action related to the Lagrangian (3.33) with respect to the scalar field Φ, leading to

$$\Box_g \Phi = V'\left(|\Phi|^2\right)\ \Phi \ , \tag{3.39}$$

where $\Box_g := g^{ab}\nabla_a\nabla_b$ is the d'Alembert operator and we have defined $V'(|\Phi|^2) := \frac{dV}{d|\Phi|^2}$.

The Equation (3.39) can be written as an evolution system by using the 3+1 decomposition (2.14) and introducing

$$\Pi \equiv -\mathcal{L}_n \Phi = -(1/\alpha)(\partial_t - \mathcal{L}_\beta)\Phi \ , \tag{3.40}$$

as a evolved field. The d'Alembert operator can be expanded as

$$\begin{aligned} \Box_g \Phi = g^{ab}\nabla_a\nabla_b\Phi &= (g^{ab} + n^a n^b)\nabla_a\nabla_b\Phi - n^a n^b \nabla_a\nabla_b\Phi \ , \\ &= \gamma^{ab} D_a D_b \Phi - \left(n^a \nabla_a (n^b \nabla_b \Phi) - n^a \nabla_a n^b \nabla_b \Phi\right) \ , \\ &= \gamma^{ab} D_a D_b \Phi + n^a \nabla_a \Pi + g^{ab}\nabla_b \ln\alpha \nabla_b \Phi \ , \end{aligned} \tag{3.41}$$

where we have used the useful relation $n^a\nabla_a n^b = \nabla^b \ln\alpha$. Finally, the **KG** equation (3.39) can be written as the following evolution system

$$\partial_t \Phi = \beta^k \partial_k \Phi - \alpha\Pi \ , \tag{3.42}$$

$$\partial_t \Pi = \beta^k \partial_k \Pi + \alpha\left[-\gamma^{ij} D_i D_j \Phi + \Pi\ \mathrm{tr}\, K + V'(|\Phi|^2)\Phi\right] - \gamma^{ij} D_i \Phi D_j \alpha \ , \tag{3.43}$$

for the evolved fields $\{\Phi, \Pi\}$. These equations can be expressed also as a function of the conformal fields of the **CCZ4** formalism, namely

$$\begin{aligned} \partial_t \Pi = \beta^k \partial_k \Pi + \alpha &\left[-\chi\tilde{\gamma}^{ij}\partial_i\partial_j\Phi + \chi\tilde{\Gamma}^k\partial_k\Phi + \frac{1}{2}\tilde{\gamma}^{ij}\partial_i\Phi\partial_j\chi + \Pi\ \mathrm{tr}\, K + V'(|\Phi|^2)\Phi\right] \\ &-\chi\tilde{\gamma}^{ij}\partial_i\Phi\partial_j\alpha \ . \end{aligned} \tag{3.44}$$

Finally note that, since Φ is a complex scalar field, it can be decomposed as:

$$\Phi = \Phi_R + i\Phi_I \ , \tag{3.45}$$

$$\Pi = -(1/\alpha)(\partial_t - \mathcal{L}_\beta)(\Phi_R + i\Phi_I) = \Pi_R + i\Pi_I \ , \tag{3.46}$$

where Φ_R is the real part and Φ_I is the imaginary part of Φ respectively. Therefore, the **KG** equation constitutes four hyperbolic scalar field evolution equations for $\{\phi_R, \Pi_R\}$ and $\{\Phi_I, \Pi_I\}$. The characteristic decomposition of the system (3.42)-(3.43) can be found in [63, p.174].

3.4.2 Boson Stars: initial data and some properties

Boson stars (**BSs**) are solutions of Einstein equations coupled to a complex scalar field, that represent a self-gravitating Bose-Einstein condensate. This family of solutions yields to useful models of dark matter, black hole (**BH**) mimickers and simple generic compact objects, see [58, 130] for a review.

Initial data for **BS** can be constructed considering spherically symmetric solutions of **EKG** equations. As we explain in detail in the above section 3.3, the first step is to considerer the most general metric for a time-dependent spherical symmetry (3.15). In this geometry, the **KG** equations (3.42)-(3.43) can be written as:

$$\partial_t \Phi = \beta^r \partial_r \Phi - \alpha \Pi \ , \tag{3.47}$$

$$\partial_t \zeta = \partial_r (\beta^r \partial_r \Phi - \alpha \Pi) \ , \tag{3.48}$$

$$\partial_t \Pi = \beta^r \partial_r \Pi - \frac{\partial_r \alpha \, \zeta}{a^2} + \alpha \left(- \frac{\zeta \left(2a \left(\frac{\partial_r b}{b} + \frac{1}{r} \right) - \partial_r a \right)}{a^3} - \frac{\partial_r \zeta}{a^2} + V'(|\Phi|^2) + \Pi \, \mathrm{tr} \, K \right) \ , \tag{3.49}$$

where $\zeta \equiv \partial_r \Phi$. The equations for the equilibrium configuration further simplify by using the maximal polar slicing condition (3.23).

On the other hand, the harmonic *ansatz* is adopted for the scalar field

$$\Phi(t, \tilde{r}) = \phi_0(\tilde{r}) \, e^{-i\omega t} \ , \tag{3.50}$$

where ω is a real frequency and $\phi_0(\tilde{r})$ is a real-value spatial function. The time-harmonic dependence for the scalar field in the ansatz (3.50) is a consequence of Derrik's theorem [58], that shows that no regular, static, non-topological localized solutions are stable in three dimensional flat space or in higher dimensions. There is another argument related to boson stars proven by Friedberg T. et in the pioneering work [134], which state

that a boson star to be in a ground state – a necessary condition for stability – Φ must have an harmonic time dependence.

Using this ansatz and under the assumption of spacetime stationarity, the **EKG** system in spherical symmetry is reduced to the following set of **ODEs**,

$$\partial_{\tilde{r}} a = -\frac{a}{2\tilde{r}}\left(a^2-1\right) + 4\pi\,\tilde{r}\,a^3\tau^{\Phi}\ , \tag{3.51}$$

$$\partial_{\tilde{r}} \alpha = -\frac{\alpha}{2\tilde{r}}(1-a^2) + 4\pi\,\tilde{r}\,\alpha\,a^2\,S_{\tilde{r}}^{\Phi\,\tilde{r}}\ , \tag{3.52}$$

$$\partial_{\tilde{r}} \phi_0 = \zeta\ , \tag{3.53}$$

$$\partial_{\tilde{r}} \zeta = -(1+a^2+4\pi\,\tilde{r}^2\,a^2)(S_{\tilde{r}}^{\Phi\,\tilde{r}}-\tau^{\Phi})\frac{\zeta}{\tilde{r}} - \left(\left(\frac{\omega}{\alpha}\right)^2 - V'(|\Phi|^2)\right)a^2\phi_0\ , \tag{3.54}$$

where

$$\tau^{\Phi} = \left(\frac{\omega\,\phi_0}{\alpha}\right)^2 + \left(\frac{\zeta}{a}\right)^2 + V(|\Phi|^2)\ ,\quad S_{\tilde{r}}^{\Phi\,\tilde{r}} = \left(\frac{\omega\,\phi_0}{\alpha}\right)^2 + \left(\frac{\zeta}{a}\right)^2 - V(|\Phi|^2)\ . \tag{3.55}$$

The boundary conditions (3.26)-(3.27) are imposed to regularized the equations at the origin and ensure asymptotic flatness at infinity. In addition, for the scalar field we assume the following conditions

$$\phi_0(0) = \phi_c\ , \tag{3.56}$$

$$\zeta(0) = 0\ , \tag{3.57}$$

being ϕ_c the central value of scalar field and at infinity $\lim_{\tilde{r}\to\infty}\phi_0(\tilde{r}) = 0$. Before solving Eq. (3.51)-(3.54), it is worth to stress some important points:

1. for a choice of interaction potential $V(|\Phi|^2)$, the solution of the equilibrium equations form a one-parameter family for ϕ_c.

2. giving values of $\{\phi_c\}$ and using boundary conditions (3.26)-(3.27)-(3.56)-(3.57), the solution is fully defined by the fields $\{a, \alpha, \Phi, \omega\}$. This means that one have to solve an initial-boundary eigenvalue problem for $\omega = \omega(\phi_c)$.

3. for a specific value of ϕ_c there exist solutions for a discrete set of ω. We are interested on the solutions with the lowest binding energy, i.e., an initial equilibrium configuration without nodes called *ground state*. This translates into the condition that the solution must have no zero-crossings.

This eigenvalue problem can be solved by integrating from $\tilde{r} = 0$ towards the exterior boundary using a shooting method. Once the solution is computed in polar coordinates, we can proceed as explained before: by rescaling the lapse function, and the frequency ω,

namely $\omega \to c\omega$. Finally, we make a (numerical) coordinate transformation into isotropic coordinates, which can be written in Cartesian ones in order to perform numerical 3D simulations.

It is worth stressing that the asymptotic condition of the scalar field is completely different to other matter solutions like neutron stars. Since the scalar field $\phi_0(r)$ has no-compact support, it is not possible to define a hard surface as in neutron stars. Nevertheless, the radius of a **BS** is usually defined as the radii R_{99} within which 99% of the total mass is contained, i.e., $M_{ADM}(R_{99}) = 0.99 M_{ADM}$. Finally, we can define the compactness of the star as $C = M_{ADM}/R_{99}$.

Until now, we have not said anything about the scalar self-potential of $V\left(|\Phi|^2\right)$. Different **BSs** models are classified according to their potential. The simplest one is called *mini-boson star*, whose scalar potential is giving by $m_b|\Phi|^2$, where m_b is a parameter which can be identified with the bare mass of the field theory. *Massive boson stars* include a fourth order self-interaction term $(\lambda/2)|\Phi|^4$, where λ is a dimensionless coupling constant. A more complicated potential is the one that we will use most in this Thesis,

$$V\left(|\Phi|^2\right) = m_b^2|\Phi|^2\left[1 - \frac{2|\Phi|^2}{\sigma_0^2}\right]^2 , \tag{3.58}$$

leading to *non-topological solitonic star*, where σ_0 is a free parameters. We shall revisit this scalar field potential in the section 5.2 since it has very important features regarding its astrophysical applications. For reviews of different scalar potential see [58, 130].

Interestingly, **BSs** have the same kind of stability behavior as neutron stars. For example, the solutions (3.51)-(3.54) for the potential $V\left(|\Phi|^2\right) = m_b|\Phi|^2$, lead to a sequences of equilibrium configurations, represented in the top panel of Figure 3.1. On the top left panel, the **ADM** mass is shown as a function of the central value of scalar field ϕ_c. The stable branch is localized in the left-hand side of the curve satisfying $\partial M/\partial\phi_c \geq 0$, [63]. On the top right panel, the **ADM** mass is shown as a function of the radius. The blue circular mark on both panels represents the maximum stable mass, which corresponds to $M_{ADM} = 0.633$, and the green circular mark correspond to a **BS** inside of the stable branch. The profiles of this stable **BS**, the conformal factor of metric (3.29) and scalar field, are shown in the bottom panel of Figure 3.1. Notice that, in the mass-radius diagram (on the top right panel) the stable branch is at the right-hand side of the maximum mass.

The maximum compactness of stable boson stars depends on the non-linearities of the self-interaction potential $V(|\Phi|^2)$, and ranges from $\mathcal{O}(10^{-3})$ for mini-boson stars to $\mathcal{O}(10^{-1})$ for non-topological solitonic **BS** [135, 136].

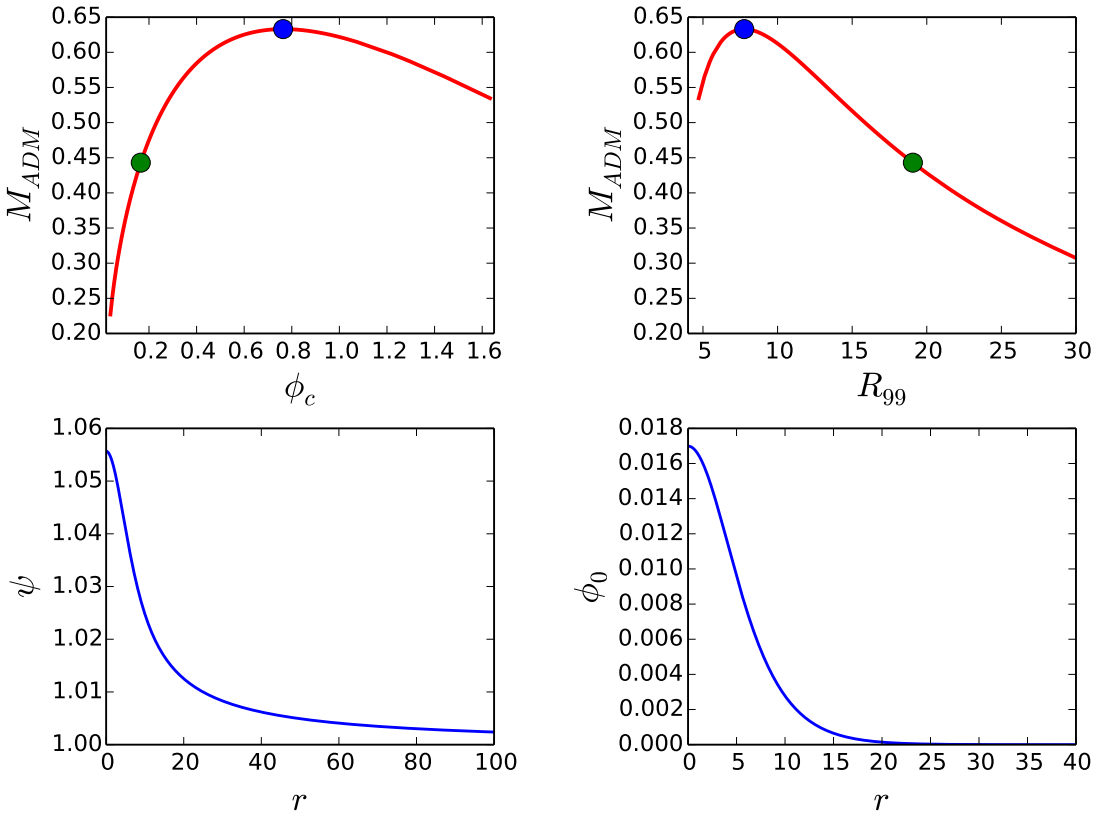

FIGURE 3.1: *Isolated mini-boson star.* (Top left) **ADM** mass as a function of the central value of the scalar field ϕ_c. (Top right) Mass-Radius diagram. (Bottom left and right) Radial profile of the conformal factor and the scalar field in isotropic coordinates. The blue circle marker corresponds to the maximum stable mass $M_{max} = 0.633$. The green circular marker refer to the stable equilibrium configuration displayed at the bottom.

Finally, notice that the Noether charge defined by the equation (3.38) can be interpreted as the number of bosonic particles [58, 130].

3.5 General Relativistic Hydrodynamics

In this section, we shall introduce the equations of general relativistic hydrodynamics (**GRHD**). These equations describe the dynamics of a fluid, coupled to Einstein Equations, in a four dimensional manifold. The equations of **GRHD** can be derived from the conservation of the energy-momentum tensor (1.14) and the baryonic number (i.e., the continuity equation)

$$\nabla_a(\rho u^a) \quad = \quad 0 \ , \tag{3.59}$$

where ρ is the rest mass density and u^a is the fluid four-velocity. In the next sections we will perform the $3+1$ decomposition to the of general relativistic hydrodynamics equations, following [77, p.102].

3.5.1 Perfect Fluids

Here we will consider only *perfect fluids*, which means that there are neither viscosity nor heat transfer in the fluid. The energy-momentum tensor for a perfect fluid is given by

$$T_{ab} = [\rho(1+\epsilon) + P]u_a u_b + P\, g_{ab} \ , \tag{3.60}$$

where ρ is the rest mass density, ϵ is internal energy. The pressure P is given by an equation of state (**EoS**), which relates the pressure with the other fluid quantities, typically the rest mass density and the internal energy [137], namely $P = P(\rho, \epsilon)$. The **EoS** provides the connection between the microscopic properties and the thermodynamic quantities of the fluid with them [63, p.189]. The most classical **EoS** are:

(a) **Ideal-Gas:**

$$P = (\Gamma - 1)\rho\epsilon \ , \tag{3.61}$$

where Γ is the adiabatic index and it assumed to be a constant.

(b) **Polytropic:**

$$P = \kappa\rho^{\Gamma} \ , \tag{3.62}$$

where κ is the polytropic constant which depends on the entropy.

Notice that all the physical quantities described above to describe the fluid are measured by a co-moving observer. Finally, the fluid four-vector velocity u^a defines how the fluid moves with respect to a local frame. We can define other quantities, also in the local rest frame, like the total energy density of the fluid $\mu = \rho(1+\epsilon)$ or its enthalpy $h = \mu + P = \rho(1+\epsilon) + P$. There is a derivation of the energy momentum tensor (3.60) trough a Lagrangian just like complex scalar field, we will not expand on the details here, but the interested reader can consult [138, 139].

3.5.2 Conservative Formulation

The **GRHD** equations are a set of **PDEs** highly non-linear with a tendency to produce shocks during their time evolution, even from an initial smooth data [63, 140]. In order

to deal with these shocks numerically, the **GRHD** equations need to be written as a conservation law, namely

$$\partial_t \mathbf{u} + \partial_k F^k(\mathbf{u}) = S(\mathbf{u}) \ , \tag{3.63}$$

where $\mathbf{u}$ is a vector of conserved densities quantities, which will be defined below. Applying a $3+1$ decomposition to the vector u^a, i.e., writing it down in terms of a parallel and orthogonal part to the vector n^a respectively, it follows that

$$u^a = W(n^a + v^a) \ , \tag{3.64}$$

where $W = -n_a u^a$ is the Lorentz factor and v^a the three velocity vector, both of them measured by Eulerian observers. Imposing the classic normalization relation of time-like four-vectors, we have that

$$-1 = u^a u_a = -W^2 + \gamma^{ij} u_i u_j \ . \tag{3.65}$$

Therefore, after a simple algebra, the components of the fluid vector u^a measured by a Eulerian observer in $3+1$ decomposition are just:

$$u^0 = \frac{W}{\alpha} \quad , \quad u^i = W\left(v^i - \frac{\beta^i}{\alpha}\right) \ , \tag{3.66}$$

$$u_0 = W(-\alpha + \beta_i v^i) \quad , \quad u_i = W v_i \ , \tag{3.67}$$

where $W = (1 - \gamma^{ij} v_i v_j)^{-1/2}$. The equation of continuity (3.59) can be easily put in a conservative form:

$$\begin{aligned} \nabla_a(\rho u^a) = \frac{1}{\sqrt{-g}} \partial_a(\sqrt{-g}\rho u^a) &= 0 \ , \\ \partial_t(\sqrt{\gamma} D) + \partial_j(\sqrt{\gamma}(\alpha\, v^j - \beta^j) D) &= 0 \ , \end{aligned} \tag{3.68}$$

where we used that $\sqrt{-g} = \alpha\sqrt{\gamma}$ and have defined the conserved quantity $D = W\rho$. Using the following identities:

$$\partial_t \sqrt{\gamma} = \sqrt{\gamma}\left(D_i \beta^j - \alpha \operatorname{tr} K\right) \ , \tag{3.69}$$

$$D_j T^j_i = \frac{1}{\sqrt{\gamma}} \partial_j(\sqrt{\gamma}\, T^j_i) - \Gamma^k_{ij} T^j_k \ , \tag{3.70}$$

$$D_j T^j = \frac{1}{\sqrt{\gamma}} \partial_j(\sqrt{\gamma}\, T^j) \ , \tag{3.71}$$

the evolution equation of the *energy density* (3.13) and *momentum density* (3.14), respectively, can be easily put it in a conservative form

$$\partial_t(\sqrt{\gamma}\tau) \quad + \quad \partial_j(\sqrt{\gamma}(\alpha\, S^j - \beta^j \tau)) = \sqrt{\gamma}(\alpha\, S^{ij} K_{ij} - S^j \partial_j \alpha)\ , \tag{3.72}$$

$$\partial_t(\sqrt{\gamma}S_i) \quad + \quad \partial_j(\sqrt{\gamma}(\alpha\, S_i^j - \beta^j S_i)) = \sqrt{\gamma}(\alpha\, \Gamma_{jki} S^{jk} + S_j \partial_i \beta^j - \tau \partial_i \alpha)\ , \tag{3.73}$$

where

$$\tau = hW^2 - P,\ S_i = hW^2 v_i,\ S_{ij} = hW^2 v_i v_j + P\,\gamma_{ij}\ . \tag{3.74}$$

The balance-law equations (3.68)-(3.73) can be written using the conformal variables of the **CCZ4** formalism with the formulas described in Section 2.3.2 and the following relations

$$S_j^k \Gamma^j_{ik} \quad = \quad \frac{1}{2\chi} S^{jk} \left(\partial_i \tilde{\gamma}_{jk} - \gamma_{jk} \partial_i \chi\right) = \frac{1}{2\chi}\left(S^{jk} \partial_i \tilde{\gamma}_{jk} - trS \partial_i \chi\right)\ , \tag{3.75}$$

$$\gamma^{jk} \Gamma^i_{jk} \quad = \quad \Gamma^i = \chi \tilde{\Gamma}^i + \frac{1}{2} \tilde{\gamma}^{ki} \partial_k \chi\ . \tag{3.76}$$

Finally, defining the following conserved densities $\bar{D} = \sqrt{\gamma} D, \bar{\tau} = \sqrt{\gamma}\tau$ and $\bar{S}_i = \sqrt{\gamma} S_i$, we have that (3.68)-(3.73) can be written in terms of the conformal variables as

$$\partial_t \bar{D} \quad + \quad \partial_k[\bar{D}(\alpha v^k - \beta^k)] = 0\ , \tag{3.77}$$

$$\partial_t \bar{\tau} \quad + \quad \partial_k[\alpha \bar{S} - \beta^k \bar{\tau}] = \frac{\alpha}{\chi} \bar{S}^{ij} \tilde{A}_{ij} + \frac{\alpha}{3} tr\bar{S}\, trK - \bar{S}^j \partial_j \alpha\ , \tag{3.78}$$

$$\partial_t \bar{S}_i \quad + \quad \partial_k[\alpha \bar{S}_i^k - \beta^k \bar{S}_i] = \frac{\alpha}{2\chi}\left(\bar{S}^{jk} \partial_i \tilde{\gamma}_{jk} - tr\bar{S} \partial_i \chi\right) + \bar{S}_j \partial_i \beta^j - \bar{\tau} \partial_i \alpha\ , \tag{3.79}$$

where $tr\bar{S} = \gamma^{jk} \bar{S}_{jk} = \chi \tilde{\gamma}^{jk} \bar{S}_{jk}$. Summarizing, the equations (3.68) together with (3.72)-(3.73) are the evolution equations for the **GRHD** written in a conservative form with flux conservative quantities (D, τ, S_i), called *conserved variables*, or alternatively (3.77)-(3.79) in conserved densities $(\bar{D}, \bar{\tau}, \bar{S}_i)$. Furthermore, to recover the physical variables (ρ, ϵ, P, v_i), also called *primitives variables*, and close the evolution system, we have to impose some **EoS**.

The **GRHD** equations form a hyperbolic system of equations which, with the addition of **EoS**, can be solved given an initial data and suitable numerical methods [141]. Due to the strong non-linearities shocks might be produced during the evolution. At the shock the solution is not differentiable. Therefore, it is not possible to use numerical approximations of the derivatives based on Taylor approximation, i.e., finite differences. Instead, one needs to use methods which might deal with shocks that solve the integral version of the equations, like for instance, the High Resolution Shock Capturing methods that will be described in detail in Section 4.2.2.

Despite its complicated structure, the characteristic structure of the **GRHD** equations can be solved analytically [141]. This is an advantage when applying **HRSC** methods, which usually rely at least on the eigenvalues of the system, see Section 4.2.2.

Finally, note that given an initial data of physical variables (ρ, ϵ, P, v_i) onto an hypersurface Σ_t, the conservative quantities are evolved (D, τ, S_i) up to the hypersurface $\Sigma_{t+\Delta t}$. Then, one can recover the physical fields on this hypersurface by using a specific **EoS**. The procedure to transform the conservative to primitive fields is not trivial because the inverse transformation is not explicit, and a numerical root-finder is usually needed. Here, we explain briefly the recovery procedure by using an Ideal-Gas **EoS** (3.61). Let us defined the variable $x \equiv h\,W^2$, being h the enthalpy and W the Lorentz factor. From the definitions of conservatives quantities, the following relationships are obtained:

$$v_i = \frac{S_i}{x} \ , \quad W = \frac{x^2}{x^2 - S_i S^i} \ , \tag{3.80}$$

from (3.61), we get

$$P = \left(\frac{\Gamma - 1}{\Gamma}\right)(h - \rho) \ , \tag{3.81}$$

thus

$$\begin{aligned} \tau &= hW^2 - P \ , & (3.82)\\ &= hW^2 - \left(\frac{\Gamma - 1}{\Gamma}\right)(h - \rho) \ , & (3.83)\\ &= hW^2 - \left(\frac{\Gamma - 1}{W^2\Gamma}\right) hW^2 + \left(\frac{\Gamma - 1}{\Gamma}\right)\rho \ . & (3.84) \end{aligned}$$

Then, the function

$$f(x) = x - \left(\frac{\Gamma - 1}{W^2\Gamma}\right) x + \left(\frac{\Gamma - 1}{\Gamma}\right)\rho - \tau \ , \tag{3.85}$$

should vanish for physical solutions. The roots of equation $f(x) = 0$ can be found numerically by a numerical root-finder, as for example Newton-Rapshon method. Once the physical solution is found, namely $x = x_{sol}$, the primitives values are constructed as follow:

$$\rho = \frac{D}{W} \ , \quad P = x_{sol} - \tau \ , \quad v_i = \frac{S_i}{x_{sol}} \ , \tag{3.86}$$

where $W = x_{sol}^2/(x_{sol}^2 - S_i S^i)$. For further discussion see [63, p.191]

3.5.3 Neutron Stars: initial data and some properties

Equilibrium configuration for a non-rotating neutron star (**NS**) can be constructed in a way analogous to **BSs**, bearing in mind that Einstein equations are now coupled to the hydrodynamic equations. Let us start again assuming the most general line element in spherically symmetric given by the equation (3.15). The **GRHD** (3.68)-(3.73) equations in this geometry are simply

$$\partial_t(\sqrt{\gamma}D) + \partial_r(\sqrt{\gamma}D(\alpha\, v^r - \beta^r)) = 0 \ , \tag{3.87}$$

$$\partial_t(\sqrt{\gamma}\tau) + \partial_r(\sqrt{\gamma}(\alpha\, S^r - \beta^r\tau)) = \sqrt{\gamma}(\alpha\,(S^r_r K^r_r + 2S^\theta_\theta K^\theta_\theta) - S^r\partial_r\alpha) \ , \tag{3.88}$$

$$\partial_t(\sqrt{\gamma}S_r) + \partial_r(\sqrt{\gamma}(\alpha\, S^r_r - \beta^r S_r)) = \sqrt{\gamma}\left[\alpha\left(\frac{\partial_r a}{a}S^r_r + 2\left(\frac{1}{r} + \frac{\partial_r b}{b}\right)S^\theta_\theta\right) \ , \right.$$
$$\left. + S_r\partial_r\beta^r - \tau\partial_r\alpha\right] \ , \tag{3.89}$$

where $\tau = hW^2 - P$, $S_r = hW^2 v_r$, $S^r_r = hW^2 v_r v^r + P$ and $S^\theta_\theta = P$. Once again, let us consider static solutions with the maximal polar slicing condition, such that the line element is given by the equation (3.23). Notice that the hydrostatic equilibrium of the star implies trivially $v^r = 0$. Therefore, Einstein equations in spherically symmetric (3.17)-(3.22) coupled to hydrodynamics (3.87)-(3.89) leads to the following set of equilibrium equations

$$\partial_{\tilde{r}} a = -\frac{a}{2\tilde{r}}\left(a^2 - 1\right) + 4\pi\,\tilde{r}\,a^3\tau \ , \tag{3.90}$$

$$\partial_{\tilde{r}}\alpha = -\frac{\alpha}{2\tilde{r}}(1 - a^2) + 4\pi\,\tilde{r}\,\alpha\,a^2\,S^{\tilde{r}}_{\tilde{r}} \ , \tag{3.91}$$

$$\partial_{\tilde{r}} P = -[\rho(1+\epsilon) + P]\frac{\partial_{\tilde{r}}\alpha}{\alpha} \ . \tag{3.92}$$

In order to solve the system of **ODEs** (3.90)-(3.92), an **EoS** must be supplemented. Here, a polytropic (3.62) **EoS** is adopted, which is a good approximation for cold star with $\Gamma = 2$ and $\kappa = 1$ [63, p.192]. Therefore, (3.90)-(3.92) can be easily integrated from the center of the star up to its surface, which is defined as the radius where the pressure vanishes. Similar to the case of **BS**, boundary conditions (3.26)-(3.27) have to be imposed by ensuring regularity at the origin and asymptotic flatness at infinity. Furthermore, for the pressure, we adopt the following conditions

$$P(0) = \kappa\rho_c^\Gamma \ , \tag{3.93}$$

$$\lim_{\tilde{r}\to\infty} P(\tilde{r}) = 0 \ , \tag{3.94}$$

where ρ_c the central value density. Finally, for a given value of ρ_c the system above can be numerically integrated from $\tilde{r} = 0$ outward using a Runge-Kutta algorithm, see section 4.1.3. Once again, the lapse function is rescaled, as we explained in section 3.4.2.

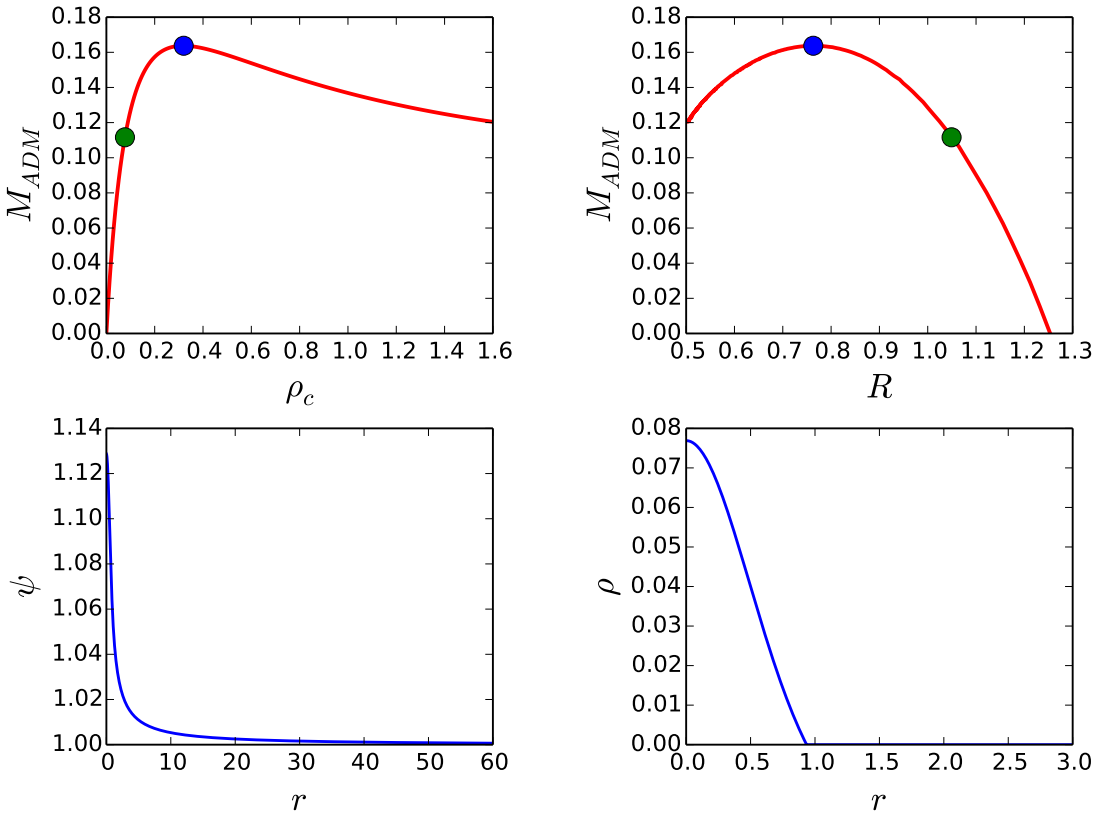

FIGURE 3.2: *Isolated non-rotating neutron star.* **ADM** mass as a function of the central density ρ_c (top left), mass-radius diagram (top right), radial profile of conformal factor (bottom left) and density (bottom right) in isotropic coordinate of an isolated non-spinning **NS** with a polytropic **EoS** with $\Gamma = 2$ and $\kappa = 1$. The green circular marker represents this stable equilibrium configuration. The blue circle marker corresponds to the maximum stable mass, which is $M_{ADM} = 0.1634$. The blue solid lines on the bottom display the profiles for the conformal factor of metric (3.29) and the density for a **NS** well inside in the stable branch.

Lastly, the same procedure for **BSs** is applied, that is, the lapse function is rescaled and a coordinate transformation into isotropic coordinates is performed, to finally write them in Cartesian coordinates in order to perform numerical 3D simulations. For a discrete family of values of $\{\rho_c^n\}_{n\in\mathbb{N}}$ and the polytropic **EoS** with $\Gamma = 2$ and $\kappa = 1$ the solutions of (3.90)-(3.92) lead to a sequences of equilibrium configurations, as we can see in both panels on the top of Figure 3.2. On the top left panel, the **ADM** mass is shown as a function of the central density ρ_c. The stable branch is the localized in the left-hand side of the curve, satisfying $\partial M/\partial\rho_c \geq 0$. The blue circular mark on both panels represents the maximum stable mass, which corresponds to $M_{ADM} = 0.1634$, and the green circular mark correspond to a **NS** inside of the stable branch. The profiles of this stable **NS**, the conformal factor of metric (3.29) and density, are shown in the bottom panel Figure 3.2.

Chapter 4

Discrete Problem

The Einstein and matter equations, written as an evolution hyperbolic system in Chapter 2 and Chapter 3, describe a non-linear set of partial differential equations in the continuum space. As we discussed in previous section, exact solutions for this system are only known assuming some simplifications, as for example in [142]: existence of symmetries, some algebraic conditions for Riemann or Weyl tensor or some non-vacuum solution related to the energy-momentum tensor (electrovacuum, fluid, scalar field). Therefore, in order to solve these equations in generic physical scenarios, it is mandatory to use numerical approximations. In this Chapter the numerical schemes used to solve hyperbolic **PDEs** are presented.

There are different numerical schemes to solve Einstein equations. If only the spacetime and the scalar field evolution are considered, the most common ones are finite difference and spectral methods, which take advantage of the smoothness of the metric components. If there is a fluid coupled to the geometry, the dynamics will be highly non-linear and shocks might be produced even from a smooth initial data. In these cases, numerical schemes able to deal with non-smooth solutions should be used, as for instance finite volume methods.

Here, we summarize the numerical techniques used to solve Einstein equations coupled with matter. Evolutions of binary systems, either of boson or neutron stars, will be presented in the next Chapters.

This chapter is organized as follows. In Section 4.1, some basic concepts of discretization for **PDEs** are introduced. Then, the Method of Lines together with a standard third and fourth order RungeKutta time integrator are presented, which are essential to evolve our evolution system. In Section 4.2 high-order spatial discretizations for smooth and non-smooth solutions are presented. We explain briefly the boundary conditions in

Section 4.3. Section 4.4 is devoted to the computational code infrastructure used for our numerical simulations. In Section 4.5, we perform some standard numerical spacetimes –robust stability test, gauge waves and isolated boson and neutron star, respectively – to test our evolution system. Finally, a discussion of the results is presented in Section 4.6. This Chapter is based mainly on books [63, 70] and the works [101, 111].

4.1 Numerical discretization

Heretofore, we have only studied analytical properties of Einstein's equations at the continuum level. In particular, the strong hyperbolicity condition has been crucial to formulate a well-posed initial-boundary value problem. However, all these interesting properties in the continuum do not translate directly to the discrete level. Here we will discuss how to preserve the properties of the continuum, mainly the well-posedness, into the discrete level.

We consider a system of **PDEs** described by

$$\mathcal{L}u = S(u) \ , \tag{4.1}$$

where $u := u(t, x, y, z)$ is the set of evolution fields, $\mathcal{L}$ is some differential operator and $S(u)$ a some source function. This continuum problem (4.1) can be transformed into a semi-discrete one by:

(i) discretizing space positions as follows: $x_i = i\Delta x$, $y_j = j\Delta y$ and $z_k = k\Delta z$, where Δx, Δy and Δz are the mesh size on each coordinate respectively, such that the solution is only defined in a grid of discrete points, $\mathcal{U} = u(t, x_i, , y_i, z_i)$.

(ii) substituting in $\mathcal{L}u$ and $S(u)$ a discrete operator $\mathscr{L}(\mathcal{U})$ and $\mathcal{S}(\mathcal{U})$ respectively, that replaces the continuum spatial partial derivatives by a suitable discrete one, as we will see in Section 4.2.1.

There are different methods in order to solve **PDEs** through numerical techniques, as for example: finite difference, finite volume, finite elements and spectral methods. An important observation is that finite difference and finite volume methods are based on the idea of a discretized space domain: while finite difference methods replace the continuum with a set of discrete points x_i which form a mesh, finite volume mesh divide it into a set of cells, centered at the grid points with interval $(x_{i-1/2}, x_{i+1/2})$, as we can see in Figure 4.3.

4.1.1 Basic concepts of discretization of PDEs

We introduce some basic concepts of discretization schemes of **PDEs**. Let us start considering a spatial interval $I = [a, b] \subset \mathbb{R}$. Notice that it possible to extend the following discussion to a generic domain $\Omega \subset \mathbb{R}^n$. As it was mentioned before, the mesh in the interval is defined by the grid points $x_i = i\,\Delta x$, where $i \in \mathbb{N}$, and $\Delta x = (b-a)/N$ is the mesh size, see Fig. 4.1. Let us consider now the system of **PDEs** described by Equation (4.1) for a function of one space variable and time, namely $u := u(t, x)$.

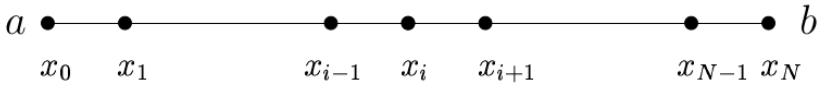

FIGURE 4.1: *Grid points.* Uniform mesh grid of the interval $I = [a, b]$.

The finite-difference approximation (**FDA**) of (4.1) is defined by

$$\mathcal{L}^{\Delta} u^{\Delta} = S^{\Delta} \,, \tag{4.2}$$

where u^{Δ} is the discrete solution, S^{Δ} is the source evaluated on the finite-difference mesh, and $\mathcal{L}^{\Delta}$ is a **FDA** operator of the differential operator $\mathcal{L}$. Now, we shall define some concepts which are crucial in order to quantify how much the discrete solution u^{Δ} differs from the continuum solution u.

(1) The *truncation error* is defined as $\tau^{\Delta} = \mathcal{L}^{\Delta} u - S^{\Delta}$, where u satisfies the continuum **PDE** (4.1).

(2) The approximation *converges* if and only if $\lim_{\Delta \to 0} u^{\Delta} = u$.

(3) The *order* of convergence measures the rate at which the error converges to zero. The discrete solution converges to the continuum solution with order p if $\lim_{\Delta \to 0} \tau^{\Delta} = O(\Delta^p)$, for some integer p.

(4) The **FDA** is said *consistent* if $\lim_{\Delta \to 0} \tau^{\Delta} = 0$.

(5) Finally, the **FDA** is *stable* if the numerical solution itself should remains uniformly bounded, with respect to a suitable norm in the discretization space.

Consistency, stability and convergence are required to ensure that the numerical solutions represents a solution of the continuous problem. A fundamental theorem of finite difference is the *Lax-Richtmeyer equivalence theorem* [143], stating that *the numerical approximation of well-posed problems is convergent if and only if the scheme is stable and consistent.*

It is worth stressing that one can show that a numerical solution converges to the continuum one, even if this continuum solution is not known a priori. Let us consider three resolutions $\Delta_1 > \Delta_2 > \Delta_3$, such that $\Delta_1/\Delta_2 = \Delta_2/\Delta_3 = r$. The discrete solution converges to the continuum one with a convergence order p if

$$\lim_{\Delta \to 0} \frac{u^{\Delta_1} - u^{\Delta_2}}{u^{\Delta_2} - u^{\Delta_3}} = r^p. \tag{4.3}$$

This is a basic test which we perform in our implementation.

4.1.2 The Method of Lines

Le us considerer now the evolution systems with only first-order time derivatives, i.e, systems of **PDE** given by Equation (4.1) which can be written as

$$\partial_t u = P(u) \ , \tag{4.4}$$

where $P(u)$ is an operator containing arbitrary space derivatives of these fields.

The method of lines (**MoL**) [63, p.112] is a technique for solving **PDEs** by discretizing all spatial dimensions and then integrating in time the semi-discrete problem as a system of **ODEs**. Therefore, at each point of the grid, the evolution system (4.4) is converted into a semi-discrete **ODE**

$$\partial_t \mathcal{U} = \mathcal{P}(\mathcal{U}) + Q_d(\mathcal{U}) \ , \tag{4.5}$$

where $\mathcal{P}$ is a discrete operator and Q_d is an artificial dissipation operator included to achieve stability. The artificial dissipation is designed to remove the high frequency modes of the solution that can not be accurately resolved in the mesh.

Note that this method to integrate evolution systems decouples the treatment of space and time, that is, the right-hand side and left-hand side of (4.5) respectively[1]. In a way, this means that the **MOL** keeps the same framework than the $3+1$ decomposition studied in Chapter 2: a continuous spacetime is approximated by a series of continuous time slices, labeled by a time index n. Each slice represents a space-like hypersurface which is approximated by a 3D grid, labeled by (i, j, k).

Then, the system can be fully discretized by choosing discrete time snapshots $t^n = n\Delta t$, such that the fully discrete solution at the current time can be represented as $\mathcal{U}^n := u(t^n, x_i, y_i, z_i)$, see Figure 4.2.

[1]Notice that the right-hand side of Eq. (4.5) can be treated by using either finite difference, finite volume or spectral methods, depending on the current problem being solved.

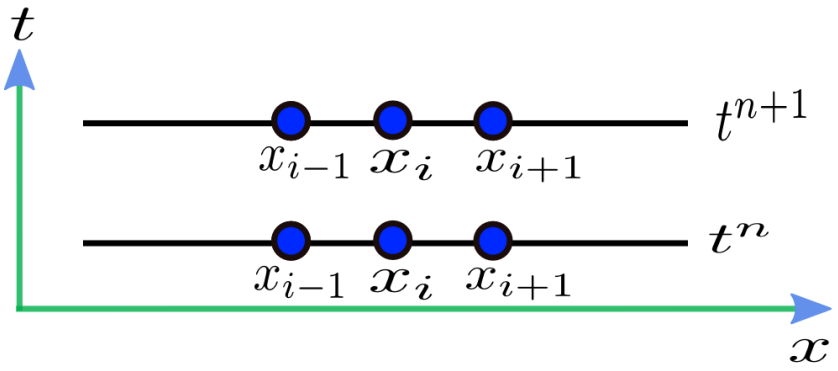

FIGURE 4.2: *Method of lines.* Schematic representation of the **MoL**. Note that the same framework of $3+1$ decomposition of the Einstein equations is kept, but at the discrete level.

We will consider here only explicit time integrator schemes for which the future solution can be written in terms of the current one, namely

$$\mathcal{U}^{n+1} = \mathcal{I}\left[\mathcal{P}(\mathcal{U}^n + Q_d(\mathcal{U}))\right], \tag{4.6}$$

where $\mathcal{I}$ can be a complicated operator depending on the specific integrator chosen to solve the **ODE**. The discrete system is stable, consistent and convergent to the continuum solution if the continuum problem is well-posed and a locally stable time integrator is employed for the time evolution, for example a Runge-Kutta (**RK**) of at least third order [83]. Notice that the numerical scheme will be stable as long as the Courant-Friedrichs-Lewy (**CFL**) condition $\Delta t \leq \Delta x/c_h$ is fulfilled in hyperbolic systems, being c_h the spectral radius, i.e., the absolute value of the maximum eigenvalue.

4.1.3 The Runge-Kutta time integrator

As we said before, locally stable integrators ensure the stability and convergence of the solution of the evolution system (4.4). An explicit **RK** scheme with s stages, applied to system (4.5), allows us to express the solution at the next time-step $\mathcal{U}^{n+1}$ as a combination of several auxiliary steps [144], namely

$$\begin{aligned}
\mathcal{U}^{(i)} &= \mathcal{U}^n + \sum_{j=1}^{i-1} b_{ij} k_j \,, \quad k_j = \Delta t \left(\mathcal{P}(\mathcal{U}^{(j)}) + Q_d(\mathcal{U})\right) \,, \\
\mathcal{U}^{n+1} &= \mathcal{U}^n + \sum_{i=1}^{s} c_i k_i \,,
\end{aligned}$$

where $\mathcal{U}^{(i)}$ are the auxiliary intermediate values of the **RK** with s stages. The matrices $B = (b_{ij})$, with $b_{ij} = 0$ for $j \geq i$, are $s \times s$ matrices such that the resulting scheme is explicit and of order p, i.e, the error in a single **RK** iteration is $\mathcal{O}(\Delta t^p)$. A **RK** is

characterized by this matrix and the coefficient vector c_i, which can be represented by a tableau in the usual Butcher notation [144] as follows

a	B
	c^T

where the coefficients c used for the treatment of non-autonomous systems are given by the consistency relation $a_i = \sum_{j=1}^{i-1} b_{ij}$. These schemes can be denoted as RK(s, p), where the doublet (s, p) characterizes the number of s stages of the explicit scheme and the order p of the scheme. The frequently used third and fourth order **RK**, which remain stable under quite large time-steps, are given in Table 4.1.

0	0	0	0
1	1	0	0
1/2	1/4	1/4	0
	1/6	1/6	4/6

0	0	0	0	0
1/2	1/2	0	0	0
1/2	0	1/2	0	0
1	0	0	1	0
	1/6	2/6	2/6	1/6

TABLE 4.1: Tableau for a very standard explicit **RK**$(3, 3)$ (on the left) and **RK**(4,4)(on the right).

Therefore, the explicit implementation of the **RK**$(3, 3)$ is:

$$\mathcal{U}^{(1)} = \mathcal{U}^n \tag{4.7}$$
$$\mathcal{U}^{(2)} = \mathcal{U}^n + k_1 \tag{4.8}$$
$$\mathcal{U}^{(3)} = \mathcal{U}^n + \frac{1}{4}k_2 + \frac{1}{4}k_3 \tag{4.9}$$
$$\mathcal{U}^{n+1} = \mathcal{U}^n + \frac{1}{6}\left(k_1 + k_2 + k_3\right) \tag{4.10}$$

and the explicit implementation of the **RK**$(4, 4)$ is:

$$\mathcal{U}^{(1)} = \mathcal{U}^n \tag{4.11}$$
$$\mathcal{U}^{(2)} = \mathcal{U}^n + \frac{1}{2}k_1 \tag{4.12}$$
$$\mathcal{U}^{(3)} = \mathcal{U}^n + \frac{1}{2}k_2 \tag{4.13}$$
$$\mathcal{U}^{(4)} = \mathcal{U}^n + k_3 \tag{4.14}$$
$$\mathcal{U}^{n+1} = \mathcal{U}^n + \frac{1}{6}\left(k_1 + 2k_2 + 2k_3 + k_4\right) \tag{4.15}$$

where $k_i = \Delta t \, \left(\mathcal{P}(\mathcal{U}^{(i)}) + Q_d(\mathcal{U})\right)$.

4.2 Space derivative discrete operators

Here, we present the operators use to discretized the derivatives appearing on the right-hand side of (4.5) in Cartesian coordinates. Note that, since $P(u)$ is an operator containing arbitrary spatial derivatives of the fields, its discretization representation will depend on the smoothness of the solution.

4.2.1 Finite difference operators for smooth solutions

Suitable high-order discrete derivative operators for the operator $\mathcal{P}(\mathcal{U}) = \mathcal{P}(\mathcal{U}, D\mathcal{U}, \ldots)$ can be found by using a Taylor expansion of the (smooth) solution around a specific position x_i of the discrete grid. By default, we will consider standard fourth-order centered finite difference such that $D_i\mathcal{U} \approx \partial_i u + \mathcal{O}(\Delta {x_i}^5)$. In 3D, the first-order derivative operators have the form

$$D_x\mathcal{U}_{i,j,k} = \frac{1}{12\Delta x}\left(\mathcal{U}_{i-2,j,k} - 8\mathcal{U}_{i-1,j,k} + 8\mathcal{U}_{i+1,j,k} - \mathcal{U}_{i+2,j,k}\right) , \tag{4.16}$$

$$D_y\mathcal{U}_{i,j,k} = \frac{1}{12\Delta y}\left(\mathcal{U}_{i,j-2,k} - 8\mathcal{U}_{i,j-1,k} + 8\mathcal{U}_{i,j+1,k} - \mathcal{U}_{i,j+2,k}\right) , \tag{4.17}$$

$$D_z\mathcal{U}_{i,j,k} = \frac{1}{12\Delta z}\left(\mathcal{U}_{i,j,k-2} - 8\mathcal{U}_{i,j,k-1} + 8\mathcal{U}_{i,j,k+1} - \mathcal{U}_{i,j,k+2}\right) , \tag{4.18}$$

where $\mathcal{U}_{i,j,k} = u(x_i, y_i, z_i)$. Second-order derivative operators can be constructed by applying twice the first-order ones. This is a convenient choice for the (commutative) cross-derivatives, for example

$$D_{xy}\mathcal{U}_{i,j} = D_{yx}\mathcal{U}_{i,j} = D_y\left(D_x\mathcal{U}_{i,j}\right) . \tag{4.19}$$

However, the grid points required for the second-order derivative along a single coordinate direction (i.e., the stencil) would be twice larger than the one of the cross-derivatives. Therefore, with scalability in mind, it is preferable to change to a different fourth-order operator which keeps the original stencil. For instance, along the x-direction the second derivative operator would be:

$$D_{xx}\mathcal{U}_{i,j,k} = \frac{1}{12\Delta x^2}\left(-\mathcal{U}_{i-2,j,k} + 16\mathcal{U}_{i-1,j,k} - 30\mathcal{U}_{i,j,k} + 16\mathcal{U}_{i+1,j,k} - U_{i+2,j,k}\right) . \tag{4.20}$$

4.2.1.1 The Dissipation

Discrete numerical solutions might also contain unphysical high-frequency modes with a wavelength smaller than the grid size Δx that can grow rapidly and spoil the real

physical solution. These modes can be suppressed by including a small artificial Kreiss-Oliger (**KO**) dissipation along each coordinate direction [145]. For instance, along the x-direction, the **KO** dissipation operator is given by:

$$Q_d^x = \sigma(-1)^{r-1}\Delta x^{2r-1}\left(D_+^x\right)^r\left(D_-^x\right)^r \ , \tag{4.21}$$

where

$$D_+^x\mathcal{U}_{i,j,k} = \frac{\mathcal{U}_{i+1,j,k}-\mathcal{U}_{i,j,k}}{\Delta x} \ , \quad D_-^x\mathcal{U}_{i,j,k} = \frac{\mathcal{U}_{i,j,k}-\mathcal{U}_{i-1,j,k}}{\Delta x} \ , \tag{4.22}$$

and $\sigma \geq 0$ is dissipative parameter. If the accuracy of the numerical scheme without artificial dissipation is q, choosing $2r-1 \geq q$ ensures that the accuracy is not affected. This means that, for a fourth order scheme, we must use $r=3$, leading to an operator for the x-direction

$$\begin{aligned} Q_d^x\mathcal{U}_{i,j,k} &= \sigma(\Delta x)^5\left(D_+^x\right)^3\left(D_-^x\right)^3\mathcal{U}_{i,j,k} \\ &= \frac{\sigma}{64\Delta x}\Big(\mathcal{U}_{i-3,j,k}-6\,\mathcal{U}_{i-2,j,k}+15\,\mathcal{U}_{i-1,j,k}-20\,\mathcal{U}_{i,j,k}+15\,\mathcal{U}_{i+1,j,k} \\ &\quad -6\,\mathcal{U}_{i+2,j,k}+\mathcal{U}_{i+3,j,k}\Big)+\mathcal{O}(\Delta x^5) \ . \end{aligned} \tag{4.23}$$

4.2.2 Finite difference operators for non-smooth solutions

In case of non-smooth solutions, it is more convenient to decompose the operator P from Equation (4.4) as a divergence term plus source terms as follows

$$P(u) = -\partial_k F^k(u) + S(u) \ . \tag{4.24}$$

where some of the terms, containing only first derivatives of the fluxes $F^k(u)$, are explicitly separated in order to take advantage of the existence of weak solutions. Notice that the fluxes F^k and the sources S might be non-linear, but depend only on the fields. This split allow us to define different discretization operators to deal with the fluxes and with the sources. In particular, finite difference schemes seen in the previous section, suitable for smooth solutions, will be applied to the generalized sources terms.

However, the possible appearance of shocks require High-Resolution-Shock-Capturing (**HRSC**) methods to discretize the fluxes [146] and find consistent solutions, as we explained in the Section 3.5.2. We shall therefore use a conservative scheme to discretize

the fluxes. For instance, in three dimensions:

$$\begin{aligned}\mathcal{P}(\mathcal{U}) &= -\frac{1}{\Delta x}\left(\mathcal{F}^x_{i+1/2,j,k} - \mathcal{F}^x_{i-1/2,j,k}\right) - \frac{1}{\Delta y}\left(\mathcal{F}^y_{i,j+1/2,k} - \mathcal{F}^y_{i,j-1/2,k}\right) \\ &\quad -\frac{1}{\Delta z}\left(\mathcal{F}^z_{i,j,k+1/2} - \mathcal{F}^z_{i,j,k-1/2}\right) + \mathcal{S}(\mathcal{U}) \ , \end{aligned} \tag{4.25}$$

where $\mathcal{F}^x_{i\pm1/2,j,k}$, $\mathcal{F}^y_{i,j\pm1/2,k}$, $\mathcal{F}^z_{i,j,k\pm1/2}$ are the set of fluxes along the x, y, z-direction evaluated at the interfaces between two neighboring cells, located at $x_{i\pm1/2}, y_{i\pm1/2}, z_{i\pm1/2}$.

The crucial issue in **HRSC** methods is how to compute the fluxes at the interfaces such that no spurious oscillations appear in the solutions. For simplicity, we restrict our discussion to the one dimensional case, but higher dimensions can be obtained repeating the same procedure on the other dimensions and adding them up. This calculation consists in two steps:

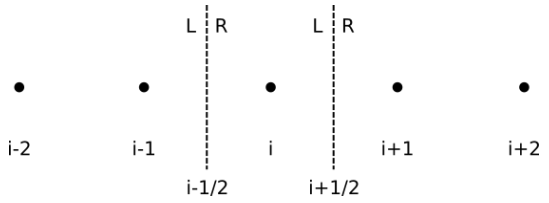

FIGURE 4.3: *The computational uniform grid* x_i. The left (L) and right (R) states reconstructed at the interfaces $x_{i\pm1/2}$ are required to evolve the solution $\mathcal{U}_i$.

- reconstruct the fields, using points from the left (L) and from the right (R), in the interfaces between points. For instance, to evolve the field $\mathcal{U}_i$ we need to reconstruct the fields from left and right at the neighboring interfaces $x_{i\pm1/2}$, that is, $\mathcal{U}^L_{i\pm1/2}$ and $\mathcal{U}^R_{i\pm1/2}$ (see Fig. 4.3).

- use a flux formula to compute the final flux at the interface, $\mathcal{F}_{i\pm1/2}$, that approximately solves the Riemann problem. One popular choice is the Harten-Lax-van Leer-Einfeldt (**HLL**) flux formula [146, 147], which does not require the characteristic decomposition of the system

$$\mathcal{F} = \frac{1}{S^R - S^L}\left[S^R\mathcal{F}^L - S^L\mathcal{F}^R + S^R S^L(\mathcal{U}^R - \mathcal{U}^L)\right] \ , \tag{4.26}$$

  where $\mathcal{F}^L = \mathcal{F}(\mathcal{U}^L)$, $\mathcal{F}^R = \mathcal{F}(\mathcal{U}^R)$ and S^L, S^R are the fastest speed traveling to the left and to the right at that interface, respectively. They can be estimated as a function of the largest positive and negative velocities ${}^{(\pm)}\lambda$, namely

$$S^L = \min({}^{(-)}\lambda^L, {}^{(-)}\lambda^R) \ , \tag{4.27}$$

$$S^R = \max({}^{(+)}\lambda^L, {}^{(+)}\lambda^R) \ . \tag{4.28}$$

A simplest and more robust choice assumes that $S^L = -S^R = S$. Substituting this expression into the **HLL** flux one can obtain the Local-Lax-Friedrichs (**LLF**) flux

$$F^{LLF} = \frac{1}{2}\left[\mathcal{F}^L + \mathcal{F}^R - S(\mathcal{U}^R - \mathcal{U}^L)\right] \ , \tag{4.29}$$

that we will consider as the standard choice in our implementations.

A important step on the discretization scheme is the reconstruction of the fields from the grid points x_i into the interfaces located at $x_{i\pm1/2}$. The reconstruction can be performed to the evolved fields, to the fluxes or to a combination of both. All these choices have advantages and disadvantages [101].

There are several reconstruction procedures, which can be performed to achieve different order of accuracy and robustness. The most commonly reconstructions methods are, for example: **PPM** [148] (explain above) and **MP5** [149]. Other interested reconstruction methods are the Weighted-Essentially-Non-Oscillatory (**WENO**) reconstructions [150, 151], for their flexibility (i.e., they can achieve any order of accuracy) and robustness. The detailed implementation of the **WENO** methods can be found in the Appendix of [101], while that details of the other methods can be found in a recent review [152]. We will present in the next section two standard method of reconstruction (i.e., linear and parabolic) applied to the fields.

4.2.3 Linear reconstruction

A very common standard reconstruction is the piecewise linear [152]. The reconstructed fields in the cell i at neighboring interfaces $x_{i+1/2}$ can be approximated as

$$\mathcal{U}^L_{i+1/2} = \mathcal{U}_i + \sigma_i \frac{\Delta x}{2} \ , \tag{4.30}$$

$$\mathcal{U}^R_{i+1/2} = \mathcal{U}_{i+1} - \sigma_{i+1} \frac{\Delta x}{2} \ , \tag{4.31}$$

where σ_i is the slope representing the linear variation of $\mathcal{U}_i$ within the cell. In order to avoid oscillations, these slopes must be limited, namely

$$\sigma_i = \text{Limiter}\Big(\mathcal{U}_{i+1} - \mathcal{U}_i, \mathcal{U}_i - \mathcal{U}_{i-1}\Big) \ . \tag{4.32}$$

One of the safest choice is probably the minmod limiter

$$\text{minmod}(a,b) = \frac{1}{2}(\text{sgn}(a) + \text{sgn}(b))\,\min(|a|,|b|) \ . \tag{4.33}$$

Another popular choice, much less dissipative, is the Monotonized Central limiter

$$\mathrm{MC}(a,b) = \frac{1}{2}(\mathrm{sgn}(a)+\mathrm{sgn}(b))\min(\frac{1}{2}|a+b|, 2|a|, 2|b|) \ . \tag{4.34}$$

Notice that the simplest zero-th reconstruction, consisting on just copying the neighbor,

$$\mathcal{U}^L_{i+1/2} = \mathcal{U}_i \ , \tag{4.35}$$
$$\mathcal{U}^R_{i+1/2} = \mathcal{U}_{i+1} \ , \tag{4.36}$$

can be recovered setting a vanishing slope $\sigma_i = 0$.

4.2.4 Piece-wise parabolic reconstruction

The next order of reconstruction involves the piecewise parabolic method (**PPM**) [148, 153–155]. The main idea of this method is to construct an interpolating parabola, said $p(x)$, inside each cell

$$p\left(\frac{x-x_{i-1/2}}{\Delta x_i}\right) = a_2\left(\frac{x-x_{i-1/2}}{\Delta x_i}\right)^2 + a_1\left(\frac{x-x_{i-1/2}}{\Delta x_i}\right) + a_0 \ , \tag{4.37}$$

where $x \in [x_{i-1/2}, x_{i+1/2}]$ and a_i are vectors of constant coefficients to be determined [153]. The procedure is at follows:

(i) We construct the limited slopes in each cell

$$\sigma(\mathcal{U}_{i+1}) = \mathrm{MC}\Big(\mathcal{U}_{i+2}-\mathcal{U}_{i+1},\ \mathcal{U}_{i+1}-\mathcal{U}_i\Big) \ , \tag{4.38}$$
$$\sigma(\mathcal{U}_i) = \mathrm{MC}\Big(\mathcal{U}_{i+1}-\mathcal{U}_i,\ \mathcal{U}_i-\mathcal{U}_{i-1}\Big) \ , \tag{4.39}$$

(ii) then, we calculate $\mathcal{U}^L_{i+1/2}$ and $\mathcal{U}^R_{i+1/2}$ in that cell by using

$$\mathcal{U}^L_{i+1/2} = \frac{1}{2}(\mathcal{U}_{i+1}+\mathcal{U}_i) - \frac{1}{6}(\sigma(\mathcal{U}_{i+1})-\sigma(\mathcal{U}_i)) \ , \tag{4.40}$$

and $\mathcal{U}^R_{i+1/2} = \mathcal{U}^L_{i+1/2}$.

- Finally, enforce the monotonicity conditions resetting $\mathcal{U}^R_{i-1/2}$ and $\mathcal{U}^L_{i+1/2}$ in each cell as follows

$$
\begin{aligned}
\mathcal{U}^L_{i+1/2} &= \mathcal{U}^R_{i-1/2} = \mathcal{U}_i \quad \text{if } (\mathcal{U}^L_{i+1/2} - \mathcal{U}_i)(\mathcal{U}_i - \mathcal{U}^R_{i-1/2}) \leq 0 \ , \\
\mathcal{U}^R_{i-1/2} &= 3\mathcal{U}_i - 2\mathcal{U}^L_{i+1/2} \\
&\text{if} \quad \left(\mathcal{U}^L_{i+1/2} - \mathcal{U}^R_{i-1/2}\right)\left(\mathcal{U}_i - \frac{1}{2}\left(\mathcal{U}^L_{i+1/2} + \mathcal{U}^R_{i-1/2}\right)\right) > \frac{1}{6}\left(\mathcal{U}^L_{i+1/2} - \mathcal{U}^R_{i-1/2}\right)^2 \ , \\
\mathcal{U}^L_{i+1/2} &= 3\mathcal{U}_i - 2\mathcal{U}^R_{i-1/2} \\
&\text{if} \quad -\frac{1}{6}\left(\mathcal{U}^L_{i+1/2} - \mathcal{U}^R_{i-1/2}\right)^2 > \left(\mathcal{U}^L_{i+1/2} - \mathcal{U}^R_{i-1/2}\right)\left(\mathcal{U}_i - \frac{1}{2}\left(\mathcal{U}^L_{i+1/2} + \mathcal{U}^R_{i-1/2}\right)\right) \ .
\end{aligned}
$$

4.3 Boundary Conditions

Since we are interested on isolated systems, we will consider radiative boundary conditions [70]. It means that, the main part of the radiative boundary conditions assumes that there is an outgoing radial wave with some speed v,

$$u = u_\infty + \frac{f(r - vt)}{r} \ , \tag{4.41}$$

where u is the sef of evolved fields, u_∞ its value at infinity and f a spherically symmetric perturbation that moves at velocity v. Notice that $\{u_\infty, v\}$ depends on the particular field (for example, $u_\infty = 1$ for the lapse function). Accordingly, the time derivative can be written as

$$\partial_t u = -v^i \partial_i u - v\frac{(u - u_\infty)}{r} \ , \tag{4.42}$$

where $v^i = v\, x^i/r$ and ∂_i is evaluated using centered finite differencing where possible and one-sided elsewhere.

4.4 Infrastructure: HAD and SAMRAI

One way to use efficiently the computational resources is increasing the grid resolution only on the localized regions of the simulation domain where the dynamics is more demanding and higher resolution is required to improve the accuracy of the solution. A mature and well-established strategy is the adaptive mesh refinement (**AMR**), which introduces new additional grid levels with higher resolution on specific regions which might change dynamically with the solution.

A necessary condition for the stability of explicit numerical schemes of hyperbolic systems is that the time step must satisfy the **CFL** condition $\Delta t \leq \lambda_{\rm CFL}\Delta x$, with $\lambda_{\rm CFL}$ a

factor depending on the dimensionality of the problem and the specific time integrator. When there are multi-levels $l = 0 \dots L$, the solution on each refinement level can be evolved in a stable way by using the time-step corresponding to the finest grid resolution Δx_L, ensuring that all the grids satisfy the **CFL** condition. This is however a very inefficient choice, since coarser grids are evolved with a time-step much smaller than the one allowed by their local **CFL** condition. A common way to avoid such a restriction is by evolving the solution with *sub-cycling in time*, meaning that each grid uses the largest Δt as set by its local **CFL** condition. This means that the finer grids must perform two or more time-steps for each one of the coarse grid. There have been several well motivated strategies to fill in the missing information at the boundaries of the refined grids: Tappering [156], Berger-Oliguer style [157], Berger-Oliger with dense output interpolator [158] and Berger-Oliger without order reduction [159, 160]. Further details of the numerical implementation of these strategies can be found in Ref. [101].

The **AMR** algorithm works as follows:

(a) First of all, it calls a subroutine, namely *refinement criteria*, to decide which regions need additional levels with smaller grid sizes to obtain an accurate solution see Figure 4.4. Once the solution is defined in all levels the simulation can start.

(b) The procedure to integrate a time-step is repeated over and over until reaching the final simulation time. The fields must be evolved in all grids each timestep, starting from the coarsest level $l = 0$ to the finest one $l = L$. Each time integration is performed by using a **RK** with S sub-steps. Therefore, the intermediate auxiliary states $\mathcal{U}^{(i)}$ and the final one $\mathcal{U}^{n+1}$ must be computed at each level. The right-hand-side of the evolution equations, which involves spatial derivatives, need to be computed at each of these sub-steps, by using the discrete spatial operators described in the previous section.

(c) The neighboring zones outside the boundary of the fine levels must be filled with points of the same resolution in order to accurately evolve the solution. This procedure is called *prolongation* and it usually involves interpolation from the coarse grid level into the fine one.

(d) After computing each intermediate **RK**-step the fields need to be synchronized among the different processors on level l in order to fill the boundaries of the domains splatted in each processor with the correct updated data.

(e) Finally, after completing all the steps of the **RK**, we need to inject the solution of the fine level l into the coarse one $l-1$, a procedure known as *restriction*. After the values on the coarse grids have been updated, the information on the level $l-1$ must be again synchronized among processors.

In this Thesis, the distributed **AMR** infrastructure is provided either by HAD [161, 162] or SAMRAI [163–165]. Both of them use the message passing interface (**MPI**) for distributed parallelism. Some of the features of each infrastructures are described below:

(i) **HAD:** computational toolkit developed since 2006 at Louisiana State University, providing distributed **AMR** for partial differential equations, and in particular, Numerical Relativity applications. This infrastructure is based on Berger-Oliger style **AMR** with full sub-cycling in time, together with an improved treatment of artificial boundaries [156]. It has a modular design, which allow to solve different sets of evolution equations with the same computational infrastructure, using different programing languages as F77, F90 and C++. Previous work with this code [111, 166–170] established that it is convergent and consistent for the evolution of boson stars and neutron stars.

(ii) **SAMRAI:** patch-based Structured Adaptive Mesh Refinement Application Infrastructure developed over more than fifteen years by the Center for Applied Scientific Computing at the Lawrence Livermore National Laboratory for generic applications, as for example hydrodynamics problems, electronic structures, etc. The evolution equations are introduced by using the platform *Simflowny* [100–102, 171] to automatically generate parallel code for the SAMRAI infrastructure [163–165]. Through *Simflowny*, Berger-Oliger without order reduction is implemented with an improved treatment of artificial **AMR** boundaries when there is sub-cycling in time [159, 160]. Further details of the numerical implementation and convergence tests performed with this new platform can be found in Ref. [101, 172].

4.5 Some Numerical Relativity tests

Finally, in this section, we perform few standard **NR** tests by evolving some numerical spacetimes: (i) robust stability test and gauge waves (some of which are included as standard testbeds [173]), and (ii) a single boson star and neutron star. These simple tests will be also useful to check our modification of the **CCZ4** formalism.

For the tests presented in this Chapter, we adopt finite difference schemes, based on the **MoL** [63], on a regular Cartesian grid. A fourth order accurate spatial centered discretization –satisfying the summation by parts rule– is used for Einstein equations, see Section 4.2.1, while the relativistic hydrodynamics equations are discretized using **HRSC** method based on the **HLL**-flux formula with **PPM** reconstruction, see Section 4.2.2. Finally, either a third or fourth order accurate **RK** time integrator is used

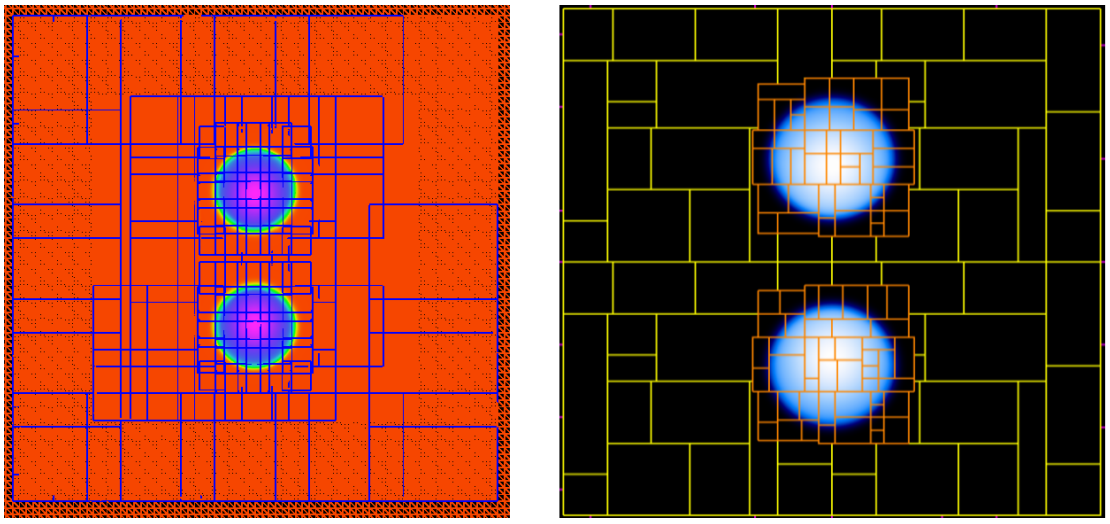

FIGURE 4.4: *Adaptative Mesh Refinement.* Structure of computational domains for simulating a binary of boson stars in an **AMR** algorithm. The left-had side panel correspond to HAD infrastructure and the right-hand side **SAMRAI**. Note that the region with smaller grids are located within the boson stars, ensuring sufficient resolution and accurate solution.

to achieve stability of the numerical implementation and to integrate the equations in time [174].

To ensure sufficient resolution, we employ **AMR** via the HAD computational infrastructure that provides distributed, Berger-Oliger style **AMR** [161, 162] with full sub-cycling in time, together with an improved treatment of artificial boundaries [156]. We adopt a Courant parameter of $\lambda_c \approx 0.25$ such that $\Delta t_l = \lambda_c \, \Delta x_l$ on each refinement level l to guarantee that the Courant-Friedrichs-Levy condition is satisfied.

Notice that, besides these solutions, this code has been used extensively for a number of other projects and it has already been rigorously tested [111, 166–170].

4.5.1 Robust stability test

We first carry out the robust stability test-bed [63, 175]. This test consists on a Minkowski background metric plus a small random perturbation in each of the evolution fields (see one of them in Figure 4.5). Since both the matter terms and all the damping coefficients are set to zero in this test, only the principal part of the evolution equation and the linear terms are significant. The element line is given by

$$ds^2 = -(1 + \delta\alpha)dt^2 + (\eta_{ij} + \delta\gamma_{ij})dx^i dx^j \tag{4.43}$$

where $\delta\alpha$ and $\delta\gamma_{ij}$ are small Gaussian random perturbations. A linear growth on any field indicates a weakly hyperbolic system. Therefore, the solution depends strongly on

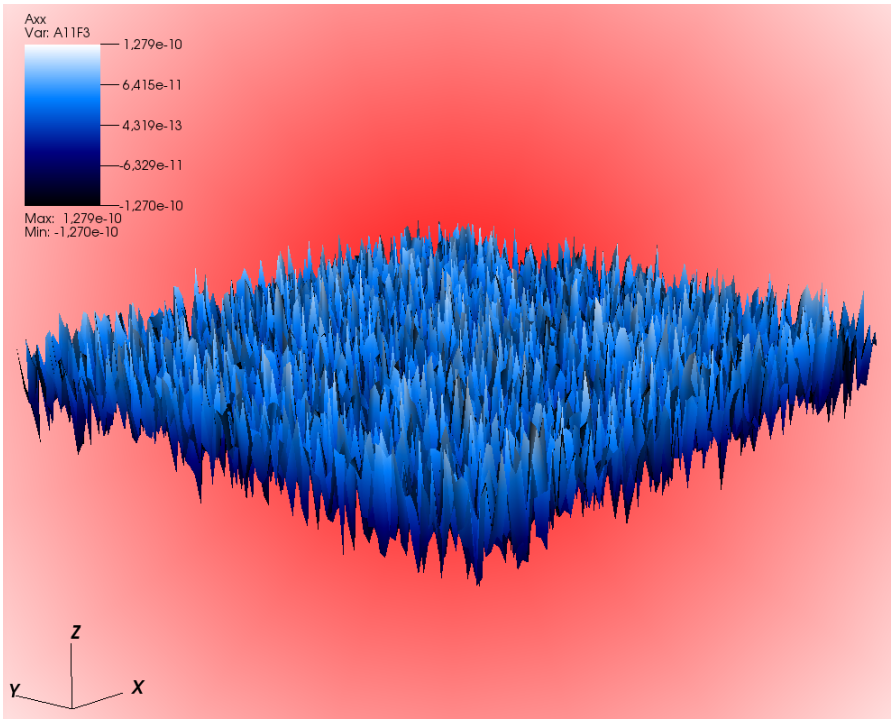

FIGURE 4.5: *Robust stability.* Component $\tilde{A}_{xx}$ of conformal trace-less extrinsic curvature at $t = 0$.

the characteristic structure of our system (2.52-2.56) and, in particular, it confirms its (strongly) hyperbolicity.

We set a 2D domain $[-0.5, 0.5]^2$ with periodic boundaries conditions and $N = 100$ grid points in each direction. No artificial Kreiss-Oliguer dissipation is included for this test. As it was shown in subsection 2.3.4, the hyperbolicity of the system depends on the parameter λ_0, so we analyze the effect of this parameter on the solutions. Besides, we use $f = 2/\alpha$, $g = 3/4$ and $\eta = 2$, that is, the $1 + \log$ slice with standard values for the Gamma-driver shift condition.

The L_2-norms of some constraints are displayed in Fig. 4.6 for three different cases. In the first one the conformal constraints are algebraically enforced after each timestep (**CCZ4e**), as it is currently done in all the flavors of **BSSN** and conformal **Z4**. The other two cases (**CCZ4**) corresponds to $\lambda_0 = 0$ and $\lambda_0 = 1$ without any algebraic enforcing. Our simulations show a linear growth on $||\tilde{\gamma} - 1||$ that propagates to $||Z_x||$ and, eventually, to all the other fields. This linear growth indicates a lack of strong hyperbolicity of the system for $\lambda_0 = 0$. All the norms are constant both for **CCZ4e** and for **CCZ4** with $\lambda_0 = 1$, as it is expected for a well-posed system. Henceforth, we are going to use the choice $\lambda_0 = 1$ for all the forthcoming simulations with **CCZ4**.

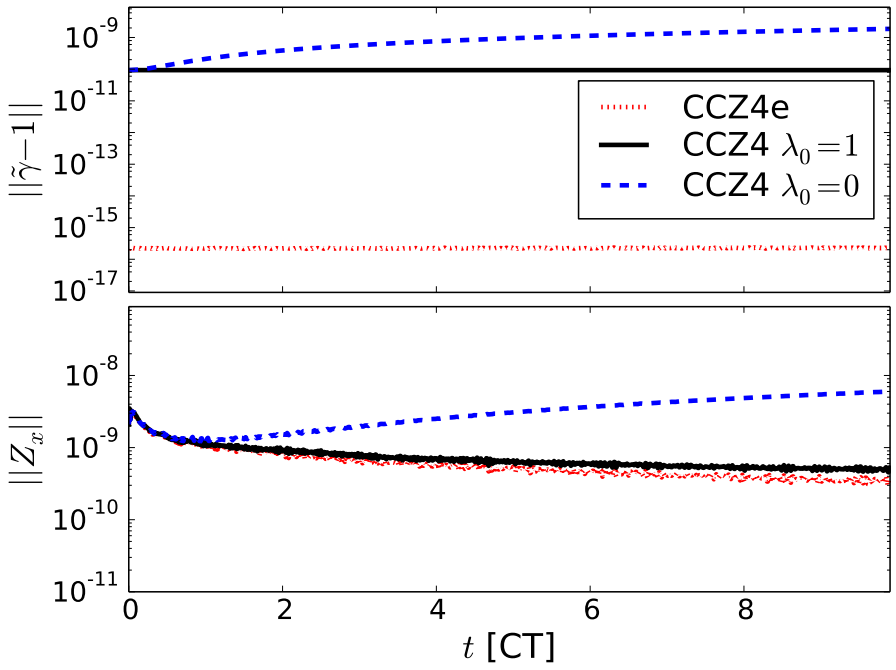

FIGURE 4.6: *Robust stability.* L_2-norm of $|\tilde{\gamma}-1|$ (top panel) and $|Z_x|$ (bottom panel) as a function of time -in crossing time units-. Some modes increase for the **CCZ4** system with $\lambda_0 = 0$ (blue dashed line), showing that this choice leads to a weakly pseudo-hyperbolic system. These modes (and all others) remain constant –a sign of the strong hyperbolicity of the system– in the other two cases; **CCZ4** with $\lambda_0 = 1$ (black solid line) and **CCZ4e** (red dotted line), where the conformal constraints are algebraically enforced.

4.5.2 Gauge waves

A family of non-trivial exact solutions can be constructed from Minkowski spacetime by performing a coordinate transformation on (x, t). The resulting line element can be written as [63, 92, 173, 175]

$$ds^2 = -H(x-t)dt^2 + H(x-t)dx^2 + dy^2 + dz^2,$$

where $H(x-t)$ is an arbitrary plane wave function propagating along the x axis. Note that this solution is exact within an harmonic slicing, $\alpha = \sqrt{\gamma}$, and zero shift, $\beta^i = 0$, corresponding to the choice $f = 1$ and $g = 0$ in our gauge conditions. We will consider $H(x-t) = 1 - A\sin[k(x-t)]$ and set an amplitude $A = 0.1$ with wave number $k = 2\pi/L$, being L the size of the domain. The domain for this one-dimensional test is $[0, 1]$ with periodic boundary conditions and 100 grid points. This test allows us to study the stability of our formulation in the non-linear regime.

The L_∞-norm for some constraints are shown in Fig. 4.7 for four different cases, which can be compared with Figure 1 in [92]. In the first two cases (i.e., **BSSN** and **CCZ4e**), the conformal constraints are algebraically enforced after each time step. The other two

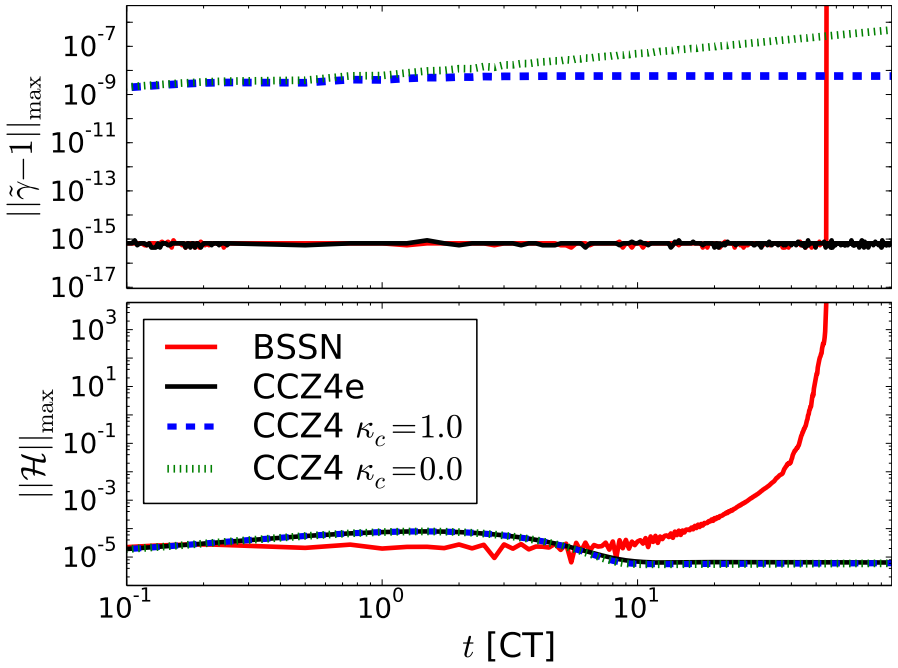

FIGURE 4.7: *Gauge waves.* L_∞-norm of $|\tilde{\gamma}-1|$ (top panel) and $|\mathcal{H}|$ (bottom panel) as a function of time -in crossing time units -. The **BSSN** system (red solid line) and **CCZ4** with $\kappa_c = 0$ (green dotted line) display an unbound growth in some constraints. Both **CCZ4e** (black solid line) and **CCZ4** with $\kappa_c = 1$ (blue dashed line) maintain the constraints under control at least for 100 crossing times.

cases correspond to **CCZ4** with either $\kappa_c = 1/L$ or $\kappa_c = 0$ (in both cases $\kappa_z = 1/L$). It is clear that the **BSSN** formulation fails in this test, as both the conformal and the Hamiltonian constraint suffer an exponential growth. In contrast, all the constraints remain under control when using the **CCZ4e**. The most important outcome of this test is the fact that the **CCZ4** formulation with $\kappa_c = 1$ is also stable, meaning that it is not required to enforce algebraically the conformal constraints to keep them under control. The last case, **CCZ4** with $\kappa_c = 0$, presents a linear growth in the conformal constraint $|\tilde{\gamma}-1|$, which unavoidably will lead to a failure due to the propagation to other fields. The same behavior is observed in simulations on generic spacetimes, indicating that the choice of the damping coefficients $\{\kappa_z, \kappa_c\}$ is crucial to achieve accurate and stable solutions.

4.5.3 Evolution of single boson star

As we discussed in the Section 3.4.2, the initial data for complex scalar field configurations in spherical symmetry can be solved numerically for the static metric (3.23) by adopting the harmonic ansatz (3.50) for the scalar field. Within these assumptions the **EKG** system reduces to a set of ordinary differential equations that can be solved by imposing appropriate boundary conditions(3.26)-(3.27) (i.e., regularity at the origin and

asymptotically flat at large distances). The equations are further simplified by using polar-areal coordinates. Therefore, the standard procedure is to solve the equations in these coordinates and then perform a (numerical) coordinate transformation into isotropic coordinates, which can be transformed to Cartesian ones [129].

Different interaction potentials $V(|\Phi|^2)$ lead to boson stars with different compactness [58]. We are interested in a particular family of very compact boson stars, commonly known as nontopological solitonic boson stars[2] [135, 136], where the potential is given by

$$V\left(|\Phi|^2\right) = m_b^2|\Phi|^2\left[1-\frac{2|\Phi|^2}{\sigma_0^2}\right]^2 . \tag{4.44}$$

Here σ_0 is a constant that determines the compactness of the star and m_b is related to the scalar field mass. Therefore, depending on the model parameters, solitonic **BSs** can be as massive as (super)-massive **BHs** and, when $\sigma_0 \ll 1$, they can be slightly more compact than ordinary neutron stars [135]. Following the definition made in Chapter 3, the effective radius R_M is defined as the radius within which 99% of the total mass is contained, i.e. $m(R_M) = 0.99M$. In the model under consideration, since the scalar field is very steep, choosing a higher threshold does not affect the radius significantly. As we said before, solitonic **BS** is a specific family with a potential that yields compactness comparable or even higher than that of neutron stars. In particular, stable configurations can reach a maximum compactness of $C_{\max} \approx 0.33$. As a reminder, the compactness for a Schwarzschild **BH** $C = 0.5$ and for a **NS** is $C \approx 0.1 - 0.2$.

Here, we test our implementation using strongly self-gravitating scalar fields, i.e., solitonic **BSs**. By setting $\sigma_0 = 0.05$ and the scaling factor $m_b\sigma_0\sqrt{8\pi} = 1$, the most massive stable star has a mass $M_{max} \approx 1.84$. A suitable stable equilibrium configuration for our test can be obtained by setting $\phi_0(r=0) = 0.0364$ and $\omega = 1.0666$. The resulting star has mass $M = 0.36$ and radius $R = 3.08$, so its compactness is $C = 0.118$. This configuration is well inside the stable branch. The profiles of $\alpha(r)$, $\psi(r)$ and $\phi_0(r)$ for this particular solution are plotted in Fig. 4.8. Note that, due to the very steep profile (see Figure 4.8 or Figure 5.1) of the scalar field, the numerical integration of the equilibrium equations becomes quite challenging, requiring very fine-tuned shooting parameters [59].

This configuration is evolved in a domain $[-16, 16]^3$ with radiative boundary conditions. There are 60 grid points in each direction and three refinement levels, such that the highest resolution is $\Delta x = 0.1$. The simulations are performed by using the **CCZ4** formulation (see section 2.3.2) coupled with the **KG** equations written in conformal variables (3.42)-(3.44) with $\kappa_z = 0.1$ and either $\kappa_c = 1$ or $\kappa_c = 0$. We also include the solutions obtained with the **BSSN** formulation for comparison purposes.

[2] From now on, we will use Φ instead of ϕ (as was used in the Chapter 3).

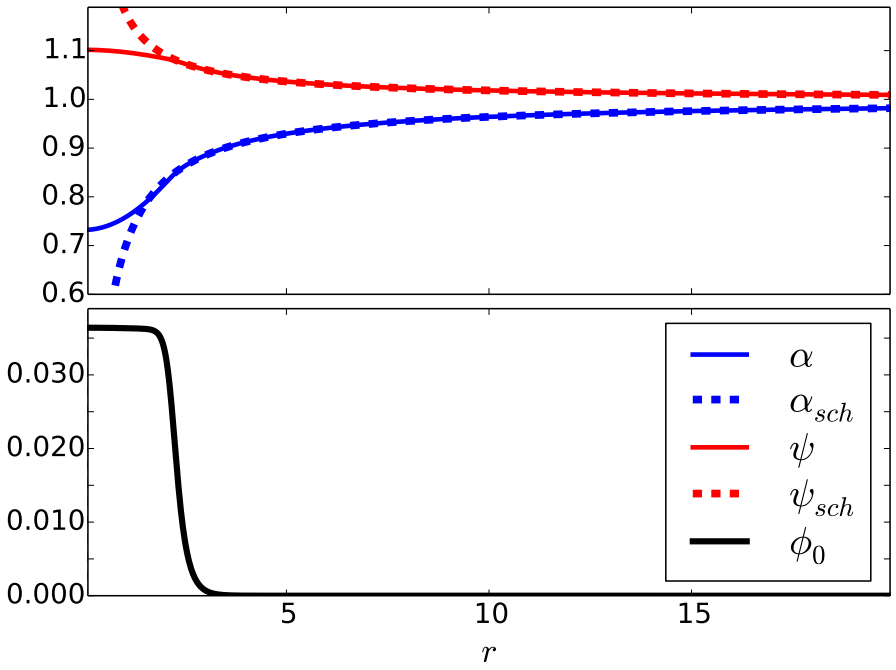

FIGURE 4.8: *Solitonic boson star.* The top panel displays the metric components $\alpha(r)$ (blue solid line) and $\psi(r)$ (red solid line) for the typical solitonic boson stars with compactness $C \approx 0.118$ used here, compared to the Schwarzschild solution (dashed lines) in isotropic coordinates. The bottom panel shows the scalar field profile $\phi_0(r)$, which is almost constant in the interior and decays rapidly at the surface of the star.

The evolution of the scalar field real part $\Phi_R(t, r = 0)$ is displayed in Fig. 4.9, together with the expected analytical behavior $\phi_0(r = 0)\cos(\omega t)$. The solutions for all the cases considered, either with **BSSN** or **CCZ4**, show a very good agreement with the analytical expectation. Differences arise however in the L_2-norm of some constraints, plotted in Fig. 4.10. Both the conformal and the physical constraint remain under control by using either **BSSN** or **CCZ4** with $\kappa_z = 0.1$ and $\kappa_c = 1$. However, notice that the errors of the physical constraints obtained with the **CCZ4** and this parameter choice are several orders of magnitude smaller than the ones obtained by using **BSSN**.

4.5.4 Evolution of single neutron star

Another interesting numerical test is based on the evolution of an isolated neutron star. The initial data can be constructed as explained in Section 3.5.3. We calculate a family of equilibrium configuration by considering a polytropic **EoS** with $\Gamma = 2.5$ and $\kappa = 8980$, such that the most massive stable star has mass $M_{max} \approx 2.6$. The specific equilibrium configuration solution for our test is obtained by setting $\rho_c = 1.223 \times 10^{-2}$, leading to a stable equilibrium configuration with mass $M = 1.35$ and radius $R = 11.23$, and therefore, a compactness of $C = 0.12$. The radial profiles of $\alpha(r)$, $\psi(r)$ and $\rho(r)$ for this particular solution are displayed in Fig. 4.11.

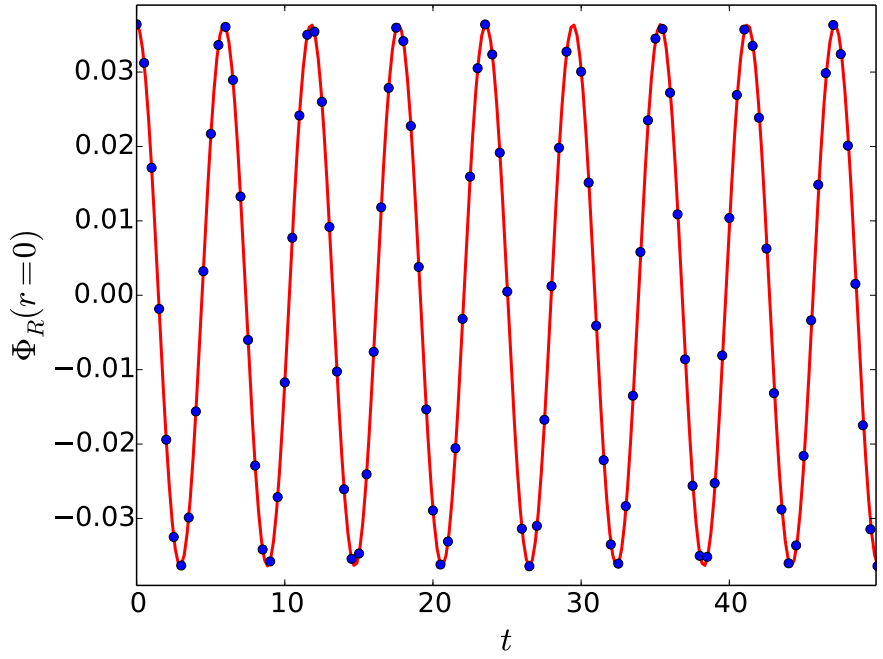

FIGURE 4.9: *Solitonic boson star.* Evolution of the real part of Φ at $r = 0$. The solid red line illustrate the analytically expected value $\phi_0(r = 0)\cos(\omega t)$ with $\omega = 1.0666$. The blue circles show the numerically solution obtained with different evolution systems (i.e., **BSSN** and **CCZ4**), which can not be distinguished by eye in this plot.

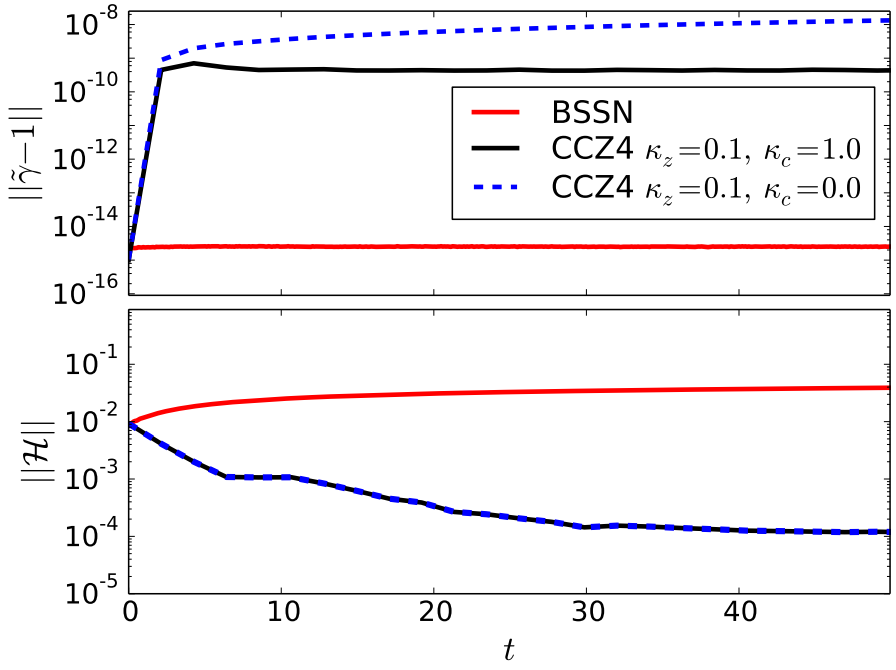

FIGURE 4.10: *Solitonic boson star.* L_2-norm of $|\tilde{\gamma} - 1|$ (top panel) and $|\mathcal{H}|$ (bottom panel) as a function of time. The solution obtained with **BSSN** (red solid line) shows a small $|\tilde{\gamma} - 1|$ constraint as a result of enforcing constraint in each integration time-step, but the Hamiltonian constraint increase over time. The solutions obtained with **CCZ4**4 are stable if we add the damping terms for the conformal constraints (black solid line) –otherwise there is a linear growth in $|\tilde{\gamma} - 1|$ that will lead to a unstable evolution (blue dashed line).

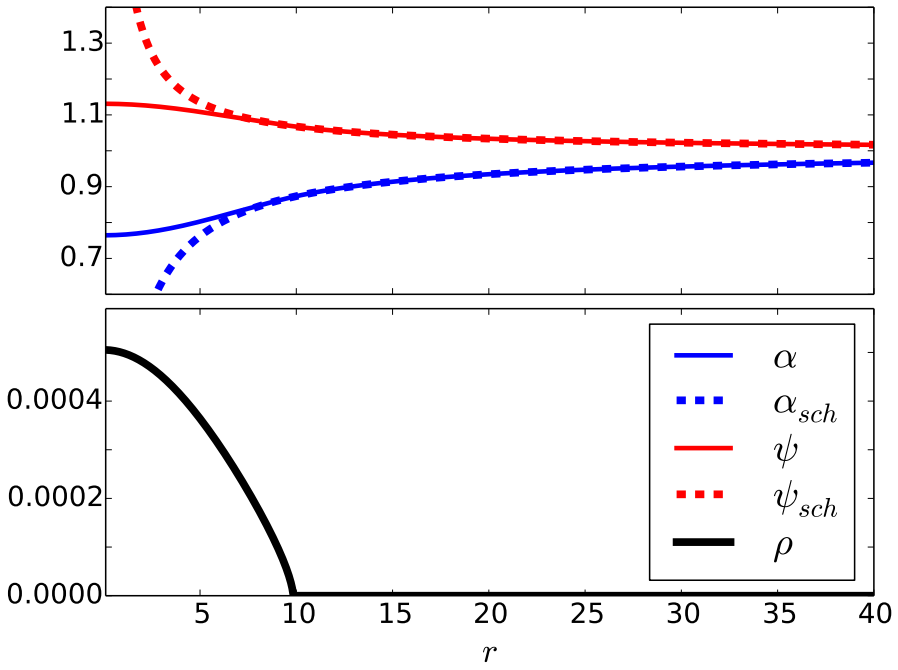

FIGURE 4.11: *Neutron star.* The top panel shows the metric components $\alpha(r)$ (blue solid line) and $\psi(r)$ (red solid line) for the equilibrium configuration of a non-rotating neutron star with mass $M \approx 1.35$ and radius $R = 11.23$ used here, compared to the Schwarzschild solution (dashed lines) in isotropic coordinates. The bottom panel displays the central rest mass density $\rho(r)$.

This configuration is evolved in a cubic domain $[-100, 100]^3$ with radiative boundary conditions. There are 120 grid points in each direction and four refinement levels, such that the highest resolution is $\Delta x = 0.2$. The simulations are performed by using the **CCZ4** formulation coupled with the relativistic hydrodynamical equations written in conformal variables (3.77)-(3.79) with $\kappa_z = 0.1$ and $\kappa_c = 1$.

The dynamical evolution of some interesting quantities are displayed in Figure 4.12. In particular, the spatial integral of the globally conserved baryonic number D is showed in the first panel. This quantity has been rescaled by their initial values. Notice that it remains approximately constant during the evolution, confirming that the initial equilibrium configuration is stable. Finally, the L_2-norm of Hamiltonian constraint is displayed in the bottom panel, showing that it remains under control with our selection of the damping terms $\kappa_z = 0.1$ and $\kappa_c = 1$.

4.6 Discussion

To summarize, we have showed that our novel modification of the **CCZ4** formalism, which does not require the algebraic enforcement of the conformal constraints after each step of the numerical integration, behaves in a stable and robust way with a variety

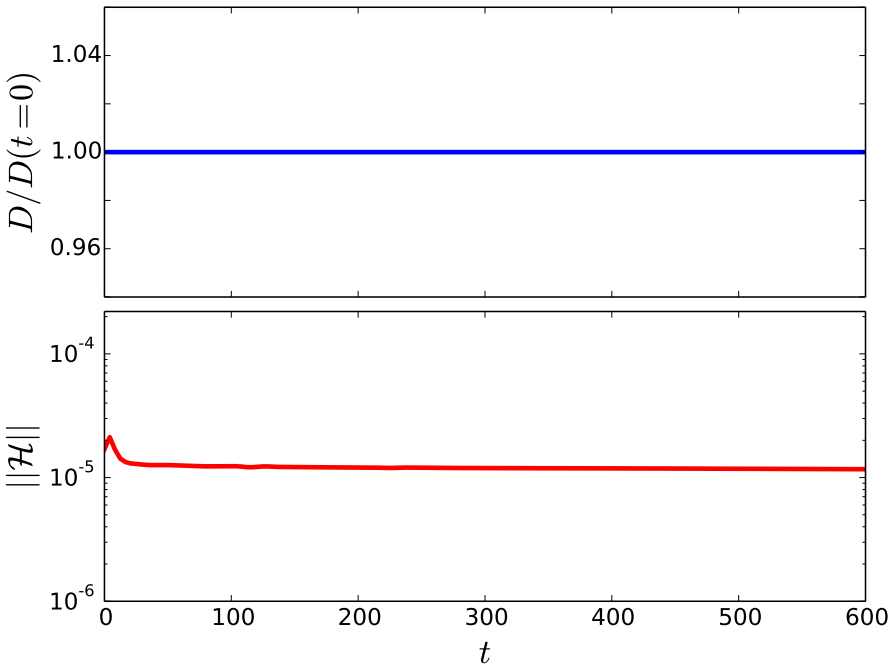

FIGURE 4.12: *Neutron star.* (Top) Evolution of the spatial integral of the global conserved quantities D. It remains roughly constant during the evolution, showing that the star is stable. (Bottom) L_2-norm of the Hamiltonian, $\mathcal{H}$, as a function of time. These results confirm that the solution with **CCZ4** is stable and the constraints remain under control by setting $\kappa_z = 0.1$ and $\kappa_c = 1$.

of known solutions, including the evolution of isolated boson and neutron star. These simulations have been performed by solving the Einstein equations coupled to matter fields, described either with a scalar field or a perfect fluids. We have used **AMR** via the HAD computational infrastructure in order to guarantee sufficient resolution. Finally, let us stress that our formulation treats the conformal constraints in the same way than the physical ones, and they are also kept under control by including damping terms.

Chapter 5

Collisions of Boson Stars

Here we study binary mergers of very compact boson stars. Our aim is to investigate the properties of the remnant resulting from the merger and the gravitational radiation produced in these scenarios by means of numerical evolutions. We consider several types of binaries by varying different parameters either of the boson star, namely the phase shift and the direction of rotation in the complex plane, or of the binary, like the angular momentum. The analysis of the gravitational waves radiated during the coalescence of such a binary will be crucial to distinguish these events from other binaries by using **LIGO** and **Virgo** observations.

These simulations, performed by using the modified **CCZ4** formalism [1] introduced in Section 2.3.2, reveal a rich phenomenology that can be summarized as follows:

(i) the final state after a head-on collision of low-mass boson stars is, in general, another boson star. However, almost complete annihilation of the stars occurs during the merger of a boson-antiboson pair.

(ii) the merger of orbiting boson stars form either a rotating bar that quickly relaxes to a non-rotating boson star or a black hole, depending on the initial compactness of the stars.

(iii) the remnant's gravitational wave signature is mainly governed by its fundamental frequency as it settles down to a non-rotating boson star, emitting significant gravitational radiation during the post-merger state.

In this Chapter we review the research presented in [6, 111] and it is organized as follows. In Section 5.1, a brief introduction and motivation about binary boson stars systems is

[1] Which does not require the algebraic enforcing of any constraint.

presented. Then, in Section 5.2, we revisit the Einstein-Klein-Gordon (**EKG**) equations considering the specific potential leading to solitonic boson stars. The procedure to construct initial data consisting for binary boson star systems is described in Section 5.3. We study the dynamics of binary boson stars in Section 5.4 by analyzing our numerical simulations of head-on and orbiting cases. In Section 5.5 we study the coalescence of binary boson stars for different compactnesses, focusing on the dynamics and the corresponding gravitational waves signal. Finally, we present a discussion of the results in Section 5.6.

5.1 Motivation

Currently, the only known astrophysical compact objects able to source strong gravitational waves are **BHs** and **NSs** [39]. Nevertheless, there might be other non-standard low-brightness stars, called generically exotic compact objects (**ECOs**) (see [176] for a review), which might be too dim to be observed by current electromagnetic telescopes. However, if they are massive and compact enough, it might be possible to detect them trough the gravitational waves (**GWs**) radiated during their coalescence.

Among the many exotic alternative compact objects that have been proposed (e.g., fuzzballs [49], gravastars [50], wormholes [51], etc), boson stars (**BSs**) [53] are arguably among the better motivated and very likely the cleanest to model (see Ref. [48] for a recent review on exotic compact objects). There are two theoretical arguments that supports the possibility of self-gravitating objects made by bosonic particles in the Universe. First, the discovery of Higgs boson [56, 57] confirmed the existence of scalar fields in Nature. Second, the existence of a formation mechanism, dubbed as gravitational cooling [177], to produce **BSs** from a generic scalar field configuration.

Despite the simplicity of these smooth solutions, there are only few studies on binary boson star collisions within General Relativity (**GR**). Preliminary head-on collisions of mini-boson stars were first studied in [178] within a 3D code. The dynamics of the merger, which showed an interesting interference pattern, was further analyzed in [128] with and axisymmetric code. Ultra-relativistic collisions were considered in [179], and head-on and orbital mergers of non-identical boson stars in [166, 167]. Other related works include the study of the orbital case within the conformally flat approximation instead of full **GR** [180], and head-on collision of oscillatons [61], a solution analogous to boson star but using just a real scalar field. Much more recently, collisions of solitonic boson stars have been numerically performed [61, 181, 182], leading to dynamics qualitatively similar to the observed for mini-boson stars, and head-on and orbital collision

of Proca stars [183], a solution modeled by a massive complex vector field (see Ref. [184] for dynamical formation of Proca stars).

Motivated by the existent and future **GW** observations of compact-object binary mergers, we study the dynamics of **BSs** mergers and, in particular, the coalescence of a binary system in a tight, quasi-circular orbit. The remnant of this merger can generally be either a **BS** or a **BH**. For the merger to result in a long-lived **BS**, however, it is required that (i) the remnant star be stable, which in turn implies that its mass is less than the maximum mass allowed for the model, and (ii) the angular momentum left over after the merger satisfy the quantization condition for boson star [58] and hence either vanish (i.e., $k = 0$) or be larger than the minimum angular momentum (i.e., $k = 1$)for a rotating **BS**.

In the same framework, we are interested in these **BSs** signals within the context of binary **BHs** and binary neutron stars. We will therefore consider that range of compactnesses for the initial binary components. For increasing compactness, the gravitational wave signal of a **BS** binary is expected to resemble more closely that of a **BH** binary. For small compactness, the structure and tidal deformability [7, 8] of the star will play a significant role, similar to the signals from binary neutron stars.

5.2 Evolution equations

Recall that, as was explained in the Chapter 3, **BSs** are described by **EKG** theory, whose action is $S = \int d^4x\sqrt{-g}\mathscr{L}_{KG}$, where Lagrangian density $\mathscr{L}_{KG}$ is given by (3.33). Variations with respect to the metric and the scalar field yield to the following evolution equations

$$R_{ab} - \frac{1}{2}g_{ab}R = 8\pi\left(\nabla_a\Phi\nabla_b\Phi^* + \nabla_a\Phi^*\nabla_b\Phi - g_{ab}\left[\nabla^c\Phi\nabla_c\Phi^* + V\left(|\Phi|^2\right)\right]\right) \quad (5.1)$$

$$g^{ab}\nabla_a\nabla_b\Phi = \frac{dV}{d|\Phi|^2}\Phi\,, \quad (5.2)$$

The compact solutions considered here are the solitonic boson stars model [135] with a self-interaction potential given by equation (4.44). In particular, here we restrict ourselves to $\sigma_0 = 0.05$ which is chosen because it allows for very compact, stable configurations. Following [59], we can rewrite the equations for the initial data Equations (3.51)–(3.54) in terms of the following dimensionless quantities

$$M(m_b\lambda),\quad N(m_b\lambda)^2,\quad r(m_b\lambda),\quad \omega/(m_b\lambda)\,, \quad (5.3)$$

C	ϕ_c/σ_0	$Mm_b\lambda$	$N(m_b\lambda)^2$	$(R_M, R_N)m_b\lambda$	$\omega/(m_b\lambda)$	m_b	M	N	(R_M, R_N)	ω	I/M^3	$k_{\rm tidal}$
0.06	1.045	0.1238	0.0605	(2.0334, 1.8288)	1.545745909	0.9880	0.5	0.9867	(8.21, 7.38)	0.3828	84.9	8420
0.12	1.030	0.3650	0.2551	(3.0831, 2.8360)	1.066612350	2.9124	0.5	0.4785	(4.22, 3.88)	0.7787	27.8	332
0.18	1.025	0.7835	0.7193	(4.2572, 3.9960)	0.790449025	6.2514	0.5	0.2929	(2.71, 2.54)	1.2386	12.5	41
0.22	1.025	1.0736	1.1147	(4.9647, 4.7068)	0.685760351	8.5663	0.5	0.2417	(2.31, 2.19)	1.4725	8.34	20

TABLE 5.1: *Characteristics of solitonic **BS** models with* $\sigma_0 = 0.05$. The table shows: compactness, central value of the scalar field, **ADM** mass, Noether charge, radius of the star (i.e, containing 99% of either the mass or of the Noether charge for R_M or R_N, respectively) and angular frequency of the phase of ϕ in the complex plane, in dimensionless units on the left and in units such that $M = 0.5$ on the right. Note that high-compactness configurations require a very fine tuning in ω. Here we show only the first nine decimal figures. In the last two columns, we give the normalized Newtonian moment of inertia (where $I = \int dm L^2$, L being the distance from the axis of rotation) and dimensionless tidal Love number ($k_{\rm tidal}$) of the corresponding configuration as computed in [7, 8]. As a reference, $k_{\rm tidal} \approx 200$ for a neutron star with an ordinary equation of state, and $k_{\rm tidal} = 0$ for a **BH**.

where $\lambda = \sigma_0\sqrt{8\pi}$. Doing so produces equations independent of m_b, and hence m_b serves to set the units of the physical solution. As such, we choose m_b so that the **BS** mass is $M = 0.5$, and the total mass of binary systems constructed with these solutions (described in the following sections) is roughly unity for any compactness of the binary components. Note that while the scaling with m_b shown in Eq. (5.3) is exact, the scaling with respect to λ is not. Only in the $\sigma_0 \ll 1$ limit does the scaling hold. For the value $\sigma_0 = 0.05$ considered here, the scaling is only approximate.

A sequence of isolated **BS** solutions can be characterized by the central value of the scalar field ϕ_c. In Fig. 5.1, a number of relevant adimensional quantities of this family of solutions are shown. Among these, we show the compactness C as a function of ϕ_c (top left) and as a function of the mass (top right), which achieves a maximum of roughly $C_{max} \approx 0.33$. The markers shown in Fig. 5.1 denote the four representative initial configurations which will be studied in detail in Section 5.5.3 to investigate the gravitational wave radiation during the coalescence. Radial profiles of $\phi_0(r)$ for these representative cases are displayed also in Fig. 5.1(bottom left panel), while that their mass-radius diagram is showed in the bottom right panel. The relevant parameters of these solutions are given in Table 5.1.

It is worth mentioning that in numerical simulations, it is more practical to estimate the radius of the final remnant through the radius containing 99% of the Noether charge, R_N, so we will also adopt this definition when needed.

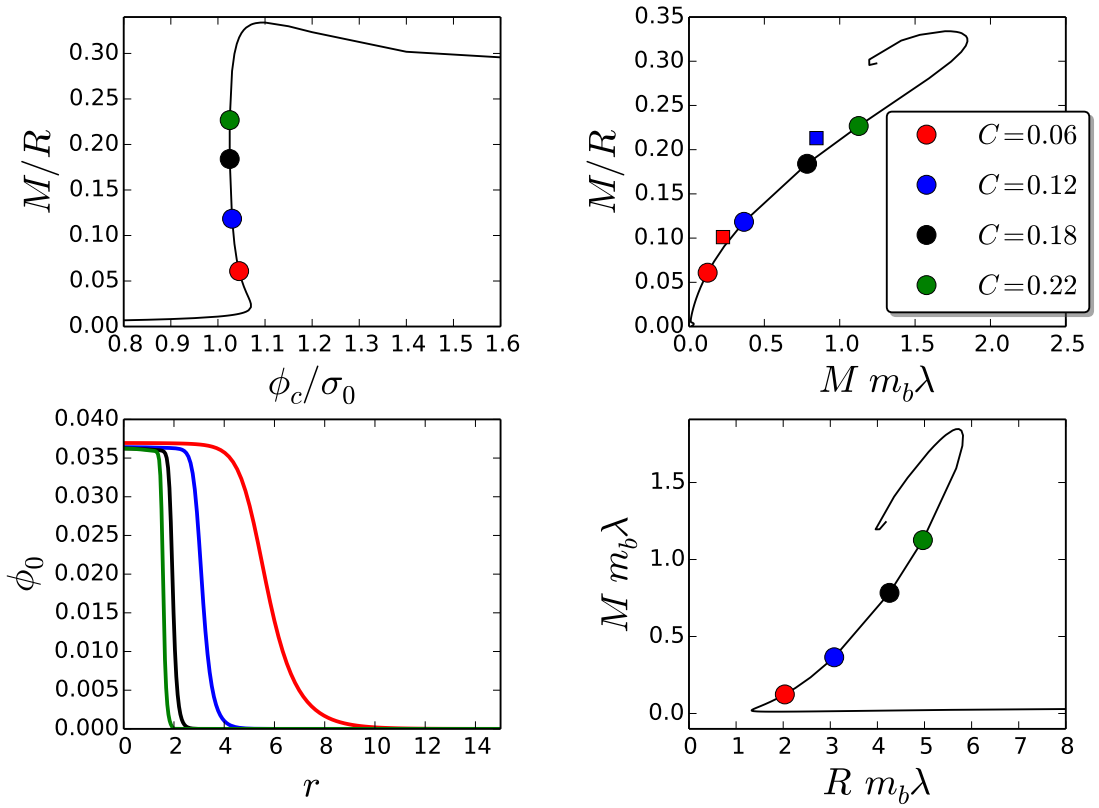

FIGURE 5.1: *Compactness as a function of the central value of the scalar field ϕ_c (top left), compactness-mass diagram (top right), radial profile of the scalar field $\phi_0(r)$ for each compactness (bottom left), and mass-radius diagram (bottom right) of an isolated nonspinning **BS** in the solitonic model* (4.44) *with $\sigma_0 = 0.05$.* Circular markers refer to the *initial* equilibrium configurations considered in this Chapter to construct initial data for **BS** binaries (see Table 5.1), whereas squared markers in the right top panel refer to the final remnant produced by the merger of stars in an initial configuration indicated by the same color (see Table 5.2). Two squares corresponding to two configurations are not shown; the remnant of the black configuration is not well-enough resolved and did not reach a quasi-stationary state, and the green configuration produces a **BH** (with $C > 0.5$) instead of a **BS**. The radius R_M is defined as that containing 99% of the mass of the star, except for the radius of the remnant which is instead defined as that containing 99% of the Noether charge, R_N.

5.3 Initial data of binary solitonic Boson Stars

Here, we describe how to construct initial data for a binary boson star system with generic angular momentum, by extending the procedure described in [185] to construct accurate boosted initial data from a spherically symmetric solution.

First of all, we will begin by performing a Lorentz transformation to the coordinates of a static **BS** solution, in order to get a boosted **BS** star along the x-axis.

As we know, the line element for spherically symmetric solutions can be easily written in Cartesian coordinates from the isotropic coordinates, namely

$$ds^2 = -\alpha_0^2 dt_0^2 + \psi_0^4(dx_0^2 + dy_0^2 + dz_0^2) = -\alpha_0^2 dt_0^2 + \psi_0^4(dr_0^2 + r_0^2 d\Omega^2) \ , \tag{5.4}$$

where $\alpha_0 = \alpha_0(r_0)$ and $\psi_0 = \psi_0(r_0)$, being $r_0 = \sqrt{x_0^2 + y_0^2 + z_0^2}$. By performing a Lorentz transformation along the x-direction

$$t = \Gamma(t_0 + v x_0) \ , \tag{5.5}$$

$$x = \Gamma(x_0 + v t_0) \ , \tag{5.6}$$

where $\Gamma = 1/\sqrt{1-v^2}$ is the usual Lorentz factor, one can obtain the following line element for the boosted solution

$$ds^2 = -\Gamma^2(\alpha_0^2 - \psi_0^4 v^2)dt^2 + 2\Gamma^2 v\,(\alpha_0^2 - \psi_0^4)dtdx + \psi_0^4(B_0^2 dx^2 + dy^2 + dz^2). \tag{5.7}$$

The lapse function and the non-zero component of the shift vector β^i are given by

$$\alpha = \frac{\alpha_0}{B_0} \ , \quad \beta^x = \left(\frac{\alpha_0^2 - \psi_0^4}{\psi_0^4 - \alpha_0^2 v^2}\right) v \ , \tag{5.8}$$

with $B_0 = \Gamma\sqrt{\left(1 - \frac{v^2\alpha_0^2}{\psi_0^4}\right)}$. Notice that r_0 can be written in terms of the new coordinates, namely $r_0 = \sqrt{\Gamma^2(x-vt)^2 + y^2 + z^2}$. Now we only have to perform the Lorentz transformation to the scalar field quantities. First, the harmonic ansatz given by eq. (3.50) can be generalized, to allow for non-identical boson stars, by including a phase shift θ and the direction of rotation $\epsilon = \pm 1$ [58], namely:

$$\Phi(t_0, r_0) = \phi_0(r_0)\, e^{-i(\epsilon\omega t_0 + \theta)} \ . \tag{5.9}$$

Besides, we can compute the field $\Pi(t, r_0)$ from its definition Equation (3.40), calculated in the boosted frame. The final expressions, evaluated at $t = 0$, are

$$\phi_R(r_0) = \phi_0\,(r_0)\cos(\theta - \Gamma v x \epsilon\omega) \ , \tag{5.10}$$

$$\phi_I(r_0) = -\,\phi_0\,(r_0)\sin(\theta - \Gamma v x \epsilon\omega) \ , \tag{5.11}$$

$$\Pi_R(r_0) = \frac{\Gamma\,\epsilon\,\omega\phi_0\,(r_0)\,(\beta^x v + 1)\sin(\theta - \Gamma v x \epsilon\omega)}{\alpha} + \frac{\Gamma^2 x(\beta^x + v)\phi_0'\,(r_0)\cos(\theta - \Gamma v x \epsilon\omega)}{\alpha r_0} \ , \tag{5.12}$$

$$\Pi_I(r_0) = \frac{\Gamma\,\epsilon\,\omega\phi_0\,(r_0)\,(\beta^x v + 1)\cos(\theta - \Gamma v x \epsilon\omega)}{\alpha} - \frac{\Gamma^2 x(\beta^x + v)\phi_0'\,(r_0)\sin(\theta - \Gamma v x \epsilon\omega)}{\alpha r_0} \ . \tag{5.13}$$

We are mainly interested on binary systems. Along the lines described in [111, 129, 185], initial data for binaries can be constructed as the superposition of two single solitonic boson star solutions. With the isolated **BS** boosted configurations in hand, the method can be summarized as follows:

(i) construct the initial data for two identical spherically symmetric **BSs**, as discussed in the previous Section 3.4.2. We denote the metric and scalar field as $\{g^{(i)}_{ab}(r), \Phi^{(i)}(r)\}$, where the super-index (i) indicates each solitonic star

(ii) extend the solution to Cartesian coordinates, with the center of the star is located at a given position x^j_c. After that, perform a Lorentz transformation to the solution for each **BS** with a boost velocity $\pm\, v_x$ along the x-direction, namely

$$\{g^{(i)}_{ab}(x^j - x^j_c, v_x), \Phi^{(i)}(x^j - x^j_c, v_x)\} \ , \tag{5.14}$$

(iii) finally, superpose the solutions for each of the two stars:

$$\Phi = \Phi^{(1)}(x^j + x^j_c, -v_x) + \Phi^{(2)}(x^j - x^j_c, v_x) \ , \tag{5.15}$$

$$g_{ab} = g^{(1)}_{ab}(x^j + x^j_c, -v_x) + g^{(2)}_{ab}(x^j - x^j_c, v_x) - \eta_{ab} \ , \tag{5.16}$$

where η_{ab} is the Minkowski metric.

It should be noted that this superposition of boosted binary **BSs** in only an approximate solution at the initial time that does not satisfy exactly the constraints. However, as it is shown in Fig. 5.6 for one of our typical simulations below, these initial constraint violations, in one of our typical simulations, are rather small and decay exponentially in a short time scale.

5.4 Numerical Simulations of Boson Stars mergers

Here the dynamics of binary boson stars is studied, focusing on the final state of the system after the merger. After describing the numerical setup, we present the results of our simulations, where we consider both head-on and orbiting binary systems.

5.4.1 Numerical setup

We adopt the covariant conformal Z4 formulation **CCZ4**, explained in Section 2.3.2, to write down the Einstein equations as a time evolution system. These equations are supplemented with suitable gauge conditions for the lapse and shift, namely the $1+\log$ slicing condition [105] and the Gamma-driver shift condition [107] (see section 2.3.3). Furthermore, the same numerical setup from Section 4.5 is used. In order to ensure sufficient resolution within the **BSs**, we employ **AMR** via the HAD computational infrastructure, see section 4.4.

In the two scenarios considered (i.e., binary BS systems with/without angular momentum) the cubical domain is given by $[-60, 60]^3$ with 120 grid points along each axis, leading to a coarsest resolution $\Delta x_0 = 1$. We set five refinement levels such that the last one, covering both stars, has a resolution $\Delta x_4 = 0.0625$ (i.e., there are approximately 96 points covering each star). Besides the constraints, additional analysis quantities are evaluated in our binary boson stars simulations: the Noether charge or boson number, given by the volume integral eq. (3.38), the **ADM** mass (2.88) and the angular momentum (2.90), described in the Section 2.4. All these quantities are computed in a sphere located at $R_{ext} = 40$.

5.4.2 Head-on collisions cases

We consider initial data of binary equal-mass **BSs** which are initially at rest[2]. This solution is constructed as a superposition of isolated **BSs**, as it was described previously, with the ansatz (5.9) for one of the stars, namely

$$\Phi = \phi_0^{(1)} e^{-i\omega t} + \phi_0^{(2)} e^{-i(\epsilon\omega t+\theta)} \ , \tag{5.17}$$

$$g_{ab} = g_{ab}^{(1)} + g_{ab}^{(2)} - \eta_{ab} \ . \tag{5.18}$$

[2]This means that we are considering $v_x = 0$ in Equation (5.14).

Note that, even for a particular solution for an isolated BS (i.e., the one described in section 4.5.3), located at fixed initial positions x_c, there is an infinite family of configurations depending on the parameters $\{\theta, \epsilon\}$. Here, each solitonic **BS** is initially centered at $(\pm 4, 0, 0)$.

We focus our study of equal-mass binaries in two essentially different scenarios:

(i) two boson stars, that is, with the same phase direction of rotation (within the complex plane), i.e., $\epsilon = +1$, but allowing for a phase shift θ, which will be denoted as B-B(θ) . We consider four different cases for B-B(θ) with phase shifts $\theta = \{0, \pi/2, \pi, 3\pi/2\}$.

(ii) and, a binary formed by a boson and an anti-boson star(still with a phase shift), denoted as B-aB(θ). Since their phases have opposite rotation direction (i.e., $\epsilon = -1$), their Noether charges will also have opposite sign. We consider two for B-aB(θ) with $\theta = \{0, \pi\}$.

Let us start by describing the dynamics of the head-on binaries. Some time snapshots of the Noether charge density –for all cases– are displayed in Figure 5.3, while that the evolution of the **ADM** mass and the Noether charge are presented in Fig. 5.2.

Note that, since the binary systems considered here have no initial boost velocity, their initial behavior is marked by their gravitational attraction. As the evolution progresses, the resulting final object will depend on each case:

(a) **B-B(0), B-B($\pi/2$), B-B($3\pi/2$):** during the first stage of the evolution, the dynamics is governed mainly by their gravitational attraction. They approach quickly and, at around $t \approx 28$, the merger occurs. It this stage, both the scalar field and gravitational interactions play a fundamental role on the dynamics by forming a massive and perturbed **BS**. Finally, the collision of these cases leads to a merger, resulting into a single solitonic **BS** with roughly the same total initial mass and Noether charge (i.e., except a small fraction that is emitted by gravitational waves and scalar field radiation, see Fig. 5.2).

(b) **B-B(π):** in the same way as the previous case, their initial approach is quick due to gravity. However, the scalar field interaction between the two stars produces a repulsive force that overcomes the gravitational attraction and repels the two compact objects. When they separate again, the repulsion force vanishes and gravitational forces dominates again, leading to another collision. Therefore, the binary suffers several inelastic collisions before relaxing to a system with two touching stars –which do not merge into a single one. As it can be noted from Fig. 5.2,

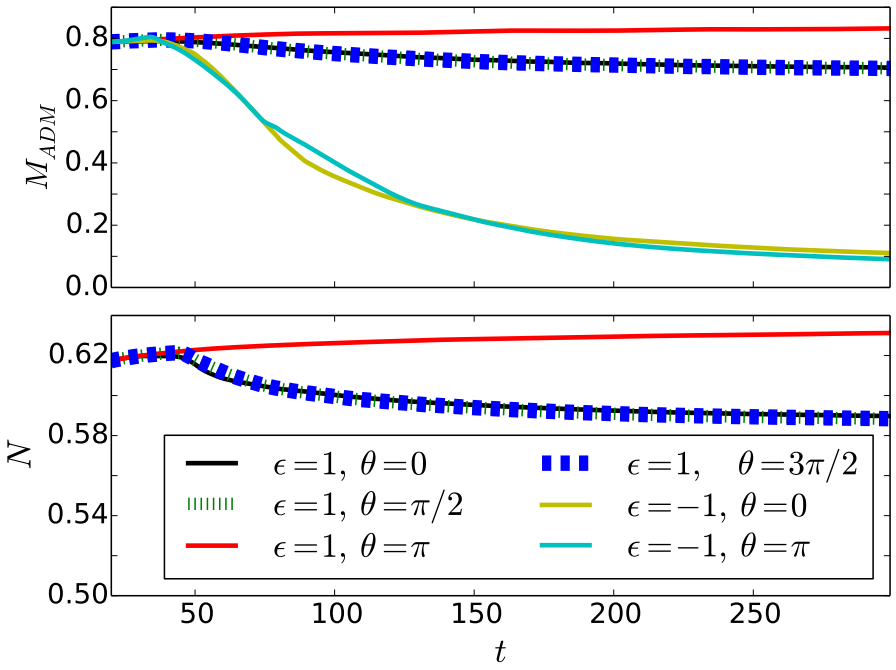

FIGURE 5.2: *Head-on binary collisions.* **ADM** mass and Noether charge as a function on time for the different cases studied. The boson-boson binaries merging into a single one losses approximately a 5% of their initial mass and Noether charge. In contrast, the boson-antiboson binaries annihilate during the merger, radiating most of the scalar field (and the corresponding mass). The total Noether charge for the boson-antiboson cases is zero through all the evolution.

for these cases the **ADM** mass and Noether charge remain roughly constant during the evolution.

(c) **B-aB(0), B-aB(π):** the dynamics is initially similar to the other cases, until that the stars make contact. The scalar field interactions of a boson-antiboson annihilates each other during the merger for the two opposite phase shifts considered here. This can be explained from the total conservation of the Noether charge. As the binary is formed by a **BS** with boson particles and another **BS** with boson anti-particles, their initial Noether charge is zero. Therefore, the only way to conserve the Noether charge during its merger is to annihilate each other. As it is diplayed in the top panel of Fig. 5.2, the **ADM** mass quickly decreases its value after the merger, indicating that the system losses all its matter: most of the scalar field is radiated away to infinity, and only a small fraction remains near the region of the collision (i.e., see the last panels of 5.3).

5.4.3 Orbiting collisions cases with angular momentum

The initial data for the orbiting cases is constructed as described in section 5.3 for boosted identical stars. It means, once the solution is written in Cartesian coordinates,

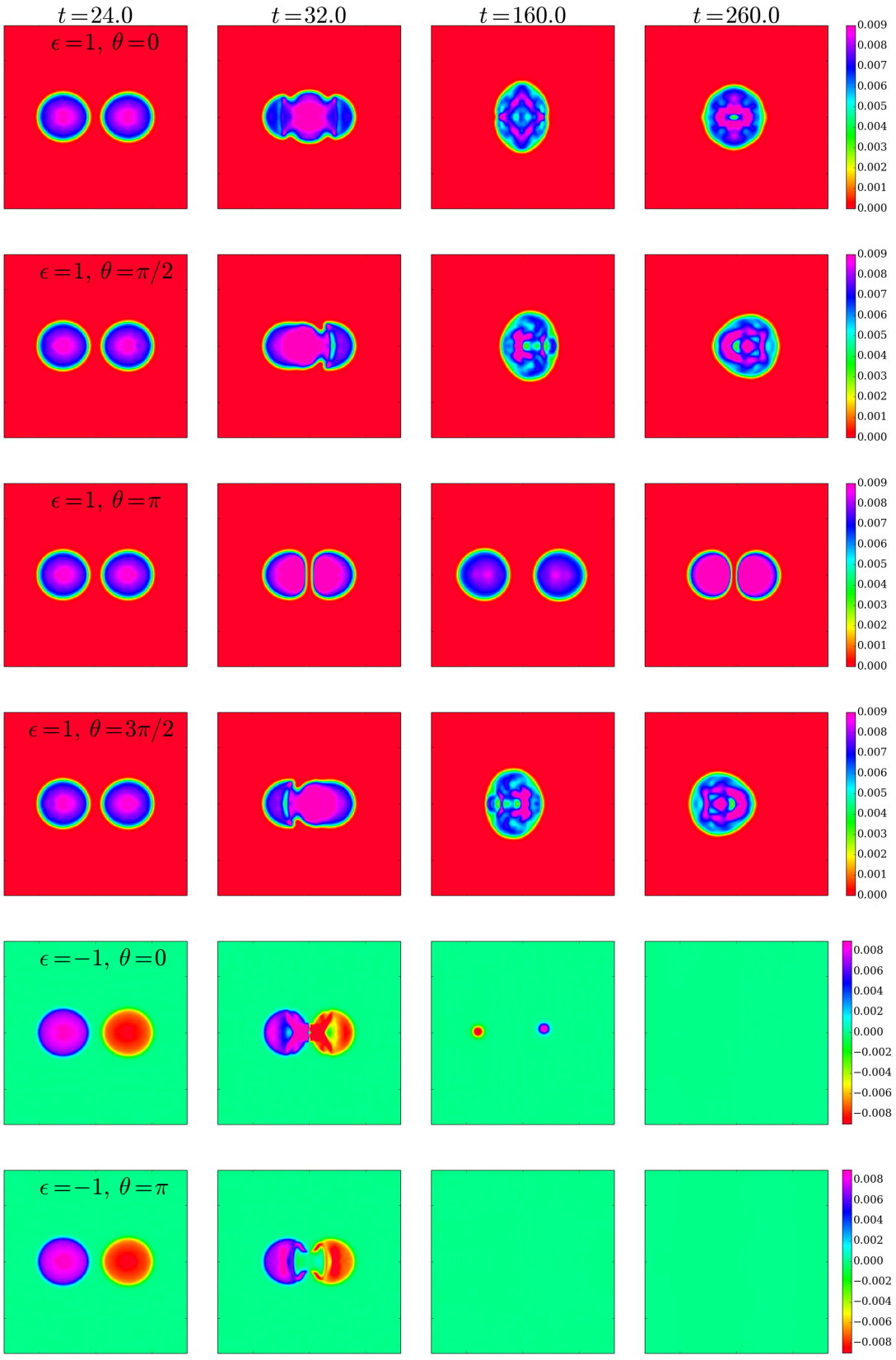

FIGURE 5.3: *Head-on binary collisions.* Time snapshots of the Noether charge in the plane $z = 0$. Each row corresponds to the different B-B(θ) and B-aB(θ) cases studied here. The collision of the stars happens approximately at $t = 28$. The result of the B-B is a single boson star except in the case of B-B(π). The stars in the B-aB case annihilate each other during the merger.

centered at some position x_c, we perform a Lorentz transformation to each **BSs** solution along the x-direction with velocity v_x, namely $\{g^{(i)}_{ab\,\mathrm{boost}} \equiv g^{(i)}_{ab}(x^j - x^j_c, v_x), \Phi^{(i)}_{\mathrm{boost}} \equiv \Phi^{(i)}(x^j - x^j_c, t, v_x)\}$. Finally, superpose the two boosted solutions for each of the two stars:

$$\Phi = \Phi^{(1)}_{\mathrm{boost}} + \Phi^{(2)}_{\mathrm{boost}}, \tag{5.19}$$

$$g_{ab} = g^{(1)}_{ab\,\mathrm{boost}} + g^{(2)}_{ab\,\mathrm{boost}} - \eta_{ab}\ . \tag{5.20}$$

They stars are centered at $(0, \pm 4, 0)$ and we consider different Lorentz boost velocities $v = \{0, 0.05, 0.10, 0.15\}$ along the x-direction, i.e, we induce an initial angular momentum into the system. The last case corresponds to a binary almost in quasi-circular orbit.

We will describe the dynamics of the orbiting binaries. Few snapshots of the evolutions are displayed in Fig. 5.5, whereas the **ADM** mass, the Noether charge and the angular momentum are shown in Fig. 5.4.

(a) $\boldsymbol{v_x = \{0, 0.05, 0.10\}}$: these three cases behave in a similar way. As the evolution proceeds, the stars approach to each other. Furthermore, as the initial velocity (and the angular momentum) increases, the stars orbit around each other for a longer time, merging into a rotating remnant that loses its angular momentum and settle down to a non-rotating boson star.

(b) $\boldsymbol{v_x = 0.15}$: here, the system is in quasi-circular orbit. The prompt radiation of angular momentum here is most extreme due to the following reason: after the merger, two blobs of scalar field are ejected from the system at speed $0.6c$, carrying a small fraction of the mass and boson number but a large amount of angular momentum (i.e., see $t = 80$ of the $v = 0.15$ in Figure 5.5, and the sudden drop of angular momentum in Fig. 5.4).

In summary, all these cases with angular momentum merge and form a rotating bar that quickly losses angular momentum and settles down to a non-rotating **BS**. Although the system only losses a small fraction of the mass during the coalescence, all the angular momentum is emitted by gravitational waves and scalar field radiation soon after the merger.

This behavior of the remnant, which approaches quickly to a non-rotating **BS**, might be a consequence of two combined effects:

(i) the quantization of the angular momentum $J_z = kN$ (being k an integer) of rotating **BSs**, that prevents stationary solutions with an arbitrary angular momentum [186]. Moreover, the resulting star from the merger should have at least

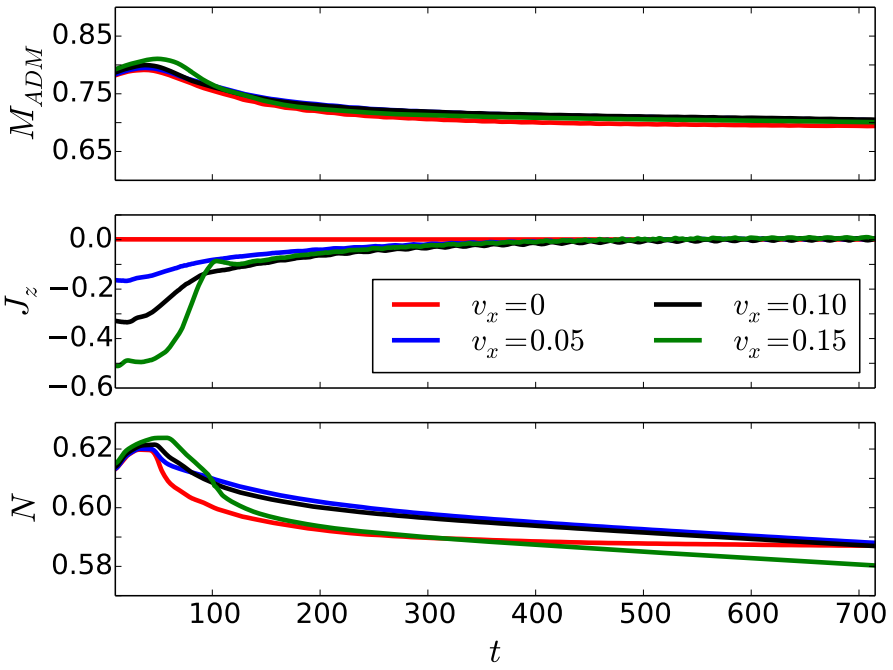

FIGURE 5.4: *Orbital binary collisions.* **ADM** mass (top pannel), angular momentum J_z (middle panel) and Noether charge (bottom panel) as a function on time for the different tangential boost velocities. During the coalescence approximately 5% of the mass and Noether charge is lost, and almost all the angular momentum.

$J_z^{rot}(k=1) \approx 0.62$ in order to correspond to a stable rotating boson star (see the bottom panel of Fig. 5.4 at $t \approx 50$). Although the (adimensional) angular momentum of the system $J_z/M^2 \approx 0.78$ is larger than $J_z^{rot}(k=1)$, the system does not relax to that state but instead it prefers to decay to the one with the lowest angular momentum $k=0$.

(ii) the rigid structure of the remnant may present difficulties for the scalar field to organize itself into a stable, rotating boson star configuration. In particular, the rotating boson star is harmonic both in time and azimuth angle with the level sets of its magnitude being toroidal. This structure contrasts with a rotating neutron star which can have a range of either rigid or differential rotational profiles.

Also, another possibility is that the first rotating configuration ($k=1$) is unstable in the high-compactness regime explored here (see Ref. [187] for a discussion of the stability of less compact rotating **BSs**). As it is shown in Fig. 5.1, the mass and the compactness are very steep functions of the central scalar field, and it is therefore possible that spinning solutions exceed the maximum mass when their non-spinning counterparts are close to such a maximum. If this is the case, the unstable spinning solution would not be formed dynamically and we expect the outcome to be a non-spinning **BS** or a **BH**, in agreement with the results of our simulations.

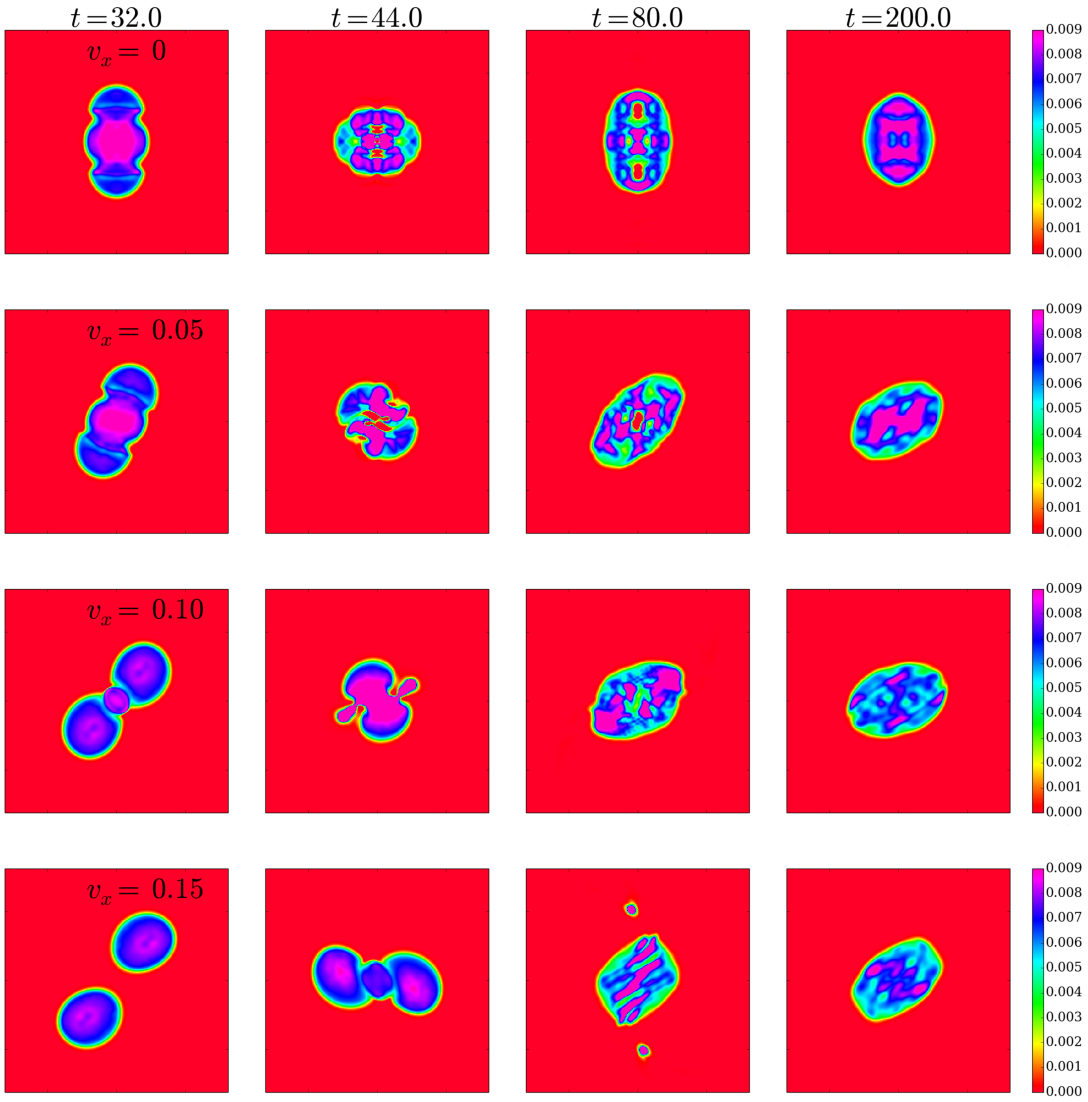

FIGURE 5.5: *Orbital binary collisions.* Noether charge in the plane $z = 0$ for the different boost velocities $v = \{0, 0.05, 0.10, 0.15\}$. The merger between solitonic boson stars happens approximately at $t \approx 30$ for the cases $v = \{0, 0.05, 0.10\}$ and at $t \approx 40$ for the quasi-circular orbit case $v = 0.15$. For the latter case, after the merger two blobs of scalar field take away a large fraction of the angular momentum from the system.

Although this seems in contradiction with the results in [167], where a rotating boson star seemed to be produced, there are two important differences. First, these stars are much more compact, so the dynamics might be more dominated by non-linear effects. Second, due also to the high compactness, the dynamics is faster (i.e., the crossing time is shorter), so we can follow the evolution until a stationary state is achieved, which might not had been possible with the mini-boson stars.

Finally, the evolution of some constraints is displayed in Fig. 5.6, showing that they are small and kept under control during all the simulation.

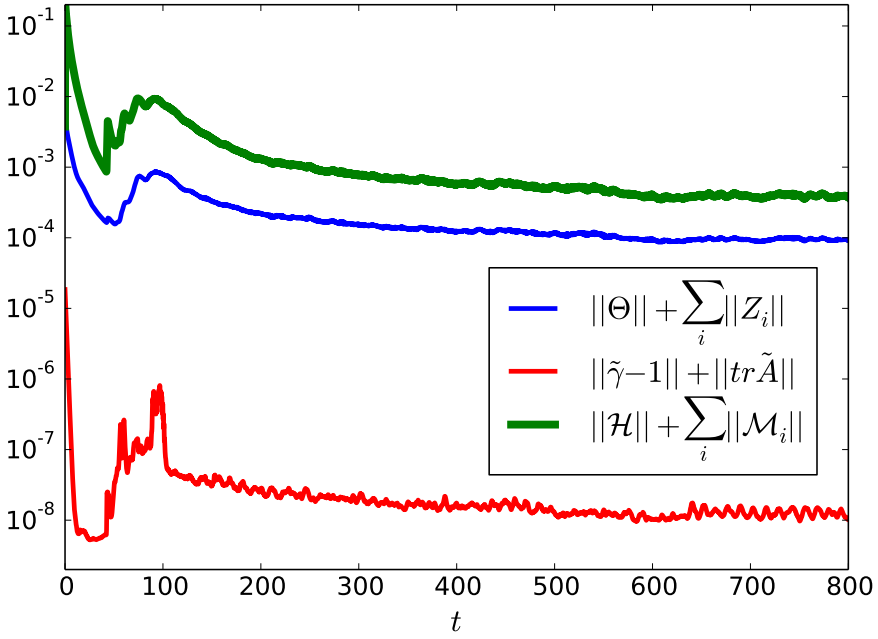

FIGURE 5.6: *Orbital binary collisions.* L_2-norm of physical (blue solid line), the conformal (redd solid line) and the energy-momentum (green solid) constraints as a function of time. With our choice of the damping parameters, all the constraints are perfectly under control during all the simulation.

5.5 Gravitational waves from binary Boson Stars

In this section we analyze the dynamics of binary **BSs**, initially in quasi-circular orbits, as a function of their individual compactness. For concreteness, we consider four binary systems composed of **BSs** on the stable branch with compactness ranging from $C \approx 0.06$ to $C \approx 0.22$ (i.e., see Figure 5.1 and Table 5.1). Notice that all the stars have been rescaled as described in Subsection 5.3 such that their individual masses in isolation are $M = 0.5$, so that the binary has approximately a total initial mass $M_0 \approx 1$. The positions and velocities of each binary system considered in this work, together with other parameters of our simulations, are presented in Table 5.2.

5.5.1 Numerical setup

We adopt the same numerical setup and infrastructure explained in the previous Section 5.4.1. Our simulations are performed in a domain $[-264, 264]^3$ with a coarse resolution of $\Delta x_0 = 4$ and either 7 or 8 levels of refinement, the last one only covering each star, such that the finest resolution is $\Delta x_7 = 0.03125$. Again, we analyze several relevant physical quantities from our simulations, such as the **ADM** mass, the angular momentum, and the Noether charge. Additionally, we compute the gravitational radiation emitted during the coalescence considering the Newman- Penrose scalar Ψ_4 (2.105) defined in section 2.4.1. **GWs**, the **ADM** mass, and the angular momentum are computed as spherical surface integrals at different extraction radii.

C	$y_c^{(i)}$	$v_x^{(i)}$	M_0	J_0	$t_{\rm contact}$	remnant	M_r	R_r^N	f_r	$M_r\omega_r$	$E_{\rm rad}/M_0$	$\mathcal{E}_{\rm rad}/M_0$
0.06	± 9	± 0.140	1.07	1.32	950	BS	0.90	8.9	0.0207	0.117	0.075	0.029
0.12	± 5	± 0.210	1.18	1.24	300	BS	0.98	4.6	0.0311	0.203	0.085	0.057
0.18	± 5	± 0.214	1.29	1.40	330	BS	1.07	2.5	0.0489	0.329	0.120	0.086
0.22	± 5	± 0.220	1.46	1.65	218	BH	1.42	–	0.0560	0.500	0.030	0.10

TABLE 5.2: *Characteristics of binary **BS** models and properties of the final remnant.* The entries of the table are, respectively: the compactness C of the individual **BSs** in the binary, the initial positions $y_c^{(i)}$, the initial velocities of the boost $v_x^{(i)}$, the initial total **ADM** mass M_0, the initial total orbital angular momentum J_0 of the system, the time of contact of the two stars t_c, the final remnant, the final total **ADM** mass M_r, the averaged final radius of the remnant star R_r^N (i.e., containing 99% of the total Noether charge), the frequency f_r of the fundamental mode of the remnant, its dimensionless value $M_r\omega_r$ (where $\omega_r = 2\pi f_r$), the total radiated energy in gravitational waves for each simulation $E_{\rm rad}$ (i.e., integrated from the beginning and extrapolated to large times after the merger) and the one estimated analytically $\mathcal{E}_{\rm rad}$ as described in appendix A.1. The final angular momentum of the **BS** remnant tends to zero quite rapidly. The final (dimensionless) angular momentum of the **BH** obtained in the $C = 0.22$ case is $J_r/M_r^2 \approx 0.64$.

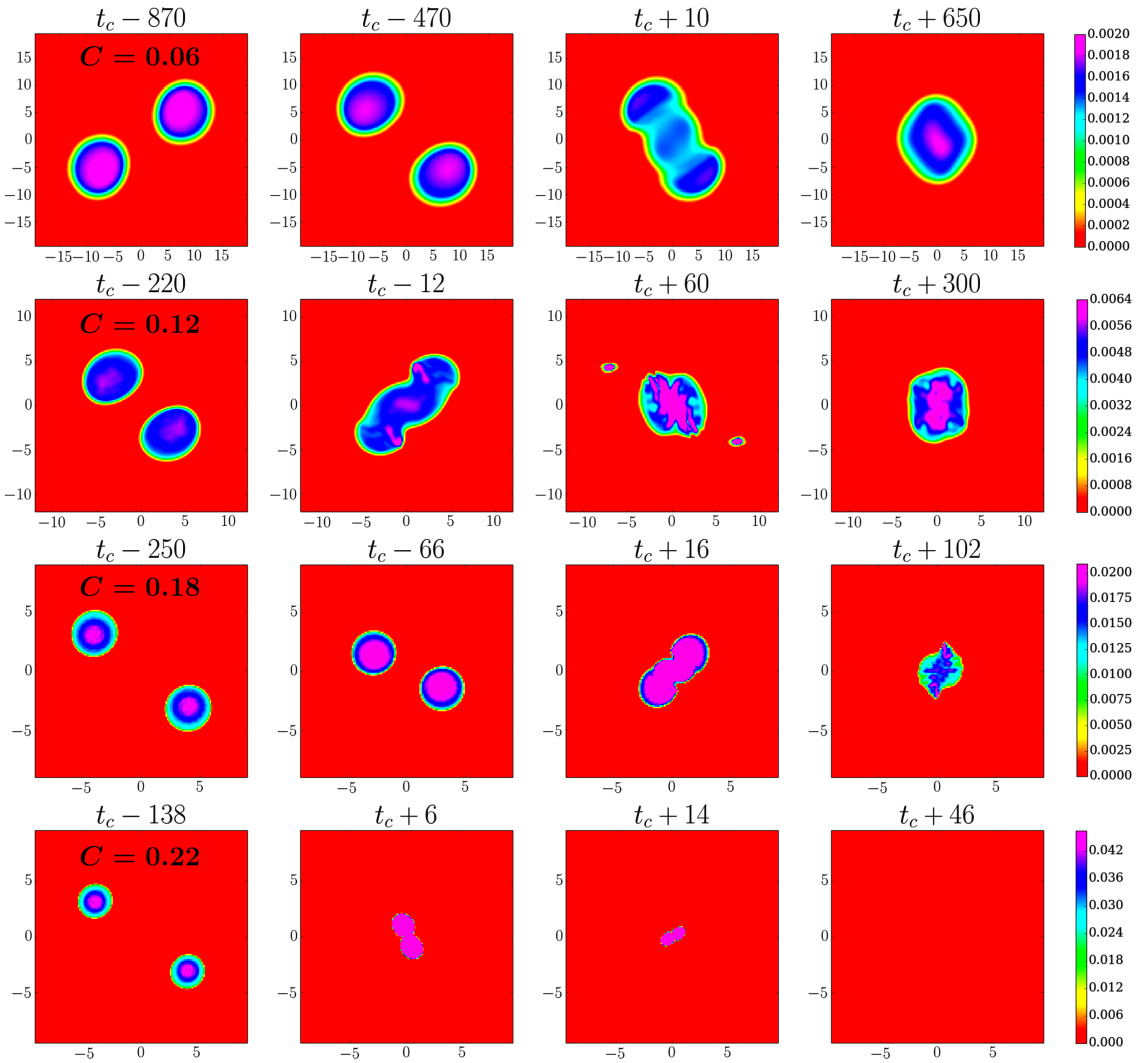

FIGURE 5.7: *Coalescence of binary **BSs***. Snapshots in time of the Noether charge density in the orbital plane. Each row corresponds to the different compactness (from top to bottom, 0.06, 0.12, 0.18, and 0.22). The collision of the stars happens at different times due to the different initial conditions and compactness of each case. Note the emission of two scalar blobs in the third panel of the $C = 0.12$ case.

5.5.2 Dynamics

Some snapshots of the Noether charge density and the norm of the scalar field during the binary coalescence are displayed in Figs. 5.7 and 5.8, respectively. The early part of the inspiral is qualitatively similar for all cases, with the stars completing at least one orbit before they make contact.

Notice that, the initial boost velocities, required to set the binary system roughly in a quasi-circular orbit, are different for each case due to several reasons. The largest difference appears for the case with $C = 0.06$ because the radius of the stars (i.e., and, consequently, their initial separation) is significantly larger than in the other cases, implying a lower boost velocity. Since the separation in all the other binary configurations

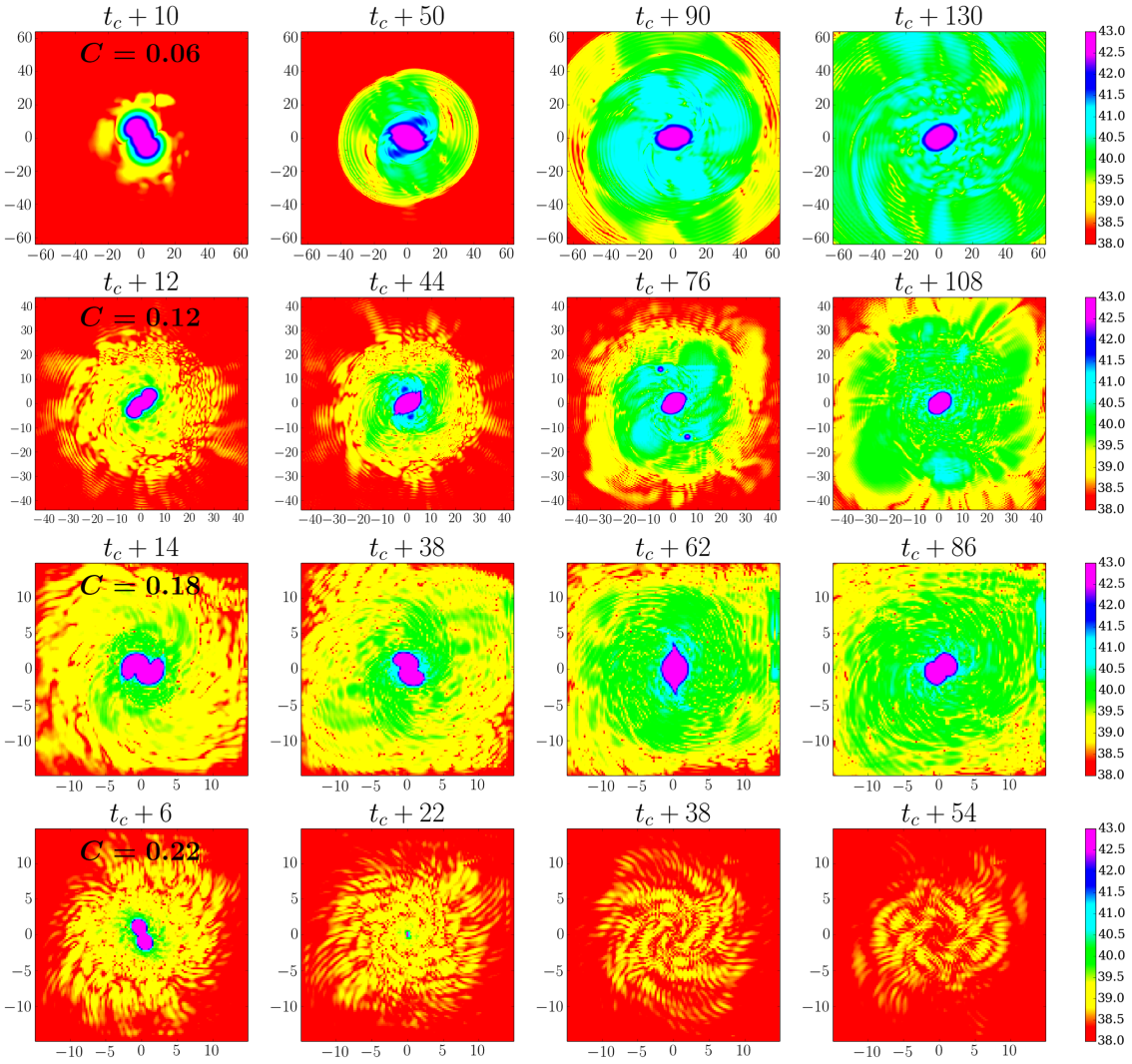

FIGURE 5.8: *Coalescence of binary **BSs***. Time snapshots of $||\Phi||$ in the plane $z = 0$ in log-scale. Each row corresponds to the different coalescence of **BSs** cases studied here. In each case the scalar field emitted during the evolution increases after the merger.

is the same, discrepancies on the boost velocities arise from slight differences on the star's compactness and total mass of the system. Consequently, the **GWs** produced during the earlier stages of the inspiral will be weaker than the corresponding stage of the larger compactness cases.

Once the stars make contact, scalar field interactions play a significant role in the dynamics of the remnant and nonlinear effects due to the scalar potential becoming significant. The combination of gravity forces and matter interactions produces a compact, rotating remnant immediately after the merger. The final fate of this remnant will depend both on the potential and on the location of the solution within the stable branch, that is, on how far from the unstable branch this specific configuration is. This distance can be parametrized in different ways, such as the fraction $M/M_{\max}$ (where $M_{\max}$ is

the maximum allowed mass on the stable branch) or, equivalently, on the initial stellar compactness.

Our results indicate a transition between binaries with small compactnesses with those of larger compactness. In particular, the critical compactness, C_T, appears to be somewhere in the range of $0.18 - 0.22$. This transition is roughly estimated by the fact that twice the individual **BS** mass above the critical value exceeds the maximum stable **BS** mass, suggesting that any remnant (less any radiated scalar field) would be unstable. We can distinguish two different behaviors depending on the initial compactness, separated by this transition value:

- $C \lesssim C_T$: the remnant is a largely perturbed **BS**, the angular momentum of which decreases through dispersion of scalar field and gravitational radiation, settling down into a non-rotating **BS**. Furthermore, for the case with $C = 0.12$, as already observed previously in Section 5.4.3 (see [111]), the angular momentum of the remnant is further reduced through the ejection of two "rather cohesive" scalar field blobs soon after the merger (see third panel, second row in Fig. 5.7).
- $C \gtrsim C_T$: the remnant mass exceeds the maximum mass and promptly collapses to a **BH** with approximately the mass and angular momentum of the system at the merger time. There is some scalar field surrounding the **BH** that carries angular momentum and is being either slowly dispersed to larger distances or falling into the **BH**.

The evolution of the **ADM** mass, angular momentum, and Noether charge are illustrated in Fig. 5.9. The binaries show only a significant loss of **ADM** mass near the merger due to scalar field dispersion/ejection and energy carried away by **GWs**. Similar behavior is reflected in the total Noether charge, when the remnant does not collapse to a **BH**. Since the Noether charge is a conserved quantity, the fact that it remains mostly constant further supports the reliability of our simulations.

Notice however that the case $C = 0.18$ shows peculiar behavior in its mass and angular momentum after merger when compared to the other cases. A close inspection of the dynamics of this case shows that large gradients develop that are not accurately tracked by the finest resolution we have allowed our adaptive grid to achieve. Indeed, it appears the system explores a near-threshold regime which is not correctly captured by our simulations and we consider the post-merger period of this case to be unreliable. Nevertheless, for reference and comparison purposes we include it in the overall discussions since, in any case, its pre-merger behavior is informative.

Angular momentum during the early inspiral is radiated mainly through **GWs**. Near the merger stage there is dispersion (and in some cases, also ejection) of scalar field, which also carries away a significant fraction of the angular momentum (notice the sharp decrease in the middle panel of Fig. 5.9). After the merger, the final object is much more compact than the initial stars and rotates rapidly, emitting **GWs** more copiously than the late inspiral. When the remnant is not a **BH**, the system radiates angular momentum until settling down to a non-rotating **BS**.

Of particular interest is the case $C = 0.12$ due to the presence of two blobs of scalar field that are ejected from the remnant at speed $v \approx 0.6c$, as already mentioned in the previous section 5.4.3. The formation of two peaks in the Noether charge density during the merger is common for all studied cases, but only for this compactness are they able to detach from the star while maintaining – at least temporarily – their character (i.e., its Noether charge). As can be surmised from Fig. 5.9, these blobs carry away little mass ($M_{\rm blob} = m_b N_{\rm blob} \approx 0.025$) but a significant fraction of angular momentum. A Newtonian estimate, assuming the distance from the blobs to the plane of symmetry is $L \approx 7.5$, yields $J_z \approx 2 M_{\rm blob} v L \approx 0.2$, consistent with the additional decrease of angular momentum displayed in the $C = 0.12$ case with respect to the $C = 0.06$ configuration, as shown in the middle panel of Fig. 5.9.

We can gain some insight into the ejection of these blobs by examining some characteristic speeds in the problem. A simple calculation shows that the Newtonian angular orbital frequency Ω_c when the two identical stars first make contact is

$$\Omega_c \approx \frac{C^{3/2}}{2\, M_0}\,, \tag{5.21}$$

where C is the compactness of the individual stars and M_0 is the total initial mass of the system. Notice that the blob velocity ($0.6c$) is considerably larger than the maximum velocity $v_c = \Omega_c(2R) \approx 0.35c$ predicted by this rotational rate for solid body rotation. Similarly one can compute the velocity associated with rotation at the angular frequency of the remnant[3]. By using the values of Table 5.2 for the case $C = 0.12$ one can obtain that the orbital frequency of the remnant is $\Omega_r = \pi f_r = 0.098$ and its radius is $R_r = 4.6$. The velocity of the remnant, $v_r = \Omega_r R_r \approx 0.45c$, also does not reach the level of the blob velocity.

However, these blobs are ejected during the time when the binary is transitioning from first contact to quasinormal ringing. As such, the characteristic angular frequency and radius change $\Omega_c \to \Omega_r$ and $2R \to R_r$. At some point during this transition the frequency and the radius might be large enough so that some of the scalar field might move with

[3]Remember that there is a factor two between the orbital frequency Ω_c and the gravitational one ω_c, namely $\omega_c = 2\Omega_c$

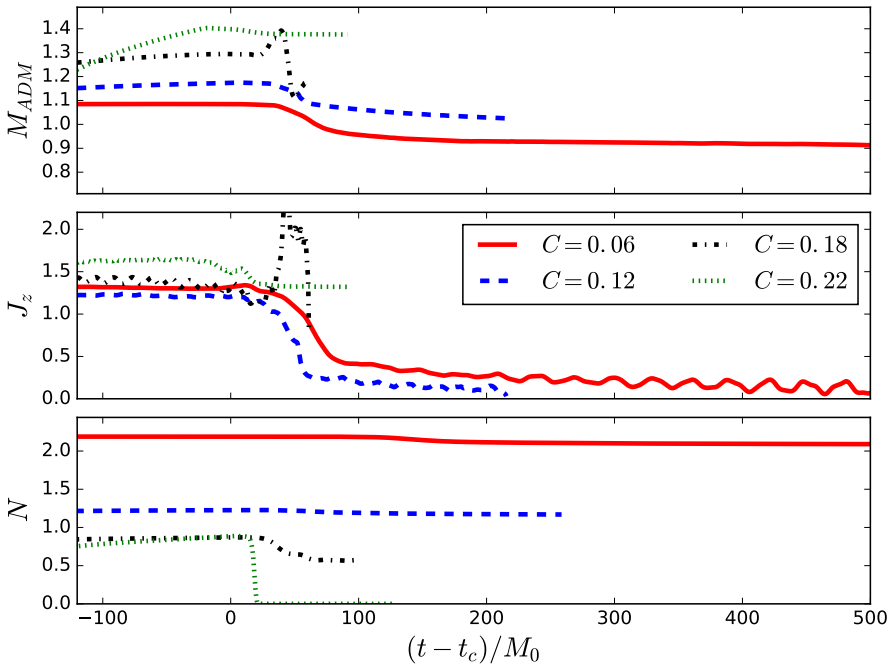

FIGURE 5.9: **ADM** mass (top), angular momentum J_z (middle) and Noether charge (bottom) as a function on time for the different binaries. During the coalescence the less compact cases (i.e., $C = 0.06$ and $C = 0.12$) lose only a small percentage of their initial mass and Noether charge, but almost all their angular momentum. The case $C = 0.18$ as discussed is suspect. The most compact case $C = 0.22$ case collapses to a **BH** after the merger, so the mass and angular momentum do not change significantly.

a speed larger than the escape velocity $v_{\rm esc} = \sqrt{2C}$ of the star. If this occurs, then it is conceivable that some amount of scalar field may be ejected from the remnant at such a speed.

5.5.3 Gravitational wave signal

The merging binaries produce **GWs** measured by the Newman-Penrose Ψ_4 (2.102) scalar, as displayed in Fig. 5.10. In Fig. 5.11 we also show the corresponding strain. Notice that the amplitude and the time scale of the strain has been rescaled with the total initial mass, and the time has been shifted such that the contact time [4] occurs at $t = 0$.

With these waveforms, we can look for the effect of compactness on the gravitational wave signal. Starting with the least compact case ($C = 0.06$), it radiates the least in the inspiral. The weakness of its inspiral signal results because its stellar constituents have the largest radii and thus they make contact at the smallest frequency of these four

[4] Defined as the time at which the individual Noether charge densities touch for the first time, roughly at a distance $2R_N$ between the stars centers.

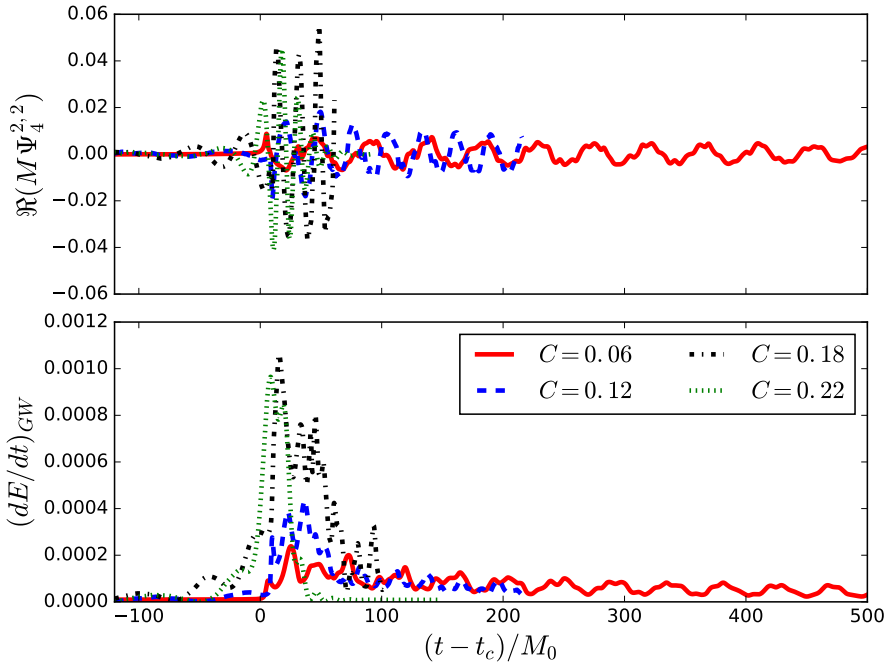

FIGURE 5.10: (Top panel) The real part of the main $l = m = 2$ mode of the Ψ_4 describing the gravitational emission of the different binaries, as a function of time. (Bottom panel) The energy radiated by the main gravitational wave modes $m = \pm 2$.

cases. As the compactness increases, the late inspiral occurs at higher frequencies and the signal becomes stronger.

Once the stars make contact, both scalar field interactions and gravitational forces determine the dynamics and tend to homogenize the scalar field profile. This period is very dynamical, producing a rapidly rotating compact remnant that radiates strongly in gravitational radiation with an amplitude and frequency much larger than during the inspiral. This contrast between pre-merger and post-merger signals is particularly marked for the two low compactness binaries, but becomes less so with increasing compactness. This trend indicates that this contrast likely results from the disparity between the initial compactness of the boson stars and the compactness of the remnant (see Table 5.2). Notice also that the strain amplitude (Fig. 5.11) does not show such disparate scales as the Newman-Penrose Ψ_4 scalar (Fig. 5.10) due to the additional frequency dependence (see Eq. (2.109)).

A simple estimate of the maximum amount of total energy the system can radiate follows from a model of energy balance presented in [188], and discussed in detail in Appendix A.1. Within some approximations, when the final object is a non-rotating **BS**, the total radiated energy in **GWs** is estimated to be

$$\mathcal{E}_{\rm rad} \approx 0.96\, CM\,, \tag{5.22}$$

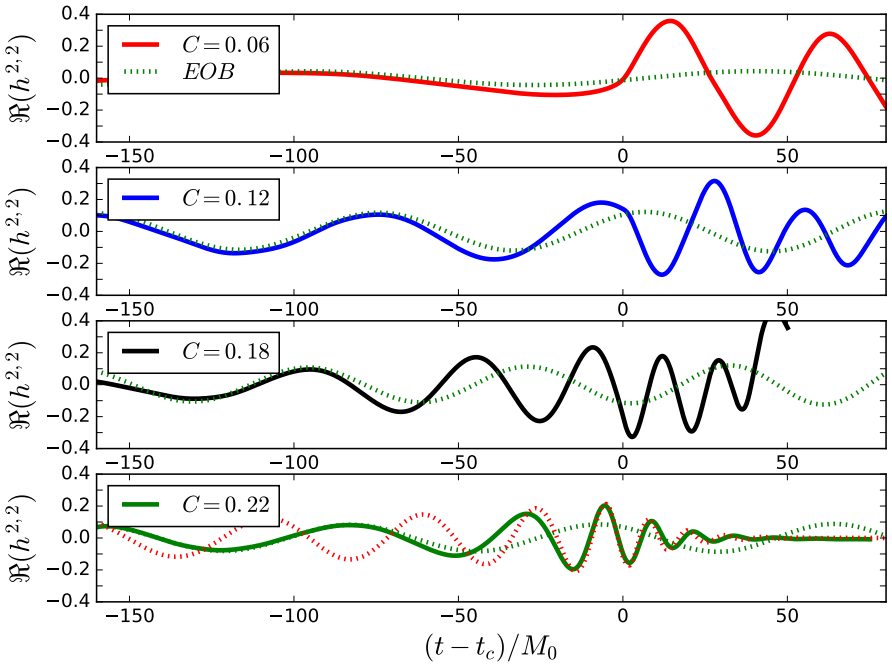

FIGURE 5.11: The main mode of the strain for the different binaries. The time has been rescaled by the initial total **ADM** mass M_0 and shifted such that $t = 0$ corresponds to the maximum of the norm of the mode. The amplitude has been also rescaled with the mass of the system. We have chosen the same range in the axes to make clear the increase in frequency as the stellar compactness also increases. The different cases are qualitatively compared with a recent version of the effective one body (**EOB**) approximation of a quasi-circular binary **BH** coalescence [4] by matching the waveforms at the early inspiral (i.e., notice that an accurate quantitative comparison with **EOB** would require initial data for binaries in quasi-circular orbits with much smaller constraint violations). For the highest compactness $C = 0.22$ we have also matched to the **EOB** waveform at the merger time (dotted red curve).

where M and C are the mass of the system and compactness of the initial stars respectively. This estimate is largely consistent (i.e., within a factor of two) with the results of our simulations, given in Table 5.2, obtained by integrating the gravitational wave luminosity displayed in the bottom panel of Fig. 5.10. Notice that the energy emitted in gravitational waves for the case with $C = 0.12$ exceeds the $\simeq 5\%$ of the total mass M_0 emitted during the analogous coalescence of a binary **BH** system; thus, boson star binaries within suitable range of compactness, can be considered super-emitters in the terminology of [188], i.e., the system emits more than the analogous binary **BH** system.

The most compact cases considered here are also interesting in the context of the recent observations of **GWs** by the **LIGO** detectors. A simple Newtonian calculation shows that the **GW** frequency at the contact of the two stars is $f_c \simeq \Omega_c/\pi$. This relation can be contrasted to the frequency at which the analogous case of binary **BHs** would make a transition from inspiral to plunge. This frequency is well approximated by the innermost stable circular orbit (**ISCO**) frequency of the resulting **BH** produced through the merger [189]. For non-spinning binary **BHs**, a handy expression for the

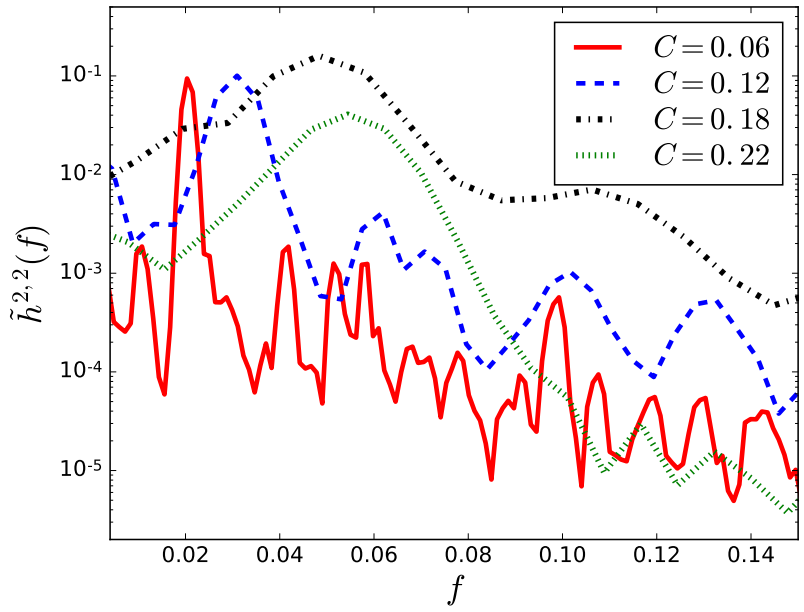

FIGURE 5.12: Fourier transform of the main mode of the strain in the post-merger phase, calculated as $\tilde{h}^{2,2}(f) \equiv \mathcal{F}[h_{22}(t > t_{\rm merger})]$. Note that peak frequency increases with compactness (similar to neutron stars).

ISCO frequency is provided in [188], which indicates that non-rotating **BSs** would have a contact frequency higher than the corresponding **ISCO** frequency for binary **BHs** provided $C \gtrsim 0.27$ (i.e., a compactness higher than any of the ones considered in this work).

For cases not collapsing to a **BH** the gravitational waveforms of the remnants have a rather simple structure with principal modes which can be tied to quasi-normal modes (**QNMs**) of boson stars (see appendices A.1.2 and A.1.1). For cases collapsing to a **BH**, the post merger gravitational wave signatures are captured well by the familiar ring-down behavior of a **BH**. We however note that the angular momentum of the remnant **BH** is slightly less than that of the analogous binary **BH** merger. Because the **BH** pair merges well within the system's **ISCO**, much of the angular momentum is trapped within the remnant. In contrast, the **BS** binary, being less compact and merging at a lower frequency than the **BH** binary, allows for the radiation of more angular momentum during the merger. Recall also that tidal effects introduce modulations in the (late) inspiral waveforms (e.g. [8, 190]) but such modulations become smaller for higher compactness (see the tidal Love numbers in Table 5.1).

To examine in more detail the after-merger behavior, we analyze the strain in the frequency domain. The Fourier transform of $h_{22}(t > t_{\rm merger})$ is shown in Fig. 5.12, where $t_{\rm merger}$ is defined as the time where the strength of the **GW** is maximum. For $C < C_T$

the final remnant rotates and oscillates while settling down to a (non-rotating) stationary configuration, producing **GWs** at certain frequencies. Clearly, the frequency of the main peak increases with the compactness of initial objects in the binary. These post-merger frequencies, reported in Table 5.2, can be fit in terms of the contact frequencies, namely

$$M_r\omega_r = 0.064 + 1.72\, M_0\omega_c \quad . \tag{5.23}$$

On the other hand, we can compare with the fit obtained for neutron stars [5, 191], that in the same units reads

$$M_r\omega_r = -0.136 + 2.96 \left(\frac{M}{2.7M_\odot}\right) M_0\omega_c \ , \tag{5.24}$$

These relations (i.e., with $M = 2.7M_\odot$ in Eq. (5.24)), together with the observed frequencies, are displayed in Fig. 5.13. The best fit lines have quite different slopes and intercepts, but for high compactness stars they produce similar frequencies. The difference in these frequencies implies that remnant **BSs** and **NSs** are potentially distinguishable with **GW** spectroscopy if either (i) a large enough **SNR** is achieved by increasingly sensitive detectors or (ii) a sufficient number of events can be combined (i.e., stacked) [192, 193].

Quite interesting is the comparison of the main gravitational wave mode (i.e., $l = m = 2$) with the quasi-normal modes of single isolated stars, displayed in Fig. 5.14 and discussed in more detail in Appendix A.1.2. Clearly, the frequencies of the remnant agree very well with the frequencies of the fundamental quasi-normal mode of single non-rotating boson stars, providing further evidence that these cases produce non-rotating, remnant **BSs**.

For $C > C_T$ the final remnant is a rotating **BH**, and its post-merger signal shows the characteristic ring-down signal. For such a case, a significant amount of energy corresponding to the rotational energy of the **BH** is retained after merger, which contrasts with the cases producing a remnant non-rotating boson star. For the **BH** case we can calculate both the frequency and the decay rate of the gravitational wave signature, which can be obtained by fitting the post-merger strain signal to

$$h_{22}(t) \approx e^{-\sigma t}\cos(2\pi f t) \quad . \tag{5.25}$$

We find that $\sigma = 0.049 \pm 0.003$ and $f = 0.056 \pm 0.002$. The final mass and angular momentum of the **BH**, calculated asymptotically at a spherical surface of radii $R = 50$, are $M_r \approx 1.42$ and $J_r \approx 1.3$ respectively. Therefore, one can also calculate from linear theory the quasi-normal-mode frequencies for a **BH** with final dimensionless spin $a_r = J_r/M_r^2 \approx 0.64$. For this spin, a perturbative calculation yields

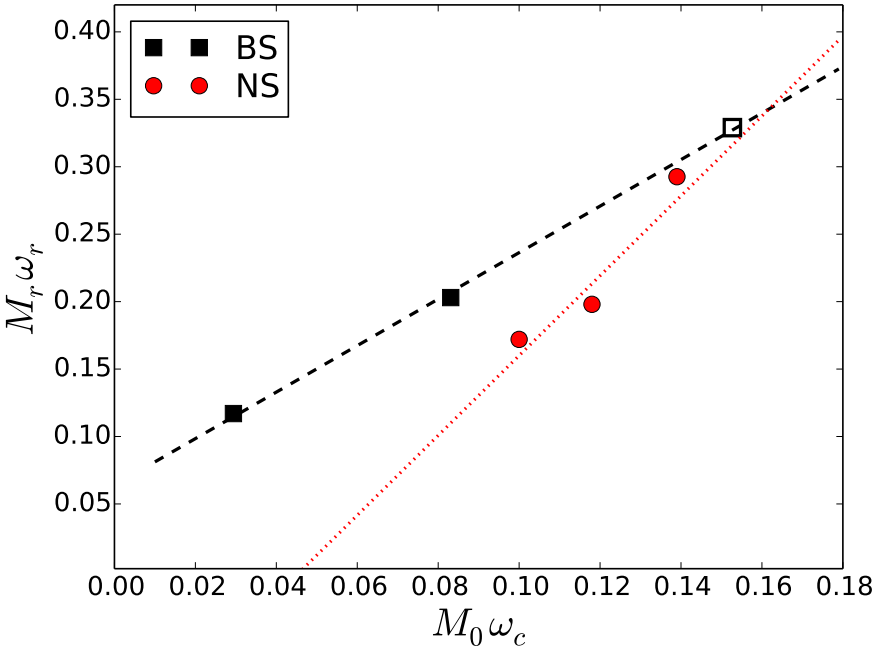

FIGURE 5.13: Relationship between the (gravitational) contact angular frequency ω_c and the (gravitational) angular frequency of the fundamental mode of the remnant ω_r for the **BS** binaries considered here. For comparison, we include the neutron star cases studied in [5]. The case $C = 0.18$ is included for reference as an unfilled square.

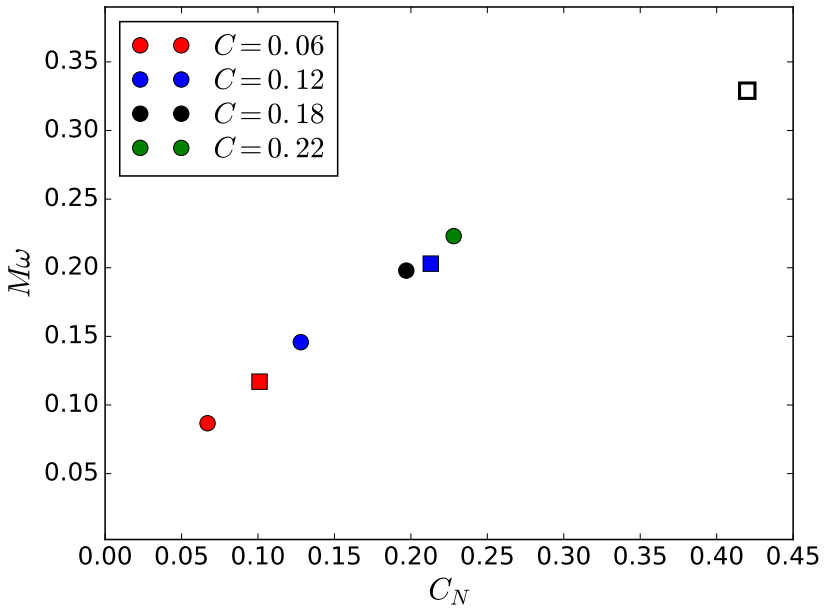

FIGURE 5.14: Comparison between the frequencies of the fundamental quasi-normal mode of single **BSs** in isolation (circles) and the gravitational frequencies of the merger remnant (squares), as a function of the compactness $C \equiv M/R_N$ (the case $C = 0.18$ is included for reference as an unfilled square) where R_N is the radius containing 99% of the Noether charge. The good agreement between these frequencies suggests that the remnant is indeed a perturbed non-rotating **BS** ringing down to a quiescent one.

$M_r\omega_{\rm QNM} = 0.50819 - 0.082748i$ [194, 195], in very good agreement with the value obtained from the fit $M_r(2\pi f - i\sigma) \approx 0.5 - 0.07i$. The small deviations might be due either to inaccuracies in the extraction of the final **BH** mass or to a sub-leading effect of the scalar field during the post-merger.

5.6 Discussion

In this Chapter, we have studied binary solitonic boson stars systems with and without angular momentum by performing 3D numerical simulations (using our modified version of the **CCZ4** studied in Chapter 2 coupled to **KG** evolution equation seen in Chapter 3, and the numerical methods explained in Chapter 4. All the binary systems considered were constituted by two equal-mass solitonic boson stars.

- **Head-on cases:** we allowed for non-identical boson stars with different rotation and shift phase. Our simulations show that the merger of a boson-boson binary leads, in general, to another solitonic boson stars. However, when the phase shift approaches π, the scalar field interaction is repulsive and stronger than gravity, preventing the merger of the two stars. The merger of a boson star and an anti-boson star completely annihilates each other for any of the phase shifts considered. This behavior, combined with the results described in [166, 167], allow us to hypothesize that the generic behavior during the collision of a boson and an antiboson star is the annihilation of both, independently on the interaction potential and the phase shift, producing large amounts of unbound scalar field that is radiated to infinity.

- **Orbital cases:** our studies with identical boson stars revealed that the merger always lead to the formation of a black hole for massive ones and for low massive a rotating bar which sheds quickly all its angular momentum by emitting scalar field and gravitational waves, to finally relax into a non-rotating boson star. This inability to form a rotating boson star from a merger might be due to the angular momentum quantization of the rotating solutions. Of particular interest is the case with the highest angular momentum considered, leading roughly to a system in quasi-circular orbits. In this case, soon after the merger, two blobs of scalar field, carrying away small amount of Noether charge but a large fraction of angular momentum, were expelled from the remnant at fraction of speed of light, $v = 0.6c$.

- **Gravitational radiation:** Gravitational waves emitted during the coalescence of these binaries show that for low-compactness **BSs** ($C < C_T$), the maximum strength achievable in the inspiral phase is rather weak but it rises rapidly during

merger with a significant amount of radiated energy during that phase. For high-compactness **BSs** ($C > C_T$), a more monotonic transition of the radiated power –as judged in the rate of upward frequency sweep– is observed between inspiral and merger phases. The final object promptly collapses to a **BH** and the post-merger gravitational wave is dominated by the typical ring-down of a spinning **BH**.

For the less compact cases with $C < C_T$, the main mode in the post-merger gravitational radiation is given by the fundamental quasi-normal frequency of the non-rotating boson star. This is in contrast with the behavior manifested in binary neutron stars (that do not collapse promptly to a **BH**), where the main mode is linked to the rotation of the newly formed (hyper) massive neutron star. Nevertheless, in both cases, the main mode can be linked to the contact frequency by a rather simple linear relation. Importantly for efforts to try and distinguish binary boson stars from binary neutron stars with gravitational waves, the relation is sufficiently distinct to be probed by third-generation detectors and/or the combination of multiple events in **aLIGO/Virgo**.

Chapter 6

Dark Stars

Gravitational wave astronomy might allow us to detect the coalescence of low-brightness astrophysical compact objects which are extremely difficult to be observed with current electromagnetic telescopes. Besides classical sources like black holes and neutron stars, other candidates include exotic compacts objects (**ECOs**), which could exist in theory but have never yet been observed in Nature. Among different possibilities, here we consider Dark Stars (**DSs**), astrophysical compact objects made of dark matter such that only interact with other stars through gravity. We study numerically the dynamics and the gravitational waves produced during the binary coalescence of equal-mass Dark Stars composed by bosonic fields. These results are compared both with Post-Newtonian (**PN**) approximations and with previous simulations of binary boson stars, which interact both through gravity and matter. Our analysis indicates that Dark Boson Stars belong to a new kind of compact objects, representing stars made with different species, whose merger produces a gravitational signature clearly distinguishable from other astrophysical objects like black holes, neutron stars and even boson stars.

In this Chapter we review the work done in [196]. It is organized as follows. In Section. 6.1 the model for Dark Boson stars (**DBSs**) binaries is introduced, describing equations of motion, numerical implementation, analysis quantities and the construction of initial data for both isolated and binary **DBSs**. In Section. 6.2, we study numerically the coalescence of binary **DBSs** for different compactness, focusing on its dynamics and the gravitational radiation emitted. Particular attention is paid to the comparison between **DBSs** and **BSs** binaries. In Section. 6.3, we summarize our results and present our discussion.

6.1 Model for Dark Boson Stars binaries

The merger of binary **BSs** has already been studied in several works: head-on and orbital collisions of mini-BSs [166, 167], head-on collision of oscillatons [61, 182], head-on collision of Proca stars [183] and orbital collision of solitonic **BSs** [6, 111]. All these studies have in common that both stars are represented by the same complex scalar field, a feature typical for classical fluid stars. However, it might not be the most realistic model to describe unconnected Bose-Einstein condensates, where the complex scalar field could represent distinct quantized wave functions. Therefore, here we are interested in a different scenario where each star is described instead by an independent complex scalar field. This model generically represents **DSs**, which can be defined as any self-gravitating astrophysical compact objects which only interact through gravity with other stars. Notice that these regular objects behave as black holes, in the sense that they also interact only gravitationally, but present a wider range of possible compactness [48]. Although **DSs** are modeled here with **BSs**, almost any kind of matter, i.e., either fermionic or bosonic, can be used to construct these objects, as far as the stars are represented with different matter species [60]. It is important to stress that any binary formed by stars made with different non-interacting species would behave as Dark Stars –objects that only interact gravitationally–, like for instance the collisions of neutron and axion stars studied recently [197, 198]. Only the tidal properties of **DSs** might depend strongly on its composition.

In the present Chapter, we aim to study the dynamics and the gravitational radiation produced during the coalescence of two **DSs** made by bosonic fields. These binary Dark Boson Stars (**DBSs**) consist on two **BSs** described by two different complex scalar fields, one for each star, satisfying the **EKG** equations. Since the scalar fields of each star are different and there are no potential coupling them, there are only gravitational interactions between both **DBSs**. Our simulations reveal not only the **GW** signature produced during the merger of **DBS** binaries as a function of the star compactness, but also that the final remnant is always either a non-rotating superposition of independent **BS** (i.e., a multi-state **BS** [199]) or a spinning **BH**. For comparison purposes, we employ the potential and the same configurations $C \in [0.06, 0.22]$, used in previous Chapter 5 ([6, 111]) for non-topological solitonic BS [135, 136], to construct our **DBSs**.

6.1.1 Equations of Motion

An arbitrary number of **DBSs** can be modeled by using a collection of N complex scalar fields (i.e., one for each star) interacting only through gravity. The dynamics of such a

system can be described by the following action [1]

$$S = \int d^4x\sqrt{-g}\left(\frac{R}{16\,\pi} - \sum_{i=1}^{N}\left[g^{ab}\nabla_a\bar{\Phi}^{(i)}\nabla_b\Phi^{(i)} - V^{(i)}(|\Phi^{(i)}|^2)\right]\right) , \tag{6.1}$$

where R is the Ricci scalar associated to the metric g_{ab} with determinant g. There are N minimally coupled complex scalar fields $\Phi^{(i)}$, being $\bar{\Phi}^{(i)}$ their complex conjugate and $V^{(i)}(|\Phi^{(i)}|^2)$ the scalar field potential.

We shall consider $N = 2$ in order to study binary systems. The **EKG** evolution equations are obtained by taking the variation of the action (6.1) with respect to the metric g_{ab} and each scalar field $\Phi^{(i)}$, namely

$$R_{ab} - \frac{1}{2}g_{ab}R = 8\pi\left(T^{(1)}_{ab} + T^{(2)}_{ab}\right) , \tag{6.2}$$

$$g^{ab}\nabla_a\nabla_b\Phi^{(i)} = \frac{dV^{(i)}}{d\left|\Phi^{(i)}\right|^2}\Phi^{(i)} , \tag{6.3}$$

where $T^{(1)}_{ab} + T^{(2)}_{ab}$ is the total scalar stress-energy tensor, being

$$T^{(i)}_{ab} = \nabla_a\Phi^{(i)}\nabla_b\bar{\Phi}^{(i)} + \nabla_a\bar{\Phi}^{(i)}\nabla_b\Phi^{(i)} - g_{ab}\left[\nabla^c\Phi^{(i)}\nabla_c\bar{\Phi}^{(i)} + V^{(i)}\left(\left|\Phi^{(i)}\right|^2\right)\right] . \tag{6.4}$$

Henceforward, we will consider a self-potential for each scalar field given by

$$V^{(i)}(|\Phi^{(i)}|^2) = m_b^2\left|\Phi^{(i)}\right|^2\left(1 - \frac{2\left|\Phi^{(i)}\right|^2}{\sigma_0^2}\right)^2 , \tag{6.5}$$

where m_b is related to the scalar field mass and σ_0 is a constant setting the compactness of the star. As we explain in Chapter 4 and Chapter 5, this kind of potential yields to non-topological solitonic boson stars [135, 136], which might have a compactness comparable or even higher than neutron stars [6]. Notice that, with this choice for the potential, each scalar field is explicitly decoupled from the others. Therefore, the scalar field corresponding to each star interacts only with itself through its **KG** equations (6.3), and with all the others through gravity by means of the spacetime metric described by Einstein equations (6.2). This class of astrophysical compact objects behaves as stars made of dark matter (whence the name of Dark Boson Stars), in the sense that they interact only gravitationally with other compact objects [60].

[1] Notice that, although the context is different, this action is the same that describes multi-state **BS** [199], where the super-index (i) would denote each state of the scalar field.

6.1.2 Numerical implementation and analysis quantities

These equations have been introduced in the platform *Simflowny* [100–102, 171] to automatically generate parallel code for the SAMRAI infrastructure [163–165], see section 4.4.

We have used the same numerical scheme explained in Chapter 5, i.e, the numerical discretization of **EKG** equations has been performed by using the **MoL**. We use fourth-order accurate finite-difference operators for the spatial derivatives, together with a fourth order accurate Runge-Kutta time integrator. A sixth-order Kreiss-Oliguer dissipation is also included to eliminate unphysical high-frequency modes from our solution.

Our simulations use Courant factors $\lambda_c \in \{0.357, 0.15\}$, such that $\Delta t_l = \lambda_c \, \Delta x_l$ on each refinement level l to guarantee that the Courant-Friedrichs-Levy condition is satisfied. We use a domain $[-280, 280]^3$ with 7 levels of refinement, each one with twice the resolution of the previous one, such that $\Delta x_0 = 4$ on the coarsest grid and $\Delta x_6 = 0.0625$ on the finest one.

Several quantities have been computed in order to analyze the dynamics of binary **DBSs** during their coalescence: (i) Noether charge (3.38), (ii) the **ADM** mass (2.88) and the angular momentum (2.90), and (iii) the gravitational radiation through the Newman-Penrose scalar Ψ_4 (2.105) (described in the Chapter 2 section 2.4.1). These global quantities are calculated in spherical surfaces at different extraction radii, although we only show the results obtained at $R_{ext} = 50$.

6.1.3 Initial data

Single Dark BS. Initial data for isolated **DBSs** is exactly the same as for **BSs** explained in detail in the Section 3.4.2.

In the present Chapter, we consider the same configurations investigated in the previous Chapter 5 ([6]). Therefore, we restrict ourselves to the choice $\sigma_0 = 0.05$, which lead to highly compact **BS**, and construct four stars with compactness $C = \{0.06, 0.12, 0.18, 0.22\}$ belonging to the stable branch (i.e., equilibrium configurations which are stable under small perturbations). The radial profile of the scalar field for each compactness is displayed in the Fig. 6.1 (see the top panel). As it is shown in Fig. 6.1 (see the bottom panel), all these initial configurations are well inside the stable branch, which is the curve on the left of the maximum compactness $C_{max} = 0.33$. Furthermore, each star has been rescaled, by a suitable choice of m_b, such that $M_{ADM} = 0.5$.

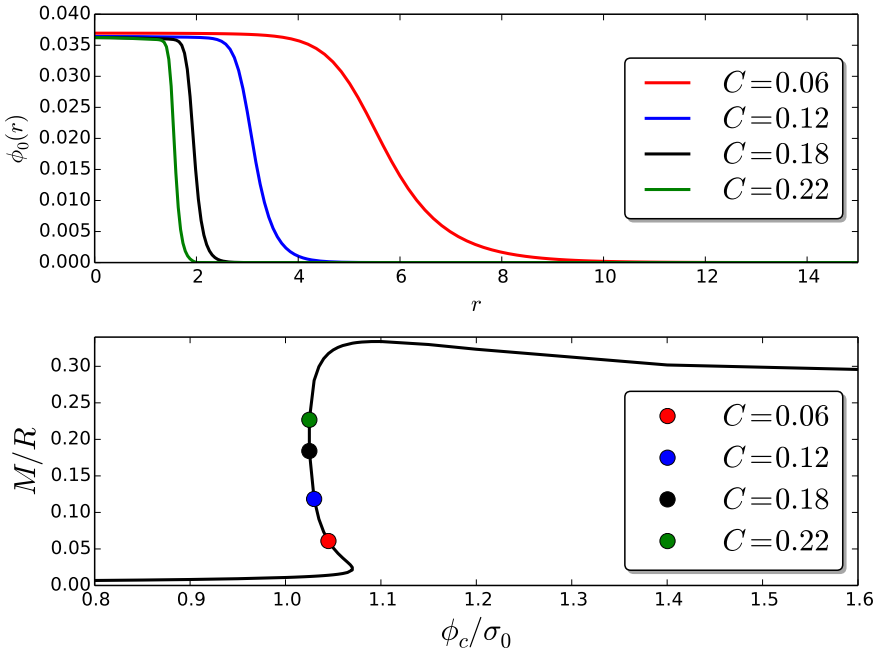

FIGURE 6.1: *Initial data of **DBS**.* (Top panel) Radial profile of the scalar field $\phi_0(r)$ for each compactness. Notice that it is nearly constant in the interior and then falls off exponentially at the surface of the star. This fall off is steeper as the compactness increases. (Bottom panel) Compactness as a function of the central value of the scalar field ϕ_c with $\sigma_0 = 0.05$. Circular markers refer to the *initial* equilibrium configurations considered both here and in previous Chapter 5 ([6]) to construct initial data for binaries.

Binary Dark BS. Initial data for binary **BS** can be constructed in the same way that it was explained in Section 5.3, i.e, by using a superposition of two boosted isolated **BS** solutions. Since we are interested on modeling **DBS** binary systems, which only interact through gravity, we proceed as follows

- the solution of each **BS** is written in Cartesian coordinates $\{g^{(i)}_{ab}(x,y,z), \Phi^{(i)}(x,y,z)\}$.
- the spacetime of binary **DBS** is obtained by a superposition of the isolated spacetimes of two **BSs**, centered at positions $(0, \pm y_c, 0)$ and with a boost $\pm v_x$ along the x-direction. The scalar field of each boosted star is not modified by the other star. The full solution can be expressed then as:

$$g_{ab} = g^{(1)}_{ab}(x, y - y_c, z; +v_x) + g^{(2)}_{ab}(x, y + y_c, z; -v_x) - \eta_{ab} \ , \tag{6.6}$$

$$\Phi^{(1)} = \Phi^{(1)}(x, y - y_c, z; +v_x) \ , \tag{6.7}$$

$$\Phi^{(2)} = \Phi^{(2)}(x, y + y_c, z; -v_x) \ , \tag{6.8}$$

where η_{ab} is the Minkowski metric in Cartesian coordinates.

Notice that a fine-tuning of the initial orbital velocity is required to set the binary in a quasi-circular orbit. It is also worthwhile to emphasize that this superposition does not satisfy the energy and momentum constraints due to the non-linear character of Einstein's equations. However, our evolution formalism enforces dynamically an exponential decay of these constraint violations (for instance, see Figure 5.6 in section 5.6). Nonetheless, convergence tests performed on the most stringent case indicates that our initial data is accurate enough to allow us investigate the problem at hand.

6.2 Coalescence of Dark Boson Stars

The coalescence of binary identical **DBSs** obtained from numerical simulations is analyzed in detailed, focusing on the dynamics and the gravitational radiation produced with different star's compactness. Furthermore, in order to infer the effect of matter interactions, these results for dark **BS** binaries (i.e., only gravity interactions) are contrasted with those for standard **BS** binaries (i.e., both gravity and matter interactions) studied in the Chapter 5. We have chosen the parameters such that the individual mass of each star in isolation is $M = 0.5$, so the binary has approximately a total initial mass $M_0 \approx 1$.

6.2.1 Dynamics

First of all, as already stressed in section 5.5.2, the initial orbital velocities differ among the binaries, mainly due to the star's compactness and total mass. More detailed information regarding the initial parameters is available in Table 6.1, together with the main properties of each binary **DBS** and its final remnant.

Some snapshots of the Noether charge density for each case, at different representative times of the coalescence, are displayed in Fig. 6.2. The conformal factor of the metric used in the **CCZ4** formalism, which represents roughly the gravitational potential, is displayed in Fig 6.3 at the same times. As stated above, the interaction between **DBSs** takes place only through gravity, even when there exists an overlap between the stars, as shown in Fig. 6.2. Therefore, the first feature that one can observe is that the transition between inspiral and merger stages depends on the star's compactness. For low compact stars $C \lesssim 0.12$, the inspiral phase does not finish suddenly at the contact time t_c (i.e., defined as the time at which the individual Noether charge densities make contact for the first time) but smoothly continues to the merger phase. The final remnant is a superposition of two coexisting orbiting **DBSs** that, at late times, are expected to settle down into a stationary spherically-symmetric configuration equivalent to a multi-state

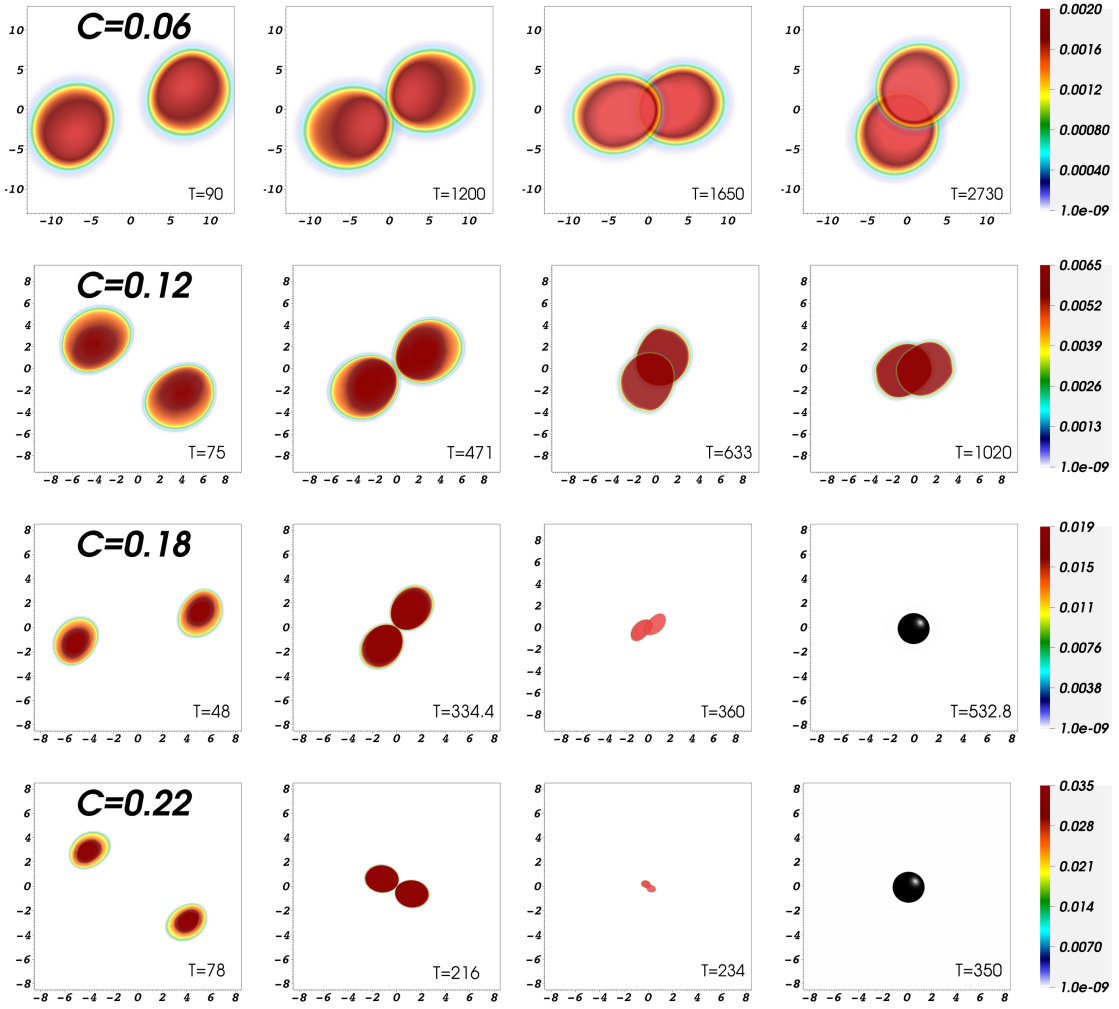

FIGURE 6.2: *Dynamics of* ***DBS*** *coalescence.* Noether charge densities, corresponding to the individual stars, in the equatorial plane at several illustrative times. Each row corresponds to a different star's compactness (from top to bottom, 0.06, 0.12, 0.18, and 0.22). First column illustrates a time in the early inspiral, the second one is roughly at contact time, the third one is during the merger stage and the fourth one at the end of our simulation. Notice that the final remnant for $C \lesssim 0.12$ is composed by two rotating co-existing **DBS**, while that for $C \gtrsim 0.18$ is a rotating **BH** (i.e., the black sphere at late times represents the apparent horizon).

BSs [199]. For high compact stars $C \gtrsim 0.18$, the transition is quite abrupt and clearly distinguishable. The final remnant is too compact and inevitably collapses to a rotating **BH**. Therefore, the final object also depends on the initial compactness of the identical stars. We can identify a critical transition compactness C_T such that below that value the remnant relaxes to a multi-state **BS** and above it collapses to a **BH**. From our simulations we can infer that $0.12 < C_T < 0.18$.

As discussed before, the most compact cases lead to the formation of a rotating **BH**, a process that is common to other binary mergers. Then, we shall focus our analysis to the more peculiar and distinctive scenario where the merger does not produce a **BH**.

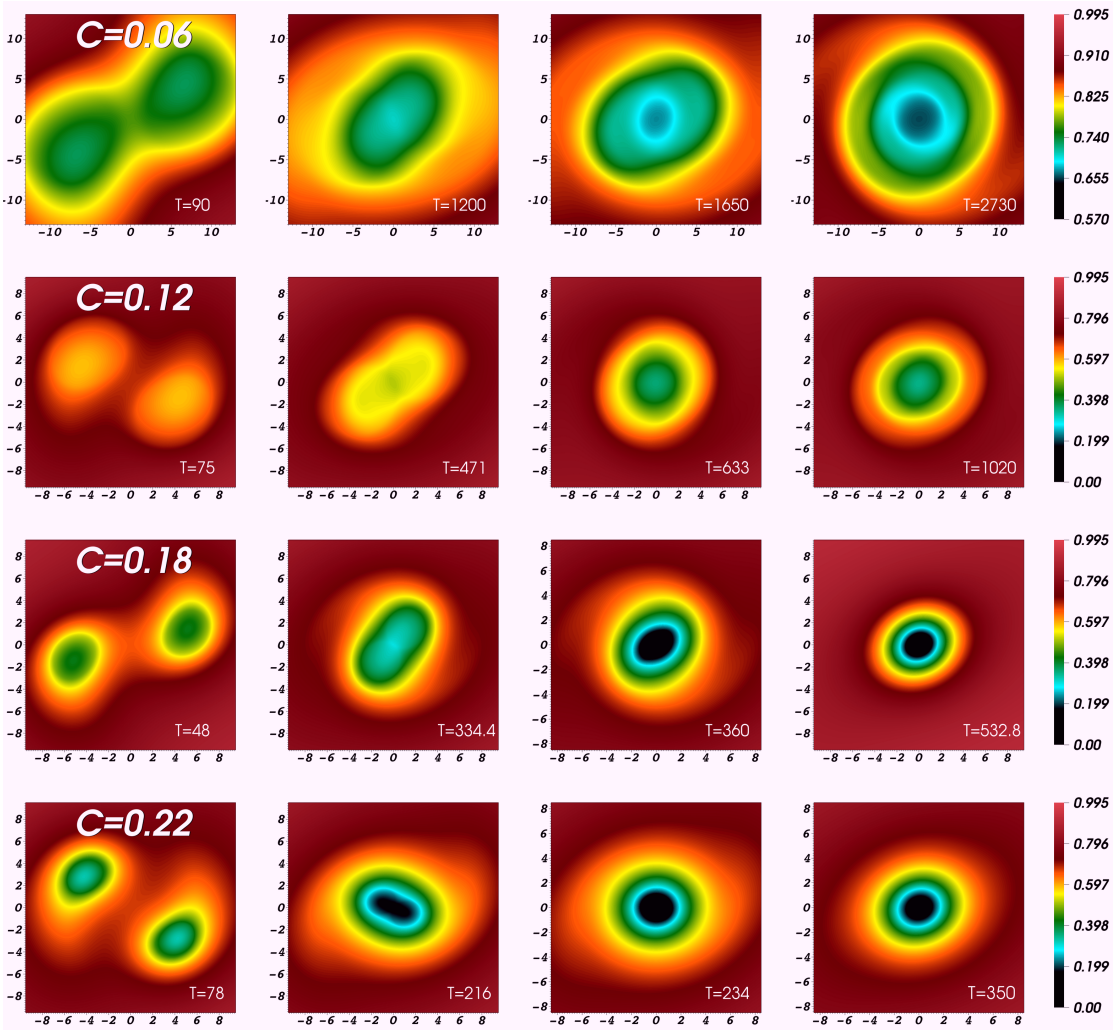

FIGURE 6.3: *Dynamics of DBS coalescence.* Conformal factor, which gives a rough description of the gravitational potential, in the equatorial plane at the same time snapshots as in Fig. 6.2. Each row corresponds to a different compactness (from top to bottom, 0.06, 0.12, 0.18, and 0.22).

Instead, the two stars keep rotating around each other while emitting **GWs**, despite a significant overlap between the individual Noether charge densities. In contrast to the inspiral phase, after the contact time the two stars can not be modeled as point sources, since the distance between their centers of mass is comparable or smaller than their radius. The evolution of angular momentum is displayed in Fig. 6.4 for these low-compact cases. Angular momentum is radiated slowly during the coalescence through gravitational waves, increasing rapidly its emission rate after the contact time. Meanwhile, the mass only decreases by roughly 10% at most, which means that the final multi-state **BS** has approximately the total initial mass of the binary system. For comparison purposes, the angular momentum evolution of the corresponding binary **BSs** have been added to the same plot. The behavior of **BS** after the contact time is clearly different, showing a sharp decay due to the interaction between the scalar fields modeling each star. A

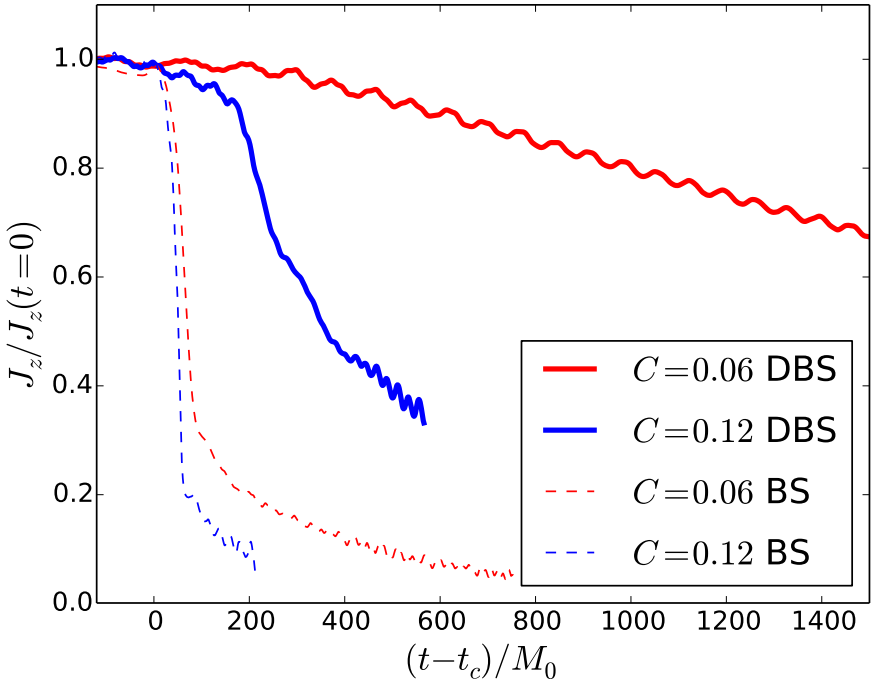

FIGURE 6.4: *Dynamics of **DBS** coalescence.* Angular momentum J_z as a function of time for **DBS** with initial compactness $C = 0.06$ and $C = 0.12$. This quantity, for the remnants of **DBS** mergers, decays to zero in a much longer timescale than those of **BS** mergers, especially for the lowest compactness $C = 0.06$. Notice that the sudden decay of the binary **BS** case with $C = 012$ was enhanced by the ejection of two blobs of scalar field during the merger [6].

C	$y_c^{(i)}$	$v_x^{(i)}$	M_0	J_0	t_c	remnant	$E_{\rm rad}^{DBS}/M_0$	$\mathcal{E}_{\rm rad}^{DBS}/M_0$	remnant	$E_{\rm rad}^{BS}/M_0$	$\mathcal{E}_{\rm rad}^{BS}/M_0$
0.06	± 8	± 0.142	1.07	1.16	1200	BS+BS	0.068	0.06	BS	0.075	0.029
0.12	± 5	± 0.210	1.18	1.24	471	BS+BS	0.127	0.12	BS	0.085	0.057
0.18	± 5	± 0.214	1.29	1.40	335	BH	0.014	0.18	BS	0.120	0.086
0.22	± 5	± 0.220	1.46	1.65	218	BH	0.030	0.22	BH	0.030	0.1

TABLE 6.1: *Characteristics of binary of **DBS** models.* The entries of the table are, respectively: the compactness C of the individual **DBSs** in the binary, the initial positions $y_c^{(i)}$, the initial velocities of the boost $v_x^{(i)}$, the initial total **ADM** mass M_0, the initial total orbital angular momentum J_0 of the system, the time of contact of the two stars t_c, the final remnant, the total radiated energy in gravitational waves for each simulation $E_{\rm rad}$ (i.e., integrated from the beginning and extrapolated to large times after the contact time) and the one estimated analytically $\mathcal{E}_{\rm rad}$ as described in in Appendix A section A.2. We also included previous results corresponding to binary **BSs** for comparison purposes.

deeper discussion of the differences between **DBS** and **BS** will be given in Section 6.2.3.

6.2.2 Gravitational Radiation

The main mode $l = |m| = 2$ of the Newman-Penrose scalar Ψ_4 (see eq. (2.105)), encoding the gravitational radiation produced during the coalescence, is displayed in Fig. 6.5.

Furthermore, the same mode of the strain, near the contact time, is shown in Fig. 6.6. Notice that time has been rescaled with the initial total mass M_0 of each binary, and shifted such that contact time occurs at $t = 0$.

Let us start with the less compact cases, $C \lesssim 0.12$, whose merger leads to a superposition of two co-existing **BSs** as a final state. As it might be expected, gravitational radiation produced during the early inspiral is weak, since the stars have large radii and therefore collide at a low frequency. After making contact, the binary enters smoothly to the merger stage, with both stars orbiting around each other for a long time and yielding to stronger gravitational waves than during the inspiral. Losses of energy and angular momentum occur mainly during this stage, while the remnant formed by the two co-existing stars rotates at a faster frequency, radiating more intense **GWs**. Although the cases with $C \gtrsim 0.18$ share the same behavior in the early inspiral, soon after the contact time the remnant becomes unstable and collapses to a rotating **BH**. The exponential decay of the gravitational wave signal observed for these cases in Fig. 6.5 and Fig. 6.6 is a clear evidence on this final **BH** state.

Furthermore, we have included the comparison with an **EOB** approximation that describes the adiabatic coalescence of quasi-circular binary **BHs** [4]. Interestingly, although the signals show a good agreement during the inspiral phase, they are quite different as they get closer to the contact time: analogous to **NSs**, binaries composed by **DBSs** are strongly affected by tidal interacting forces only when they are in a close orbit. This means that, even though **DBSs** only suffer gravitational interactions, they behave yet rather different than **BHs**. The most compact case, $C = 0.22$ shows that even when the final fate of the remnant is a **BH**, **DBSs** and **BHs** are still different in the late inspiral and merger. An accurate quantitative comparison of our simulations with the **EOB** approximation would require initial data for **DBS** binaries in quasi-circular orbits with much smaller constraint violation, which is not yet available.

It is also illustrative to analyze the instantaneous **GW** frequencies f_{GW} of **DBS** binaries and compared them to: (i) **BS** binaries, (ii) a **PN-T4** approximation for point particles(i.e., **BHs**) [200], and (iii) a **PN-T4** approximation including also the lowest order tidal effects [201, 202], whose strength can be measured by the tidal Love number [7, 8]. Fig. 6.7 displays these four models (i.e., **DBS**, **BS** and **T4** with and without tidal effects) for each compactness. Again, all models behave similarly during the inspiral, with differences arising near the contact time. While the **DBS** binary with $C \lesssim 0.12$ exhibits a smooth and soft increase on the frequency, the corresponding **BS** binary shows an abrupt rise as a consequence of the stronger dynamics of the remnant, induced by scalar field interactions. The **PN-T4** approximation, either with or without tidal effects, leads to different frequencies than the **DBS** binary after the contact time, such that f_{GW} of

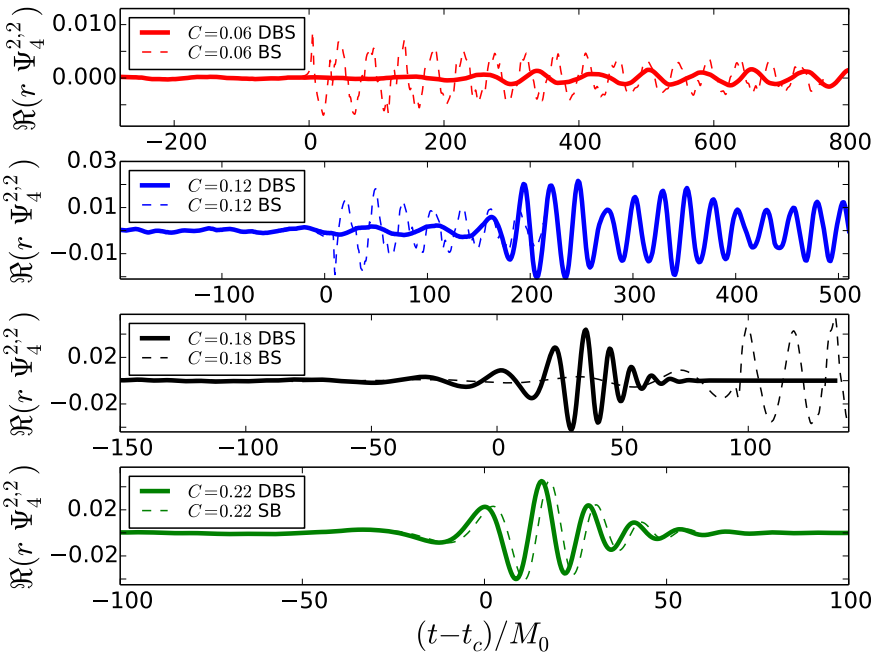

FIGURE 6.5: *Gravitational waves.* The real part of the main $l = m = 2$ mode of Ψ_4 describing the gravitational emission produced by **DBS** and **BSs** binaries as a function of time.

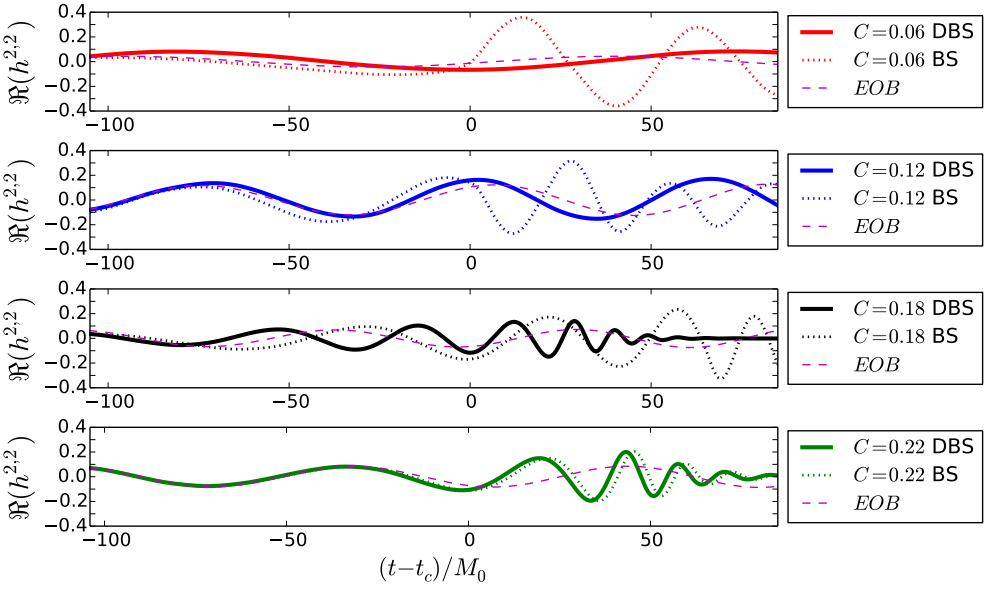

FIGURE 6.6: *Gravitational waves.* Main mode of the strain for **DBS** binaries with different compactness near the contact time. All cases are compared to the **EOB** approximation of a quasi-circular binary **BH** coalescence [4] by matching the waveforms at early inspiral.

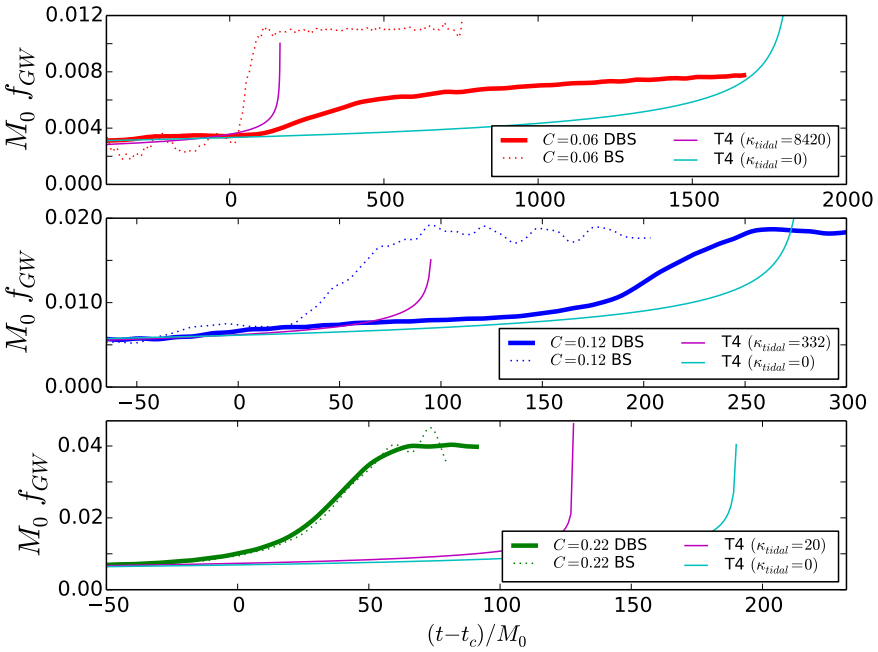

FIGURE 6.7: *Gravitational waves.* **GW** wave frequency $f_{GW} = \omega_{GW}/2\pi$ as a function of time, where ω_{GW} is the instantaneous **GW** angular frequency from the main $l = m = 2$ mode. The frequencies calculated numerically for **DBS** and **BS** are displayed in thick solid and dashed lines, respectively, while that frequencies calculated by Taylor **T4** approximation with and without tidal effects are plotted in thin solid lines. Notice that significant differences arise just after contact time.

DBS is somewhere in between these two approximations. This means that, although including tidal effects at the lowest order might be acceptable during the inspiral phase, it is not accurate enough after the contact time when the effects of extended bodies become important. Notice also that the frequencies calculated from **PN-T4** are closer to those of the **BS** binary when tidal effects are activated, probably because both matter interactions and tidal effects accelerate the dynamics of the system.

The post-merger frequency of **DBS** and **BS** reach roughly the same value in the case $C = 0.12$. We presume that in the case $C = 0.06$ both models will also reach the same frequency at the end state, although the time scales for the remnant to settle down are much longer than considered on this work. In the most compact cases, $C = 0.22$, there are no significant differences between **BS** and **DBS** frequencies, as we have seen in the waveform as well. These high-compact cases are noticeably different than the **T4** approximations (i.e., with and without tidal effects), showing again that such merger is still different from the one of a binary **BH**. Notice that the case $C = 0.18$ is not directly comparable since the remnants of binary **DBS** and **BS** are different.

Finally, the luminosity and total radiated energy produced by the main gravitational wave modes $l = 2$ are displayed in Figs. 6.8 and 6.9, with the specific values listed

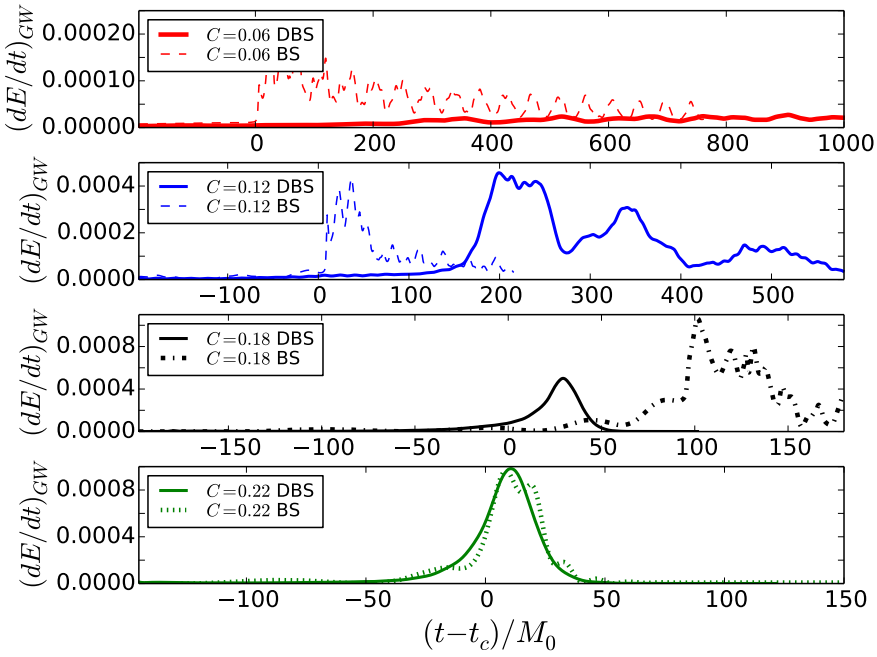

FIGURE 6.8: *Gravitational waves.* Luminosity of gravitational waves radiated during the coalescence of **DBS** and **BS** binaries.

in Table 6.1. The total energy obtained disclose that the cases $C \lesssim 0.12$ are *super-emiters* [188], since the system emits more than the analogous binary **BH** system (i.e., about 5% of its initial total mass). Following [6, 188], we can estimate the amount of energy radiated by **DBS** binaries as

$$\mathcal{E}^{ac}_{\rm rad} \approx M_0 C, \tag{6.9}$$

which is roughly in agreement with the results of our simulations for the low compact cases (i.e., not collapsing to a **BH**). The detailed calculation can be found in Appendix A section A.2.

6.2.3 DBS versus BSs

In order to analyze the effect of scalar field interactions, most of the previous plots included not only the analysis of our binary **DBS** simulations, but also previous binary **BS** results in Chapter 5([6]). Let us here stress some of the most significant differences which have not been discussed yet.

An unexpected behavior was recognized in the binary **BSs** case with compactness $C = 0.12$: the formation of two scalar field blobs which were ejected during the merger, carrying away little mass but an important amount of angular momentum. However, none of the **DBS** binaries show any evidence of such scalar field blobs. A snapshot at

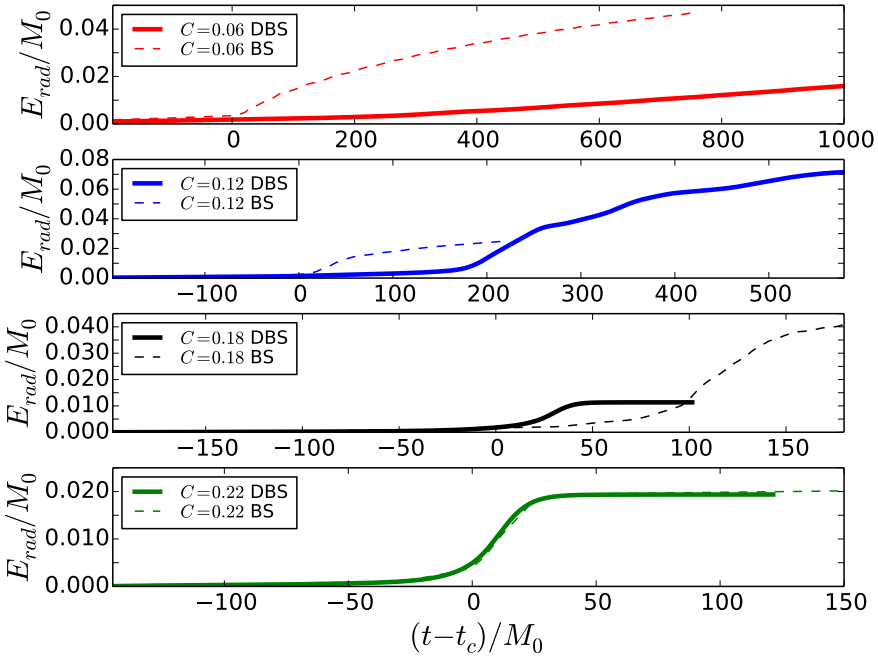

FIGURE 6.9: *Gravitational waves.* Total **GW** energy radiated during the coalescence, calculated by integrating in time the quantities displayed in Fig. 6.8

$t = t_c + 60$ of the Noether charge density for **DBS** and **BS** binaries with $C = 0.12$ is displayed in Fig. 6.10 to illustrate the different dynamical behavior. The evolution of angular momentum in Fig. 6.4 also shows considerable losses in the **BS** case (i.e., resulting into a sudden decrease after the contact time) as a result of the matter ejection.

It is also quite interesting that, in the **BS** binary with compactness $C = 0.18$, the remnant settles down to a non-rotating **BS**, while that the remnant of the corresponding **DBS** binary collapses to a rotating **BH**. Therefore, one of the effects of matter interactions is to induce an additional pressure that supports the collapse to a **BH**, increasing effectively the critical transition compactness C_T. Consequently, the range of $0.12 < C_T \leq 0.18$ valid for **DBS** is increased to $0.18 < C_T \leq 0.22$ for **BS**.

The gravitational radiation also show interesting differences. During the inspiral phase, the gravitational radiation of **DBS** and **BS** binaries are exactly the same, as it is expected. The main difference appears near the contact time. On one hand, binary **BS** coalescence is governed by scalar field and gravitational forces, which accelerates the dynamics of the system and reduces the time for the remnant to settle down. In this case, after the contact time the two boson stars merge into a rotating **BSs** which radiate stronger **GWs** and at a higher frequency than during the inspiral phase. On the other hand, binary **DBSs** dynamics is driven only by gravitational interactions and there is a smooth slow transition from inspiral to merger, which can also be appreciated on the **GW** frequency displayed in Fig 6.7.

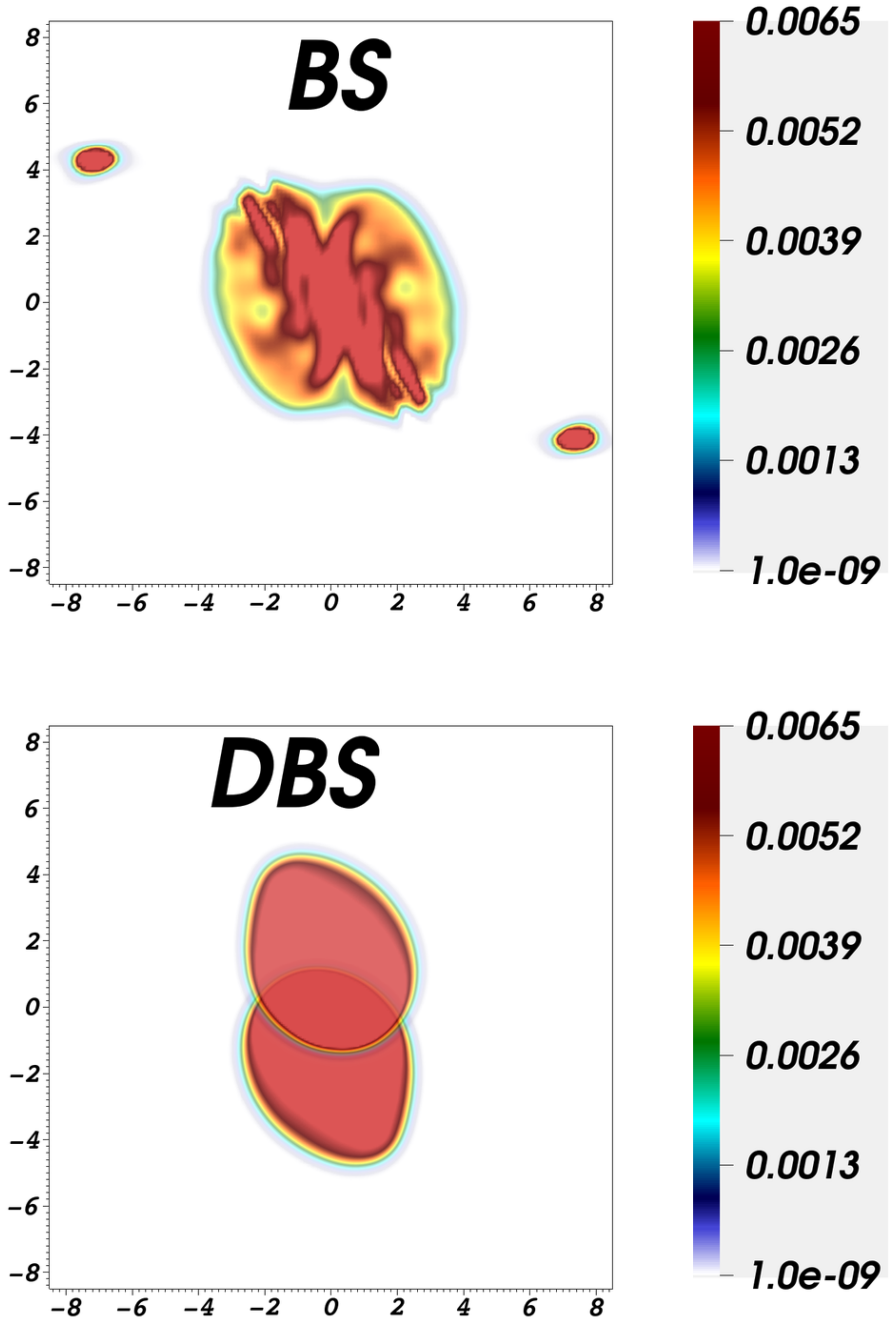

FIGURE 6.10: *Comparison of **DBS** vs **BSs**.* Noether charge densities of **DBS** and **BS** binaries, roughly at time $t = t_c + 60$, for the stars with compactness $C = 0.12$. Notice that there are two scalar blobs in the **BS** merger which do not form in **DBS** collisions.

6.3 Discussion

In the present Chapter we have studied, through full numerical simulations, the dynamics and the gravitational radiation produced during the coalescence of binary **DBSs** − self-gravitating compact objects composed by bosonic matter that can only interact through gravity −. We have considered four initial compactness, given by $C = \{0.06, 0.12, 0.18, 0.22\}$, of the identical stars forming the binary. For the less compact cases, $C \lesssim 0.12$, the dynamics showed a smooth transition from inspiral to merger, leading to a superposition of two close-orbiting **DBSs**. Gravitational radiation emitted on these cases is quite weak during the inspiral phase, although it increases considerably after the contact time. For the highest compactness cases $C \gtrsim 0.18$, the transition from inspiral to merger is quite abrupt. After the merger, the remnant is excessively compact and it inevitably collapses to a **BH**. **GWs** on this post-merger stage are given by the classical **BH** ring-down. Therefore, our research reveals that binaries composed by these dark bosonic objects form either; (i) a multi-state **BSs** for $C < C_T$, which emits **GW** continuously for a long time, or (ii) a rotating **BH** for $C > C_T$ with its typical ring-down signal after the collapse.

We have also compared these **DBS** mergers with previous simulations of **BS** collisions, see Chapter 5 ([6]), where the scalar field behaves as a fluid (i.e., there exists interaction between the stars through both gravity and the scalar field), leading to important differences. Despite presenting the same dynamics during the inspiral phase, scalar field interactions precipitate the plunge of the stars after the contact time and accelerates the dynamics of the remnant. For the **DBS** binary with compactness $C = 0.12$, there is no ejection of blobs, contrary to what happened in the **BSs** case. Finally, **DBS** with a compactness $C = 0.18$ collapses to a rotating **BH** after the merger, while the corresponding binary **BSs** case settles down to a non-rotating **BS**.

Finally, the comparison of the instantaneous **GW** frequencies of **DBSs** binaries with standard **BS** binaries and the **PN-T4** approximation reveals, in the cases when the remnant is not a **BH**, a very particular and distinguishable signature of these compact objects made of dark matter. All these results indicate that, if they exist, the coalescence of dark stars would produce gravitational waveforms clearly different and potentially distinguishable from other astrophysical objects like **BHs**, **NSs** or even **BSs**. These distinctive waveforms could be interesting to contrast future observations of **aLIGO/Virgo**.

Chapter 7

Neutron star binaries with dark matter cores

The coalescence of binary neutron star has been recently observed both via gravitational waves by the **LIGO/Virgo** interferometric detectors and via electromagnetic waves. In this last Chapter, we present the results of recent work done in [203] which aims to model, through numerical simulations, the merger of binary neutron stars with dark matter particles trapped on their interior. We study gravitational wave signatures due to the possible presence of these dark matter particles. Comparison of this emission from our simulations with future observations might allow us to constraint different dark matter models.

This final Chapter is organized as follows. In Section 7.1 a brief motivation about neutron stars mergers including dark matter is presented, stressing that these objects can be modeled with mixed fermion-boson stars. In Section 7.2 the evolution equations of fermion-boson stars are introduced, followed by the numerical implementation in Section 7.3. The construction of initial data to fermion-boson stars, either isolated or in binaries, is described extensively in Section 7.4. In Section 7.5, we study the dynamics and the gravitational radiation during the coalescence of binaries of mixed fermion-boson stars. Finally, we discuss our results in Section 7.6.

7.1 Motivation

Recently, **GWs** from the coalescence of a binary neutron star system **(GW170817)** have been observed by **LIGO** [16, 204], followed by several electromagnetic counterparts: a gamma-ray burst **GRB170817A** [18] and a thermal infrared/optical spectra

consistent with a kilonova [19]. These electromagnetic **(EM)** and **GW** observations start a fruitful era of multi-messenger astronomy, which will inevitably lead to breakthroughs in our understanding of some of the most exciting objects and phenomena in the universe.

On a much larger scale, there is overwhelming evidence of the existence of dark matter (**DM**) in the Universe, like for instance the observation of missing mass in galaxy clusters and the precise measurements of the cosmological baryonic fraction [205]. Measurements of the matter density and its baryonic component imply that the **DM** density contribution is about 25% of the total content in the Universe [206]. Most models in particle physics require dark matter particles to be weakly interacting with mass range from 100 GeV to several TeV.

Despite the poor knowledge of the dark matter-baryon interaction (see for instance the experimental upper limits constraints for weakly interacting massive particles in [207]), these **DM** particles will more easily cluster in a dense astrophysical object. Due to its orbital motion, a star will sweep through the Galactic dark matter halo and eventually capture some particles on its way. Despite the surface area of a typical **NS** being much smaller than other stars, two properties make it very efficient in capturing galactic **DM** particles [208]. First, the high baryonic density inside a **NS** provides a much higher probability for **DM** particles to interact and lose energy, compared to other stars. As a matter of fact, for a given star, the particle will interact if the cross-section of the dark matter-baryon interaction, σ_{DM} is at least of the order of the typical area occupied by each baryon, $\sigma_{DM} \gtrsim m_p\, R_\star^2/M_\star$, where the latter values decreases with density and for a neutron star is $\sim 6 \times 10^{-46}$ cm^2 (while for the Sun is ten orders of magnitude larger). Second, the strong gravitational force prevents most **DM** particles from escaping from a **NS** once it loses some of its energy through interactions. It may be only a matter of time for a neutron star to capture enough number of **DM** particles to affect its observational properties, which may then be used to constrain the nature of dark matter.

On one hand, if **DM** particles are self-annihilating, this process modifies the thermal evolution of the **NS** and could be observed as a bright **EM** emission of old **NS**, since the released energy due to the annihilation inside the **NS** can increase the temperature beyond its natural value [209]. On the other hand, if **DM** particles do not self-annihilate, they will cluster in a small region at the center of the neutron star, increasing their compactness and changing its internal structure. Ultimately, this clustering could even lead to a gravitational collapse [210]. Either way, **NSs** may be therefore sensitive to indirect probes of the presence of **DM**, and can be used to set constraints both on the density and on the physical properties of **DM**.

Recent studies [211] investigate possible changes in the structure of the star by the presence of (non self-annihilating) **DM** by using a two-fluid model. We find more accurate to describe these systems by modeling the neutron star matter with a fermionic perfect fluid and the bosonic dark matter with a complex scalar field [61, 62]. The resulting objects, known as fermion-boson (**FB**) stars, allow only a coupling between the boson and the fermion particles through gravity. Notice also that current observations already set some bounds on the amount of **DM** particles inside **NSs** for different **DM** models [61, 62, 212]. The effect of weakly-interacting **DM** on the structure of the star will be stronger in non-linear dynamical scenarios like the coalescence of two **NSs**. As we will see later, our simulations reveal that the presence of **DM** cores leaves a distinct imprint in the **GWs** during the post-merger phase.

7.2 Evolution equations of Fermion-Boson Stars

In order to study binary neutron stars with dark matter clustered inside, we use binaries made of **FB** stars. **FB** stars are modeled by an energy momentum tensor which have a contribution from a perfect fluid and a complex scalar field [62], namely

$$T_{ab} = \kappa \left(T^{\Phi}_{ab} + T^{M}_{ab} \right) \ . \tag{7.1}$$

Notice that, as we are interested in dark matter cores inside of neutron stars, we assume that the bosonic matter is composed by two independent complex scalar fields, one for each star, which only interact gravitationally, as we studied in Chapter 6.

The evolution equations of **FB** stars are then governed by the Einstein-Klein-Gordon-Hydrodynamics system of equations, which are

$$G_{ab} = \kappa T_{ab} \ , \tag{7.2}$$

$$g^{ab}\nabla_a\nabla_b\Phi^{(1)} = \frac{dV^{(1)}}{d\left|\Phi^{(1)}\right|^2}\Phi^{(1)} \ , \tag{7.3}$$

$$g^{ab}\nabla_a\nabla_b\Phi^{(2)} = \frac{dV^{(2)}}{d\left|\Phi^{(2)}\right|^2}\Phi^{(2)} \ , \tag{7.4}$$

$$\nabla^a T^M_{ab} = 0 \ , \tag{7.5}$$

$$\nabla_a(\rho u^a) = 0 \ , \tag{7.6}$$

being T^{Φ}_{ab} the energy-momentum tensor considered in Dark stars models given by the equation (6.4), and T^{M}_{ab} is the energy-momentum tensor for a perfect fluid one (3.60).

Here, we consider a self-potential for each scalar field given by

$$V\left(|\Phi|^2\right) = m_b^2|\Phi|^2\,, \tag{7.7}$$

where m_b is a free parameter related to boson mass. Recall that this interaction potential lead to *mini Boson stars*, as we studied in Section 3.4.2. Finally, it is worth stressing that the scalars fields are coupled to each other and to the perfect fluid only through gravity.

7.3 Numerical implementation

The Einstein-Klein-Gordon equations can be written as a time evolution system by using the formulation studied in Chapter 6. The hydrodynamical (**HD**) equations of motion (7.5)-(7.6), describing the perfect fluid, are written in balance law form

$$\partial_t \mathbf{u} + \partial_k F^k(\mathbf{u}) = S(\mathbf{u})\ , \tag{7.8}$$

where $\mathbf{u}$ is a set of conservatives variables $\{D, \tau, S_i\}$, defined in Section 3.5.2. Finally, the **HD** evolution system in conservative form are given in equations (3.77)-(3.79). Furthermore, the primitive quantities $\{\rho, \epsilon, P, v_i\}$ are recovered from the conservative ones by solving a system of nonlinear equations, as described in Section 3.5.2.

The numerical setup to be considered here it is the same used from Section 4.5, i.e.: we employ **AMR** via the HAD computational infrastructure, which ensure sufficient resolution within the **FB** stars, see Section 4.4. We use finite difference schemes, based on the **MoL**, on a regular Cartesian grid, see Section 4.1.2. A fourth order accurate spatial centered discretization –satisfying the summation by parts rule– is used for Einstein equations, see Section 4.2.1. The relativistic hydrodynamics equations are discretized by using **HRSC** method based on the **HLL**-flux formula with **PPM** reconstruction, see Section 4.2.2 and 4.2.4 respectively. Finally, a third order accurate Runge-Kutta time integrator is used to achieve stability of the numerical implementation and to integrate the equations in time [174], see section 4.1.3.

Note that, our numerical approach to solving Einstein equations combining hydrodynamical fluid and complex scalar field is developed by using two widely tested codes: (i) to solve the Einstein-Klein-Gordon equations [6, 111, 166, 167, 196] and (ii) the general relativistic hydrodynamic [168–170].

7.4 Initial data

Here, we explain in detail how to construct initial data for equilibrium configuration of non-rotating isolated **FB** stars by using the methodology explained in Reference [62]. We also explain the procedure to construct initial data for binary **FB** star.

7.4.1 Single Fermion-Boson stars

The equilibrium configuration equations for a single **FB** can be obtained by combining the procedures to obtain isolated non-rotating neutron and boson stars respectively, explained in detail in Chapter 3. The method is summarized as follows: assuming a static metric as in Equation (3.23), imposing the harmonic time dependence Equation (3.50) and the static fluid condition $v^i = 0$, the Einstein-Klein-Gordon-Hydrodynamics system equations in these coordinates lead to the following system of **ODE** :

$$\partial_{\tilde{r}} a = -\frac{a}{2\tilde{r}}\left(a^2-1\right) + 4\pi\,\tilde{r}\,a^3\tau\ , \tag{7.9}$$

$$\partial_{\tilde{r}} \alpha = -\frac{\alpha}{2\tilde{r}}(1-a^2) + 4\pi\,\tilde{r}\,\alpha\,a^2\,S^{\tilde{r}}_{\tilde{r}}\ , \tag{7.10}$$

$$\partial_{\tilde{r}} \phi_0 = \zeta\ , \tag{7.11}$$

$$\partial_{\tilde{r}} \zeta = -(1+a^2+4\pi\,\tilde{r}^2\,a^2)(S^{\tilde{r}}_{\tilde{r}}-\tau)\frac{\zeta}{\tilde{r}} - \left(\left(\frac{\omega}{\alpha}\right)^2 - V'(|\Phi|^2)\right)a^2\phi_0\ , \tag{7.12}$$

$$\partial_{\tilde{r}} P = -(\rho(1+\epsilon)+P)\frac{\partial_{\tilde{r}}\alpha}{\alpha}\ , \tag{7.13}$$

where

$$\tau = \left(\frac{\omega\,\phi_0}{\alpha}\right)^2 + \left(\frac{\zeta}{a}\right)^2 + V(|\Phi^2|) + h - P\ , \tag{7.14}$$

$$S^{\tilde{r}}_{\tilde{r}} = \left(\frac{\omega\,\phi_0}{\alpha}\right)^2 + \left(\frac{\zeta}{a}\right)^2 - V(|\Phi^2|) + P\ . \tag{7.15}$$

An **EoS**, relating $P = P(\rho, \epsilon)$, is necessary to close the system (7.9)-(7.13). For cold neutron stars, the polytropic **EoS** $P = \kappa\rho^\Gamma$ is a good approximation. The above system can be solved numerically by using boundary conditions guarantying regularity at the origin and asymptotic flatness, namely

$$a(0)=1,\quad \alpha(0)=1,\quad \phi_0(0)=\phi_c,\quad \zeta(0)=0,\quad P(0)=\kappa\rho_c^\Gamma\ , \tag{7.16}$$

$$\lim_{r\to\infty}\phi_0(\tilde{r})=0,\quad \lim_{r\to\infty}\alpha(\tilde{r})=\frac{1}{a(\tilde{r})},\ \lim_{r\to\infty}P(\tilde{r})=0\ , \tag{7.17}$$

where ϕ_c is the central value of scalar field and ρ_c the central value of density.

Notice that the final **ODE** system is an eigenvalue problem for ω as a function of $\{\phi_c, \rho_c\}$. Therefore, a shooting method can be used in order to integrate the system (7.9)-(7.13) from $\tilde{r} = 0$ towards the outer boundary. In addition, we can add two differential expressions to help on the characterization of the solutions, namely the fermionic rest-mass and the bosonic rest-mass

$$\frac{\partial N_B}{\partial \tilde{r}} = 8\pi\, m_b\, \omega \frac{\phi_0^2\, a\, \tilde{r}^2}{\alpha} \,, \tag{7.18}$$

$$\frac{\partial N_F}{\partial \tilde{r}} = 4\pi \rho \tilde{r}^2 \,, \tag{7.19}$$

with boundary conditions $N_B(0) = N_F(0) = 0$. Notice that, since $N_B = N\, m_b$, by setting $m_b = 1$ both the total Noether charge and the total bosonic mass have the same value. The radius of the boson star will be denoted as R_B[1] and the neutron star one as R_F [2]. Finally, in the same way as we did with **BSs** and **NSs** in Chapter 3, after the equilibrium configuration is found, a coordinate transformation from polar to isotropic coordinates is performed. Then, the solution can be written in Cartesian coordinates to perform numerical 3D simulations.

As it was already mentioned, the equilibrium configurations of **FB** depend on two parameters, the central values of the scalar field ϕ_c and the density ρ_c. By varying these parameters, together with the **EoS** and the potential of the scalar field, it is possible to find star solutions composed mostly either by fermions (i.e., $N_F >> N_B$) or bosons (i.e., $N_B >> N_F$). Solutions can be characterized then by the boson-to-fermion ratio [62]:

$$Y_B = \frac{N_B}{N_F} \,. \tag{7.20}$$

For a fixed value of the total mass of the star, the mass of bosons N_B grows as ϕ_c (or ρ_c) increases, reaching a maximum and decreasing afterwards. The mass of fermions N_F has the complementary behavior to N_B, i.e., decay reaching a minimum and then increases. It is worth stressing that the stability of **FB** can be quite complicated due to the freedom of these two parameters $\{\phi_c, \rho_c\}$. The stability theorems for single parameter solutions might not be applied directly, for further discussion see [62] and references therein.

By considering a fixed total mass $M_{ADM} = 1.35$, and taking a polytropic **EoS** with $\Gamma = 2.5$ and $\kappa = 8980$ (in geometric units), a family of equilibrium configurations can be found. The behavior of N_F and N_B explained above for this particular family is shown in the top panel of Fig. 7.1. A specific solution is obtained for the choice $\phi_c = 1.223 \times 10^{-2}$ and $\rho_c = 5.0244 \times 10^{-4}$, leading to a stable equilibrium configuration with $Y_B = 10\%$,

[1] Recall that, R_B is the R_{99} radius defined in Section 3.4.2.

[2] Recall that, R_F is the radius of the neutron stars defined as the radius where the pressure vanishes, as was studied in Section 3.5.3.

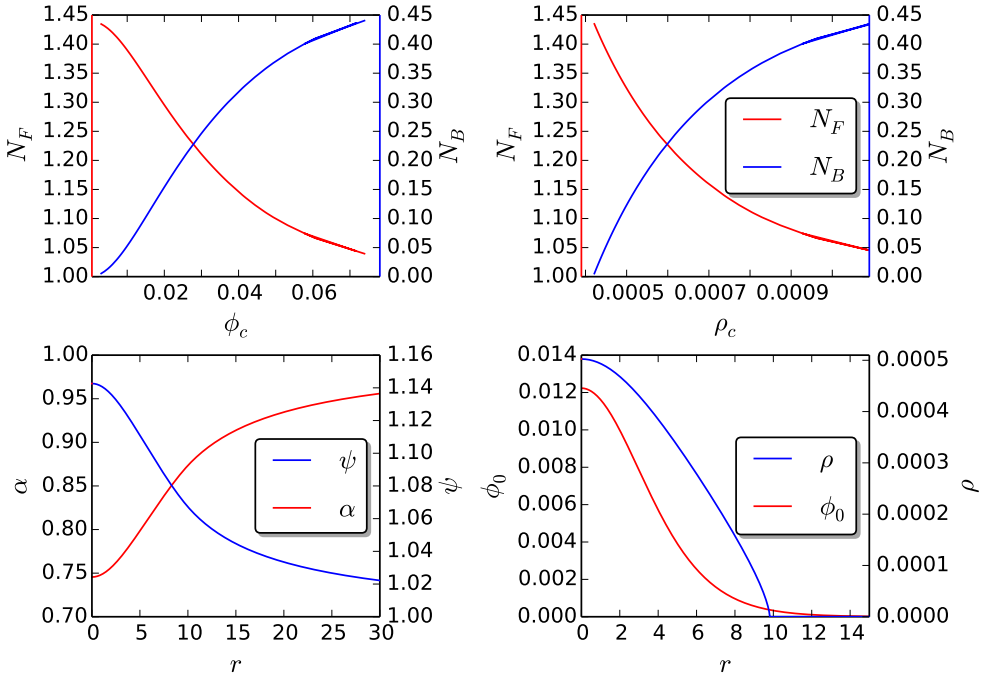

FIGURE 7.1: *Initial data of an isolated **FB** star.* (Top) The mass of fermions N_F and bosons N_B for the equilibrium configurations with a fixed total ADM mass $M = 1.35$, as a function of the central value of scalar field ϕ_c (left) and rest-mass density ρ_c (right). (Bottom) The metric component radial profiles $\alpha(r)$ and $\psi(r)$, together with the ones for scalar field $\phi_0(r)$ and density $\rho(r)$ (right), for a specific stable equilibrium with boson-to-fermion ratio $Y_B = 10\%$.

compactness $C = M_{ADM}/R_F = 0.12$ and $R_F = 11.2$. The profiles of $\alpha(r)$, $\psi(r)$, $\phi_0(r)$ and $\rho(r)$ are displayed in the bottom panel of Figure 7.1.

The implementation of our evolution equations can be tested by evolving these stationary solutions. This configuration is evolved in a domain $[-100, 100]^3$ with radiative boundary conditions by using 120 grid points in each direction and four refinement levels, such that the last one has a resolution of $\Delta x_3 = 0.21$. Finally, the same damping terms of the Section 4.5 are used for this test, namely $\kappa_z = 0.1$ and $\kappa_c = 1$.

The dynamical evolution of some interesting quantities are displayed in Figure 7.2. In particular, the evolution of the real part of the scalar field at the center $\Phi_R(t, r = 0)$ is displayed at the top panel and compared to the expected analytical behavior $\phi_0(r = 0)\cos(\omega t)$, showing a perfect agreement. The spatial integral of globally conserved quantities, namely the rest-mass density D and the Noether charge N, are showed in the second and third panel. These quantities have been rescaled by their initial values. Notice that they remain roughly constant during the evolution, confirming that the initial equilibrium configuration is stable. Finally, the L_2-norm of Hamiltonian constraint is displayed in the bottom panel, showing that it remains under control with the selection

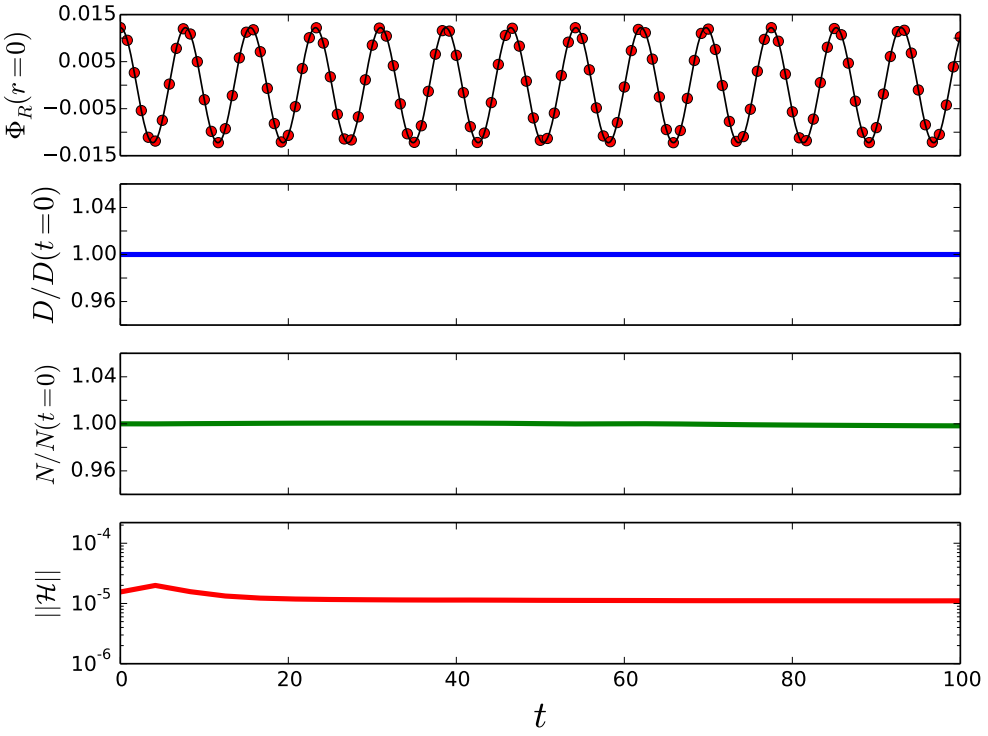

FIGURE 7.2: *Evolution of an isolated Fermion-Boson star.* In the first panel, the evolution of the real part of Φ at $r = 0$. The solid black line shows the analytically expected value $\phi_0(r = 0)\cos(\omega t)$, being $\omega = 1.0878$. The red circles are the numerical solution obtained by using **CCZ4** evolution systems, which illustrates the good agreement between the numerical and analytical solutions. In the second and third panel, the evolution of the integrated rest-mass density D and the Noether charge N, showing that they remain roughly constant during the evolution. This suggest that the star is stable. Finally, in the fourth panel, the L_2-norm of the Hamiltonian, $\mathcal{H}$, as a function of time, showing that the solution with **CCZ4** is stable and remain under control by setting $\kappa_z = 0.1$ and $\kappa_c = 1$.

of the damping terms used in Section 4.5, and it is comparable to its initial value, which is given mainly by discretization errors.

7.4.2 Binary Fermion-Boson stars

Initial data for binary **FB** can be constructed by using a superposition of two boosted isolated **FB** stars solutions, as was explained in Section 6.1.3. So far, in the Section 5.3, we have explained in detail how to boost a static spherically symmetric solution and the scalar fields quantities along of x-axis with a velocity v. Here, we extend this procedure to the hydrodynamical fields. From Chapter 3, we know that the fluid four-velocity can be decomposed as

$$u_0 = W(-\alpha + \beta_i v^i) \ , \tag{7.21}$$

$$u_i = W v_i \ , \tag{7.22}$$

where W is the general relativistic Lorentz factor related to the fluid. Then, performing the Lorentz transformations (see equations (5.5)-(5.6)) to equations (7.21)-(7.22), at time $t = 0$, we obtain

$$\tilde{u}_t = -\Gamma\,\alpha\ , \quad \tilde{u}_x = \Gamma\, v\,\alpha\ , \tilde{u}_y = \tilde{u}_z = 0\ , \tag{7.23}$$

where Γ is the general relativistic Lorentz factor related to the transformation. Therefore, the final expression for the hydrodynamics fields of the boosted star, evaluated at $t = 0$ are:

$$\tilde{\rho} = \rho\ ,\ \tilde{v}_x = \frac{\tilde{u}_x}{\tilde{W}}\ , \quad \tilde{v}_y = \tilde{v}_z = 0\ , \tag{7.24}$$

where $\tilde{W}^2 = \tilde{u}_i\tilde{u}^i + 1$.

The method to construct initial data for **FB** star binaries can be summarized as follows:

- the solution of each **FB** star is written in Cartesian coordinates, namely

$$\{g^{(i)}_{ab}(x,y,z), \Phi^{(i)}(x,y,z), \rho^{(i)}(x,y,z), v^{(i)}_j(x,y,z)\}\ . \tag{7.25}$$

- the spacetime and the hydrodynamics fields of binary **FB** stars are obtained by a superposition of the isolated spacetimes and hydrodynamics variables of two **FB** star, centered at positions $(0, \pm y_c, 0)$ and with a boost $\pm v_x$ along the x-direction, namely

$$\begin{aligned} g_{ab} &= g^{(1)}_{ab}(x, y - y_c, z; +v_x) + g^{(2)}_{ab}(x, y + y_c, z; -v_x) - \eta_{ab}\ , && (7.26)\\ \rho &= \rho^{(1)}(x, y - y_c, z; +v_x) + \rho^{(2)}(x, y + y_c, z; -v_x)\ , && (7.27)\\ v_j &= v^{(1)}(x, y - y_c, z; +v_x) + v^{(2)}(x, y + y_c, z; -v_x)\ , && (7.28) \end{aligned}$$

  where η_{ab} is the Minkowski metric in Cartesian coordinates.

- we are interested on modeling **FB** stars binary systems in two different scenarios in which: (i) the bosonic matter of each star only interact through gravity with the bosonic matter of the other one, and (ii) the bosonic matter allows for gravity and scalar field interactions. Therefore, the full solution for these cases can be divided in two cases:

  (a) **Non-interacting scalar field (NIST):**

$$\begin{aligned} \Phi^{(1)} &= \Phi^{(1)}(x, y - y_c, z; +v_x)\ , && (7.29)\\ \Phi^{(2)} &= \Phi^{(2)}(x, y + y_c, z; -v_x)\ . && (7.30) \end{aligned}$$

(b) **Interacting scalar field**: described by a Single Scalar field (**ISF**):

$$\Phi \quad = \quad \Phi^{(1)}(x, y - y_c, z; +v_x) + \Phi^{(2)}(x, y + y_c, z; -v_x) \ . \tag{7.31}$$

As in **BSs** and **DBS** cases, a fine-tuning of the initial orbital velocity is required to set the binary in a quasi-circular orbit. Notice that the superposition explained above does not satisfy the energy and momentum constraints due to the non-linear character of Einstein's equations. Nevertheless, the **CCZ4** formalism used enforces dynamically an exponential decay of these constraint violations, see Section 5.6.

7.5 Coalescence of Fermion-Boson Stars

In the present section, binaries of neutron star, with different fractions of bosonic dark matter in their interiors, are modeled by using **FB** stars. We evolve numerically three different binary **FB** stars belonging to the stable branch, with individual mass of $M_{ADM} = 1.35$, compactness $C = 0.12$ and the following boson-to-fermion ratios $Y_B = \{0\%, 5\%, 10\%\}$. These equilibrium configurations are constructed by using a polytropic **EoS** with $\Gamma = 2.5$, but varying the polytropic constant κ to achieve solutions with the same total mass and compactness.

The radial profiles of some relevant quantities (i.e, the metric components $\alpha(r)$ and $\psi(r)$, the scalar field $\phi_0(r)$ and the density $\rho(r)$) for these three configurations are displayed in Figure 7.3. Obviously, the number of boson increases with the scalar field.

The characteristics of our isolated **FB** stars models are summarized in Table 7.1: the boson-to-fermion ratio Y_B, central value of the density ρ_c, central value of the scalar field ϕ_c, polytropic constant κ, angular frequency in the complex plane ω, boson and fermionic radius of the star R_B and R_F, and bosonic and fermionic masses. We also include some quantities of the coalescence: merger time, defined as the maximum of the norm of the $\Psi_4^{2,2}$, and the frequency of the dominant peak in the Fourier spectral power distribution, calculated as the Fourier transform of $\Re(\Psi_4^{2,2})$ during the post-merger stage.

Our simulations are performed in a domain $[-480, 480]^3$ with a coarse resolution of $\Delta x_0 = 6.8$. There are 6 levels of refinement, the last one only covering both star during their coalescence, such that the finest resolution is $\Delta x_5 = 0.21$. Furthermore, each **FB** star is initially centered at $(0, \pm 16, 0)$ and have a boost velocity $v_x = \pm 0.173$, leading to a binary system in a tight quasi-circular orbit. During the evolution, we employ an ideal-gas **EoS** (3.61), which is able to capture the fluid heating due to strong shocks produced in the merger stage [63, 123]. Additionally, the gravitational radiation emitted during the coalescence, described by the Newman-Penrose scalar Ψ_4 (2.105), see Section 2.4.1

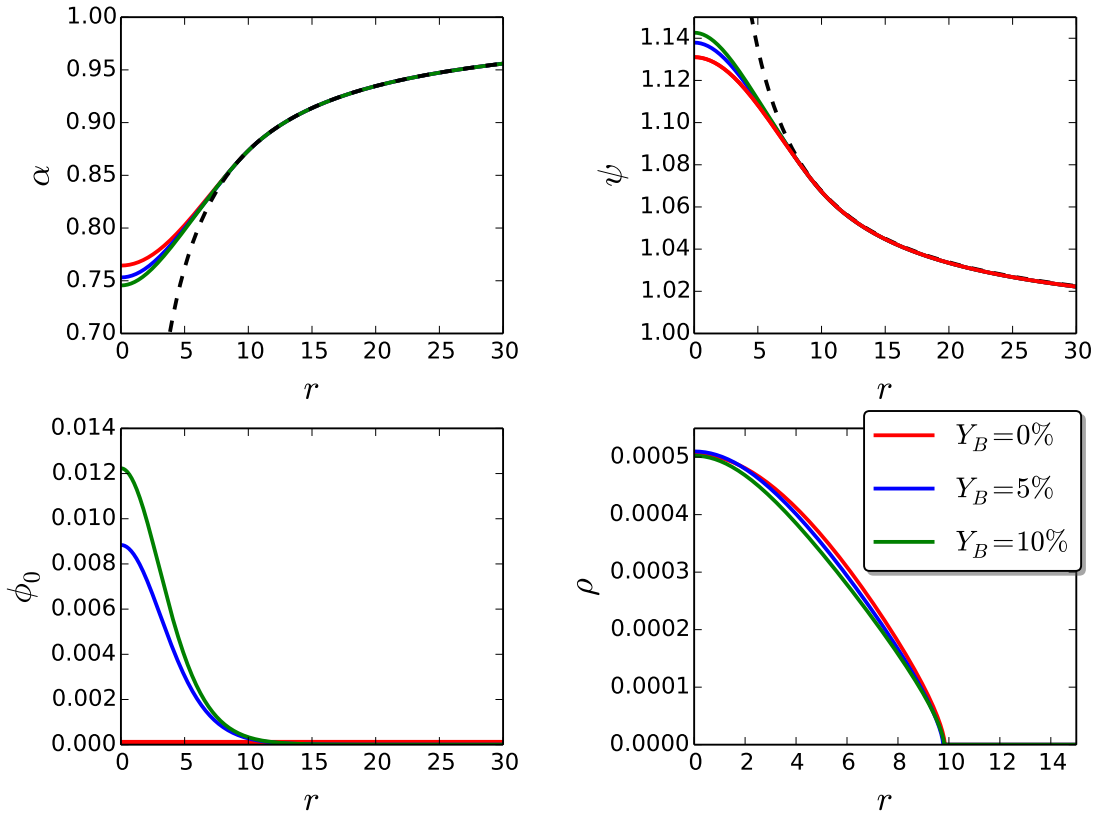

FIGURE 7.3: *Initial configuration for each FB star considered in the binary system.* The metric component profiles of $\alpha(r)$ and $\psi(r)$ (top panel), and the radial scalar field $\phi_0(r)$ and radial density profiles (bottom panel) respectively, for each boson-to-fermion ratio. As the boson-to-fermion ratio grows the radial profile of the scalar field increases. The dashed black lines show the Schwarzchild solution with the same mass of the FB star.

Y_B	Model	ρ_c	ϕ_c	κ	ω	R_B	R_F	N_B	N_F	$t_{\rm merger}$	$f_{\rm peak}$[kHz]
0	NS	5.0525×10^{-4}	0.0	7405	0	0	11.23	0.0	1.44	1650	1.62
5	NISF	5.0989×10^{-4}	8.838×10^{-3}	8136	0.814704559507	10.37	11.16	0.0721	1.37	1626	1.81
10	NISF	5.0244×10^{-4}	1.223×10^{-2}	8980	0.811068278806	10.15	11.20	0.1262	1.32	1606	1.87
10	ISF	5.0244×10^{-4}	1.223×10^{-2}	8980	0.811068278806	10.15	11.20	0.1262	1.32	1616	1.93

TABLE 7.1: *Summary of the binary FB star configurations.* The table shows: boson-to-fermion rate Y_B, central value of the scalar field, polytropic constant κ, angular frequency of the phase of Φ in the complex plane, bosonic radius (containing 99% of the Noether charge), fermionic radius (i.e, the radius where the fluid pressure vanishes), bosonic and fermionic masses. All models have ADM mass $M = 1.35$ and compactness $C = 0.12$. The last two columns are related to the simulation results: merger time, defined as the one corresponding to the maximum of the norm of the $\Psi_4^{2,2}$, and frequency of the dominant peak in the power spectral density of the $\Psi_4^{2,2}$, evaluated during the post-merger stage.

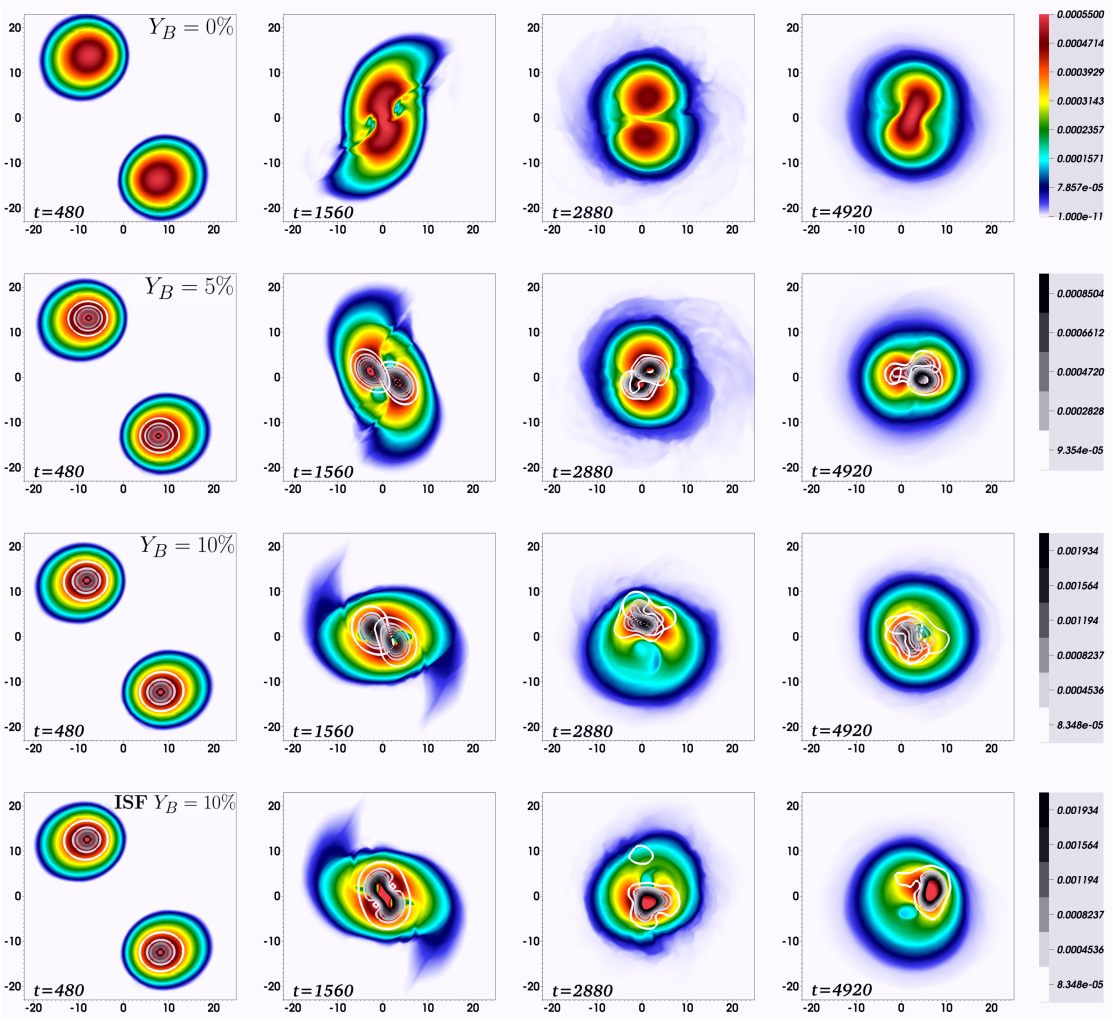

FIGURE 7.4: *Dynamics of **FB** stars coalescence.* Rest-mass densities for the fermionic components are represented in colors, while Noether charge densities are displayed in white-to-black contours, in the equatorial plane ($z = 0$), at different representatives times. The rows correspond to the cases (from top to bottom) **NS, NISF** with $Y_B = \{5\%, 10\%\}$, and **ISF** with $Y_B = 10\%$. The first column illustrates a time in the early inspiral, the second one is roughly at merger time, the third one is during the post-merger stage and the fourth one at the end of our simulation.

is analyzed. Recall that, **GWs** are computed as spherical surface integrals at different extraction radii.

7.5.1 Dynamics

The main dynamics can be inferred from the snapshot on the equatorial plane of the rest-mass densities and the Noether charge densities for each case, at relevant times of the coalescence, displayed in Figure 7.4.

All the binaries behave quite similar during the inspiral stage, completing at least two full orbits before the merger. Both the fermionic and the bosonic part of each star moves

perfectly synchronized during this stage. After roughly two orbits, the fermionic components of both stars collide and form a new object, which can be described basically as a differentially rotating massive neutron stars with a shape dominated by a quadrupolar structure, as can be seen in the second and the third panel, first row in Figure 7.4. This rotating remnant produces gravitational waves in the dominant modes $l = |m| = 2$, see Reference [213] and references therein.

This behavior changes as the bosonic matter core inside of the neutron stars is increased. Although the dark cores inside of the **NSs** during the inspiral phase follow the same trajectory of the baryonic matter, differences appear at the merger for the cases $Y_B = 5\%$ and $Y_B = 10\%$ studied here: while the neutron stars are plunging and forming a rotating remnant with a quadrupole structure which bounces radially back and forth, the bosonic cores remain in a tight orbit until the contact time, defined as the same way as in the previous Chapter 6. Thereafter, the bosonic cores overlap in space and forming a superposition of two coexisting orbiting dark boson cores, see previous Chapter 6 ([196]).

During the post-merger stage, in the case **NISF** with $Y_B = 10\%$, the dark matter in the remnant excites the one-armed spiral instability [214–216] that breaks the quadrupolar structure of the system. Figure 7.5 displays the differences on the density profile in the equatorial plane ($z = 0$) between the cases $Y_B = 0\%$ and $Y_B = 10\%$ in the post-merger phase, showing the symmetry breaking of the quadrupole structure when there is a significant amount of bosonic component inside the **NS**. Once this single baryonic overdensity appears, the scalar field clusters in that region and then the two matter fields (i.e., the fluid and the dark matter) rotate together. This lack of quadupolar symmetry is also found in the case $Y_B = 5\%$, although the full development of the $|m| = 1$ overdensity can not be seen as clearly within the time reached by our simulation.

For comparison purposes, we also evolve the case with ratio $Y_B = 10\%$ with **ISF**. In this particular case, the dynamics during the inspiral is similar to the case **NISF** $Y_B = 10\%$. Differences arise after the merger: in this stage, the scalar field interactions play an important role by forming a single largely-perturbed bosonic core inside the **NS** remnant. Nevertheless, the one-armed spiral instability is seen anyway, probably because it is triggered by the initial presence of four components, which are strongly coupled only two by two (fermionic cores between them, and bosonic components between them).

As it was discussed in [216], this instability can develop gravitational radiation with a significant $l = 2$, $m = 1$ component at frequencies in which the sensitivity of the detector is higher [217], which can be relevant in future observation of gravitational waves from neutron stars mergers.

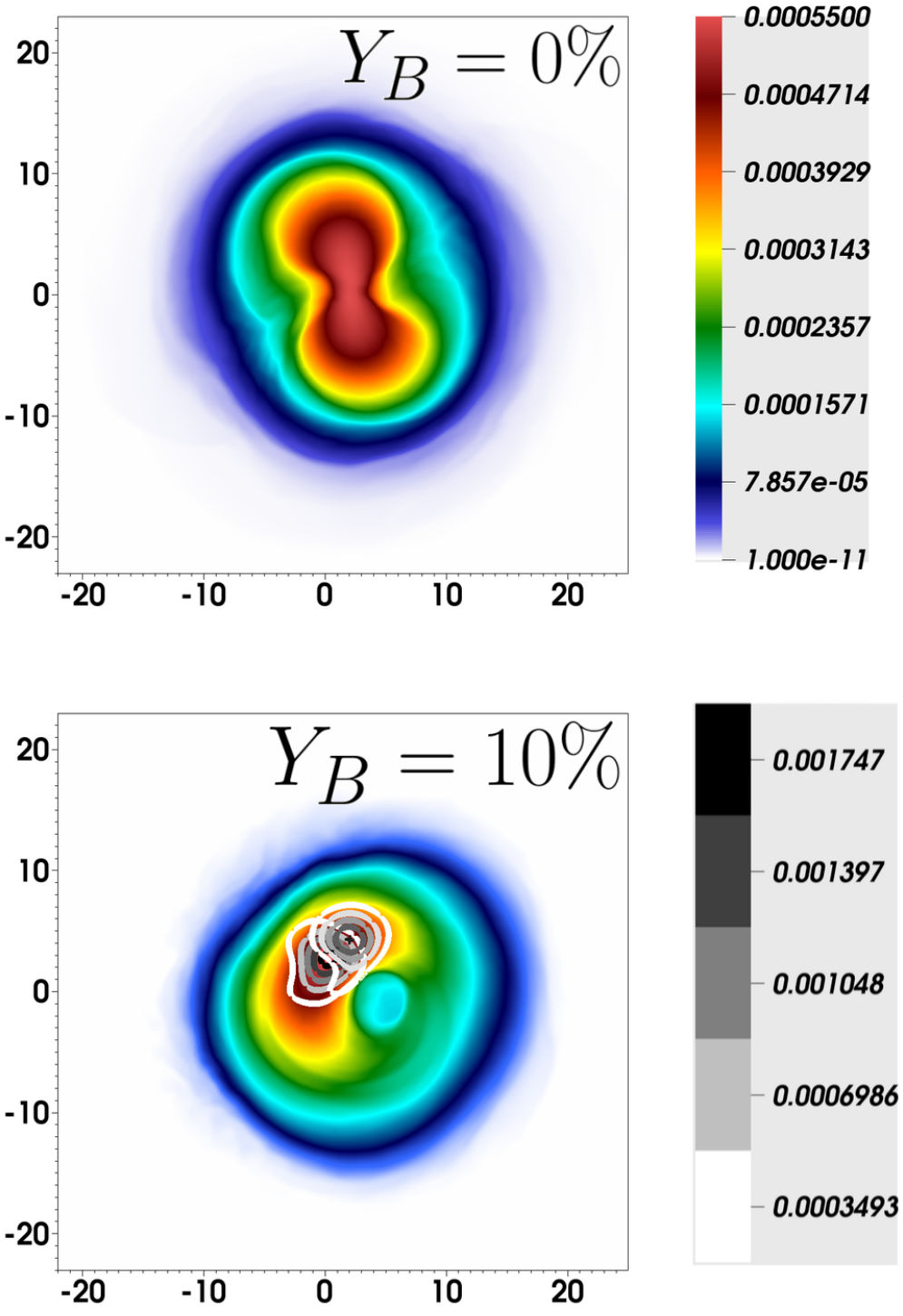

FIGURE 7.5: *Comparison of* $Y_B = 0\%$ *versus* $Y_B = 10\%$. Rest-mass fermionic densities in the equatorial plane in the post-merger stage (i.e., roughly at $t \simeq 4440$) of the $Y_B = 0\%$ (top panel) and **NISF** with $Y_B = 10\%$ models. The Noether charge densities are added as white-to-black contours in the case $Y_B = 10\%$.

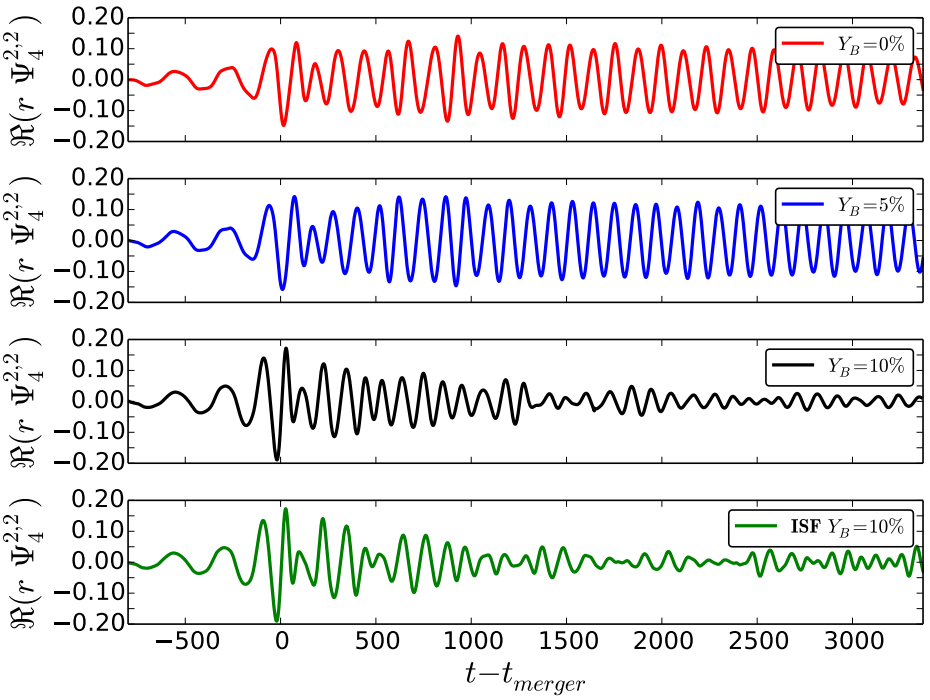

FIGURE 7.6: *Gravitational waves.* The real part of the main $l = m = 2$ mode of Ψ_4 describing the gravitational emission produced by **FB** binaries, as a function of time on from the merger, for all models (top to bottom).

7.5.2 Gravitational wave radiation

The main mode $l = |m| = 2$ of the Newman-Penrose scalar Ψ_4 is displayed in Figure 7.6 for the four different cases considered previously, where the time has been shifted such that the merger time occurs at $t = 0$.

The gravitational radiation produced during the early inspiral is roughly the same for all the cases, with differences arising at and after the merger. As the boson-to-fermion ratio Y_B increases, the strength of the gravitational waves achieves a slightly larger amplitude maximum at the merger time. In all cases, strong oscillations are present soon after the merger, but notably they decay quickly in the case with largest **DM** cores $Y_B = 10\%$, both for **NISF** and **ISF** models. As the ratio Y_B decreases, these oscillations are stronger with a larger amplitude. This huge difference could be possibly due to a quick redistribution of the density profile on the remnant, such that the quadrupole moment transfers energy to the $m = 1$ mode (i.e., for instance by the one-arm instability [218]). As discussed in [216], to develop of $m = 1$ one-arm instability a mechanism is needed in order to break the symmetry allowing odd modes.

To analyze this symmetry breaking, the strength of the dominant $l = 2$ modes of the **GWs** are displayed in Figure 7.7 for all cases. As we can observe, the mode $m = 1$ has a similar behavior for all the cases, achieving roughly the same saturation level after the

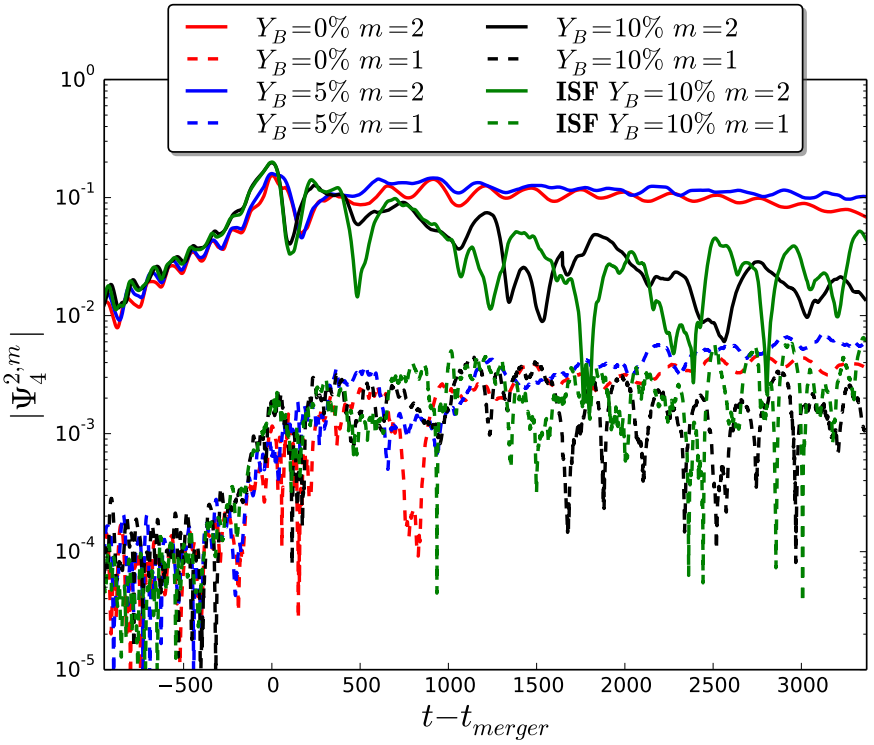

FIGURE 7.7: *Gravitational waves.* The norm of a given mode $(l = 2, m)$ of the gravitational radiation described by the Newman-Penrose scalar Ψ_4 as a function of time from the merger for the different cases.

merger. However, significant differences arise in the mode $m = 2$: while the strength of this mode is roughly constant for the cases $Y_B = \{0\%, 5\%\}$, the other cases with the largest **DM** cores (i.e. $Y_B = 10\%$ and **ISF** $Y_B = 10\%$) display an exponential decay soon after the merger.

In order to check if there is any transfer of energy through others m-modes, the strength of the total gravitational radiation is compared with the main mode $l = |m| = 2$ in Figure 7.8. Clearly, the main radiative contribution comes from the main mode. Thus, we can conclude that the loss of quadrupole symmetry does not induce a significant additional radiation in the modes $m = 1$.

Finally, we can learn further information about the properties of the **FB** stars by analyzing the gravitational waves after the merger [170]. The power spectral density of the Fourier transform for the Ψ_4 modes $(l = 2, m)$ at this stage is displayed in Figure 7.9. The frequency of the dominant mode corresponds to the double of the orbital period at the merger time, and it is associated to a mixture of the rotational motion and the quadrupolar structure. The values of these peak frequencies are presented in Table 7.1. The peak in frequency spectrum for the $|m| = 1$ mode is more than one order of magnitude weaker than the $|m| = 2$ mode. However, as already previously noted for unequal binary NS mergers [191, 216], for the model with $Y_B = 10\%$, in which the

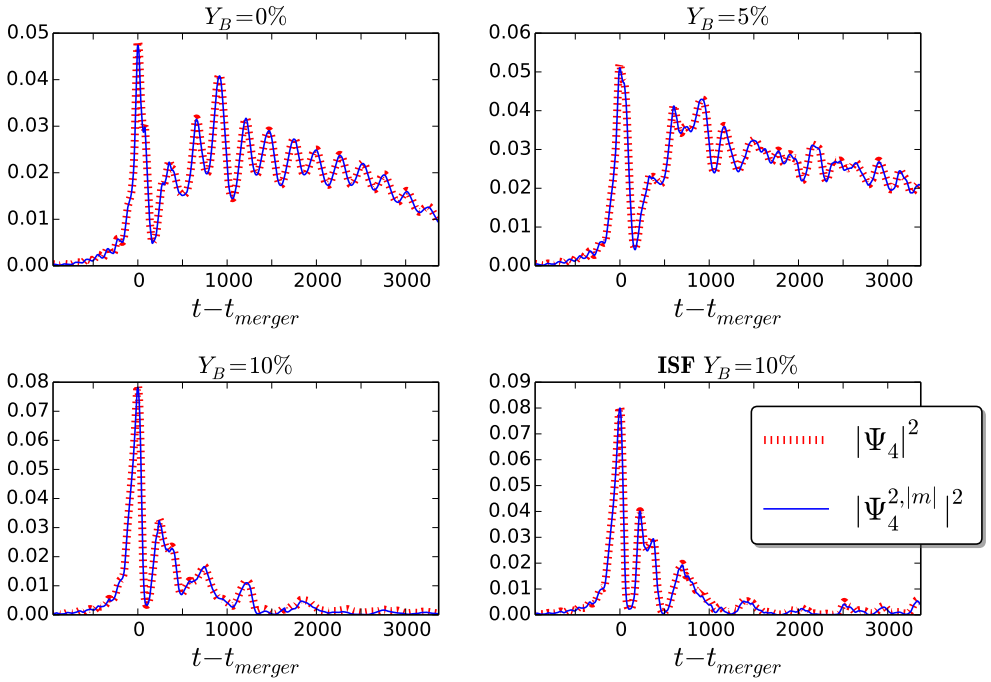

FIGURE 7.8: *Gravitational waves.* The norm of the total gravitational radiation emitted during the coalescence and the norm of the $l = |m| = 2$ dominant modes, as a function of time from merger, for the different cases. They basically overlap, showing that the main contribution to **GW** emission always comes from the $l = |m| = 2$ mode.

one-arm instability fully develops, the peak of the $|m| = 1$ mode is at half the frequency of the one corresponding to the $|m| = 2$ mode. Quantitatively, for that case we obtain $f_{m=1} = 0.935$ kHz and $f_{m=2} = 1.87$ kHz, when the one-arm instability fully develops. The exact value depends on the chosen **EoS**, and for a realistic one, the typical value of $f_{m=2}$ are found to be between $\sim [2 - 3.5]$ kHz, see Refs. [170, 191]. Regardless on the specific value, for frequencies corresponding to the $|m| = 1$ mode, the Earth-based detectors are more sensitive and might be able to distinguish these features, for close enough events. In particular, finding a peak with $f \sim 1$ kHz in equal-mass low-spinning binaries could be a signature of **DM** presence.

7.6 Discussion

In this last Chapter, we have studied by using full 3D numerical simulations, the dynamics and gravitational radiation emitted during the coalescence of binary **NSs** with **DM** clustered in their interior. These objects have been modeled by using **FB** stars, i.e, compact stellar objects made with a mixture of a perfect fluid and a complex scalar field. In our model, we have considered that in each star the fermionic matter interacts with the bosonic matter cores only through gravity. In particular, we have considered

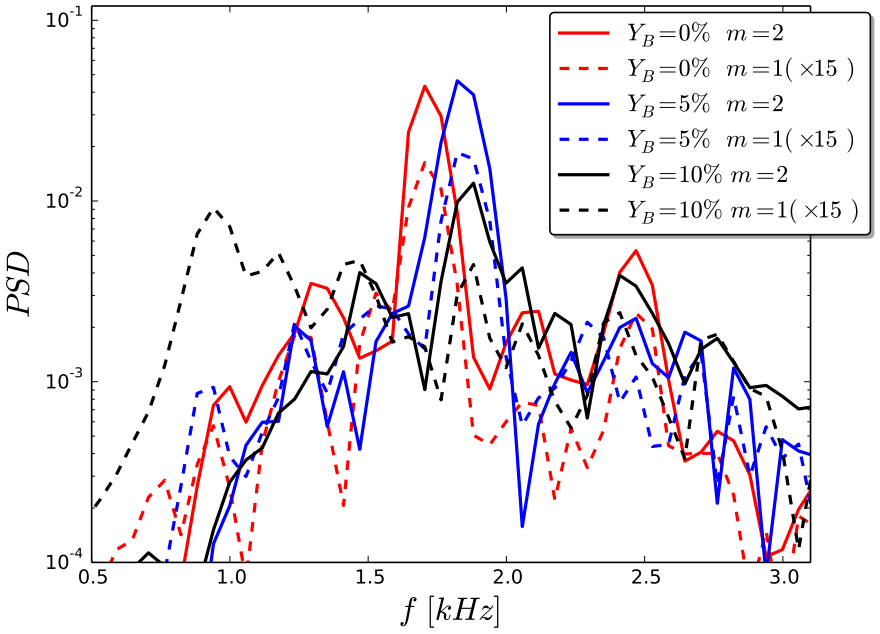

FIGURE 7.9: *Gravitational waves.* Fourier transform of the real part of Ψ_4, considering from the merger time on, for the models **NS** and **NISF** with $Y_B = \{5\%, 10\%\}$. We show the $(l = 2, |m| = 1)$ mode, amplified by a factor 15 for visualization purposes, and the dominant $(l = 2, |m| = 2)$ mode. The dominant radiation mode after the merger is given by $(l = 2, |m| = 2)$, achieving peaks at frequencies $f_{\rm peak} = \{1.62, 1.81, 1.87\}$ kHz respectively. The only significant $(l = 2, |m| = 1)$ mode corresponds to the case $Y_B = 10\%$, with a peak at $f_{\rm m=1} = 0.935$ kHz, at half the frequency of the $|m| = 2$ one.

binaries formed for stars with the same individual **ADM** mass $M = 1.35$ and compactness $C = 0.12$, but with three different boson-to-fermion ratio $Y_B = \{0\%, 5\%, 10\%\}$, to study the dependence on the amount of **DM** in the stars.

We have found that, during the inspiral, both the dynamics and the **GWs** radiated in these three cases are roughly the same, making it very difficult to distinguish differences with respect to a canonical binary **NS** with $Y_B = 0\%$. At the merger stage differences arise in the dynamics for the cases $Y_B = 5\%$ and $Y_B = 10\%$: while the **NSs** merge and form a rotating remnant, the boson components keep orbiting maintaining its individual shape for longer times. In the late post-merger differences grow larger with respect to the case $Y_B = 0\%$, where the dynamics is governed by a massive **NS** which rotates differentially with a dominant quadrupolar shape, and producing **GWs** in the $l = |m| = 2$ modes. In the case $Y_B = 10\%$, the dark bosonic cores cause a redistribution of the fermionic matter, breaking the quadrupolar symmetry of the remnant and forming an $|m| = 1$ over-density through the one-arm instability, which is excited by the asymmetries introduced by the three-body interaction (i.e., fermionic matter plus two bosonic cores coupled only through gravity). In this case, the dominant **GW** mode $l = |m| = 2$ decay exponentially much faster than for $Y_B = 0\%$. For comparison purposes, we have also considered a binary where the bosonic **DM** interacts through both

gravity and scalar field interactions, obtaining roughly the same results as before. This seems to indicate that the one-arm spiral instability develops generically in the merger of **NSs** with **DM** cores due to the many-body-interaction after the merger.

Let us stress the differences of our results with respect to the ones obtained in Reference [219], where they introduce a Lagrangian with four coupled objects (i.e., two **NSs** and two **DM** cores) to describe the post-merger dynamics. They pointed out the presence of supplementary peaks at higher frequencies than the $|m| = 2$ mode in the post-merger spectrum of **NSs** mergers, but could not anticipate the lower frequency peak due to the one-arm instability.

As it was also notice in [216], although the $|m| = 1$ modes strength in our case is at least fifteen times smaller, it becomes more relevant as a contributor to the post-merger **GW** signal since it occurs at a frequency half of the dominant mode $|m| = 2$, where the **GW** detectors are more sensitive. Notice however that there is some degeneracy, since this instability has also been observed to happen in several binary **NS** merger simulations [217], especially with spin and/or eccentricity [214, 218] and for unequal mass stars [191, 216]. There are two distinct features of our case with respect to those ones. First, the one-arm instability strongly develops even for equal mass no-spinning objects, a feature that could be measured from the **GW** during the inspiral. Therefore, the waveform before the merger might contain enough information to break partially the degeneracy and discard some of the asymmetries which could produce a strong one-arm instability. Second, although the exponential decay affecting the $|m| = 2$ mode also occurs in unequal mass or highly spinning binaries, it shows a faster attenuation in our cases. Therefore, possible detection of these modes with current or future detectors, combined with a detailed analysis of the signal during the inspiral, could constraint the presence of **DM** cores inside **NSs** and enhance our understanding of its nature.

Concluding remarks

In this Thesis, I have studied the gravitational waves produced during the binary coalescence of Exotic compact objects, by solving numerically Einstein equations coupled with different types of matter. The main new results presented on this manuscript are the following.

We have modified the **CCZ4** formalism, see Chapter 2, such that it does not require the algebraic enforcement of any constraint after each step of the numerical integration. Furthermore, the pseudo-hyperbolicity of the resulting evolution system has been analyzed by using a linear plane-wave analysis to show that, for a specific choice of some free parameters, the system is strongly hyperbolic (i.e., it has a complete set of eigenvectors with real eigenvalues). Therefore, the linearized system is well-posed. In addition, in Chapter 4, we have performed some **NR** test to check the robustness of our implementation of the modified **CCZ4** formalism, including the evolution of isolated solitonic boson stars, an non-rotating neutron star and a mixed fermion-boson star (see Chapter 7). Our numerical results – stable evolutions with small and bounded constraints – confirm the analytical analysis.

Solitonic boson star binaries are studied in Chapter 5. Recall that solitonic **BSs** are a specific family of **BS** with a potential leading to solutions with compactness that is comparable or even higher than that of neutron stars. The first part of the chapter studies the dynamics of these systems, focusing on binaries where each star has a fixed compactness $C = 0.12$ but with different phases and signs in their harmonic time dependence. We have found that the head-on collision of two **BSs**, differing only by a relative phase, generically produced a massive and significantly perturbed **BS**. However, a **BS** that collides with an anti-**BS** (i.e. another **BS** with the opposite frequency but otherwise identical), annihilates the Noether charge of the system and most of the scalar field disperses to infinity. Surprisingly, the addition of angular momentum does not seem to change this qualitative picture. Although the merger of a pair of orbiting **BSs** produces a rotating remnant, the final object eventually settles down into a stationary

non-rotating **BS** by radiating all its angular momentum via **GW** radiation and scalar field dispersion.

The second part of Chapter 5 is based on the dynamics and the gravitational radiation produced by the coalescence of solitonic **BS** binaries, where we have considered four different initial compactnesses $C = \{0.06, 0.12, 0.18, 0.22\}$. Here, we have found a critical compactness, C_T, belonging to the interval $C_T \in (0.18, 0.22)$ where the dynamics behaves in a different way. For instance, for $C \lesssim C_T$ (low compactness) the remnants loss angular momentum and decay to non-rotating **BSs**. The signal is really small during the inspiral phase, but it rises quickly at the merger. Otherwise, for $C \gtrsim C_T$, the remnant collapses to a **BH**, being the signal in the post-merger stage dominated by the shape of the typical ring-down of a spinning **BH**. Therefore, the results of this numerical study suggest that binary boson stars generically merge into either a black hole or a non-rotating boson stars.

In the Chapter 6, we have considered dark stars, astrophysical compact objects made of dark matter such that they only interact with other stars through gravity. Here, we have studied binaries of dark stars made by bosonic scalar field considering the same range of compactness as the Chapter 5. The dynamics and the gravitational radiation generated during its coalescence have been analyzed, contrasting both with previous simulations of binary **BSs** (where there exists interaction between the stars through both gravity and the scalar field) and with Post-Newtonian T4 approximation with and without tidal effects. Our numerical simulations have shown that dark boson stars define a new kind of compact objects whose merger produce a gravitational signature noticeable from black holes, neutron stars and boson stars.

Finally, in Chapter 7, we have studied binaries of neutron stars with a small fraction of dark matter on their interiors, modeling them through mixed fermion-boson stars. We have investigated the dynamics and gravitational radiation emitted during their coalescence. We have found, as the amount of dark matter cores within the neutron stars increases, some noticeable differences appear in the post-merger regime. In particular, our results have revealed the presence of a strong $m = 1$ mode in the waveforms during the post-merger stage, together with redistribution of the fermionic matter, which causes a break the quadrupolar symmetry of the remnant by forming an $|m| = 1$ over-density through the one-arm instability.

a break of the quadrupolar symmetry, generating a over-density . Certainly, we will extend our analysis of those binaries studying, for example, the lifetime of the remnant and the ejected mass during the merger.

All these studies might be important to distinguish these events from other binaries with current/future detection by either ***LIGO*** *and* ***Virgo*** *ground-based interferometers or* ***LISA*** *space-based interferometer, as well as to set constraints on some dark matter models.*

There are natural research lines to be extended and further studied. For instance, one could consider binaries with unequal masses and see the differences with respect to the equal mass case. One of the most interesting projects would be to repeat some of the coalescences of binary systems composed by exotic objects mentioned above, but starting from an accurate initial data in quasi-circular orbit. This would allow us to construct reliable gravitational waves templates for the entire coalescence, namely, inspiral, merger and post-merger. Another interesting work is to study the tidal Love numbers of the mixed fermion-boson stars considered in Chapter 7 in order to compare their gravitational waves frequencies with the neutron stars, black holes or even boson and dark boson stars.

Appendix A

Some estimation for Boson Stars and Dark Stars

A.1 Estimate of the gravitational radiation in the post-merger stage for boson stars

A simple estimate of the amount of energy the system can radiate can be obtained following the model presented in [188]. Aided by the results from numerical simulations of Chapter 5, we can further refine such a model for the behavior observed in the merger of binary **BSs**. Namely, we observe that, in the case where collapse to a **BH** is avoided, the final result is a **BS** remnant with no angular momentum and with radius R_r having mass M_r that is roughly the total initial mass M_0 (i.e., $M_r \approx M_0 = M_1 + M_2$) . The merger takes place at "contact", that is, when the stars are separated by $R_1 + R_2$. Thus, the energy of the system at such an instant is roughly

$$\begin{aligned} E_{\rm contact} &= E_{12}^{\rm pot} + E_{12}^{\rm kin} + E_1^{\rm pot} + E_2^{\rm pot} \ , \\ &= -\frac{M_1 M_2}{R_1 + R_2} + \frac{1}{2} I_c \Omega_c^2 - \frac{3M_1^2}{5R_1} - \frac{3M_2^2}{5R_2} \ , \end{aligned} \tag{A.1}$$

where we have included the binding energy of each star and have assumed that the stars have constant density. The moment of inertia I_c with respect to the center of mass, assuming the stars are irrotational, can be written at contact time as

$$I_c \equiv \frac{M_1 M_2}{M_1 + M_2} (R_1 + R_2)^2. \tag{A.2}$$

Notice that at contact time the orbital frequency can be estimated as $\Omega_c^2 = \frac{M_1 + M_2}{(R_1 + R_2)^3}$. Following the discussion in [188], for the equal mass case ($M_1 = M_2 = M$ and $R_1 =$

$R_2 = R$) this energy can be expressed as a function of the compactness $C = C_1 = C_2$ as

$$E_{\rm contact} \approx -\frac{29}{20} MC \ . \tag{A.3}$$

As the collapse takes place, the system ultimately settles into a non-rotating **BS**. The energy left in the system (beyond the rest mass) is given by the potential energy of the **BS** which, assuming a spherical object of uniform density, can be estimated as

$$E_{\rm final} = -\frac{3M_r^2}{5R_r} \ , = -\frac{12}{5} MC \frac{R}{R_r} \ , \tag{A.4}$$

where we have considered an upper bound $M_r \approx 2M$. Assuming no scalar radiation, we can now estimate the radiated energy in gravitational waves during different states of the system. In particular, the total amount of energy radiated $\mathcal{E}_{\rm rad}$ and radiated after contact $\mathcal{E}^{ac}_{\rm rad}$ are,

$$\begin{aligned} \mathcal{E}_{\rm rad} &= -(E_{\rm final} - E_{\rm initial}) \ , & \text{(A.5)} \\ &\approx \frac{6}{5}(2\frac{R}{R_r} - 1)\, CM \ , & \text{(A.6)} \\ &\approx 0.96\, CM = 0.48\, CM_0 \ , & \text{(A.7)} \end{aligned}$$

and

$$\begin{aligned} \mathcal{E}^{ac}_{\rm rad} &= -(E_{\rm final} - E_{\rm contact}) \ , & \text{(A.8)} \\ &\approx \frac{MC}{20}\left(-29 + 48\frac{R}{R_r}\right) \ , & \text{(A.9)} \\ &\approx 0.71\, CM = 0.36\, CM_0 \ , & \text{(A.10)} \end{aligned}$$

and we have estimated the ratio $R/R_r \approx 0.9$ from our simulations (alternatively, assuming the effective density of the individual **BSs** is similar to that of the merged **BS**, one has $R/R_r = 1/2^{1/3} \approx 0.8$). Notice that for $C \gtrapprox 0.1$, if no collapse to a black hole takes place, this implies that highly compact binary boson star systems are examples of "super-emitters," in the terminology introduced in [188] (as the analogous **BH** binary system emits $\approx 5\%$ of their total mass).

A.1.1 Estimate of after-merger frequency of gravitational waves

We can also attempt to estimate the frequency of gravitational waves soon after merger has taken place. For this, we begin *assuming* angular momentum is nearly conserved around the moment where the collision (contact) takes place. For the case of irrotational

binaries, the angular momentum at contact can be approximated by the expression

$$L_c = I_c \Omega_c \ , \tag{A.11}$$

with I_c and Ω_c as defined in Appendix A.1. Soon after contact, we have instead

$$L_r = I_r \Omega_r \ , \tag{A.12}$$

where I_r is the moment of inertia of the newly formed object (i.e, the remnant) assuming no prompt collapse to a **BH** takes place. Let us now assume a relation of these angular momentum given by $L_r = \kappa L_c$ with $\kappa \in [0, 1]$ a factor introduced to account for loss of angular momentum during the merger. Now, since the angular frequency of gravitational waves $\omega = 2\Omega$, we have (specializing to the equal mass case)

$$\begin{aligned} I_r \omega_r &= \kappa 2 M R^2 \omega_c \ , \\ M_r^3 (I_r / M_r^3) \omega_r &= \kappa 2 M^3 C^{-2} \omega_c \ , \end{aligned} \tag{A.13}$$

with C denoting the compactness of the individual stars, M their individual masses, and M_r and I_r the mass of the remnant and its moment of inertia respectively soon after contact. Rearranging, the gravitational wave frequency soon after contact implies

$$\omega_r = \frac{\kappa}{4} \frac{C^{-2}}{\bar{I}_r} \omega_c \ , \tag{A.14}$$

where we have defined $\bar{I}_r = I_r M_r^{-3}$.

In the case of binary neutron star mergers, extensive studies already indicate a small amount of angular momentum is radiated during the merger, so we can adopt $\kappa \simeq 1$. For realistic equations of state, we can make use of thorough investigations of the values of $\bar{I}_r$ for isolated stars for a wide range of compactness and mass (e.g. [220]) to evaluate Eq. (A.14). This gives $\omega_r \approx 2.8\, \omega_c$, in excellent agreement with results from numerical simulations (e.g. [191]). This is not surprising since the angular momentum in the system right before contact is primarily transferred to the object formed after merger.

This is not the case for binary boson stars. As opposed to the case for neutron stars, general values of $\bar{I}_r$ for boson stars are not available but we can estimate them either from our isolated **BS** solutions or by considering that they behave as constant density spheres, namely $I = (2/5) M R^2$. Since the result will not change significantly, we use the latter approximation which yields

$$\omega_r = \kappa \frac{5}{2} \left(\frac{R}{R_f} \right)^2 \omega_c \approx 2\, \kappa\, \omega_c \ , \tag{A.15}$$

where again we estimated $R/R_f \approx 0.9$ from our simulations. The corresponding estimate would give an upper bound factor (taking $\kappa = 1$) in $[2 - 2.5]$ which is higher than the fit in Eq. (5.23). However, as we have seen, a large amount of angular momentum is lost through the merger. From Fig. 5.9 one would expect $\kappa \approx 1/4$ making the "expected" frequencies from this naive estimate much too low when compared with the measured peak frequency in gravitational waves. This is in strong contrast to what is observed in the case of binary neutron star mergers.

As the next section illustrates, the after-merger radiation of boson stars is determined by the quasi-normal modes of the produced boson star or by the **BH** in the case of collapse. This is a consequence of our observation that the merger of boson stars does not produce a rotating boson star and that the speed of propagation of perturbations in boson stars is faster than that in neutron stars.

A.1.2 Quasi-normal modes of isolated solitonic boson star

Quasi-normal modes for isolated solitonic boson stars can be computed by evolving numerically a perturbed star and analyzing the gravitational wave radiation. The formalism and numerical schemes are the same as the ones used in Chapter 5 for binaries, such that only the initial data differs. We have chosen stable boson stars with total mass $M = 1$ for different compactnesses ranging from $C = 0.06 - 0.22$. These equilibrium configurations are deformed by adding a small perturbation on the conformal factor which introduces constraint violations below the truncation error of the unperturbed configuration, and so we need not re-solve the constraints. In order to ensure the excitation of gravitational modes, the perturbation has a toroidal shape with a $m = 2$ dependence in the axial direction.

The top panel of Fig. A.1 shows the Fourier transform of the main gravitational wave mode (i.e., $l = m = 2$) as a function of frequency. Although there are several peaks in the spectra, we focus only on the two strongest modes at the lowest frequencies. Clearly, the frequencies of the fundamental and the secondary quasi-normal modes increase with compactness. The bottom panel displays the adimensional frequency of these two modes as a function of the compactness. We have also included the frequencies of the remnant after the merger of the case studied here, given in Table 6.1. There is a good agreement between the **QNM** of the single stars and the fundamental mode of the remnant of the binary.

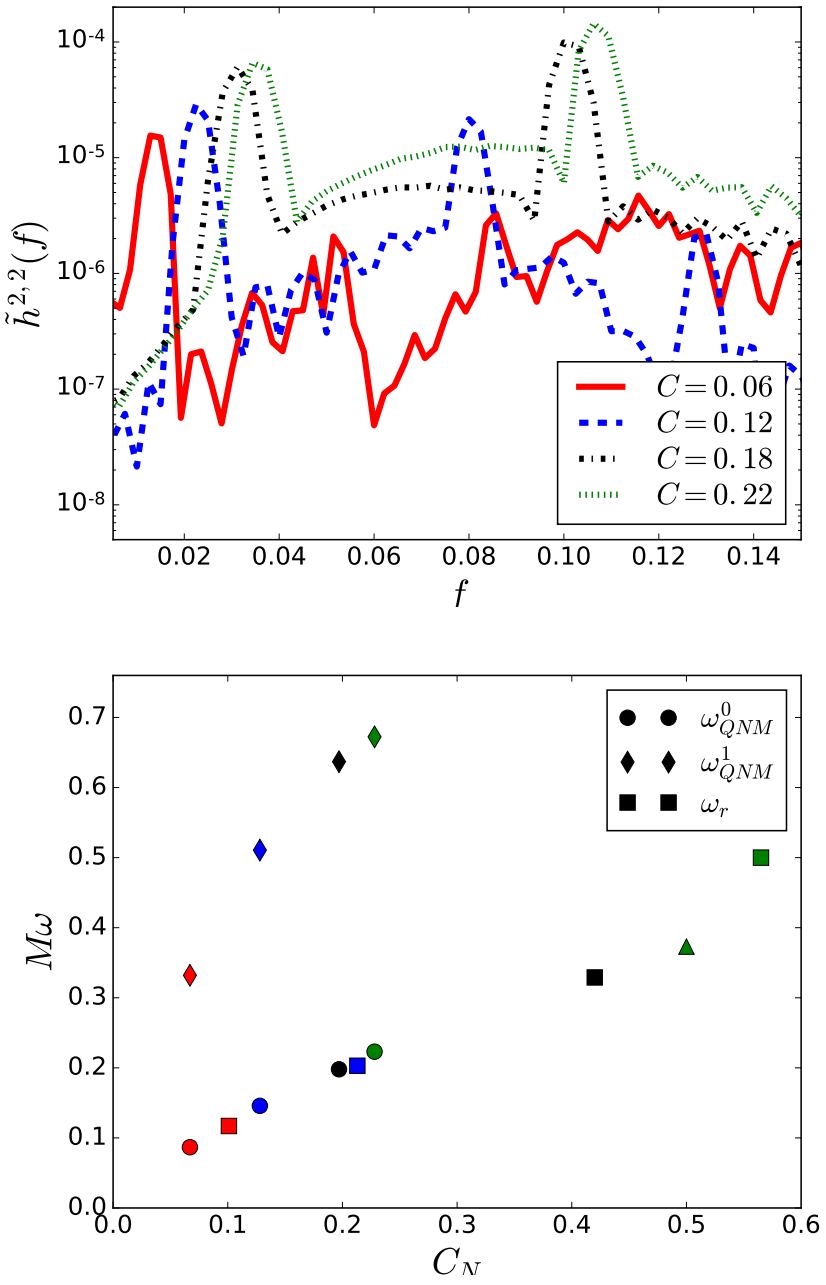

FIGURE A.1: (Top) Fourier spectrum of the main mode of the strain $\tilde{h}^{2,2}(f) \equiv \mathcal{F}[h_{22}(t)]$ for several isolated solitonic boson stars. (Bottom) The circles and the diamonds correspond,respectively, to the frequencies $\omega^0_{\rm QNM}$ and $\omega^1_{\rm QNM}$ of the lowest quasi-normal modes (i.e., fundamental and secondary peaks), as a function of the compactness $C_N \equiv M/R_N$. Squares represent the gravitational frequencies of the remnant resulting from a binary merger with that initial compactness. Notice that we have included the case with $C = 0.18$, which we do not trust completely, and the case $C = 0.22$ that ends up in Kerr **BH**. For comparison purposes, we have included also the **QNM** of a Schwarzschild **BH** (triangle).

A.2 Estimate of the gravitational radiation in the post-merger stage for DBSs

Following previous works [6, 188], we can estimate the amount of energy radiated by **DBS** binaries during their coalescence. This energy has been calculated for binary **BSs** in the previous section A.1 (or appendix of Ref. [6]). Considering the same assumptions for the equal mass case ($M_1 = M_2 = M$ and $R_1 = R_2 = R$), the energy when both stars make contact can be expressed as:

$$E_{\rm contact} = E_{12}^{\rm pot} + E_{12}^{\rm kin} + E_1^{\rm pot} + E_2^{\rm pot} \approx -\frac{29}{20} MC \ .$$

As the merger takes place, the system ultimately settles down into a non-rotating remnant composed by two coexisting **DBSs**. Therefore, the final energy in the system (beyond the rest mass) is just given by the binding energy, that for a spherical object with uniform density is:

$$E_{\rm final} = -\frac{3M_r^2}{5R_r} = -\frac{12}{5} MC \frac{R}{R_r} \ , \tag{A.16}$$

where we have considered an upper bound $M_r \approx 2M$. Assuming no scalar radiation, we can now estimate the radiated energy in gravitational waves radiated after contact $\mathcal{E}_{\rm rad}^{ac}$:

$$\mathcal{E}_{\rm rad}^{ac} = -(E_{\rm final} - E_{\rm contact}) \approx M_0 C \ , \tag{A.17}$$

where we have estimated the ratio $R/R_r \approx 1.4$ from our simulations. Notice that this energy estimate for **DBS** mergers is almost twice than the one obtained for **BSs** [6] (i.e., $\mathcal{E}_{\rm rad}^{ac} \approx 0.48\, M_0\, C$). The main difference comes from the ratio R/R_r, that in the remnant of **BSs** mergers was 0.9 but for **DBS** mergers is 1.4.

Bibliography

[1] Christopher J. Moore, Robert H. Cole, and Christopher P. L. Berry. Gravitational-wave sensitivity curves. *Classical and Quantum Gravity*, 32(1):015014, dec 2014. doi: 10.1088/0264-9381/32/1/015014. URL https://doi.org/10.1088%2F0264-9381%2F32%2F1%2F015014.

[2] Gravitational wave detectors and sources. http://gwplotter.com/.

[3] Javier M. Antelis and Claudia Moreno. Obtaining gravitational waves from inspiral binary systems using ligo data. *The European Physical Journal Plus*, 132(1): 10, Jan 2017. ISSN 2190-5444. doi: 10.1140/epjp/i2017-11283-5. URL https://doi.org/10.1140/epjp/i2017-11283-5.

[4] Alejandro Bohé et al. Improved effective-one-body model of spinning, nonprecessing binary black holes for the era of gravitational-wave astrophysics with advanced detectors. *Phys. Rev. D*, 95:044028, Feb 2017. doi: 10.1103/PhysRevD.95.044028. URL https://link.aps.org/doi/10.1103/PhysRevD.95.044028.

[5] Carlos Palenzuela, Steven L. Liebling, David Neilsen, Luis Lehner, O. L. Caballero, Evan O'Connor, and Matthew Anderson. Effects of the microphysical equation of state in the mergers of magnetized neutron stars with neutrino cooling. *Phys. Rev. D*, 92:044045, Aug 2015. doi: 10.1103/PhysRevD.92.044045. URL https://link.aps.org/doi/10.1103/PhysRevD.92.044045.

[6] Carlos Palenzuela, Paolo Pani, Miguel Bezares, Vitor Cardoso, Luis Lehner, and Steven Liebling. Gravitational wave signatures of highly compact boson star binaries. *Phys. Rev. D*, 96:104058, Nov 2017. doi: 10.1103/PhysRevD.96.104058. URL https://link.aps.org/doi/10.1103/PhysRevD.96.104058.

[7] Vitor Cardoso, Edgardo Franzin, Andrea Maselli, Paolo Pani, and Guilherme Raposo. Testing strong-field gravity with tidal love numbers. *Phys. Rev. D*, 95: 084014, Apr 2017. doi: 10.1103/PhysRevD.95.084014. URL https://link.aps.org/doi/10.1103/PhysRevD.95.084014.

[8] Noah Sennett, Tanja Hinderer, Jan Steinhoff, Alessandra Buonanno, and Serguei Ossokine. Distinguishing Boson Stars from Black Holes and Neutron Stars from Tidal Interactions in Inspiraling Binary Systems. *Phys. Rev.*, D96(2):024002, 2017. doi: 10.1103/PhysRevD.96.024002.

[9] B. P. Abbott et al. Observation of Gravitational Waves from a Binary Black Hole Merger. *Phys. Rev. Lett.*, 116(6):061102, 2016. doi: 10.1103/PhysRevLett.116.061102.

[10] B. P. Abbott et al. GW151226: Observation of Gravitational Waves from a 22-Solar-Mass Binary Black Hole Coalescence. *Phys. Rev. Lett.*, 116(24):241103, 2016. doi: 10.1103/PhysRevLett.116.241103.

[11] B. P. Abbott et al. GW170104: Observation of a 50-Solar-Mass Binary Black Hole Coalescence at Redshift 0.2. *Physical Review Letters*, 118(22):221101, June 2017. doi: 10.1103/PhysRevLett.118.221101.

[12] B. P. Abbott et al. GW170608: Observation of a 19 Solar-mass Binary Black Hole Coalescence. *Astrop. J. Lett.*, 851:L35, December 2017. doi: 10.3847/2041-8213/aa9f0c.

[13] B. P. Abbott et al. GW170814: A Three-Detector Observation of Gravitational Waves from a Binary Black Hole Coalescence. *Physical Review Letters*, 119:141101, Oct 2017. doi: 10.1103/PhysRevLett.119.141101. URL https://link.aps.org/doi/10.1103/PhysRevLett.119.141101.

[14] B. P. Abbott et al. GWTC-1: A Gravitational-Wave Transient Catalog of Compact Binary Mergers Observed by LIGO and Virgo during the First and Second Observing Runs. *arXiv e-prints*, art. arXiv:1811.12907, Nov 2018.

[15] J. M. Weisberg, J. H. Taylor, and L. A. Fowler. Gravitational waves from an orbiting pulsar. *Scientific American*, 245:74–82, October 1981. doi: 10.1038/scientificamerican1081-74.

[16] B. P. Abbott et al. GW170817: Observation of gravitational waves from a binary neutron star inspiral. *Phys. Rev. Lett.*, 119:161101, Oct 2017. doi: 10.1103/PhysRevLett.119.161101. URL https://link.aps.org/doi/10.1103/PhysRevLett.119.161101.

[17] B. P. Abbott et al. Multi-messenger Observations of a Binary Neutron Star Merger. *Astrophys. Journal*, 848:L12, October 2017. doi: 10.3847/2041-8213/aa91c9.

[18] B. P. Abbott et al. Gravitational waves and gamma-rays from a binary neutron star merger: GW170817 and GRB170817A. *Astrop. J. Lett.*, 848(2):L13, 2017. URL http://stacks.iop.org/2041-8205/848/i=2/a=L13.

[19] B. P. Abbott et al. Estimating the contribution of dynamical ejecta in the kilonova associated with GW170817. *The Astrophysical Journal*, 850(2):L39, dec 2017. doi: 10.3847/2041-8213/aa9478. URL https://doi.org/10.3847%2F2041-8213%2Faa9478.

[20] Xisco Jiménez Forteza. *Hierarchical data-driven modelling of binary black hole mergers*. PhD thesis, Sep.s 2017. URL https://www.tdx.cat/handle/10803/565409.

[21] B. P. Abbott et al. First all-sky search for continuous gravitational waves from unknown sources in binary systems. *Phys. Rev. D*, 90:062010, Sep 2014. doi: 10.1103/PhysRevD.90.062010. URL https://link.aps.org/doi/10.1103/PhysRevD.90.062010.

[22] B. P. Abbott et al. All-sky search for continuous gravitational waves from isolated neutron stars using Advanced LIGO O2 data. *arXiv e-prints*, art. arXiv:1903.01901, Mar 2019.

[23] B. P. Abbott et al. First targeted search for gravitational-wave bursts from core-collapse supernovae in data of first-generation laser interferometer detectors. *Phys. Rev. D*, 94:102001, Nov 2016. doi: 10.1103/PhysRevD.94.102001. URL https://link.aps.org/doi/10.1103/PhysRevD.94.102001.

[24] Kei Kotake, Katsuhiko Sato, and Keitaro Takahashi. Explosion mechanism, neutrino burst and gravitational wave in core-collapse supernovae. *Reports on Progress in Physics*, 69(4):971–1143, mar 2006. doi: 10.1088/0034-4885/69/4/r03. URL https://doi.org/10.1088%2F0034-4885%2F69%2F4%2Fr03.

[25] B. P. Abbott et al. First upper limits from ligo on gravitational wave bursts. *Phys. Rev. D*, 69:102001, May 2004. doi: 10.1103/PhysRevD.69.102001. URL https://link.aps.org/doi/10.1103/PhysRevD.69.102001.

[26] Nelson Christensen. Stochastic gravitational wave backgrounds. *Reports on Progress in Physics*, 82(1):016903, nov 2018. doi: 10.1088/1361-6633/aae6b5. URL https://doi.org/10.1088%2F1361-6633%2Faae6b5.

[27] B. P. Abbott et al. A search for the isotropic stochastic background using data from Advanced LIGO's second observing run. *arXiv e-prints*, art. arXiv:1903.02886, Mar 2019.

[28] B. P. Abbott et al. Analysis of first LIGO science data for stochastic gravitational waves. *Phys. Rev. D*, 69:122004, Jun 2004. doi: 10.1103/PhysRevD.69.122004. URL https://link.aps.org/doi/10.1103/PhysRevD.69.122004.

[29] Richard Easther, John T. Giblin, and Eugene A. Lim. Gravitational wave production at the end of inflation. *Phys. Rev. Lett.*, 99:221301, Nov 2007. doi: 10.1103/PhysRevLett.99.221301. URL https://link.aps.org/doi/10.1103/PhysRevLett.99.221301.

[30] KAGRA Collaboration. First cryogenic test operation of underground km-scale gravitational-wave observatory KAGRA. *arXiv e-prints*, art. arXiv:1901.03569, Jan 2019.

[31] Indigo. http://www.gw-indigo.org/tiki-index.php.

[32] Lisa. https://www.elisascience.org.

[33] Soumi De, Daniel Finstad, James M. Lattimer, Duncan A. Brown, Edo Berger, and Christopher M. Biwer. Tidal deformabilities and radii of neutron stars from the observation of gw170817. *Phys. Rev. Lett.*, 121:091102, Aug 2018. doi: 10.1103/PhysRevLett.121.091102. URL https://link.aps.org/doi/10.1103/PhysRevLett.121.091102.

[34] B. P. Abbott et al. GW170817: Measurements of neutron star radii and equation of state. *Phys. Rev. Lett.*, 121:161101, Oct 2018. doi: 10.1103/PhysRevLett.121.161101. URL https://link.aps.org/doi/10.1103/PhysRevLett.121.161101.

[35] Sajad Bhat and Debades Bandyopadhyay. Neutron star equation of state and GW170817. *Journal of Physics G: Nuclear and Particle Physics*, 46(1):014003, nov 2018. doi: 10.1088/1361-6471/aaef45. URL https://doi.org/10.1088%2F1361-6471%2Faaef45.

[36] Zack Carson, Andrew W. Steiner, and Kent Yagi. Constraining nuclear matter parameters with gw170817. *Phys. Rev. D*, 99:043010, Feb 2019. doi: 10.1103/PhysRevD.99.043010. URL https://link.aps.org/doi/10.1103/PhysRevD.99.043010.

[37] Nicolás Yunes, Kent Yagi, and Frans Pretorius. Theoretical physics implications of the binary black-hole mergers GW150914 and GW151226. *Phys. Rev. D*, 94:084002, Oct 2016. doi: 10.1103/PhysRevD.94.084002. URL https://link.aps.org/doi/10.1103/PhysRevD.94.084002.

[38] B. P. Abbott et al. Astrophysical Implications of the Binary Black-hole Merger GW150914. *Astrop. J. Lett.*, 818:L22, February 2016. doi: 10.3847/2041-8205/818/2/l22. URL https://doi.org/10.3847%2F2041-8205%2F818%2F2%2Fl22.

[39] Leo Barack, Vitor Cardoso, Samaya Nissanke, Thomas. P. Sotiriou, and et al. Black holes, gravitational waves and fundamental physics: a roadmap. art. arXiv:1806.05195, Jun 2018.

[40] B. P. Abbott et al. Tests of General Relativity with the Binary Black Hole Signals from the LIGO-Virgo Catalog GWTC-1. *arXiv e-prints*, art. arXiv:1903.04467, Mar 2019.

[41] B. P. Abbott et al. Tests of general relativity with gw150914. *Phys. Rev. Lett.*, 116:221101, May 2016. doi: 10.1103/PhysRevLett.116.221101. URL https://link.aps.org/doi/10.1103/PhysRevLett.116.221101.

[42] B. P. Abbott et al. Tests of General Relativity with GW170817. *arXiv e-prints*, art. arXiv:1811.00364, Nov 2018.

[43] Luc Blanchet. Gravitational radiation from post-newtonian sources and inspiralling compact binaries. *Living Reviews in Relativity*, 17(1):2, Feb 2014. ISSN 1433-8351. doi: 10.12942/lrr-2014-2. URL https://doi.org/10.12942/lrr-2014-2.

[44] Alessandra Buonanno and Thibault Damour. Effective one-body approach to general relativistic two-body dynamics. *Phys. Rev. D*, 59:084006, Mar 1999. doi: 10.1103/PhysRevD.59.084006. URL https://link.aps.org/doi/10.1103/PhysRevD.59.084006.

[45] Paolo Pani. Advanced methods in black-hole perturbation theory. *International Journal of Modern Physics A*, 28(22n23):1340018, 2013. doi: 10.1142/S0217751X13400186. URL https://doi.org/10.1142/S0217751X13400186.

[46] Emanuele Berti, Alberto Sesana, Enrico Barausse, Vitor Cardoso, and Krzysztof Belczynski. Spectroscopy of kerr black holes with earth- and space-based interferometers. *Phys. Rev. Lett.*, 117:101102, Sep 2016. doi: 10.1103/PhysRevLett.117.101102. URL https://link.aps.org/doi/10.1103/PhysRevLett.117.101102.

[47] Andreas Bauswein, Hans-Thomas Janka, Kai Hebeler, and Achim Schwenk. Equation-of-state dependence of the gravitational-wave signal from the ringdown phase of neutron-star mergers. *Phys. Rev. D*, 86:063001, Sep 2012. doi: 10.1103/PhysRevD.86.063001. URL https://link.aps.org/doi/10.1103/PhysRevD.86.063001.

[48] Vitor Cardoso and Paolo Pani. The observational evidence for horizons: from echoes to precision gravitational-wave physics. art. arXiv:1707.03021, 2017.

[49] Samir D. Mathur. The Fuzzball proposal for black holes: An Elementary review. *Fortsch. Phys.*, 53:793–827, 2005. doi: 10.1002/prop.200410203.

[50] Pawel O. Mazur and Emil Mottola. Gravitational condensate stars: An alternative to black holes. art. gr-qc/0109035, 2001.

[51] Thibault Damour and Sergey N. Solodukhin. Wormholes as black hole foils. *Phys. Rev.*, D76:024016, 2007. doi: 10.1103/PhysRevD.76.024016.

[52] Guilherme Raposo, Paolo Pani, Miguel Bezares, Carlos Palenzuela, and Vitor Cardoso. Anisotropic stars as ultracompact objects in General Relativity. *arXiv e-prints*, art. arXiv:1811.07917, Nov 2018.

[53] Remo Ruffini and Silvano Bonazzola. Systems of self-gravitating particles in general relativity and the concept of an equation of state. *Phys. Rev.*, 187:1767–1783, Nov 1969. doi: 10.1103/PhysRev.187.1767. URL https://link.aps.org/doi/10.1103/PhysRev.187.1767.

[54] Richard Brito, Vitor Cardoso, Carlos A.R. Herdeiro, and Eugen Radu. Proca stars: Gravitating boseeinstein condensates of massive spin 1 particles. *Physics Letters B*, 752:291 – 295, 2016. ISSN 0370-2693. doi: https://doi.org/10.1016/j.physletb.2015.11.051. URL http://www.sciencedirect.com/science/article/pii/S0370269315009077.

[55] Monica Colpi, Stuart L. Shapiro, and Ira Wasserman. Boson stars: Gravitational equilibria of self-interacting scalar fields. *Phys. Rev. Lett.*, 57:2485–2488, Nov 1986. doi: 10.1103/PhysRevLett.57.2485. URL https://link.aps.org/doi/10.1103/PhysRevLett.57.2485.

[56] Serguei Chatrchyan et al. Observation of a new boson at a mass of 125 GeV with the CMS experiment at the LHC. *Physics Letters B*, 716(1):30 – 61, 2012. ISSN 0370-2693. doi: https://doi.org/10.1016/j.physletb.2012.08.021. URL http://www.sciencedirect.com/science/article/pii/S0370269312008581.

[57] Georges Aad et al. Observation of a new particle in the search for the Standard Model Higgs boson with the ATLAS detector at the LHC. *Phys. Lett.*, B716:1–29, 2012. doi: 10.1016/j.physletb.2012.08.020. URL https://www.sciencedirect.com/science/article/pii/S037026931200857X.

[58] Steven L. Liebling and Carlos Palenzuela. Dynamical boson stars. *Living Reviews in Relativity*, 15(1):6, May 2012. ISSN 1433-8351. doi: 10.12942/lrr-2012-6. URL https://doi.org/10.12942/lrr-2012-6.

[59] Caio F. B. Macedo, Paolo Pani, Vitor Cardoso, and Luís C. B. Crispino. Astrophysical signatures of boson stars: Quasinormal modes and inspiral resonances. *Phys. Rev. D*, 88:064046, Sep 2013. doi: 10.1103/PhysRevD.88.064046. URL https://link.aps.org/doi/10.1103/PhysRevD.88.064046.

[60] Andrea Maselli, Pantelis Pnigouras, Niklas Grønlund Nielsen, Chris Kouvaris, and Kostas D. Kokkotas. Dark stars: Gravitational and electromagnetic observables.

Phys. Rev. D, 96:023005, Jul 2017. doi: 10.1103/PhysRevD.96.023005. URL https://link.aps.org/doi/10.1103/PhysRevD.96.023005.

[61] Richard Brito, Vitor Cardoso, Caio F. B. Macedo, Hirotada Okawa, and Carlos Palenzuela. Interaction between bosonic dark matter and stars. *Phys. Rev. D*, 93: 044045, Feb 2016. doi: 10.1103/PhysRevD.93.044045. URL https://link.aps.org/doi/10.1103/PhysRevD.93.044045.

[62] Susana Valdez-Alvarado, Carlos Palenzuela, Daniela Alic, and L. Arturo Ureña López. Dynamical evolution of fermion-boson stars. *Phys. Rev. D*, 87:084040, Apr 2013. doi: 10.1103/PhysRevD.87.084040. URL https://link.aps.org/doi/10.1103/PhysRevD.87.084040.

[63] Carles Bona, Carlos Palenzuela-Luque, and Carles Bona-Casas, editors. *Elements of Numerical Relativity and Relativistic Hydrodynamics*, volume 783 of *Lecture Notes in Physics, Berlin Springer Verlag*, 2009. doi: 10.1007/978-3-642-01164-1.

[64] Albert Einstein. Zur allgemeinen Relativitätstheorie. *Sitzungsberichte der Königlich Preußischen Akademie der Wissenschaften (Berlin), Seite 778-786.*, 1915.

[65] John Lee. *Introduction to Smooth Manifolds*. Springer-Verlag New York, 2012. ISBN 978-1-4899-9475-2. doi: 10.1007/978-1-4419-9982-5. URL https://www.springer.com/la/book/9781441999818#aboutBook.

[66] Robert Wald. *General Relativity*. University of Chicago Press, 1984.

[67] Michele Maggiore. *Gravitational waves: Theory and Experiments*. Oxford University Press, Oxford, 2007.

[68] Kurt Lechner. *Classical Electrodynamics. A Modern Perspective*. Springer, 2018.

[69] Albert Einstein. Über Gravitationswellen. *Sitzungsberichte der Königlich Preußischen Akademie der Wissenschaften (Berlin), Seite 154-167.*, 1918.

[70] Miguel Alcubierre. *Introduction to 3+1 Numerical Relativity*. Oxford University Press, 2008.

[71] Karl Schwarzschild. Über das Gravitationsfeld eines Massenpunktes nach der Einsteinschen Theorie. *Sitzungsberichte der Königlich Preußischen Akademie der Wissenschaften (Berlin), 1916, Seite 189-196*, 1916.

[72] Roy P. Kerr. Gravitational field of a spinning mass as an example of algebraically special metrics. *Phys. Rev. Lett.*, 11:237–238, Sep 1963. doi: 10.1103/PhysRevLett.11.237. URL https://link.aps.org/doi/10.1103/PhysRevLett.11.237.

[73] Von A. Friedman. Über die krümmung des raumes. *Zeitschrift für Physik*, 10(1): 377–386, Dec 1922. ISSN 0044-3328. doi: 10.1007/BF01332580. URL https://doi.org/10.1007/BF01332580.

[74] Yvonne Fourès-Bruhat. Théorème d'existence pour certains systèmes d'équations aux dérivées partielles non linéaires. *Acta Mathematica, Volume 88, Issue 1, pp 141-225*, 88, 1952. doi: 10.1007/BF02392131.

[75] James W. York. Kinematics and dynamics of general relativity. In L. L. Smarr, editor, *Sources of Gravitational Radiation*, pages 83–126, 1979.

[76] Robert Geroch. Domain of dependence. *Journal of Mathematical Physics*, 11 (2):437–449, 1970. doi: 10.1063/1.1665157. URL https://doi.org/10.1063/1.1665157.

[77] Eric Gourgoulhon. *3+1 Formalism in General Relativity*, volume 846. Lecture Notes in Physics, Springer Verlag, Berlin, 2012.

[78] Richard Arnowitt, Stanley Deser, and Charles W. Misner. Republication of: The dynamics of general relativity. *General Relativity and Gravitation*, 40(9):1997–2027, Sep 2008. ISSN 1572-9532. doi: 10.1007/s10714-008-0661-1. URL https://doi.org/10.1007/s10714-008-0661-1.

[79] Simonetta Frittelli. Note on the propagation of the constraints in standard 3+1 general relativity. *Phys. Rev. D*, 55:5992–5996, May 1997. doi: 10.1103/PhysRevD.55.5992. URL https://link.aps.org/doi/10.1103/PhysRevD.55.5992.

[80] Silvano Bonazzola, Eric Gourgoulhon, Philippe Grandclément, and Jérôme Novak. Constrained scheme for the einstein equations based on the dirac gauge and spherical coordinates. *Phys. Rev. D*, 70:104007, Nov 2004. doi: 10.1103/PhysRevD.70.104007. URL https://link.aps.org/doi/10.1103/PhysRevD.70.104007.

[81] Jacques Hadamard. Sur les problemes aux derivees partielles et leur signification physique. *Princeton university bulletin*, pages 49–52, 1902.

[82] David Hilditch. An introduction to well-posedness and free-evolution. *International Journal of Modern Physics A*, 28(22n23):1340015, 2013. doi: 10.1142/S0217751X13400150. URL https://doi.org/10.1142/S0217751X13400150.

[83] Bertil Gustafsson, Heinz-Otto Kreiss, and Joseph Oliger. *Time-Dependent Problems and Difference Methods, Second Edition*. 1995. doi: 10.1002/9781118548448.

[84] Olivier Sarbach and Manuel Tiglio. Continuum and discrete initial-boundary value problems and einstein's field equations. *Living Reviews in Relativity*, 15(1):9, Aug

2012. ISSN 1433-8351. doi: 10.12942/lrr-2012-9. URL https://doi.org/10.12942/lrr-2012-9.

[85] Oscar A. Reula and Marcelo E. Rubio. Ill posedness of force-free electrodynamics in euler potentials. *Phys. Rev. D*, 95:064005, Mar 2017. doi: 10.1103/PhysRevD.95.064005. URL https://link.aps.org/doi/10.1103/PhysRevD.95.064005.

[86] Oscar A. Reula. Hyperbolic methods for einstein's equations. *Living Reviews in Relativity*, 1(1):3, Jan 1998. ISSN 1433-8351. doi: 10.12942/lrr-1998-3. URL https://doi.org/10.12942/lrr-1998-3.

[87] Masaru Shibata and Takashi Nakamura. Evolution of three-dimensional gravitational waves: Harmonic slicing case. *Phys. Rev. D*, 52:5428–5444, Nov 1995. doi: 10.1103/PhysRevD.52.5428. URL https://link.aps.org/doi/10.1103/PhysRevD.52.5428.

[88] Thomas W. Baumgarte and Stuart L. Shapiro. Numerical integration of einstein's field equations. *Phys. Rev. D*, 59:024007, Dec 1998. doi: 10.1103/PhysRevD.59.024007. URL https://link.aps.org/doi/10.1103/PhysRevD.59.024007.

[89] Frans Pretorius. Evolution of binary black-hole spacetimes. *Phys. Rev. Lett.*, 95:121101, Sep 2005. doi: 10.1103/PhysRevLett.95.121101. URL https://link.aps.org/doi/10.1103/PhysRevLett.95.121101.

[90] David Garfinkle. Harmonic coordinate method for simulating generic singularities. *Phys. Rev. D*, 65:044029, Jan 2002. doi: 10.1103/PhysRevD.65.044029. URL https://link.aps.org/doi/10.1103/PhysRevD.65.044029.

[91] Isabel Cordero-Carrión, José María Ibáñez, Eric Gourgoulhon, José Luis Jaramillo, and Jérôme Novak. Mathematical issues in a fully constrained formulation of the einstein equations. *Phys. Rev. D*, 77:084007, Apr 2008. doi: 10.1103/PhysRevD.77.084007. URL https://link.aps.org/doi/10.1103/PhysRevD.77.084007.

[92] Daniela Alic, Carles Bona-Casas, Carles Bona, Luciano Rezzolla, and Carlos Palenzuela. Conformal and covariant formulation of the z4 system with constraint-violation damping. *Phys. Rev. D*, 85:064040, Mar 2012. doi: 10.1103/PhysRevD.85.064040. URL https://link.aps.org/doi/10.1103/PhysRevD.85.064040.

[93] Carles Bona, Thomas Ledvinka, Carlos Palenzuela, and M. Žáček. General-covariant evolution formalism for numerical relativity. *Phys. Rev. D*, 67:104005, May 2003. doi: 10.1103/PhysRevD.67.104005. URL https://link.aps.org/doi/10.1103/PhysRevD.67.104005.

[94] Carles Bona, Thomas Ledvinka, Carlos Palenzuela, and M. Žáček. Symmetry-breaking mechanism for the Z4 general-covariant evolution system. *Phys. Rev. D*, 69:064036, Mar 2004. doi: 10.1103/PhysRevD.69.064036. URL https://link.aps.org/doi/10.1103/PhysRevD.69.064036.

[95] Carles Bona, Carles Bona-Casas, and Carlos Palenzuela. Action principle for numerical-relativity evolution systems. *Phys. Rev. D*, 82:124010, Dec 2010. doi: 10.1103/PhysRevD.82.124010. URL https://link.aps.org/doi/10.1103/PhysRevD.82.124010.

[96] Carsten Gundlach, Gioel Calabrese, Ian Hinder, and Jos M Martn-Garca. Constraint damping in the z4 formulation and harmonic gauge. *Classical and Quantum Gravity*, 22(17):3767, 2005. URL http://stacks.iop.org/0264-9381/22/i=17/a=025.

[97] Smirnov M. M. Koshylakov N. S. and Gliner E. B. *Differential Equations of Mathematical Physics*. New York: Interscience, 1964.

[98] Sebastiano Bernuzzi and David Hilditch. Constraint violation in free evolution schemes: Comparing the bssnok formulation with a conformal decomposition of the z4 formulation. *Phys. Rev. D*, 81:084003, Apr 2010. doi: 10.1103/PhysRevD.81.084003. URL https://link.aps.org/doi/10.1103/PhysRevD.81.084003.

[99] A. Arbona et al. Simflowny: A general-purpose platform for the management of physical models and simulation problems. *Computer Physics Communications*, 184(10):2321 – 2331, 2013. ISSN 0010-4655. doi: http://dx.doi.org/10.1016/j.cpc.2013.04.012. URL http://www.sciencedirect.com/science/article/pii/S0010465513001471.

[100] A. Arbona et al. Simflowny 2: An upgraded platform for scientific modeling and simulation. *Computer Physics Communications*, 184:2321–2331, feb 2017. ISSN 00104655. doi: 10.1016/j.cpc.2018.03.015. URL http://dx.doi.org/10.17632/g9mcw8s64f.1http://linkinghub.elsevier.com/retrieve/pii/S0010465518300870http://arxiv.org/abs/1702.04715.

[101] Carlos Palenzuela et al. A simflowny-based finite-difference code for high-performance computing in numerical relativity. *Classical and Quantum Gravity*, 35(18):185007, 2018. URL http://stacks.iop.org/0264-9381/35/i=18/a=185007.

[102] Simflowny project website., 2018. URL https://bitbucket.org/iac3/simflowny/overview.

[103] Larry Smarr and James W. York. Kinematical conditions in the construction of spacetime. *Phys. Rev. D*, 17:2529–2551, May 1978. doi: 10.1103/PhysRevD.17.2529. URL https://link.aps.org/doi/10.1103/PhysRevD.17.2529.

[104] Miguel Alcubierre. Hyperbolic slicings of spacetime: singularity avoidance and gauge shocks. *Classical and Quantum Gravity*, 20(4):607–623, jan 2003. doi: 10.1088/0264-9381/20/4/304. URL https://doi.org/10.1088%2F0264-9381%2F20%2F4%2F304.

[105] Carles Bona, Joan Massó, Edward Seidel, and Joan Stela. New formalism for numerical relativity. *Phys. Rev. Lett.*, 75:600–603, Jul 1995. doi: 10.1103/PhysRevLett.75.600. URL https://link.aps.org/doi/10.1103/PhysRevLett.75.600.

[106] Masaru Shibata. 3D numerical simulation of black hole formation using collisionless particlestriplane symmetric case. *Progress of Theoretical Physics*, 101(2):251–282, 1999. doi: 10.1143/PTP.101.251. URL http://dx.doi.org/10.1143/PTP.101.251.

[107] Miguel Alcubierre, Bernd Brügmann, Peter Diener, Michael Koppitz, Denis Pollney, Edward Seidel, and Ryoji Takahashi. Gauge conditions for long-term numerical black hole evolutions without excision. *Phys. Rev. D*, 67:084023, Apr 2003. doi: 10.1103/PhysRevD.67.084023. URL https://link.aps.org/doi/10.1103/PhysRevD.67.084023.

[108] James R. van Meter, John G. Baker, Michael Koppitz, and Dae-Il Choi. How to move a black hole without excision: Gauge conditions for the numerical evolution of a moving puncture. *Phys. Rev. D*, 73:124011, Jun 2006. doi: 10.1103/PhysRevD.73.124011. URL https://link.aps.org/doi/10.1103/PhysRevD.73.124011.

[109] Heinz-Otto Kreiss and Omar E. Ortiz. 19. Some Mathematical and Numerical Questions Connected with First and Second Order Time-Dependent Systems of Partial Differential Equations. In J. Frauendiener and H. Friedrich, editors, *The Conformal Structure of Space-Time*, volume 604 of *Lecture Notes in Physics, Berlin Springer Verlag*, pages 359–370, 2002.

[110] Carles Bona and Carlos Palenzuela. Dynamical shift conditions for the z4 and bssn formalisms. *Phys. Rev. D*, 69:104003, May 2004. doi: 10.1103/PhysRevD.69.104003. URL https://link.aps.org/doi/10.1103/PhysRevD.69.104003.

[111] Miguel Bezares, Carlos Palenzuela, and Carles Bona. Final fate of compact boson star mergers. *Phys. Rev. D*, 95:124005, Jun 2017. doi: 10.1103/PhysRevD.95.124005. URL https://link.aps.org/doi/10.1103/PhysRevD.95.124005.

[112] Gabriel Nagy, Omar E. Ortiz, and Oscar A. Reula. Strongly hyperbolic second order einstein's evolution equations. *Phys. Rev. D*, 70:044012, Aug 2004. doi: 10.1103/PhysRevD.70.044012. URL https://link.aps.org/doi/10.1103/PhysRevD.70.044012.

[113] Horst Beyer and Olivier Sarbach. Well-posedness of the baumgarte-shapiro-shibata-nakamura formulation of einstein's field equations. *Phys. Rev. D*, 70: 104004, Nov 2004. doi: 10.1103/PhysRevD.70.104004. URL https://link.aps.org/doi/10.1103/PhysRevD.70.104004.

[114] Carsten Gundlach and José M. Martín-García. Well-posedness of formulations of the einstein equations with dynamical lapse and shift conditions. *Phys. Rev. D*, 74: 024016, Jul 2006. doi: 10.1103/PhysRevD.74.024016. URL https://link.aps.org/doi/10.1103/PhysRevD.74.024016.

[115] José Luis Jaramillo and Eric Gourgoulhon. *Mass and Angular Momentum in General Relativity*, pages 87–124. Springer Netherlands, Dordrecht, 2011. ISBN 978-90-481-3015-3. doi: 10.1007/978-90-481-3015-3_4. URL https://doi.org/10.1007/978-90-481-3015-3_4.

[116] Thomas W. Baumgarte and Stuart L. Shapiro. *Numerical Relativity: Solving Einstein's Equations on the Computer*. June 2010.

[117] Nigel T. Bishop and Luciano Rezzolla. Extraction of gravitational waves in numerical relativity. *Living Reviews in Relativity*, 19(1):2, Oct 2016. ISSN 1433-8351. doi: 10.1007/s41114-016-0001-9. URL https://doi.org/10.1007/s41114-016-0001-9.

[118] Christian Reisswig, Christian D. Ott, Ulrich Sperhake, and Erik Schnetter. Gravitational wave extraction in simulations of rotating stellar core collapse. *Phys. Rev. D*, 83:064008, Mar 2011. doi: 10.1103/PhysRevD.83.064008. URL https://link.aps.org/doi/10.1103/PhysRevD.83.064008.

[119] E. T. Newman and R. Penrose. Note on the bondi-metzner-sachs group. *Journal of Mathematical Physics*, 7(5):863–870, 1966. doi: 10.1063/1.1931221. URL https://doi.org/10.1063/1.1931221.

[120] R. K. Sachs and Hermann Bondi. Gravitational waves in general relativity viii. waves in asymptotically flat space-time. *Proceedings of the Royal Society of London. Series A. Mathematical and Physical Sciences*, 270(1340):103–126, 1962. doi: 10.1098/rspa.1962.0206.

[121] Roger Penrose. Gravitational collapse and space-time singularities. *Phys. Rev. Lett.*, 14:57–59, Jan 1965. doi: 10.1103/PhysRevLett.14.57. URL https://link.aps.org/doi/10.1103/PhysRevLett.14.57.

[122] Ian Hinder, Barry Wardell, and Eloisa Bentivegna. Falloff of the weyl scalars in binary black hole spacetimes. *Phys. Rev. D*, 84:024036, Jul 2011. doi: 10.1103/PhysRevD.84.024036. URL https://link.aps.org/doi/10.1103/PhysRevD.84.024036.

[123] Masaru Shibata. *Numerical Relativity*. World Scientific Publishing Co., Inc., River Edge, NJ, USA, 2015. ISBN 9789814699716, 9814699713.

[124] Bernd Brügmann, José A. González, Mark Hannam, Sascha Husa, Ulrich Sperhake, and Wolfgang Tichy. Calibration of moving puncture simulations. *Phys. Rev. D*, 77:024027, Jan 2008. doi: 10.1103/PhysRevD.77.024027. URL https://link.aps.org/doi/10.1103/PhysRevD.77.024027.

[125] Roberto De Pietri, Alessandra Feo, Francesco Maione, and Frank Löffler. Modeling equal and unequal mass binary neutron star mergers using public codes. *Phys. Rev. D*, 93:064047, Mar 2016. doi: 10.1103/PhysRevD.93.064047. URL https://link.aps.org/doi/10.1103/PhysRevD.93.064047.

[126] Carlos O. Lousto, Hiroyuki Nakano, Yosef Zlochower, and Manuela Campanelli. Intermediate-mass-ratio black hole binaries: Intertwining numerical and perturbative techniques. *Phys. Rev. D*, 82:104057, Nov 2010. doi: 10.1103/PhysRevD.82.104057. URL https://link.aps.org/doi/10.1103/PhysRevD.82.104057.

[127] Christian Reisswig and Denis Pollney. Notes on the integration of numerical relativity waveforms. *Classical and Quantum Gravity*, 28(19):195015, sep 2011. doi: 10.1088/0264-9381/28/19/195015. URL https://doi.org/10.1088%2F0264-9381%2F28%2F19%2F195015.

[128] Chi Wai Lai. *A Numerical Study of Boson Stars*. PhD thesis, The University of British Columbia, 2004.

[129] B. C. Mundim. *A Numerical Study of Boson Star Binaries*. PhD thesis, The University of British Columbia, 2010.

[130] Franz E Schunck and Eckehard W Mielke. General relativistic boson stars. *Classical and Quantum Gravity*, 20(20):R301–R356, sep 2003. doi: 10.1088/0264-9381/20/20/201. URL https://doi.org/10.1088%2F0264-9381%2F20%2F20%2F201.

[131] L. D. Landau and E. M. Lifshitz. *The classical theory of fields*. Pergamon Press, Oxford, 1987.

[132] Alan R. Parry. A survey of spherically symmetric spacetimes. *Analysis and Mathematical Physics*, 4(4):333–375, Dec 2014. ISSN 1664-235X. doi: 10.1007/s13324-014-0085-x. URL https://doi.org/10.1007/s13324-014-0085-x.

[133] James M. Bardeen and Tsvi Piran. General relativistic axisymmetric rotating systems: Coordinates and equations. *Physics Reports*, 96(4):205 – 250, 1983. ISSN 0370-1573. doi: https://doi.org/10.1016/0370-1573(83)90069-8. URL http://www.sciencedirect.com/science/article/pii/0370157383900698.

[134] R. Friedberg, T. D. Lee, and Y. Pang. Mini-soliton stars. *Phys. Rev. D*, 35:3640–3657, Jun 1987. doi: 10.1103/PhysRevD.35.3640. URL https://link.aps.org/doi/10.1103/PhysRevD.35.3640.

[135] R. Friedberg, T. D. Lee, and Y. Pang. Scalar soliton stars and black holes. *Phys. Rev. D*, 35:3658–3677, Jun 1987. doi: 10.1103/PhysRevD.35.3658. URL https://link.aps.org/doi/10.1103/PhysRevD.35.3658.

[136] T. D. Lee and Y. Pang. Nontopological solitons. *Physics Reports*, 221:251–350, November 1992. doi: 10.1016/0370-1573(92)90064-7.

[137] Feryal zel and Paulo Freire. Masses, radii, and the equation of state of neutron stars. *Annual Review of Astronomy and Astrophysics*, 54(1):401–440, 2016. doi: 10.1146/annurev-astro-081915-023322. URL https://doi.org/10.1146/annurev-astro-081915-023322.

[138] J. E. Marsden, R. Montgomery, P. J. Morrison, and W. B. Thompson. Covariant poisson brackets for classical fields. *Annals of Physics*, 169:29–47, June 1986. doi: 10.1016/0003-4916(86)90157-0.

[139] Olivier Minazzoli and Tiberiu Harko. New derivation of the lagrangian of a perfect fluid with a barotropic equation of state. *Phys. Rev. D*, 86:087502, Oct 2012. doi: 10.1103/PhysRevD.86.087502. URL https://link.aps.org/doi/10.1103/PhysRevD.86.087502.

[140] José A. Font. Numerical hydrodynamics in general relativity. *Living Reviews in Relativity*, 3(1):2, May 2000. ISSN 1433-8351. doi: 10.12942/lrr-2000-2. URL https://doi.org/10.12942/lrr-2000-2.

[141] Francesc Banyuls, Jos A. Font, Jos Ma. Ibez, Jos Ma. Mart, and Juan A. Miralles. Numerical 3 + 1 general relativistic hydrodynamics: A local characteristic approach. *The Astrophysical Journal*, 476(1):221, 1997. URL http://stacks.iop.org/0004-637X/476/i=1/a=221.

[142] Hans Stephani, Dietrich Kramer, Malcolm MacCallum, Cornelius Hoenselaers, and Eduard Herlt. *Exact Solutions of Einstein's Field Equations*. Cambridge Monographs on Mathematical Physics. Cambridge University Press, 2 edition, 2003. doi: 10.1017/CBO9780511535185.

[143] P. D. Lax and R. D. Richtmyer. Survey of the stability of linear finite difference equations. *Comm. Pure Appl. Math*, 9:267–293, 1956. URL https://doi.org/10.1002/cpa.3160090206.

[144] J. C. Butcher. *Numerical Methods for Ordinary Differential Equations*. John Wiley and Sons, Ltd, 2008. ISBN 9780470753767. doi: 10.1002/9780470753767.fmatter. URL http://dx.doi.org/10.1002/9780470753767.fmatter.

[145] Gioel Calabrese, Luis Lehner, Oscar Reula, Olivier Sarbach, and Manuel Tiglio. Summation by parts and dissipation for domains with excised regions. *Classical and Quantum Gravity*, 21(24):5735–5757, nov 2004. doi: 10.1088/0264-9381/21/24/004. URL https://doi.org/10.1088%2F0264-9381%2F21%2F24%2F004.

[146] Eleuterio F. Toro. *Riemann Solvers and Numerical Methods for Fluid Dynamics: A Practical Introduction*. Springer, 1997. ISBN 9783540616764.

[147] Amiram Harten, Peter D. Lax, and Bram van Leer. On upstream differencing and godunov-type schemes for hyperbolic conservation laws. *SIAM Review*, 25(1):35–61, 1983. doi: 10.1137/1025002. URL https://doi.org/10.1137/1025002.

[148] P. Colella and P. R. Woodward. The Piecewise Parabolic Method (PPM) for Gas-Dynamical Simulations. *Journal of Computational Physics*, 54:174–201, September 1984. doi: 10.1016/0021-9991(84)90143-8.

[149] A. Suresh and H.T. Huynh. Accurate monotonicity-preserving schemes with rungekutta time stepping. *Journal of Computational Physics*, 136(1):83 – 99, 1997. ISSN 0021-9991. doi: https://doi.org/10.1006/jcph.1997.5745. URL http://www.sciencedirect.com/science/article/pii/S0021999197957454.

[150] Guang-Shan Jiang and Chi-Wang Shu. Efficient implementation of weighted eno schemes. *Journal of Computational Physics*, 126(1):202 – 228, 1996. ISSN 0021-9991. doi: https://doi.org/10.1006/jcph.1996.0130. URL http://www.sciencedirect.com/science/article/pii/S0021999196901308.

[151] Chi-Wang Shu. *Essentially non-oscillatory and weighted essentially non-oscillatory schemes for hyperbolic conservation laws*, pages 325–432. Springer Berlin Heidelberg, Berlin, Heidelberg, 1998. ISBN 978-3-540-49804-9. doi: 10.1007/BFb0096355. URL https://doi.org/10.1007/BFb0096355.

[152] Dinshaw S. Balsara. Higher-order accurate space-time schemes for computational astrophysics—part i: finite volume methods. *Living Reviews in Computational Astrophysics*, 3(1):2, Dec 2017. ISSN 2365-0524. doi: 10.1007/s41115-017-0002-8. URL https://doi.org/10.1007/s41115-017-0002-8.

[153] Luciano Rezzolla and Olindo Zanotti. *Relativistic Hydrodynamics*. Oxford University Press, 2013.

[154] José M. Martí and Ewald Müller. Extension of the piecewise parabolic method to one-dimensional relativistic hydrodynamics. *Journal of Computational Physics*, 123(1):1 – 14, 1996. ISSN 0021-9991. doi: https://doi.org/10.1006/jcph.1996.0001. URL http://www.sciencedirect.com/science/article/pii/S0021999196900017.

[155] Phillip Colella and Michael D. Sekora. A limiter for ppm that preserves accuracy at smooth extrema. *Journal of Computational Physics*, 227(15):7069 – 7076, 2008. ISSN 0021-9991. doi: https://doi.org/10.1016/j.jcp.2008.03.034. URL http://www.sciencedirect.com/science/article/pii/S0021999108001435.

[156] Luis Lehner, Steven L. Liebling, and Oscar Reula. AMR, stability and higher accuracy. *Classical and Quantum Gravity*, 23(16):S421–S445, jul 2006. doi: 10.1088/0264-9381/23/16/s08. URL https://doi.org/10.1088%2F0264-9381%2F23%2F16%2Fs08.

[157] Marsha J. Berger and Joseph Oliger. Adaptive mesh refinement for hyperbolic partial differential equations. *Journal of Computational Physics*, 53(3):484 – 512, 1984. ISSN 0021-9991. doi: https://doi.org/10.1016/0021-9991(84)90073-1. URL http://www.sciencedirect.com/science/article/pii/0021999184900731.

[158] Ernst Hairer, Syvert P. Norsett, and Gerhard Wanner. *Solving Ordinary Differential Equations I*. Springer-Verlag Berlin Heidelberg, 1987. ISBN 978-3-662-12607-3.

[159] Peter McCorquodale and Phillip Colella. A high-order finite-volume method for conservation laws on locally refined grids. *Commun. Appl. Math. Comput. Sci.*, 6 (1):1–25, 2011. doi: 10.2140/camcos.2011.6.1. URL https://doi.org/10.2140/camcos.2011.6.1.

[160] Bishop Mongwane. Toward a consistent framework for high order mesh refinement schemes in numerical relativity. *General Relativity and Gravitation*, 47(5):60, Apr 2015. ISSN 1572-9532. doi: 10.1007/s10714-015-1903-7. URL https://doi.org/10.1007/s10714-015-1903-7.

[161] Had. http://had.liu.edu/.

[162] Steven L. Liebling. Singularity threshold of the nonlinear sigma model using 3d adaptive mesh refinement. *Phys. Rev. D*, 66:041703, Aug 2002. doi: 10.1103/PhysRevD.66.041703. URL https://link.aps.org/doi/10.1103/PhysRevD.66.041703.

[163] Richard D. Hornung and Scott R. Kohn. Managing application complexity in the samrai object-oriented framework. *Concurrency and Computation: Practice and Experience*, 14(5):347–368, 2002. ISSN 1532-0634. doi: 10.1002/cpe.652. URL http://dx.doi.org/10.1002/cpe.652.

[164] Brian T.N. Gunney and Robert W. Anderson. Advances in patch-based adaptive mesh refinement scalability. *Journal of Parallel and Distributed Computing*, 89:65 – 84, 2016. ISSN 0743-7315. doi: https://doi.org/10.1016/j.jpdc.2015.11.005. URL http://www.sciencedirect.com/science/article/pii/S0743731515002129.

[165] Samrai project website., 2015. URL https://computation.llnl.gov/project/SAMRAI/.

[166] Carlos Palenzuela et al. Head-on collisions of boson stars. *Phys. Rev. D*, 75:064005, Mar 2007. doi: 10.1103/PhysRevD.75.064005. URL https://link.aps.org/doi/10.1103/PhysRevD.75.064005.

[167] Carlos Palenzuela et al. Orbital dynamics of binary boson star systems. *Phys. Rev. D*, 77:044036, Feb 2008. doi: 10.1103/PhysRevD.77.044036. URL https://link.aps.org/doi/10.1103/PhysRevD.77.044036.

[168] Matthew Anderson, Eric W. Hirschmann, Luis Lehner, Steven L. Liebling, Patrick M. Motl, David Neilsen, Carlos Palenzuela, and Joel E. Tohline. Simulating binary neutron stars: Dynamics and gravitational waves. *Phys. Rev. D*, 77:024006, Jan 2008. doi: 10.1103/PhysRevD.77.024006. URL https://link.aps.org/doi/10.1103/PhysRevD.77.024006.

[169] Matthew Anderson, Eric W. Hirschmann, Luis Lehner, Steven L. Liebling, Patrick M. Motl, David Neilsen, Carlos Palenzuela, and Joel E. Tohline. Magnetized neutron-star mergers and gravitational-wave signals. *Phys. Rev. Lett.*, 100:191101, May 2008. doi: 10.1103/PhysRevLett.100.191101. URL https://link.aps.org/doi/10.1103/PhysRevLett.100.191101.

[170] Carlos Palenzuela, Steven L. Liebling, David Neilsen, Luis Lehner, O. L. Caballero, Evan O'Connor, and Matthew Anderson. Effects of the microphysical equation of state in the mergers of magnetized neutron stars with neutrino cooling. *Phys. Rev. D*, 92:044045, Aug 2015. doi: 10.1103/PhysRevD.92.044045. URL https://link.aps.org/doi/10.1103/PhysRevD.92.044045.

[171] A. Arbona et al. Simflowny: A general-purpose platform for the management of physical models and simulation problems. *Computer Physics Communications*, 184(10):2321 – 2331, 2013. ISSN 0010-4655. doi: http://dx.doi.org/10.1016/j.cpc.2013.04.012. URL http://www.sciencedirect.com/science/article/pii/S0010465513001471.

[172] Daniele Viganó et al. A simflowny-based high-performance 3D code for the generalized induction equation. *Computer Physics Communications*, 237:168 – 183, 2019. ISSN 0010-4655. doi: https://doi.org/10.1016/j.cpc.2018.11.022. URL http://www.sciencedirect.com/science/article/pii/S0010465518304144.

[173] Apples with apples: Numerical relativity comparisons and tests. http://www.AppleswithApples.org.

[174] Matthew Anderson, Eric W. Hirschmann, Luis Lehner, Steven L. Liebling, Patrick M. Motl, David Neilsen, Carlos Palenzuela, and Joel E. Tohline. Simulating binary neutron stars: Dynamics and gravitational waves. *Phys. Rev. D*, 77:024006, Jan 2008. doi: 10.1103/PhysRevD.77.024006. URL https://link.aps.org/doi/10.1103/PhysRevD.77.024006.

[175] Miguel Alcubierre et al. Towards standard testbeds for numerical relativity. *Classical and Quantum Gravity*, 21:589–613, January 2004. doi: 10.1088/0264-9381/21/2/019.

[176] Vitor Cardoso and Paolo Pani. Tests for the existence of horizons through gravitational wave echoes. *Nat. Astron.*, 1:586–591, 2017. doi: 10.1038/s41550-017-0225-y.

[177] E. Seidel and W.-M. Suen. Formation of solitonic stars through gravitational cooling. *Physical Review Letters*, 72:2516–2519, April 1994. doi: 10.1103/PhysRevLett.72.2516.

[178] Jayashree Balakrishna. *A numerical study of boson stars: Einstein equations with a matter source*. PhD thesis, WASHINGTON UNIVERSITY, 1999.

[179] Matthew W. Choptuik and Frans Pretorius. Ultrarelativistic particle collisions. *Phys. Rev. Lett.*, 104:111101, Mar 2010. doi: 10.1103/PhysRevLett.104.111101. URL https://link.aps.org/doi/10.1103/PhysRevLett.104.111101.

[180] Bruno C. Mundim. *A Numerical Study of Boson Star Binaries*. PhD thesis, PhD Thesis, 2010, 2010.

[181] Vitor Cardoso, Seth Hopper, Caio F. B. Macedo, Carlos Palenzuela, and Paolo Pani. Gravitational-wave signatures of exotic compact objects and of quantum corrections at the horizon scale. *Phys. Rev. D*, 94:084031, Oct 2016.

doi: 10.1103/PhysRevD.94.084031. URL https://link.aps.org/doi/10.1103/PhysRevD.94.084031.

[182] Thomas Helfer, Eugene A. Lim, Marcos A. G. Garcia, and Mustafa A. Amin. Gravitational wave emission from collisions of compact scalar solitons. *Phys. Rev. D*, 99:044046, Feb 2019. doi: 10.1103/PhysRevD.99.044046. URL https://link.aps.org/doi/10.1103/PhysRevD.99.044046.

[183] Nicolas Sanchis-Gual, Carlos Herdeiro, José A. Font, Eugen Radu, and Fabrizio Di Giovanni. Head-on collisions and orbital mergers of proca stars. *Phys. Rev. D*, 99:024017, Jan 2019. doi: 10.1103/PhysRevD.99.024017. URL https://link.aps.org/doi/10.1103/PhysRevD.99.024017.

[184] Fabrizio Di Giovanni, Nicolas Sanchis-Gual, Carlos A. R. Herdeiro, and José A. Font. Dynamical formation of proca stars and quasistationary solitonic objects. *Phys. Rev. D*, 98:064044, Sep 2018. doi: 10.1103/PhysRevD.98.064044. URL https://link.aps.org/doi/10.1103/PhysRevD.98.064044.

[185] Masaru Shibata, Hirotada Okawa, and Tetsuro Yamamoto. High-velocity collision of two black holes. *Phys. Rev. D*, 78:101501, Nov 2008. doi: 10.1103/PhysRevD.78.101501. URL https://link.aps.org/doi/10.1103/PhysRevD.78.101501.

[186] Shijun Yoshida and Yoshiharu Eriguchi. Rotating boson stars in general relativity. *Phys. Rev. D*, 56:762–771, Jul 1997. doi: 10.1103/PhysRevD.56.762. URL https://link.aps.org/doi/10.1103/PhysRevD.56.762.

[187] Burkhard Kleihaus, Jutta Kunz, and Stefanie Schneider. Stable phases of boson stars. *Phys. Rev. D*, 85:024045, Jan 2012. doi: 10.1103/PhysRevD.85.024045. URL https://link.aps.org/doi/10.1103/PhysRevD.85.024045.

[188] Chad Hanna, Matthew C. Johnson, and Luis Lehner. Estimating gravitational radiation from super-emitting compact binary systems. *Phys. Rev.*, D95(12):124042, 2017. doi: 10.1103/PhysRevD.95.124042.

[189] Alessandra Buonanno, Lawrence E. Kidder, and Luis Lehner. Estimating the final spin of a binary black hole coalescence. *Phys. Rev.*, D77:026004, 2008. doi: 10.1103/PhysRevD.77.026004.

[190] Justin Vines, Éanna É Flanagan, and Tanja Hinderer. Post-1-newtonian tidal effects in the gravitational waveform from binary inspirals. *Physical Review D*, 83 (8):084051, 2011.

[191] L. Lehner, S. L. Liebling, C. Palenzuela, O. L. Caballero, E. O'Connor, M. Anderson, and D. Neilsen. Unequal mass binary neutron star mergers and multimessenger signals. *Classical and Quantum Gravity*, 33(18):184002, September 2016. doi: 10.1088/0264-9381/33/18/184002.

[192] Huan Yang, Kent Yagi, Jonathan Blackman, Luis Lehner, Vasileios Paschalidis, Frans Pretorius, and Nicols Yunes. Black hole spectroscopy with coherent mode stacking. *Phys. Rev. Lett.*, 118(16):161101, 2017. doi: 10.1103/PhysRevLett.118.161101.

[193] Huan Yang, Vasileios Paschalidis, Kent Yagi, Luis Lehner, Frans Pretorius, and Nicols Yunes. Gravitational wave spectroscopy of binary neutron star merger remnants with mode stacking. 2017.

[194] Emanuele Berti, Vitor Cardoso, and Andrei O. Starinets. Quasinormal modes of black holes and black branes. *Class. Quant. Grav.*, 26:163001, 2009. doi: 10.1088/0264-9381/26/16/163001.

[195] Webpage with Mathematica notebooks and numerical quasinormal mode Tables: http://centra.tecnico.ulisboa.pt/network/grit/files/ http://www.phy.olemiss.edu/~berti/ringdown/ http://www.roma1.infn.it/~pani/ .

[196] Miguel Bezares and Carlos Palenzuela. Gravitational waves from dark boson star binary mergers. *Classical and Quantum Gravity*, 35(23):234002, 2018. URL http://stacks.iop.org/0264-9381/35/i=23/a=234002.

[197] Katy Clough, Tim Dietrich, and Jens C. Niemeyer. Axion star collisions with black holes and neutron stars in full 3D numerical relativity. *Phys. Rev. D*, 98:083020, Oct 2018. doi: 10.1103/PhysRevD.98.083020. URL https://link.aps.org/doi/10.1103/PhysRevD.98.083020.

[198] Tim Dietrich, Francesca Day, Jens Niemeyer, Katy Clough, and Michael Coughlin. Neutron staraxion star collisions in the light of multimessenger astronomy. *Monthly Notices of the Royal Astronomical Society*, 483(1):908–914, 11 2018. ISSN 0035-8711. doi: 10.1093/mnras/sty3158. URL https://dx.doi.org/10.1093/mnras/sty3158.

[199] A. Bernal, J. Barranco, D. Alic, and C. Palenzuela. Multistate boson stars. *Phys. Rev. D*, 81:044031, Feb 2010. doi: 10.1103/PhysRevD.81.044031. URL https://link.aps.org/doi/10.1103/PhysRevD.81.044031.

[200] Michael Boyle, Duncan A. Brown, Lawrence E. Kidder, Abdul H. Mroué, Harald P. Pfeiffer, Mark A. Scheel, Gregory B. Cook, and Saul A. Teukolsky. High-accuracy

comparison of numerical relativity simulations with post-newtonian expansions. *Phys. Rev. D*, 76:124038, Dec 2007. doi: 10.1103/PhysRevD.76.124038. URL https://link.aps.org/doi/10.1103/PhysRevD.76.124038.

[201] Justin Vines, Éanna É. Flanagan, and Tanja Hinderer. Post-1-newtonian tidal effects in the gravitational waveform from binary inspirals. *Phys. Rev. D*, 83: 084051, Apr 2011. doi: 10.1103/PhysRevD.83.084051. URL https://link.aps.org/doi/10.1103/PhysRevD.83.084051.

[202] Kenta Hotokezaka, Koutarou Kyutoku, and Masaru Shibata. Exploring tidal effects of coalescing binary neutron stars in numerical relativity. *Phys. Rev. D*, 87: 044001, Feb 2013. doi: 10.1103/PhysRevD.87.044001. URL https://link.aps.org/doi/10.1103/PhysRevD.87.044001.

[203] Miguel Bezares, Daniele Vigano, and Carlos Palenzuela. Signatures of dark matter cores in binary neutron star mergers. *arXiv e-prints*, art. arXiv:1905.08551, May 2019.

[204] B. P. Abbott et al. Multi-messenger observations of a binary neutron star merger. *The Astrophysical Journal*, 848(2):L12, oct 2017. doi: 10.3847/2041-8213/aa91c9. URL https://doi.org/10.3847%2F2041-8213%2Faa91c9.

[205] Timothy J. Sumner. Experimental searches for dark matter. *Living Reviews in Relativity*, 5(1):4, Jul 2002. ISSN 1433-8351. doi: 10.12942/lrr-2002-4. URL https://doi.org/10.12942/lrr-2002-4.

[206] Jonathan L. Feng. Dark matter candidates from particle physics and methods of detection. *Annual Review of Astronomy and Astrophysics*, 48(1):495–545, 2010. doi: 10.1146/annurev-astro-082708-101659. URL https://doi.org/10.1146/annurev-astro-082708-101659.

[207] E. Aprile et al. Dark matter results from 100 live days of xenon100 data. *Phys. Rev. Lett.*, 107:131302, Sep 2011. doi: 10.1103/PhysRevLett.107.131302. URL https://link.aps.org/doi/10.1103/PhysRevLett.107.131302.

[208] Chris Kouvaris. Limits on self-interacting dark matter from neutron stars. *Phys. Rev. Lett.*, 108:191301, May 2012. doi: 10.1103/PhysRevLett.108.191301. URL https://link.aps.org/doi/10.1103/PhysRevLett.108.191301.

[209] Chris Kouvaris. Wimp annihilation and cooling of neutron stars. *Phys. Rev. D*, 77:023006, Jan 2008. doi: 10.1103/PhysRevD.77.023006. URL https://link.aps.org/doi/10.1103/PhysRevD.77.023006.

[210] Itzhak Goldman and Shmuel Nussinov. Weakly interacting massive particles and neutron stars. *Phys. Rev. D*, 40:3221–3230, Nov 1989. doi: 10.1103/PhysRevD.40.3221. URL https://link.aps.org/doi/10.1103/PhysRevD.40.3221.

[211] S.-C. Leung, M.-C. Chu, and L.-M. Lin. Dark-matter admixed neutron stars. *Phys. Rev. D*, 84:107301, Nov 2011. doi: 10.1103/PhysRevD.84.107301. URL https://link.aps.org/doi/10.1103/PhysRevD.84.107301.

[212] Chris Kouvaris and Peter Tinyakov. Can neutron stars constrain dark matter? *Phys. Rev. D*, 82:063531, Sep 2010. doi: 10.1103/PhysRevD.82.063531. URL https://link.aps.org/doi/10.1103/PhysRevD.82.063531.

[213] Luis Lehner and Frans Pretorius. Numerical relativity and astrophysics. *Annual Review of Astronomy and Astrophysics*, 52(1):661–694, 2014. doi: 10.1146/annurev-astro-081913-040031. URL https://doi.org/10.1146/annurev-astro-081913-040031.

[214] Vasileios Paschalidis, William E. East, Frans Pretorius, and Stuart L. Shapiro. One-arm spiral instability in hypermassive neutron stars formed by dynamical-capture binary neutron star mergers. *Phys. Rev. D*, 92:121502, Dec 2015. doi: 10.1103/PhysRevD.92.121502. URL https://link.aps.org/doi/10.1103/PhysRevD.92.121502.

[215] Takami Kuroda, Tomoya Takiwaki, and Kei Kotake. Gravitational wave signatures from low-mode spiral instabilities in rapidly rotating supernova cores. *Phys. Rev. D*, 89:044011, Feb 2014. doi: 10.1103/PhysRevD.89.044011. URL https://link.aps.org/doi/10.1103/PhysRevD.89.044011.

[216] Luis Lehner, Steven L. Liebling, Carlos Palenzuela, and Patrick M. Motl. $m = 1$ instability and gravitational wave signal in binary neutron star mergers. *Phys. Rev. D*, 94:043003, Aug 2016. doi: 10.1103/PhysRevD.94.043003. URL https://link.aps.org/doi/10.1103/PhysRevD.94.043003.

[217] David Radice, Sebastiano Bernuzzi, and Christian D. Ott. One-armed spiral instability in neutron star mergers and its detectability in gravitational waves. *Phys. Rev. D*, 94:064011, Sep 2016. doi: 10.1103/PhysRevD.94.064011. URL https://link.aps.org/doi/10.1103/PhysRevD.94.064011.

[218] William E. East, Vasileios Paschalidis, Frans Pretorius, and Stuart L. Shapiro. Relativistic simulations of eccentric binary neutron star mergers: One-arm spiral instability and effects of neutron star spin. *Phys. Rev. D*, 93:024011, Jan 2016. doi: 10.1103/PhysRevD.93.024011. URL https://link.aps.org/doi/10.1103/PhysRevD.93.024011.

[219] John Ellis, Andi Hektor, Gert Htsi, Kristjan Kannike, Luca Marzola, Martti Raidal, and Ville Vaskonen. Search for dark matter effects on gravitational signals from neutron star mergers. *Physics Letters B*, 781:607 – 610, 2018. ISSN 0370-2693. doi: https://doi.org/10.1016/j.physletb.2018.04.048. URL http://www.sciencedirect.com/science/article/pii/S0370269318303423.

[220] Kent Yagi and Nicolas Yunes. I-Love-Q Relations in Neutron Stars and their Applications to Astrophysics, Gravitational Waves and Fundamental Physics. *Phys. Rev.*, D88(2):023009, 2013. doi: 10.1103/PhysRevD.88.023009.